Numerical studies of transition in wall-bounded flows

by

Ori Levin

December 2005
Technical Reports from
KTH Mechanics
SE-100 44 Stockholm, Sweden

Typsatt i $\mathcal{A}_{\mathcal{M}}\mathcal{S}$-LaTeX.

Akademisk avhandling som med tillstånd av Kungliga Tekniska Högskolan i Stockholm framlägges till offentlig granskning för avläggande av teknologie doktorsexamen fredagen den 16:e december 2005 kl 10.15 i sal F3, F-huset, Kungliga Tekniska Högskolan, Lindstedsvägen 26, Stockholm.

Universitetsservice US-AB, Stockholm 2005

Numerical studies of transition in wall-bounded flows

Ori Levin 2005
KTH Mechanics
SE-100 44 Stockholm, Sweden

Abstract

Disturbances introduced in wall-bounded flows can grow and lead to transition from laminar to turbulent flow. In order to reduce losses or enhance mixing in energy systems, a fundamental understanding of the flow stability and transition mechanism is important. In the present thesis, the stability, transition mechanism and early turbulent evolution of wall-bounded flows are studied. The stability is investigated by means of linear stability equations and the transition mechanism and turbulence are studied using direct numerical simulations. Three base flows are considered, the Falkner–Skan boundary layer, boundary layers subjected to wall suction and the Blasius wall jet. The stability with respect to the exponential growth of waves and the algebraic growth of optimal streaks is studied for the Falkner–Skan boundary layer. For the algebraic growth, the optimal initial location, where the optimal disturbance is introduced in the boundary layer, is found to move downstream with decreased pressure gradient. A unified transition prediction method incorporating the influences of pressure gradient and free-stream turbulence is suggested. The algebraic growth of streaks in boundary layers subjected to wall suction is calculated. It is found that the spatial analysis gives larger optimal growth than temporal theory. Furthermore, it is found that the optimal growth is larger if the suction begins a distance downstream of the leading edge. Thresholds for transition of periodic and localized disturbances as well as the spreading of turbulent spots in the asymptotic suction boundary layer are investigated for Reynolds number $Re = 500$, 800 and 1200 based on the displacement thickness and the free-stream velocity. It is found that the threshold amplitude scales like $Re^{-1.05}$ for transition initiated by streamwise vortices and random noise, like $Re^{-1.3}$ for oblique transition and like $Re^{-1.5}$ for the localized disturbance. The turbulent spot is found to take a bullet-shaped form that becomes more distinct and increases its spreading rate for higher Reynolds number. The Blasius wall jet is matched to the measured flow in an experimental wall-jet facility. Both the linear and nonlinear regime of introduced waves and streaks are investigated and compared to measurements. It is demonstrated that the streaks play an important role in the breakdown process where they suppress pairing and enhance breakdown to turbulence. Furthermore, statistics from the early turbulent regime are analyzed and reveal a reasonable self-similar behavior, which is most pronounced with inner scaling in the near-wall region.

Descriptors: Boundary layer, suction, wall jet, streaks, waves, periodic disturbance, localized disturbance, turbulent spot, algebraic growth, exponential growth, stability, transition thresholds, transition prediction, PSE, DNS.

Preface

This thesis considers the disturbance growth, transition and turbulent evolution of wall-bounded flows. The thesis is divided in two parts, the first part is a short introduction to the field and a summary of the following papers. The papers are re-set in the present thesis format and included in the second part of the thesis.

Paper 1. Levin, 0. & Henningson, D. S. 2003 Exponential vs algebraic growth and transition prediction in boundary layer flow. *Flow, Turbulence and Combustion* **70**, 183–210.

Paper 2. Byström, M. G., Levin, 0. & Henningson, D. S. 2005 Optimal disturbances in suction boundary layers. Submitted in a revised version.

Paper 3. Levin, 0., Chernoray, V. G., Löfdahl, L. & Henningson, D. S. 2005 A study of the Blasius wall jet. *Journal of Fluid Mechanics* **539**, 313–347.

Paper 4. Levin, 0., Davidsson, E. N. & Henningson, D. S. 2005 Transition thresholds in the asymptotic suction boundary layer. *Physics of Fluids*, In press.

Paper 5. Levin, 0. 2005 Turbulent spots in the asymptotic suction boundary layer.

Paper 6. Levin, 0., Herbst, A. H. & Henningson, D. S. 2005 Early turbulent evolution of the Blasius wall jet. Submitted.

Division of work between authors

The first paper deals with the energy growth of eigenmodes and non-modal optimal disturbances in the Falkner–Skan boundary layer with favorable, zero and adverse pressure gradients. The numerical codes are based on already existing codes at KTH Mechanics. The numerical implementations needed for this work were performed by Ori Levin (OL). The development of the theory as well as the writing of the manuscript itself were both carried out by OL with some assistance from Dan Henningson (DH).

The second paper is devoted to the energy growth of non-modal optimal disturbances in boundary layers subjected to wall suction. The numerical code for the spatial analysis is the same as for paper 1 with new subroutines for the base flow. The work was performed by Martin Bystöm (MB) as part of his Master Thesis with OL as the advisor. The writing was done by MB with some assistance from OL and DH.

The third paper is a numerical and experimental study of the stability of the Blasius wall jet. The work is a cooperation between KTH Mechanics and Thermo and Fluid Dynamics at Chalmers University of Technology (TFD). The numerical codes for the linear analysis are the same as for paper 1 with new subroutines for the base flow. The Direct Numerical Simulations were performed with a numerical code, already in use for many research projects. The code is based on a pseudospectral technique and is developed originally by Anders Lundbladh and DH. The numerical implementations needed for this work were performed by OL. The experimental work was done by Valery Chernoray (VC) at TFD. The writing was carried out by OL with some assistance from VC, Lennart Löfdahl at TFD and DH.

The fourth paper deals with energy thresholds for transition in the asymptotic suction boundary layer disturbed by streamwise vortices, oblique waves and noise. The numerical code for the temporal simulations is the same as for paper 3 with minor implementations by OL in order to account for the mass flux through the wall. The work was performed by OL and Niklas Davidsson (ND) and the writing was done by OL and ND with some advise from DH.

The fifth paper is on the thresholds for transition of localized disturbances, their breakdown to turbulence and the development of turbulent spots in the asymptotic suction boundary layer. The numerical code for the temporal simulations is the same as for paper 4. All the work was carried out by OL with some advise from DH.

The sixth paper is devoted to the early turbulent evolution of the Blasius wall jet. The numerical code for the spatial simulation, carried out by OL, is the same as for paper 3. All the figures and animations were prepared by OL. The analysis of the statistics was performed by OL and Astrid Herbst (AH). The writing was done by OL and AH with some advise from DH.

Contents

Part 1

Summary

CHAPTER 1

Introduction

A solid material possesses the property of rigidity, implying that it can withstand moderate shear stress without a permanent deformation. A true fluid, on the other hand, is by definition a material with no rigidity at all. Subjected to shear stress, no matter how small this stress may be, a fluid is bound to continuously deform. The fluids that all of us are most familiar with are water and air. Water is a liquid, while air is a gas, but that distinction is less important than might be imagined when it comes to fluid dynamics.

A fluid flow is usually defined as either laminar or turbulent. The laminar flow is characterized by an ordered, layered and predictable motion while the turbulent state consists of a chaotic, swirly and fluctuating motion. The difference between the two kinds of motions can easily be visualized in the kitchen while pouring water from the tap. If the tap is opened only a bit, the water that flows from the faucet is smooth and glassy, because the flow is laminar. When the tap is opened further, the flow speed increases and the water all of a sudden becomes white with small bubbles, accompanied by a louder noise. The jet of water has then become irregular and turbulent and air is mixed into it. The same phenomenon can be seen in the smoke streaming upward into still air from a burning cigarette. Immediately above the cigarette, the flow is laminar. A little higher up, it becomes rippled and diffusive as it becomes turbulent.

The two above everyday examples illustrate the effect of flow speed and distance on the cause of turbulence. As the flow velocity or the characteristic length of the flow problem increases, small disturbances introduced in the flow amplify and the laminar flow break down to turbulence. This phenomenon is called *transition.* There is one more quantity affecting the state of the flow, namely the viscosity of the fluid. For sufficiently large viscosity, motions that would cause turbulence are damped out and the flow stays laminar. For example, it is very hard to get the flow from a bottle of sirup to become turbulent since the viscosity of sirup is very high. Air with its considerably lower viscosity becomes turbulent very easily.

The basic difference between laminar and turbulent flows was dramatically demonstrated by Osborne Reynolds in a classical experiment at the hydraulics laboratory of the Engineering Department at Manchester University. Reynolds (1883) studied the flow inside a glass tube by injecting ink at the centerline of the pipe inlet. At low flow rates, the flow stayed laminar and the dye stream was observed to follow a well-defined straight path inside the tube. As the flow rate was increased, at some point in the tube, the dye streak broke up into a turbulent motion and spread throughout the cross section of the tube. He found that the value of a dimensionless parameter, now called Reynolds number, $Re = Ud/\nu$, where U is the mean velocity of the water through the tube, d the diameter of the tube and ν the kinematic viscosity of the water, governs the transition from laminar to turbulent flow. Reynolds made it clear, however, that there is no single *critical* value of Re, above which the flow becomes unstable and transition may occur. The whole matter is much more complicated and very sensitive to disturbances from the surroundings entering the pipe inlet. In fact, transition and its triggering mechanisms are even today not fully understood.

In a laminar flow, the shear stresses are smaller than in a turbulent flow and as a consequence, the friction drag over the surface of a wing is much lower. On the other hand, a laminar flow can not stay attached to the upper surface of a wing as far downstream as a turbulent flow since the pressure increases downstream. Instead, laminar separation occurs resulting in the formation of a wake and increased pressure drag. However, for a turbulent flow, separation is delayed due to the mixing provided of the chaotic motion and the total drag force decreases. That is also the reason why golf balls have dimples over the surface, to enforce turbulence and a smaller wake behind it. Due to the excellent mixing of a turbulent flow, it is required in chemical reactors and combustion engines. In some applications, it is important to keep the flow laminar and in others to enforce turbulence. Therefore an increased understanding of the triggering mechanisms of transition from laminar to turbulent flow and its foregoing amplification of introduced disturbances is important.

For transition to take place, some part of the flow has to be unstable to introduced disturbances. Such flows usually possess some kind of velocity shear, like the boundary layer and the free shear layer shown in figure 1.1. The boundary layer is the flow, in the lower part of the figure, over the horizontal flat plate subjected to a uniform oncoming flow with velocity U_0. Due to viscosity, the flow velocity varies from zero at the wall to the free-stream velocity a distance of the boundary layer thickness above the wall. The free shear layer, in the upper part of the figure, evolves from the difference in the streamwise velocity below the vertical wall and behind it. The streamwise velocity varies from the maximum velocity U_0 below the shear flow to zero above it. The thickness of the shear layers grow as the flow develops downstream. The combined flow field in figure 1.1 and the downstream interaction of the shear layers are defined as the Blasius wall jet.

The whole transition process consists of three stages: receptivity, disturbance growth and breakdown. In the *receptivity* stage, disturbances are initiated in the part of the flow where velocity shear is present. Typical sources from which disturbances can enter the shear flow are free-stream vortical structures, free-stream turbulence, acoustic waves, and for the case of wall-bounded shear

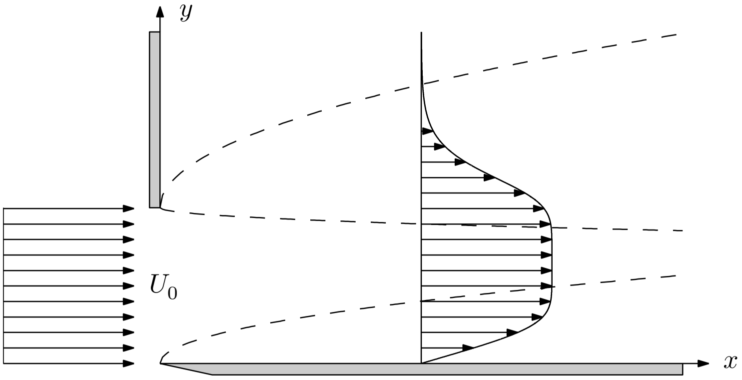

FIGURE 1.1. Wall-bounded and free shear layer flow that together form a wall jet.

flows, surface roughness and vibrations. Once a disturbance is introduced in the shear flow, it may *grow* or decay according to the stability characteristics of the base flow (the undisturbed flow field). When the disturbances are yet weak compared to the base flow, one can study linearized stability equations to determine the disturbance growth. In fact, the linear mechanisms are responsible for any disturbance energy growth, while the nonlinear effects only redistribute energy among different frequencies and scales of the flow (Henningson 1996). As the disturbances amplify, nonlinear effects start to be important and the distortion of the base flow begins to be apparent. The disturbances usually saturate when they have reached a large enough amplitude and a new laminar base flow, which normally is unstable to new disturbances, is established. In this stage, the usually rapid final nonlinear *breakdown* begins, followed by a multitude of scales and frequencies typical for a turbulent flow.

One way to stabilize a boundary layer and keep it laminar is to apply suction at the wall. As more suction that is applied the more persistent to incoming disturbances the boundary layer becomes. But the cost is the energy required to maintain the suction and an increased friction drag as the shear stress at the wall increases. If too much suction is applied, the friction drag can in fact exceed the value for a turbulent boundary layer. The optimal performance is the balance between retaining the flow laminar while keeping the energy consumption as low as possible. When uniform suction is used, the downstream growth of the boundary layer thickness changes and the flow evolves to a boundary layer with constant thickness, given that it is free from disturbances. Such a flow is defined as an asymptotic suction boundary layer.

In the present thesis, the disturbance growth, transition mechanism and early turbulent evolution of wall-bounded flows are studied. Three cases of base flows are considered:

(*i*) The Falkner–Skan boundary layer, which is the boundary layer over a flat plate with a favorable, zero or adverse streamwise pressure gradient. This flow is a good approximation to what can be found in parts of the boundary layer over a wing in flight. Over the front part of a wing, the pressure decreases downstream and the pressure gradient is said to be favorable. A short distance behind the leading edge, the pressure receives its lowest value and the pressure gradient is close to zero. Downstream, the pressure starts to increase again, what is defined as an adverse pressure gradient. The case with zero pressure gradient is also called Blasius boundary layer.

(*ii*) Boundary layers subjected to wall suction are appropriate flows to study if you are interested of stabilizing the flow over a wing. Both the semi suction boundary layer where constant suction is applied a distance downstream of the leading edge of a flat plate and the asymptotic suction boundary layer are studied. The latter case is the simplest boundary layer with wall suction and its flow profile is an analytical solution to the equations governing incompressible fluid motion.

(*iii*) The Blasius wall jet is the most unstable flow of the three studied cases. Laminar wall jets break down very easily with a rapid transition process. Most applications concern turbulent wall jets where they serve as cooling of gas turbine blades and combustion chambers and boundary layer control on wings and flaps to prevent turbulent separation.

In Chapter 2, the growth of weak disturbances are investigated by means of linearized disturbance equations. Both waves propagating in the direction of the flow and steady streaks orientated in the streamwise direction are considered. In Chapter 3, the behavior and breakdown of strong disturbances are studied by the use of direct numerical simulations (DNS) of the Navier–Stokes equations. The disturbances considered are streamwise propagating waves, streamwise elongated streaks, oblique waves, random noise and localized disturbances. In Chapter 4, the development of turbulent spots is investigated as well as turbulence statistics computed with direct numerical simulations. In Chapter 5, the main conclusions are summarized.

CHAPTER 2

Weak disturbances

2.1. Waves

The prediction of the stability of a given flow and the amplification of weak disturbances have been of interest to the fluid dynamics community for more than a century. An equation for the evolution of a disturbance, linearized around a mean velocity were first derived by Reyleigh (1880) for parallel inviscid flow. He also derived the criterion that for an unstable mode to exist in an inviscid flow, the mean velocity profile has to possess an inflection point. Fjørtoft (1950) later derived that a necessary condition for instability is that the inflection point has to be a maximum (rather than a minimum) of the shear stress. The traditional stability-analysis technique for viscous flow, independently derived by Orr (1907) and Sommerfeld (1908), is to solve the eigenvalue problem of the Orr–Sommerfeld (OS) equation, which is the linearized stability equation based on the assumption of parallel flow with wave-like disturbances. The unstable eigenmodes are historically referred to as Tollmien–Schlichting (TS) waves, after the work of Tollmien (1929) and Schlichting (1933), usually taking the form of exponentially growing two-dimensional waves. In fact, Squire (1933) stated that parallel shear flows first become unstable to two-dimensional waves at a value of the Reynolds number that is smaller than any value for which unstable three-dimensional waves exist. The stability of such waves depends on their frequency and the Reynolds number of the flow.

The effect of streamwise pressure gradients on the stability of boundary layers were studied by Pretsch (1941), who carried out stability calculations of the Falkner–Skan family. It was found that boundary layers subjected to adverse pressure gradients are more unstable and that accelerated flows are less unstable to two-dimensional waves than the Blasius boundary layer. The first successful experimental study of TS-waves was carried out by Schubauer & Skramstad (1947) who showed that wave disturbances may occur naturally in a Blasius boundary layer over a flat plate. They also confirmed the strong influence of the pressure gradient on the stability predicted by theory.

The application of wall suction is dramatically changing the stability of a boundary layer. Hocking (1975) modified the OS-equation in order to account for uniform suction. He found the critical Reynolds number (the lowest Reynolds number for unstable modes to exist) to be two orders of magnitude larger for the asymptotic suction boundary layer than that for the Blasius boundary layer.

The streamwise amplitude function of TS-waves in boundary layers has one large peak in the boundary layer and normally one smaller peak in the free stream. For wall jets, one more peak can be found. The temporal linear stability of a wall jet was examined theoretically by Chun & Schwarz (1967) by solving the OS-equation. The streamwise velocity fluctuation was found to exhibit two large peaks, one peak on each side of the wall-jet core and one smaller peak in the ambient flow. Bajura & Szewczyk (1970) performed hot-wire measurements in an air wall jet and found that the amplification rate of the peak in the outer shear layer is larger, and hence, the instability of the wall jet is controlled by the outer region. By solving the OS-equation, Mele *et al.* (1986) clarified the existence of two unstable modes in the wall jet. One mode, unstable at low disturbance frequencies, shows the highest amplitude close to the inflection point in the outer region of the wall jet, while the other mode, unstable at higher frequencies, attains the highest amplitude close to the wall. They concluded that the inviscid instability in the outer region governs the large-scale disturbances while the viscous instability governs the small-scale disturbances in the near-wall region.

The drawback of the assumption of parallel flow in the OS-problem is that it does not account for the growth of the thickness of a shear layer as the flow develops downstream. The idea of solving the parabolic evolution of disturbances in non-parallel boundary layers was first introduced by Floryan & Saric (1979) and later also by Hall (1983) for steady Görtler vortices. Bertolotti *et al.* (1992) developed the method of parabolic evolution of eigenmodes in boundary layers and derived the parabolized stability equations (PSE). The method is computationally very fast and has been shown to be in excellent agreement with DNS and experiments (see e.g. Hanifi 1995).

2.2. Streaks

In low disturbance environments, the transition in boundary layers is usually preceded by the exponential growth and breakdown of TS-waves. However, exponential instability involving unstable eigenmodes is not the only transition scenario. For a sufficiently large disturbance amplitude, algebraic non-modal growth can lead to so-called bypass transition, not associated with exponential instabilities. At a moderate or high lever of free-stream turbulence, many experimentalists have observed streaky structures, taking the form of elongated streamwise structures with narrow spanwise scales and much larger streamwise scales. This type of disturbance is historically denoted as the Klebanoff mode after the boundary-layer experiments of Klebanoff (1971). More recent experiments displaying streaky structures in boundary layers, subjected to various levels of free-stream turbulence, have been performed by e.g. Westin *et al.* (1994) and Matsubara & Alfredsson (2001).

Ellingsen & Palm (1975) performed linear stability analysis of inviscid channel flow. They showed that finite three-dimensional disturbances without streamwise variation can lead to instability, even though the basic velocity does not possess any inflection point. The instability leads to an increase linearly with time of the streamwise disturbances, producing alternating low and high velocity streaks. Landahl (1980) demonstrated that all parallel inviscid shear flows can be unstable to three-dimensional disturbances, which lead to a growth of the disturbance energy at least as fast as linearly in time. The physical interpretation of the formation of streaks is the lift-up effect, i.e. that fluid elements initially retain their horizontal momentum when displaced in the wall-normal direction, hence causing a streamwise disturbance.

Andersson *et al.* (1999) solved the linear stability equations for the Blasius boundary layer, taking the non-parallel effects into account, to optimize the input disturbance at the leading edge giving rise to the largest disturbance energy gain at the final downstream location. By going to the limit of large Reynolds number, it was shown that the optimal initial disturbance consists of streamwise vortices developing into streamwise streaks with zero frequency. The results agreed remarkably well with experimental data produced by Westin *et al.* (1994), irrespective of the absent optimization procedure in the experiments.

Since the asymptotic suction boundary layer is such stable to TS-waves, the formation and breakdown of streaks are the most likely transition scenario. The first measurements of streaks in a fully developed asymptotic suction boundary layer subjected to free-stream turbulence were performed by Fransson & Alfredsson (2003). The experimental results were also compared to the streaks evolving from optimal disturbances calculated by means of linear stability equations in the temporal framework (Fransson & Corbett 2003). The algebraic growth was found to be less but of the order of that occurring in the Blasius boundary layer. On the other hand, algebraically exited disturbances were shown to persist longer in the asymptotic suction boundary layer.

Wall jets are very unstable to two-dimensional waves and bypass transition due to breakdown of streaks is not likely. On the other hand, three-dimensional disturbances are needed, yet of a very small level, for breakdown of the waves to happen. Therefore, the presence of streaks in the unstable upper shear layer of the wall jet may enhance transition to turbulence.

2.3. Growth of weak disturbances

Waves and streaks are associated with different scales. Waves propagating in the downstream direction have a wavelength in the order of the thickness of the shear layer while streaks usually have much larger streamwise scales. The result is that the corresponding frequency is much larger for waves than for streaks. The opposite is true for the associated spanwise scales, which are narrow for streaks and much larger for waves. Yet, the exponential growth of waves and the algebraic growth of streaks can be described by a common set of stability equations.

2.3.1. *Linear disturbance equations*

Consider an incompressible wall-bounded flow over a flat plate, such as the boundary layer and the wall jet illustrated in figure 1.1. Fluid is blown tangentially along a wall and shear layers are growing downstream. When working with such flows subjected to weak disturbances, the boundary-layer scalings are appropriate. Thus, the streamwise coordinate x is scaled with an arbitrary distance l from the leading edge, while the wall-normal and spanwise coordinates y and z, respectively, are scaled with the boundary-layer parameter $\delta = \sqrt{\nu l / U_l}$, where ν is the kinematic viscosity of the fluid and U_l is the undisturbed streamwise velocity in the free stream above the boundary layer and in the wall jet core, at the location l. In the case of a boundary layer with zero pressure gradient, the free-stream velocity is constant, thus $U_l = U_0$, where U_0 is the free-stream velocity at the leading edge. The streamwise velocity U is scaled with U_l, while the wall-normal and spanwise velocities V and W, respectively, are scaled with U_l/Re_δ, where $Re_\delta = U_l\delta/\nu$. The pressure P is scaled with $\rho U_l^2/Re_\delta^2$, where ρ is the density of the fluid, and the time t is scaled with l/U_l.

We want to study the linear stability of the flow at a high Reynolds number. The incompressible Navier–Stokes equations are linearized around the two-dimensional steady base flow $\big(U(x,y),\, V(x,y),\, 0\big)$ to obtain the stability equations for the spatial evolution of three-dimensional time-dependent disturbances $\big(u(x,y,z,t),\, v(x,y,z,t),\, w(x,y,z,t),\, p(x,y,z,t)\big)$. The disturbances, which are scaled as the base flow, are assumed to be periodic in the spanwise direction and in time and are decomposed into an amplitude function with weak streamwise variation and a phase function as

$$\boldsymbol{f} = \hat{\boldsymbol{f}}(x,y) \exp\Big(\mathrm{i} Re_\delta \int_{x_0}^{x} \alpha(x)\, dx + \mathrm{i}\beta z - \mathrm{i}\omega t\Big), \tag{2.1}$$

where $\boldsymbol{f} = (u,v,w,p)^T$. The complex streamwise wavenumber α captures the fast wave-like variation of the modes and is therefore scaled with $1/\delta$ but α itself is assumed to vary slowly with x. The real spanwise wavenumber β and the real angular frequency ω are scaled in a consistent way with z and t, respectively. By introducing (2.1) in the linearized Navier–Stokes equations, the parabolized stability equations can be written

$$\frac{\partial \hat{\boldsymbol{f}}}{\partial x} = \mathcal{L}\hat{\boldsymbol{f}}, \tag{2.2}$$

where $\mathcal{L}$ is a linear operator. The initial conditions and the boundary conditions are specified for the disturbance velocities. The boundary conditions are, no-slip conditions at the wall and homogeneous conditions far above the wall. The state equation (2.2) is integrated in the downstream direction from the location x_0, where initial conditions are specified, to the location x_1. The solution may be written in an input-output formulation

$$\hat{\boldsymbol{f}}_1 = \mathcal{A}\hat{\boldsymbol{f}}_0, \tag{2.3}$$

where $\mathcal{A}$ is a linear operator. The disturbance growth is measured by the increase of the kinetic disturbance energy E, which depends on x, β, ω and the Reynolds number of the flow.

2.3.2. *Algebraic growth*

Consider solutions to (2.2) associated with disturbances with weak streamwise variations. Since the amplitude function captures weak variations, the streamwise wavenumber is set to zero. We are interested of maximizing the disturbance energy in the downstream location x_1 by optimizing the initial disturbance in the initial location x_0 with given initial energy. That is, we want to maximize the disturbance growth

$$G(x_0, x_1, \beta, \omega, Re_\delta) = \frac{E(x_1)}{E(x_0)}. \tag{2.4}$$

The optimization procedure is based on the adjoint equation to the state equation (2.2). By taking the inner product between an adjoint state vector $\boldsymbol{g}$ and the state equation and integrating by parts

$$\big(\boldsymbol{g}, \frac{\partial \hat{\boldsymbol{f}}}{\partial x} - \mathcal{L}\hat{\boldsymbol{f}}\big) = \mathrm{BT} - \big(\hat{\boldsymbol{f}}, \frac{\partial \boldsymbol{g}}{\partial x} + \mathcal{L}^*\boldsymbol{g}\big), \tag{2.5}$$

the adjoint equation follows

$$-\frac{\partial \boldsymbol{g}}{\partial x} = \mathcal{L}^*\boldsymbol{g}, \tag{2.6}$$

where $\mathcal{L}^*$ denotes the adjoint operator to $\mathcal{L}$. The appropriate boundary conditions and initial conditions to the adjoint state equation (2.6) follows from the boundary terms BT and are specified in paper 1. The adjoint state equation is integrated in the upstream direction and the solution may be written

$$\boldsymbol{g}_0 = \mathcal{A}^*\boldsymbol{g}_1, \tag{2.7}$$

where $\mathcal{A}^*$ denotes the adjoint operator to $\mathcal{A}$. The maximum growth, where the energy is evaluated as an inner product, can be written

$$G_{max} = \max \frac{(\hat{\boldsymbol{f}}_1, \hat{\boldsymbol{f}}_1)}{(\hat{\boldsymbol{f}}_0, \hat{\boldsymbol{f}}_0)} = \max \frac{(\mathcal{A}^*\mathcal{A}\hat{\boldsymbol{f}}_0, \hat{\boldsymbol{f}}_0)}{(\hat{\boldsymbol{f}}_0, \hat{\boldsymbol{f}}_0)}, \tag{2.8}$$

and is attained as the largest eigenvalue of the eigenvalue problem

$$\mathcal{A}^*\mathcal{A}\hat{\boldsymbol{f}}_0 = G\hat{\boldsymbol{f}}_0. \tag{2.9}$$

The most natural attempt to calculate the optimal initial disturbance and its associated maximum growth is by power iterations

$$\hat{\boldsymbol{f}}_0^{n+1} = \mathcal{A}^*\mathcal{A}\hat{\boldsymbol{f}}_0^{n}, \tag{2.10}$$

where the initial disturbance is scaled to the given initial energy in each iteration n. The optimization procedure is valid in the limit of large Reynolds number. Because of the difference in scales between the streamwise velocity and the velocities in the cross-flow plane, the maximum growth is obtained for initial disturbances with a zero streamwise component resulting in streamwise streaks with negligible cross-flow components. Furthermore, a growth that are independent of Reynolds number can be defined as

$$\overline{G} = \lim_{Re_\delta \to \infty} \frac{G}{Re_\delta^2} \tag{2.11}$$

2.3.3. *Exponential growth*

Consider solutions to (2.2) associated with wave-like disturbances, i.e. where α in the phase function is not equal to zero. As both the amplitude function and the phase function depend on x, one more equation is required. We require both the amplitude function and the wavenumber α to change slowly in the streamwise direction, and specify a normalization condition on the amplitude function

$$\int_0^\infty \left(\overline{\hat{u}}\frac{\partial \hat{u}}{\partial x} + \frac{\overline{\hat{v}}}{Re_\delta^2}\frac{\partial \hat{v}}{\partial x} + \frac{\overline{\hat{w}}}{Re_\delta^2}\frac{\partial \hat{w}}{\partial x}\right) \mathrm{d}y = 0, \tag{2.12}$$

where bars denote complex conjugate. The Reynolds number appears due to the different scaling of streamwise and cross-flow velocities. Other conditions are possible and are presented in Bertolotti *et al.* (1992). The normalization condition specifies how much growth and sinusoidal variation are represented by the amplitude function and the phase function, respectively. The initial condition is taken as the least stable eigenfunction from parallel theory with corresponding eigenvalue $\alpha(x_0)$. The exponential growth is maximized in the sense that the envelope of the most amplified eigenmode is calculated.

2.4. Application to the Falkner–Skan boundary layer

In the first paper, the stability of the Falkner–Skan boundary layer to exponentially growing waves and non-modal streaks is analyzed. A comparison of the algebraic growth with the exponential growth is performed and a unified transition prediction method based on available experimental data is suggested.

2.4.1. *Comparison of algebraic and exponential growth*

Linear stability analysis is performed with the Falkner–Skan boundary layer as the base flow. The acceleration of the free-stream velocity driven by the pressure gradient is described by the Hartree parameter β_H in the formulation of a similarity solution. The stability of optimal disturbances and exponentially growing waves are examined for three base flows with favorable, zero and adverse pressure gradients. The corresponding Hartree parameters are $\beta_H = 0.1, 0, -0.1$. Figure 2.1 shows the stremwise velocity profiles and the downstream growth of the boundary layer thickness for the three cases. The dashed lines show Blasius boundary layer with zero pressure gradient and therefore also constant free-stream velocity. The solid lines show the accelerated flow with favorable pressure gradient and a thinner boundary layer. The

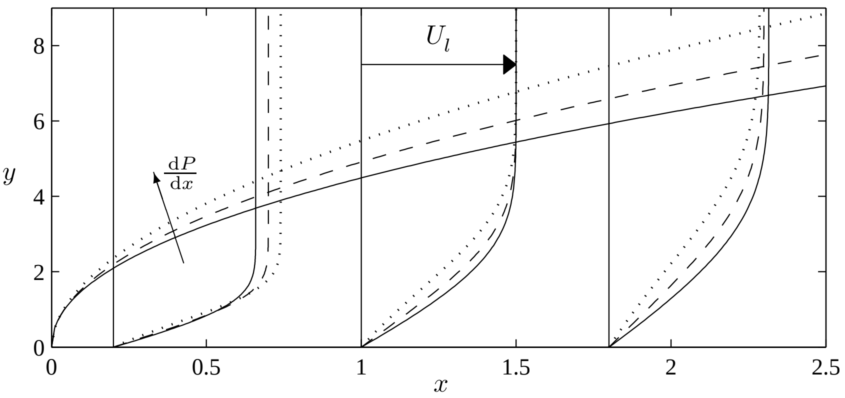

FIGURE 2.1. Downstream development of streamwise velocity profiles and thickness of the Falkner–Skan boundary layer with favorable (—), zero (– – –) and adverse (···) pressure gradients.

dotted lines show the decelerated flow with adverse pressure gradient and a thicker boundary layer.

The initial streamwise location, where the disturbance is introduced in the boundary layer, has a significant impact on the algebraic growth. Figure 2.2(a) shows the amplification, $N = \ln\sqrt{G}$, of the optimal disturbances as a function of initial location for $\beta = 0.5$ and $\omega = 0$. Disturbances introduced closer to the leading edge, than the optimal initial location, grow with a slower rate, while disturbances introduced further downstream grow in a larger rate but do not have distance enough to grow as much before the final location. The slower growth rate for disturbances introduced close to the leading edge is due to the influence of the boundary layer thickness. Upstream of the optimal initial location, which moves downstream with decreased pressure gradient, the boundary layer is not thick enough for the lift-up effect to cause the optimal disturbance. The optimization of the initial location has the advantage of ensuring that the true optimal disturbances are found. Since the adjoint-based optimization technique optimizes the initial disturbance with respect to the disturbance energy in the final location and we are interested in the maximum energy in the whole domain, the true optimum only results when the maximum energy appears in the final location. The optimization of the initial location does not only give the optimal growth, it also ensures that the maximum energy is reached at the final location.

For algebraic growth of optimal disturbances, the optimal initial location moves downstream with increased spanwise wavenumber and angular frequency of the disturbance. Furthermore, the optimal spanwise wavenumber increases with decreased pressure gradient, while the optimal angular frequency is equal

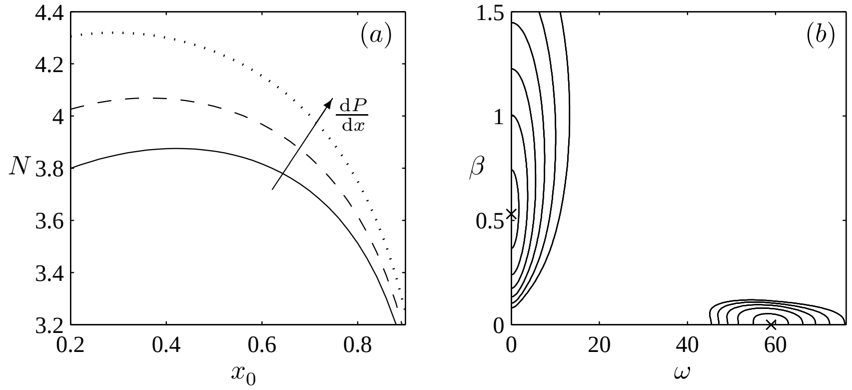

FIGURE 2.2. (*a*) Lines as in figure 2.1. Algebraic amplification versus initial location for Falkner–Skan flow at $Re_\delta = 1000$ with $\beta = 0.5$ and $\omega = 0$. (*b*) Contours of constant algebraic and exponential amplification for the Blasius boundary layer at $Re_\delta = 1000$. The contour spacing is 0.2 and the peak values are indicated with crosses. The optimal disturbances are calculated with the optimal initial locations.

to zero. For exponential growth of modal disturbances, the optimal angular frequency increases with decreased pressure gradient, while the optimal spanwise wavenumber is equal to zero, as expected according to the Squire's theorem (Squire 1933).

In both the algebraic and exponential growth scenarios, the growth increases with increased pressure gradient, although the effect is much more pronounced for the exponential growth. Therefore, in a comparison of the two different growth scenarios at $Re_\delta = 1000$, the algebraic growth is much larger for the base flow with a favorable pressure gradient and the exponential growth is much larger for the base flow with an adverse pressure gradient, while they are comparable for the Blasius boundary layer. Figure 2.2(*b*) shows the contours of constant algebraic and exponential amplification for the Blasius boundary layer at $Re_\delta = 1000$. The optimal disturbances are calculated with the optimal initial locations. The exponential growth is maximized in the sense that the most amplified eigenmode is calculated from the lower-branch neutral point to $x_1 = 1$ or the upper-branch neutral point, if it appears for a lower value.

2.4.2. *Transition prediction based on linear theory*

In the transition community, the e^N-method is a well known transition-prediction tool and has been shown to fairly accurately predict transition for simple flows. It was developed independently by Smith & Gamberoni (1956) and van Ingen (1956) and empirically correlates the exponentially growing amplification of linear eigenmodes with the onset of transition. Transition takes place when the amplitude of the most amplified disturbance reaches e^N times its initial amplitude. The e^N-method does not account for the receptivity process. However, Smith & Gamberoni (1956) and van Ingen (1956) reported, after analyzing data from a large number of low-disturbance experiments, that the amplification between 8 and 11 fairly well describes the onset and end of the transition region. They also concluded that those values decrease with increasing free-stream turbulence. A modification of the e^N-method in order to account for free-stream turbulence was proposed by Mack (1977). The free-stream turbulence level Tu was correlated to the amplification N by comparing the transition Reynolds number Re_T from experimental flat-plate boundary layer data collected by Dryden (1959) with parallel linear stability theory for the Blasius boundary layer. Mack (1977) suggested the following relation for the amplification at transition

$$N = -8.43 - 2.4 \ln Tu, \tag{2.13}$$

which he claimed is valid in the range $0.1\,\% < Tu < 2\,\%$. For a free-stream turbulence level less than $0.1\,\%$, he mentioned that the dominant disturbance source is thought to be wind-tunnel noise rather than turbulence.

Andersson *et al.* (1999) made an attempt at prediction of bypass transition due to algebraic growth by correlating the transition Reynolds number and the free-stream turbulence level

$$Re_T Tu = K, \tag{2.14}$$

where K should be constant for free-stream turbulence levels in the range $1\,\% < Tu < 5\,\%$. By comparison of different experimental studies, the constant was chosen as $K = 12$.

Other empirical transition-prediction correlations involving the effects of free-stream turbulence and streamwise pressure gradient have been developed. van Driest & Blumer (1963) postulated that transition occurs when the maximum vorticity Reynolds number reaches a critical value, to be correlated with the pressure gradient and free-stream turbulence level. In the case of zero pressure gradient, their formula correlated with experiments agrees well with (2.14). Another example is a model of Abu-Ghannam & Shaw (1980), which gives the Reynolds number based on the momentum thickness θ, at the start and end of the transition region. The only inputs to the model are the free-stream turbulence level and the pressure gradient parameter $\lambda_\theta = (\theta^2/\nu)\partial U_l/\partial x$. More advanced transition prediction and studies of the transition phenomena itself can be made by numerical simulations such as the nonlinear PSE technique (e.g. Hein *et al.* 1999) and DNS.

The transition model of Andersson *et al.* (1999) can be complemented with the addition of base flows with various pressure gradients. The model is based on three assumptions.

1. Assume that the initial disturbance energy is proportional to the free-stream turbulence energy

$$E(x_0) \propto Tu^2, \tag{2.15}$$

for isotropic turbulence with the free-stream turbulence level defined as $Tu = \sqrt{\overline{u'^2}}/U_l$. Here u' is the fluctuating streamwise velocity in the free stream and the overbar denotes the temporal mean.

2. Assume that the initial disturbance grows with the optimal rate
$$E(x_1) = GE(x_0) = \overline{G}Re_\delta^2 E(x_0). \tag{2.16}$$
3. Assume that transition occurs when the final energy reaches a specific value E_T, regardless of the pressure gradient of the base flow
$$E(x_1) = E_T. \tag{2.17}$$

Combining assumptions (2.15–2.17) yields the transition model
$$Re_T Tu = \frac{k}{\sqrt{\overline{G}}}, \tag{2.18}$$
where k should be constant. Using the same correlation as Andersson *et al.* (1999) and the optimal growth in the Blasius boundary layer gives $k = 0.70$. This model differs from the one of Andersson *et al.* (1999) in the sense that the growth is optimized over the initial location and the disturbances does not evolve from the leading edge.

The influence of free-stream turbulence on the generation of TS-waves is not conclusive. In fact, Boiko *et al.* (1994) made experiments on the behavior of controlled TS-waves, introduced by means of a vibrating ribbon, in a boundary layer subjected to $Tu = 1.5\,\%$. The measured amplification rates for the waves in the presence of the turbulence generating grid were smaller than for regular TS-waves, and damping set in further upstream than in the absence of the turbulence generating grid. Thus, we make the simple assumption that transition resulting from exponentially growing disturbances occurs at $N = 8$, the dashed line in figure 2.3(a), irrespective of the free-stream turbulence level.

Figure 2.3(b) shows the transition Reynolds number based on the results from the linear stability analysis and the transition model discussed above for free-stream turbulence. The straight part of the lines represents the transition Reynolds number for exponentially growing modal disturbances and the curved part represents bypass transition. For high free-stream turbulence levels, transition occurs as a result of the breakdown of streaky structures and for low free-stream turbulence levels as a result of exponentially growing disturbances. The cross-over point occurs where the bypass-transition model predicts a higher transition Reynolds number than for the exponentially growing disturbances. According to the model, bypass transition occurs in the Blasius boundary layer (dashed lines) for a free-stream turbulence level higher than 0.76 %. Similar results have been found in experiments. Suder *et al.* (1988) found in their experiment that the bypass mechanism prevailed for free-stream turbulence levels of 0.65 % and higher. Kosorygin & Polyakov (1990) suggested that TS-waves and streaks can coexist and interact for free-stream turbulence levels up to approximately 0.7 %. However, the model does not account for the interaction between TS-waves and streaks.

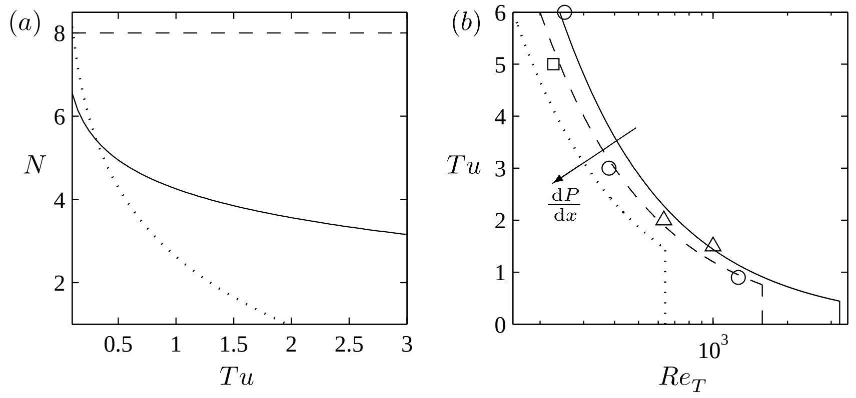

FIGURE 2.3. (*a*) Predicted amplification at transition versus free-stream turbulence level given in percent for algebraic (—) and exponential (− − −) growth. Model of Mack (1977) (···). (*b*) Lines as in figure 2.1. Predicted transition contour in the Re_T-Tu plane with the turbulence level given in percent. Experimental data for the Blasius boundary layer from Matsubara & Alfredsson (2001) (△) and Roach & Brierley (1992) (○). Numerical data from Yang & Voke (1991) (□).

2.5. Application to boundary layers with wall suction

In the second paper, a comparison of the algebraic growth of spatially developing streaks in the asymptotic suction boundary layer and the semi suction boundary layer is done. The difference between spatial and temporal theory is also considered.

2.5.1. *Suction boundary layers*

In the boundary-layer experiment of Fransson & Alfredsson (2003), suction was applied through a plate of porous material. However, the leading-edge part of the flat plate was made of an impermeable material allowing the boundary layer to develop and grow downstream until it reaches the porous plate. Downstream of this position, the flow undergoes an evolution from the Blasius profile towards that of the asymptotic suction boundary layer, which have a constant boundary layer thickness. The semi suction boundary layer, where uniform suction is applied from the distance l downstream of the leading edge of a flat plate can be calculated with the boundary-layer equations. Figure 2.4 shows the displacement thickness of the calculated flow compared with measurements from Fransson & Alfredsson (2003). In order to avoid a discontinues jump in the suction rate with a corresponding kink in the development of the boundary layer thickness, the suction is smoothly increased from zero to its full value over a short distance, see the zoom-up in figure 2.4. On the right-hand side of figure 2.4, the profile of the asymptotic suction boundary layer is shown. It is

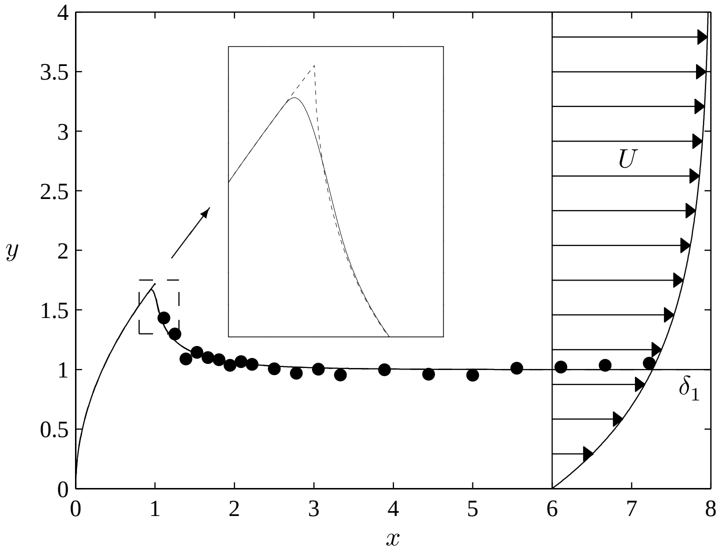

Figure 2.4. Calculated displacement thickness of the semi suction boundary layer compared with measurements (●) from Fransson & Alfredsson (2003). The zoom-up shows the starting position of abruptly (— — —) and smoothly (—) applied suction. On the right-hand side, the profile of the asymptotic suction boundary layer is shown.

an analytical solution to the Navier–Stokes equations and can be written as

$$U(y) = U_0\,[1 - \exp(-y^* V_0/\nu)]\,, \quad V = -V_0, \tag{2.19}$$

where y^* is the dimensional wall-normal coordinate and $-V_0$ is the suction velocity. The analytical solution allows the displacement thickness to be calculated exactly, $\delta_1 = \nu/V_0$, and the Reynolds number based on the displacement thickness to be expressed as the velocity ratio, $Re_{\delta_1} = U_0/V_0$. Thus, for this flow it is natural to use the displacement thickness as the length scale. However, if we choose $l = Re_{\delta_1}\delta_1$ it follows that $\delta = \delta_1$ and accordingly $Re_\delta = Re_{\delta_1}$. In the experiment of Fransson & Alfredsson (2003), the suction was applied from 360 mm downstream of the leading edge and the suction Reynolds number was $Re_{\delta_1} = 347$.

2.5.2. *Algebraic growth*

Fransson & Corbett (2003) performed temporal stability analysis of the asymptotic suction boundary layer and compared the spanwise scales of optimally growing streaks with those observed in the experiment of Fransson & Alfredsson (2003). Here, a twofold improvement is done by performing a spatial stability analysis of the semi suction boundary layer. Fransson & Corbett (2003)

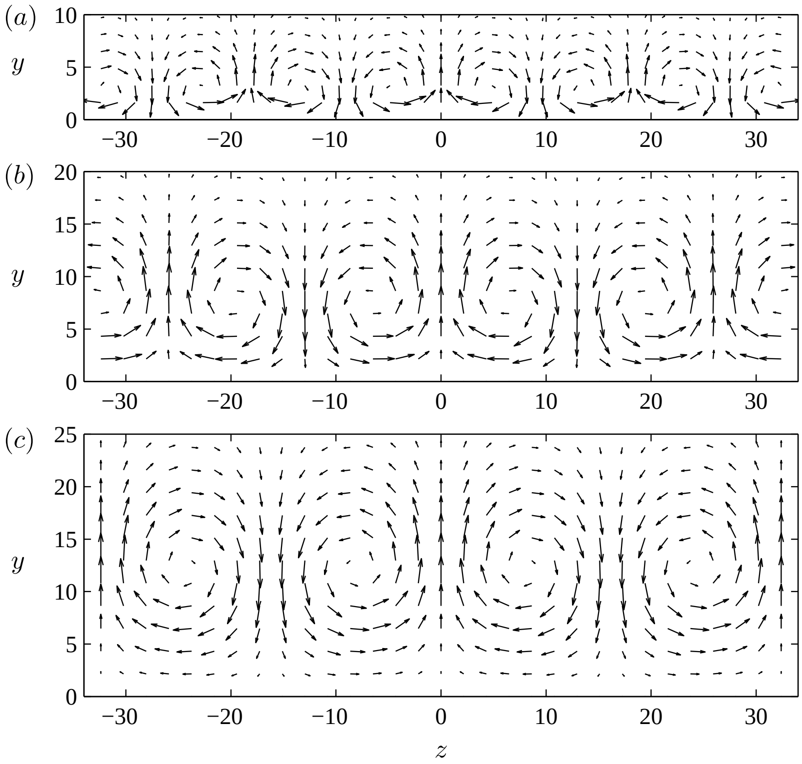

FIGURE 2.5. Optimal disturbances in the semi suction boundary layer at $Re_{\delta_1} = 347$. (*a*) $0 \le x \le 2$. (*b*) $0 \le x \le 6$. (*c*) $0 \le x \le 10$.

found that the optimal disturbance has the spanwise wavenumber $\beta = 0.53$. With spatial analysis, the optimal growth is 16 % higher corresponding to a disturbance with spanwise wavenumber $\beta = 0.52$.

The suction boundary layers are studied over nine streamwise intervals, starting at $x_0 = 0$ and with suction from $x = 1$ to the end of the interval. The length of the interval is varied by changing the end position from $x_1 = 2$ to $x_1 = 10$ in steps of one. The optimal disturbance at the initial position takes the form of streamwise aligned vortex pairs, as seen in figure 2.5, which shows the optimal disturbances in the semi suction boundary layer at $Re_{\delta_1} = 347$ for three intervals. It can be seen that the vortex cores of the optimal disturbance move upward and the vortices grow in size when the streamwise interval is prolonged. Thus, the optimal spanwise wavenumber decreases as the interval is prolonged. Furthermore, the corresponding optimal growth decreases with increased interval and the optimal angular frequency is zero.

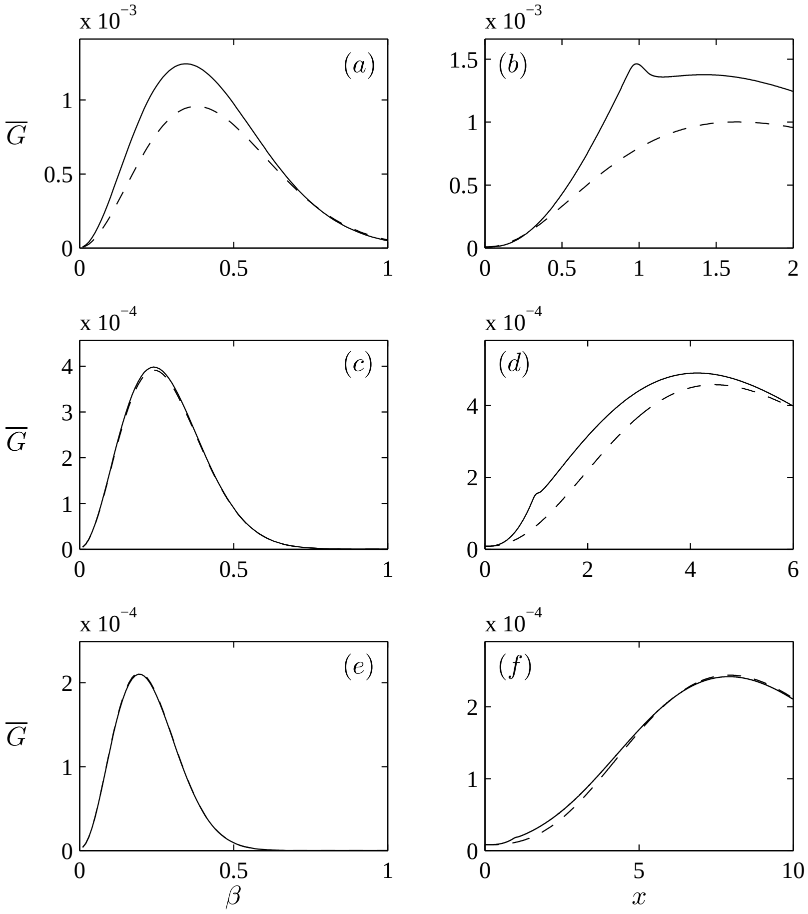

FIGURE 2.6. Comparison of algebraic growth in the asymptotic suction boundary layer (– – –) and the semi suction boundary layer (—) at $Re_{\delta_1} = 347$. (a, b) $0 \leq x \leq 2$. (c, d) $0 \leq x \leq 6$. (e, f) $0 \leq x \leq 10$.

Figure 2.6 shows a comparison of the optimal growth versus spanwise wavenumber and streamwise coordinate, with the optimal spanwise wavenumber, between the semi suction boundary layer and the asymptotic suction boundary layer. It reveals that for the shortest interval, the semi suction boundary layer gives a 25 % higher optimal growth than for the asymptotic suction boundary layer. The optimal growth also occurs at a lower spanwise wavenumber. Studying the growth as function of streamwise coordinate, we conclude that the reason for the difference in growth is the contribution from the Blasius profile at the beginning of the interval. However, the differences in growth and optimal spanwise wavenumber decrease as the interval is prolonged.

2.6. Application to the Blasius wall jet

In the third paper, the Blasius wall jet is constructed and matched to an experimental set-up. The stability of the flow to eigenwaves and non-modal streaks is analyzed and compared to the experiments.

2.6.1. *Comparison of linear theory with experiments*

Linear stability analysis is performed with the Blasius wall jet as the base flow. The stability of optimal disturbances and exponential growing waves is examined and compared to measurements performed in the wall-jet facility at Chalmers University of Technology. The base flow is matched to the experiment with the maximum outlet velocity $U_0 = 15.4\,\mathrm{m\,s^{-1}}$, corresponding to the Reynolds number $Re_\delta = 173$. Due to growing boundary layers in the experimental nozzle, a virtual slot is placed the distance $l = 29\,\mathrm{mm}$ upstream of the experimental nozzle opening and the virtual slot height is $b^* = 2.06\,\mathrm{mm}$ corresponding to the non-dimensional value $b = 12.3$. A comparison of the base flow with the measured hot-wire data is shown in figure 2.7(a). The agreement increases downstream of the nozzle opening. The largest disagreement is observed in the upper part of the wall jet. This is due to a jump of the boundary conditions that occur on the top lip of the nozzle as the flow leaves, resulting in a kink of the experimental velocity profile. However, with increased downstream distance, the influence of the nozzle disappears.

The stability analysis reveals a very high instability of the flow to two-dimensional eigenmodes and a rather high instability to non-modal streaks. The waves are triggered by a loudspeaker in the experiment and the frequency was chosen close to the natural dominating flow frequency, namely 1221 Hz corresponding to $\omega = 14.4$. Both in the experiment and in the computation, the most amplified frequency decreases with increased streamwise location. Figure 2.7(b) shows a comparison of the computed streamwise amplitude distribution and the measurement at the location $x = 1.55$. The measurement was performed with three different forcing amplitudes, 0.3 %, 1.1 % and 1.7 %, measured at $x = 1.55$, and the agreement in the results between the different forcing amplitudes indicates the linearity of the disturbance. The disturbance has a very typical shape and the peak in the shear-layer region is in antiphase to the peak near the wall. The deviation between the linear stability analysis and the experiment in the upper part of the wall jet is because the waves in the experiment are not fully developed eigenmodes so close to the nozzle opening, however, the agreement improves downstream.

The computed optimal disturbance consists of streamwise vortices developing into streamwise streaks. Between two vortices, the flow is either moving upward or downward. Where the flow is moving upward between two vortices, high-momentum fluid is moved up from the jet core, producing a high-velocity streak in the shear-layer region of the wall jet. In the boundary-layer region, a weak low-velocity streak is formed below the high-velocity streak, since the upward motion of fluid there carries low-momentum fluid from the wall region.

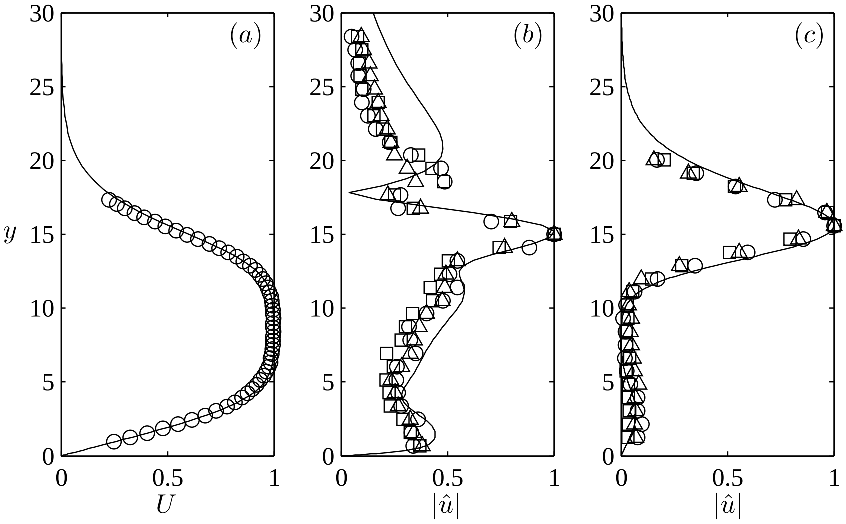

FIGURE 2.7. Comparison of computations (—) and measurements of the Blasius wall jet at $x = 1.55$ for $Re_\delta = 173$. The disturbance amplitudes are normalized with their maximum value. (*a*) Computed and measured (○) base flow. (*b*) Streamwise wave amplitude for $\omega = 14.4$. The disturbance are triggered in the experiment by a loudspeaker and have the amplitudes 0.3 % (○), 1.1 % (□) and 1.7 % (△). (*c*) Streamwise streak amplitude. The optimal disturbance are calculated for $\beta = 0.211$, $\omega = 0$, $x_0 = 0.403$ and $x_1 = 1.55$. The experimental results are taken from three spanwise scales corresponding to $\beta = 0.176$ (○), $\beta = 0.218$ (□) and $\beta = 0.264$ (△).

The opposite motion results, half a wavelength away, where the flow is moving downward between two vortices, producing a low-velocity streak in the shear-layer region and a weak high-velocity streak in the boundary-layer region. In figure 2.7(*c*), the resulting normalized streak from the optimal disturbance, calculated for $\beta = 0.211$, $\omega = 0$, $x_0 = 0.403$ and $x_1 = 1.55$ is compared with the measured streaks with spanwise scales $\beta = 0.264$, 0.218 and 0.176. In the experiment, the streaks are introduced in the flow by periodically distributed roughness elements that are located onto the top lip of the nozzle. Both in the computation and in the experiment, the streak remains very similar for different spanwise wavenumber β. The same is true in the computation for different initial location, x_0.

CHAPTER 3

Strong disturbances

3.1. Numerical method and disturbance generation

In the present chapter as well as the next one, all simulations of the flows are performed by solving the Navier–Stokes equations directly. That is, the equations governing incompressible fluid motion are numerically solved without any simplifying assumptions. This requires that all the relevant scales of the flow must by resolved and results in large computational efforts, both in terms of memory and effective time of the calculation.

The in-house numerical code at KTH Mechanics (Lundbladh *et al.* 1999) uses spectral methods to solve the three-dimensional time-dependent incompressible Navier–Stokes equations. All velocities and lengths are scaled by the free-stream velocity and the displacement thickness at the inlet of the computational box, respectively. The time, frequency and wavenumbers are scaled correspondingly. The discretization in the streamwise and spanwise directions makes use of Fourier series expansions, which enforces periodic solutions. The discretization in the wall-normal direction is represented with Chebyshev polynomial series. A pseudospectral treatment of the nonlinear terms is used. The time advancement used is a second-order Crank–Nicolson method for the linear terms and a four-step low-storage third-order Runge–Kutta method for the nonlinear terms. Aliasing errors arising from the evaluation of the convective terms are removed by dealiasing by padding and truncation using the 3/2-rule when the FFTs are calculated in the wall-parallel planes. In the wall-normal direction, it has been found that increasing the resolution is more efficient than the use of dealiasing.

At the wall, a no-slip boundary condition is specified and at the upper boundary, a generalized boundary condition is applied in Fourier space with different coefficients for each wavenumber. The condition represents a potential flow solution decaying away from the upper edge of the computational box. This condition decreases the required box height by damping the higher frequencies rather than forcing the disturbance velocities to a rapid decay. In the horizontal directions, periodic boundary conditions are used.

For spatially growing flows such as the Falkner–Skan boundary layer and the Blasius wall jet, a fringe region (Nordström *et al.* 1999) is added in the downstream end of the computational domain to fulfill the necessary periodic boundary condition in the streamwise direction, required by the spectral discretization. In this region, the flow is smoothly forced to the desired inflow solution. When studying parallel flows, such as the asymptotic suction boundary layer with periodic or localized disturbances, the advantage of omitting the fringe region can be used.

The present numerical implementation provides several possibilities for disturbance generation. Disturbances can be included in the flow by a body force, by blowing and suction at the wall through non-homogeneous boundary conditions and by adding them in the initial velocity field. When a fringe region is present, disturbances can be forced in it and thereby be included in the desired inflow solution.

3.2. DNS of the Blasius wall jet

In the third paper, waves and streaks are introduced in the Blasius wall jet and the nonlinear interaction and transition process are studied by means of DNS.

3.2.1. *Spectral analysis*

Waves and streaks from the linear stability calculations (figure 2.7) are excited in the DNS. The amplitudes, which are chosen to obtain a similar transition scenario as in the experiment, are prescribed in the beginning of the computational box to 0.1 % and 3 % of the wall-jet core velocity, respectively.

A convenient way to study the nonlinear interaction between the waves and the streaks is to look at the energy development of the Fourier components shown in figure 3.1. The velocity components are Fourier transformed in time and in the spanwise direction and (ω_1, β_1) denotes the frequency and spanwise wavenumber, each normalized with the corresponding fundamental frequency and wavenumber. Thus, the waves and the streaks are represented by $(1, 0)$ and $(0, 1)$, respectively, and are shown as black solid lines. Before nonlinear interaction sets in, the modes amplify in agreement with the linear theory as observed in the beginning of the computational box, where the waves grow exponentially and the streaks have an algebraic growth. The results from the PSE are shown as circles and the agreement is excellent. Close to the nozzle opening, the two-dimensional effects are dominating over the stronger forced stationary streaks. At about $x = 30$ to 40, nonlinear effects begin to be apparent when energy is transferred to the modes $(1, 1)$, $(2, 0)$ and $(2, 1)$. Further downstream, the streak mode $(0, 1)$ is decaying and a dip in the energy can be observed at approximately $x = 55$. At this location, the wave mode $(1, 0)$ starts to saturate and an abrupt change of the breakdown process happens, namely, an exponential growth of the streak mode.

Flows such as free shear layers and wall jets can undergo pairing of the fundamental vortex rollers as a result of a subharmonic instability. In order to asses whether the pairing mode $(1/2, 0)$ is present in the simulation, the energy content in this subharmonic frequency is evaluated and shown as the gray line in figure 3.1. However, since this mode is not forced (in the fringe region),

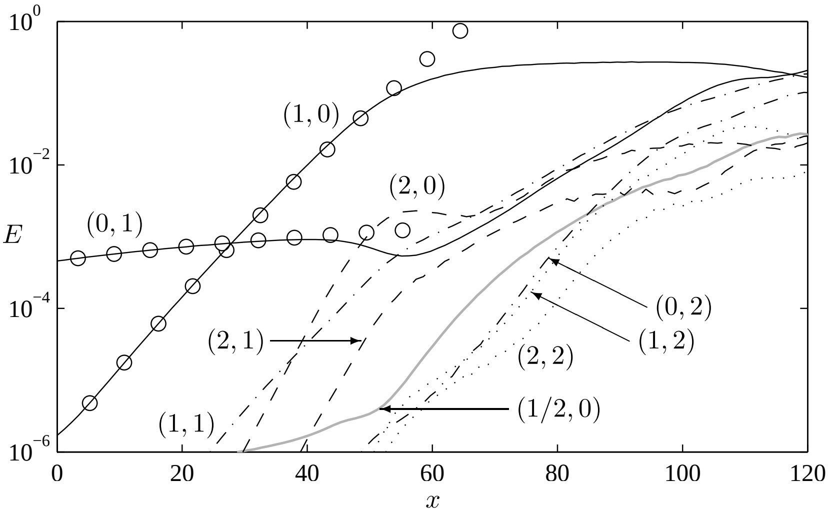

FIGURE 3.1. Energy in different Fourier modes (ω_1, β_1) from the DNS. Initially excited wave and streak modes (black solid lines). Nonlinearly generated modes (dashed and dotted lines). Pairing mode (gray line) grows up from numerical noise. Results from the PSE (○) are shown for comparison.

but only grows out of numerical noise, its amplitude is small. Upstream of the location where nonlinear interactions set in, the amplification rate of the subharmonic mode is about half of the fundamental one. This is consistent with linear theory, indicating that an eigenmode is born. At about $x = 55$, the amplification rate doubles as a result of nonlinear effects. However, the energy content in this mode stays at least one magnitude below the exponentially growing streak mode.

3.2.2. *Flow structures*

Structures appearing in the flow can be visualized and contribute to an increased understanding of the transition process. In figure 3.2, the streamwise velocity is visualized, where dark areas display high velocity and white areas show regions of backflow. Figures 3.2(*a*–*e*) show cross-flow slices from streamwise locations indicated in the figure. The high-velocity streak is lifted up from the shear-layer region forming a mushroom-shaped structure. Such structures have also been observed by, for example, Wernz & Fasel (1996, 1997) and Gogineni & Shih (1997). Figure 3.2(f) shows the (x, y)-plane through the middle of the low-velocity streak (the edges of the cross-flow slices). Counterclockwise rotating rollers are moving with the wave troughs in the outer shear layer. Slightly downstream of each shear-layer roll-up, clockwise rotating rollers in the boundary layer exist, associated with small regions of separated flow. The

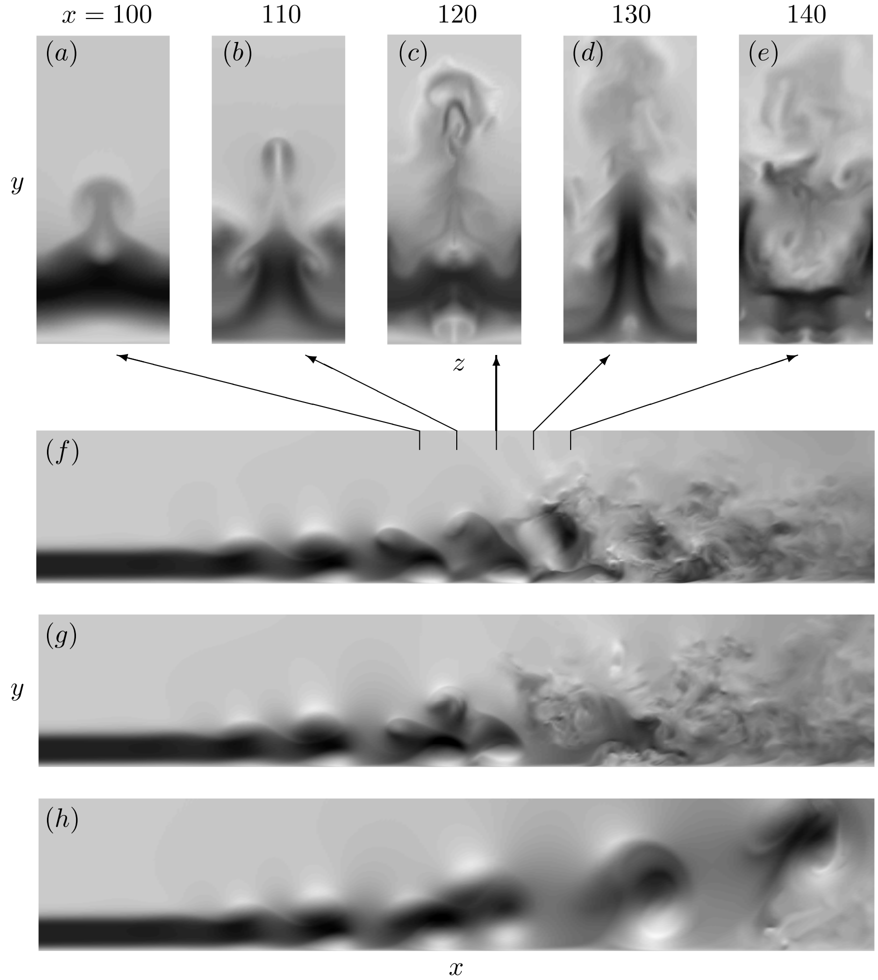

FIGURE 3.2. Visualization of streamwise velocity with dark areas displaying high velocity and white areas regions of backflow. (*a*–*e*) Cross-flow slices. (*f*–*h*) (x, y)-planes corresponding to the edge of the box. The flow is from left to right. (*f*) Streaks and fundamental waves are forced. (*g*) Streaks, fundamental and subharmonic waves are forced. (*h*) Fundamental and subharmonic waves are forced.

breakdown to turbulence start in the mushroom-shaped structure and spreads through the whole wall jet.

The transition mechanisms can be described by the development of vortical structures in the flow. Figure 3.3 shows the vortical structures from the

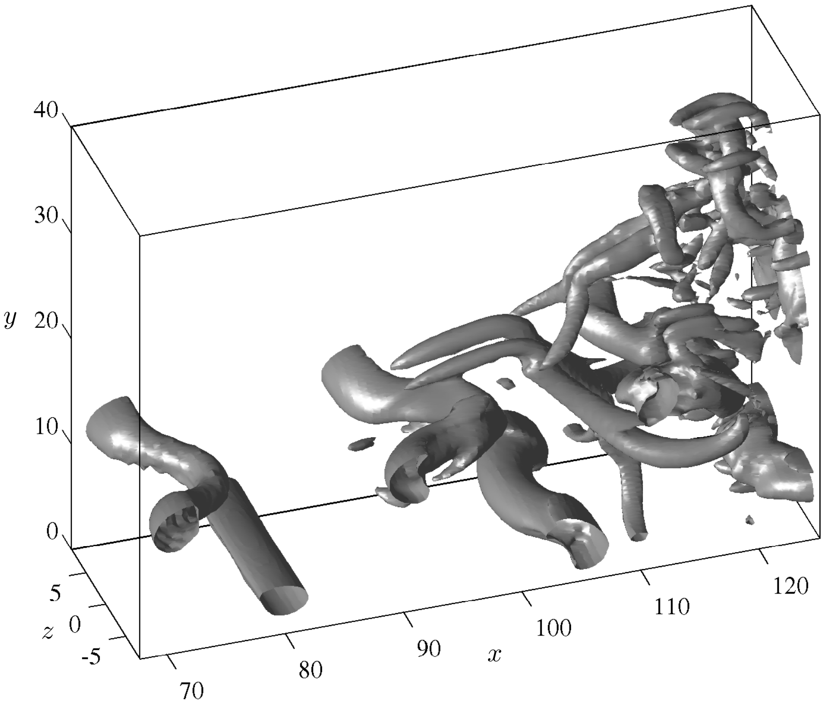

Figure 3.3. Vortex visualization using the same instantaneous data as in figures 3.2(a–f)

same instantaneous data as the visualizations shown in figures 3.2(a–f). Spanwise rollers are formed in the wave troughs in the outer shear layer and move downstream. In the boundary layer close to the wall beneath the wave crests, counter-rotating rollers are formed. In the presence of streaks, the shear-layer rollers are sinuously modified with the boundary-layer rollers deforming in the opposite direction. Vortex ribs are formed in the braids of the waves, extending from the top of the shear-layer roller to beneath the previous one. Such rib vortices have been observed in many experimental and computational studies of mixing layers (e.g. Bernal & Roshko 1986; Lasheras *et al.* 1986; Metcalfe *et al.* 1987; Schoppa *et al.* 1995). The vortex ribs follow the upward flow between two neighboring shear-layer rollers and are associated with the mushroom-shaped structures ejected from the wall jet into the ambient flow. The tail legs of the vortex ribs, generated one fundamental period earlier, separate and form a vortex ring around the upcoming vortex ribs and additional counter-rotating vortex rings are created preceding breakdown to turbulence.

3.2.3. *Subharmonic waves and pairing*

The primary instability in inflectional base flows such as free shear layers and wall jets is a strong inviscid exponential instability resulting in the roll-up of waves into strong spanwise vortices. These two-dimensional vortices can experience two different types of secondary instability. For low initial three-dimensional excitation, the secondary instability is subharmonic and associated with vortex pairing, like that observed by Bajura & Catalano (1975). If the initial three-dimensional excitation is large enough, a three-dimensional secondary instability is predominant, which suppresses the vortex pairing (see e.g. Metcalfe *et al.* 1987).

In order to determine the role of pairing in the Blasius wall jet, the subharmonic disturbance is studied. The Orr–Sommerfeld mode with half the frequency of the fundamental one is forced in the DNS. Apart from the simulation showed in figure 3.2(f), where streaks and fundamental waves are excited, two additional simulations are performed, one with streaks, fundamental and subharmonic waves forced in the flow (figure 3.2g) and the other with only the fundamental and subharmonic waves and noise in the initial field (figure 3.2h). When the subharmonic waves are not forced, the pairing mode is weak, as is also seen in the energy content of the corresponding Fourier mode $(1/2, 0)$ in figure 3.1. In this case pairing does not occur. On the other hand, when the subharmonic waves are forced, the pairing mode is stronger and can be seen as the staggered pattern of the vortex rollers in the outer shear layer. In the absence of streaks, pairing occurs between rollers in the outer shear layer as well as in the boundary layer. The pairing originates from the subharmonic wave displacing one vortex to the low-velocity region and the next to the high-velocity region. The vortex traveling in the high-velocity region overtakes the slower vortex in the low-velocity region, and pairing appears. However, in the presence of streaks, pairing is suppressed and breakdown to turbulence is enhanced.

3.3. DNS of the asymptotic suction boundary layer

The numerical code does not allow for non-zero mean mass flow through the lower and upper boundaries. However, the wall-normal suction in the asymptotic suction boundary layer can be moved from the boundary condition to the governing equations. Hence, instead of solving the Navier–Stokes equations for the wall-normal velocity V with the boundary condition $V = -V_0$, the same solution can be obtained by solving for $V - V_0$ with the boundary condition $V = 0$.

3.3.1. *Energy thresholds for periodic disturbances*

In the fourth paper, energy thresholds for bypass transition in the asymptotic suction boundary layer are studied by means of DNS. The growth and breakdown of streaks triggered by streamwise vortices (SV) and oblique waves (OW) are investigated as well as the development of random noise (N).

Three transition scenarios are investigated where the disturbances are introduced in the initial field and allowed to evolve temporally. Because the disturbances are assumed to be periodic in the horizontal directions and the base flow is parallel, the fringe region can be omitted. In scenario (SV), the initial flow field consists of two counter-rotating streamwise vortices. These vortices produce streaks by the lift-up effect as time proceeds. Transition can take place if the streak amplitude becomes sufficiently large for secondary disturbances to amplify and break down. In scenario (OW), the initial flow field consists of two superposed oblique waves with equal and opposite angle to the streamwise direction. The pair of growing waves interact nonlinearly and streamwise vortices are created. This is essentially a different and quicker way of triggering growth of streaks, which in turn are subjected to secondary instability. The streamwise vortices and oblique waves are added in the form

$$\boldsymbol{u} = \hat{\boldsymbol{u}}(y)\exp(\mathrm{i}\alpha x + \mathrm{i}\beta z), \tag{3.1}$$

where the amplitude function $\hat{\boldsymbol{u}}(y)$, with given horizontal wavenumbers (α, β), is optimized over a specified time period (Corbett & Bottaro 2000; Fransson & Corbett 2003). In scenario (N), the initial flow field consists of three-dimensional random noise added to the base flow. The thresholds for transition are expressed in terms of the energy density of the initial disturbance, thus the initial disturbance energy E_0 divided by the volume $\mathscr{V}$ of the computational box.

The streamwise vortices are optimized for $(\alpha, \beta) = (0, 0.53)$ over a time period of 300. The horizontal lengths of the computational box are $2\pi/\beta$, which corresponds to one spanwise wavelength of the optimal disturbance. Apart from the streamwise vortices, the initial condition consists of a small amount of random noise, which is necessary to set off a secondary instability. The flow pattern of the simulation for $Re = 800$ and $E_0/\mathscr{V} = 3 \cdot 10^{-5}$ is shown in figure 3.4(a, b), where the streamwise velocity is visualized in a horizontal plane (with two box lengths in each direction) at $y = 2$. As can be seen in figure 3.4(a) that shows the state at $t = 700$, a secondary instability has developed and deforms the streaks in a sinuous manner with a streamwise wavelength equal to the computational box length. Figure 3.4(b) shows the breakdown of the streaks at $t = 820$.

The oblique waves are optimized for $(\alpha, \beta) = (0.265, \pm 0.265)$ over a time period of 75. Hence, they are oriented 45° to the free-stream direction. The horizontal lengths of the computational box are twice as large as for scenario (SV) in order to fit one streamwise and spanwise wavelength of the oblique waves. The same random noise as for scenario (SV) is added to the initial field, although it is not necessary for secondary instability to occur. The flow pattern of the simulation for $Re = 800$ and $E_0/\mathscr{V} = 1 \cdot 10^{-5}$ is shown in figure 3.4(c, d), where the size of the horizontal plane at $y = 2$ is equal to the horizontal size of the computational box. In the initial stage, the pair of oblique waves interact with each other and streamwise vortices with half the spanwise wavelength are created. As a result, two spanwise wavelengths of streaks can

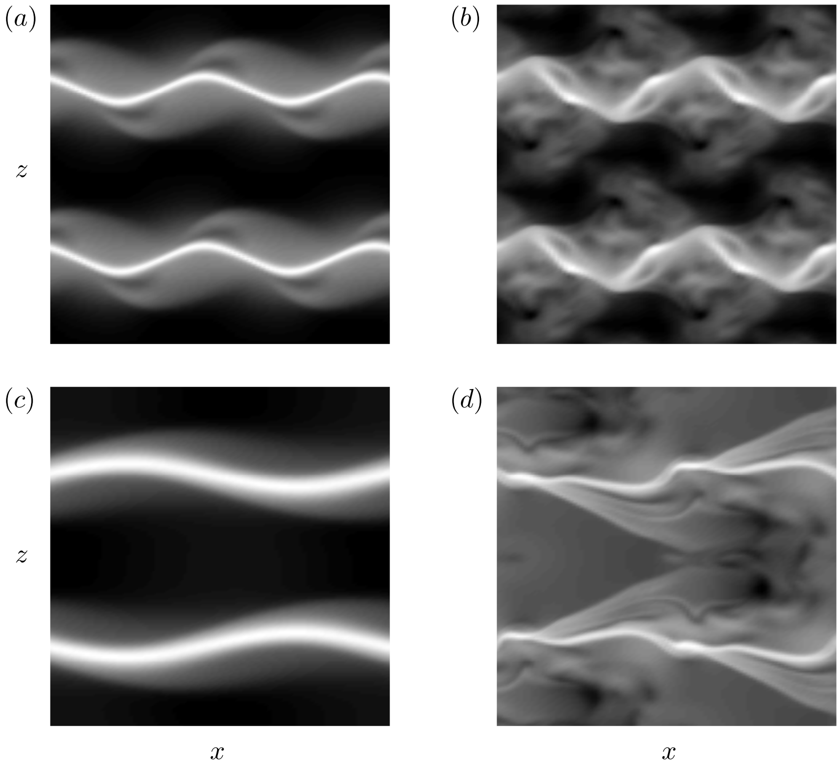

FIGURE 3.4. Visualization of periodic disturbances in the asymptotic suction boundary layer for $Re = 800$ in a horizontal plane at $y = 2$ of size: 23.71×23.71. Dark and light areas show regions of high and low streamwise velocity, respectively, and the flow is from left to right. Scenario (SV) at (*a*) $t = 700$ and (*b*) $t_T = 820$. Scenario (OW) at (*c*) $t = 600$ and (*d*) $t_T = 731$.

be seen in figure 3.4(*c*) that shows the state at $t = 600$. In the presence of the oblique modes, the secondary instability is of the varicose type with horizontal wavelengths equal to these of the oblique waves, and thus also of the horizontal dimensions of the computational box. Figure 3.4(*d*) shows the breakdown of the streaks at $t = 731$.

The Reynolds number based on the mean friction velocity, Re_τ, provides a good measure of when transition to turbulence appears. Transition is defined to appear when the friction velocity Reynolds number exceeds a certain critical value. This value is chosen to be 26, 38 and 50 for Reynolds number 500, 800 and 1200, respectively. Examples of the evolution of the friction velocity Reynolds number are shown in figure 3.5(*a*), which shows one case from each

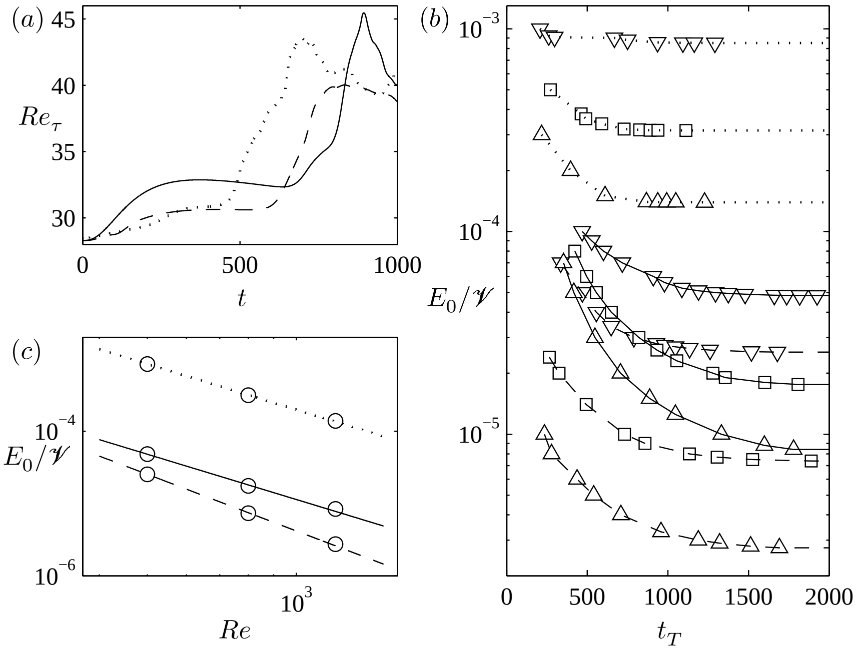

FIGURE 3.5. Scenarios (N) (dotted lines), (SV) (solid lines) and (OW) (dashed lines) in the asymptotic suction boundary layer. (*a*) Friction velocity Reynolds number versus time for $Re = 800$ with initial energies $E_0/\mathscr{V} = 3.4 \cdot 10^{-4}$ (N), $E_0/\mathscr{V} = 3 \cdot 10^{-5}$ (SV) and $E_0/\mathscr{V} = 1 \cdot 10^{-5}$ (OW). (*b*) Transition time as a function of initial energy for Reynolds number 500 ($\bigtriangledown$), 800 ($\Box$) and 1200 ($\bigtriangleup$). (*c*) Energy threshold versus Reynolds number. Lines are fits to the DNS data indicated by circles.

scenario for $Re = 800$. For the undisturbed base flow $Re_\tau = \sqrt{Re}$, which is very close to the initial value in the figure. The friction velocity Reynolds number changes slowly while the flow is laminar, followed by a rapid growth as the flow break down and transition occurs.

In order to compare the energy thresholds for the three scenarios, the time of transition t_T for each initial energy density of the simulations carried out are summarized in figure 3.5(*b*). The lines connecting the data are extrapolated towards $t_T \to \infty$ for the lowest obtained energy that leads to breakdown before $t = 2000$ of each case. The figure shows how the time of transition decreases as the initial energy of the primary disturbance increases. This trend is less significant for scenario (N) where rather high energies are required to obtain transition. The most competitive initial disturbance in terms of transition at low energy/short time is the pair of oblique waves. However, the

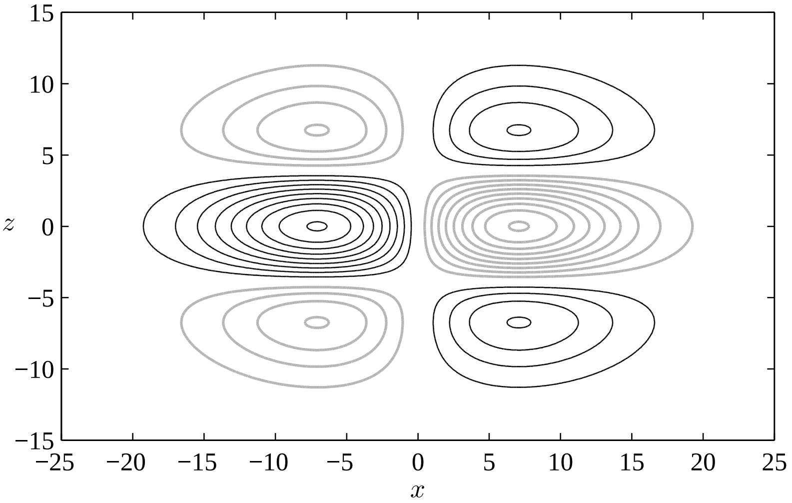

FIGURE 3.6. Contours of wall-normal velocity, at $y = 1$, of a localized disturbance consisting of two counter-rotating vortex pairs with the scales $l_x = 10$, $l_y = 1.0$ and $l_z = 5.5$. Black and gray lines display positive and negative values, respectively.

obtained energy thresholds must be considered as an upper bound, since only one disturbance configuration is simulated in each case.

It is difficult to define the energy threshold as a function of Reynolds number for growing boundary layers as the local Reynolds number changes with the boundary layer thickness. In parallel flows, however, such as the asymptotic suction boundary layer, the Reynolds number based on the boundary layer thickness is constant and therefore the procedure to find the energy threshold is straightforward. The energy thresholds for transition, extracted from figure 3.5(*b*) (where the lines approach the time 2000), are plotted for their respective Reynolds number in figure 3.5(*c*). The values from the DNS are displayed by circles and the lines represent least square fits of the formula $E_0 \propto Re^{\gamma}$. The obtained energy thresholds for the three transition scenarios scale with Reynolds number as $Re^{-2.6}$ (OW), $Re^{-2.1}$ (SV) and $Re^{-2.1}$ (N).

3.3.2. *Amplitude thresholds for localized disturbances*

In the fifth paper, amplitude thresholds for transition from localized disturbances to turbulent spots are studied with DNS. The localized disturbance is superposed to the asymptotic suction boundary layer in the initial velocity field. The type of disturbance is centered around a pair of oblique waves, in the streamwise-spanwise wavenumber plane, consisting of two counter-rotating vortex pairs, see figure 3.6. In terms of a stream function, it is defined by

$$\psi = A\bar{x}\bar{y}^3\bar{z}\exp\left(-\bar{x}^2 - \bar{y}^2 - \bar{z}^2\right), \tag{3.2}$$

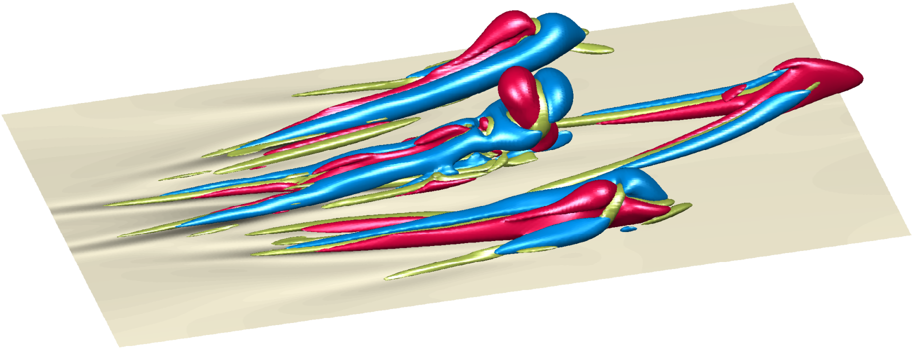

FIGURE 3.7. A growing localized disturbance in the asymptotic suction boundary layer. Typical vortex structures (green) are visualized together with their associated velocity normal to the wall (red indicating upward moving fluid and blue fluid moving downward). The dark regions at the wall show areas of increased friction.

where $\bar{x} = x/l_x$, $\bar{y} = y/l_y$ and $\bar{z} = z/l_z$. The velocity components are given by $(u, v, w) = (0, -\psi_z, \psi_y)$ and normalized so that the amplitude A is given by the maximum absolute value of the wall-normal disturbance velocity. This type of initial disturbance can be experimentally reproduced with the down-up motion of a membrane at the wall and has been used in earlier studies of transient growth and transition in channel flows (Henningson *et al.* 1993) and boundary layers (Breuer & Haritonidis 1990; Breuer & Landahl 1990; Bech *et al.* 1998).

The initial disturbance develops into a hairpin vortex aligned with the streamwise direction. Its legs are close to the wall at the trailing edge of the disturbance while the head is located higher up and further downstream. Between the legs, an upward motion is present. On each side of the head, counter-rotating structures develop. Figure 3.7 shows an instant of a developing localized disturbance and the friction distribution at the wall (the figure was originally prepared for the book ‘KTH in Your Pocket 2005’ and appears on its cover). The head is detached as a result of vortex stretching and a new head is formed in its place. This head detachment continues as time proceeds. Spiral vortices appear at the counter-rotating structures on each side. Later, the flow pattern becomes complex with many hairpin and spiral vortices characterizing a young turbulent spot.

Amplitude thresholds for transition from a localized disturbance to a turbulent spot is investigated by a numerous of direct numerical simulations. If the initial amplitude of the disturbance exceeds a certain threshold value, A_T, transition occurs. Simulations are carried out with varied initial amplitudes of the localized disturbance at the Reynolds numbers 500, 800 and 1200. When evaluating whether transition occurs or not, the disturbance energy, extreme values of velocity and vorticity components and visual examinations of the

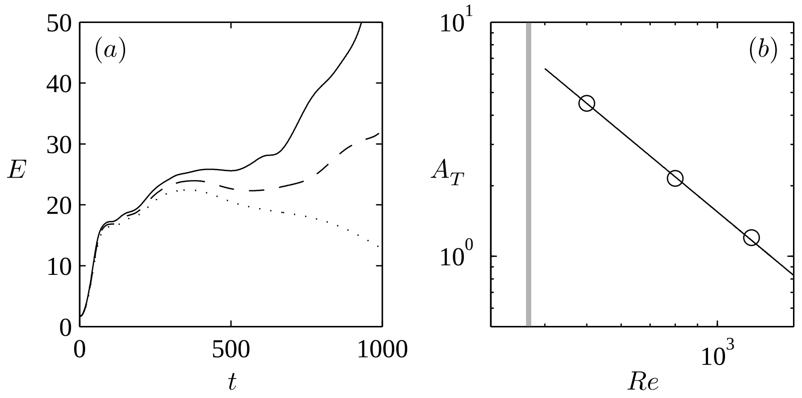

FIGURE 3.8. (a) Evolution of disturbance energy at Re = 500 and $A = 0.046$ (solid line), 0.045 (dashed line) and 0.044 (dotted line). (b) Threshold amplitude as function of Reynolds number. The circles correspond to the lowest amplitudes from the DNS that lead to transition. The black line is a least square fit to the data corresponding to $A_T = 6.36 \cdot 10^4 Re^{-1.54}$. The gray line indicates the critical Reynolds number of 367.

flow field are taken into account. Figure 3.8(a) shows the evolution of the disturbance energy for three initial amplitudes close to the threshold value at $Re = 500$. In this case, transition occurs for the amplitudes $A = 0.045$ and 0.046 but not for 0.044 for which the disturbance energy and flow extreme values decay after the initial transient growth.

The circles in figure 3.8(b) summarizes the amplitude thresholds taken as the lowest amplitudes for which transition is attained in the DNS before $t = 1000$ for the three Reynolds numbers. The black line is the least square fit to the data and for this range of Reynolds numbers, the threshold amplitude is found to scale as $Re^{-1.5}$. An attempt of finding the critical Reynolds number for transition initiated of the localized disturbance is also carried out. Simulations are performed with an initial amplitude of the localized disturbance of 0.1 and varied Reynolds numbers. Relaxation of the localized disturbance appears for $Re = 367$ or below. This value is indicated in figure 3.8(b) as the thick gray line.

CHAPTER 4

Turbulence

4.1. The essence of turbulence

As was mentioned in the Introduction, turbulent flow is characterized by a chaotic, swirly and fluctuating motion, like the white jet of water from the kitchen tap. Turbulence is unpredictable in its nature, because a very small difference in the initial conditions, causes a completely different solution at a later instant. An example of this sensitivity on initial conditions is the Butterfly Effect, an expression coined after the work by Lorenz (1963), that the flap of a butterfly's wings will create a disturbance that in the chaotic motion of the atmosphere will become amplified and eventually change the weather. As a result, it is impossible to predict the weather, one can only compute possible outcomes of how the weather will be. That is actually what is done, the meteorological institutes perform one simulation with initial conditions based on weather observations, then additional simulations are done with slightly disturbed initial conditions in order to test the sensitivity and thereof the reliability of the forecast.

If we consider the white turbulent flow from the kitchen tap again, and take a photograph with a very short shutter time, we will see a picture of all the fluctuations with lots of small bubbles in it. If we take one more photograph, it will look different. On the other hand, if we take a photograph with a very long shutter time, we will see a diffusive smooth picture showing the mean behavior of the jet of water. Now we do not need to take another photograph, because it will look the same. In applications one is not usually interested in knowing all the details about the fluctuations of the flow, but rather satisfied with the influence of the turbulence on the averaged flow. For this purpose we divide the total flow into an average and a fluctuating component

$$u_i = U_i + u_i', \quad p = P + p', \tag{4.1}$$

where U_i denotes the mean velocity and u_i' the fluctuation. The index denotes either one of the three spatial directions. As well as one can take the average in time, as the photograph taken with a very long shutter time, one can take the average in either of the spatial directions what ever is convenient for the particular flow case. In the case of the jet of water, it is convenient to average in time and in the azimuthal direction, but not in the streamwise or the radial directions.

By introducing (4.1) into the Navier–Stokes equations and taking the average, we receive the Reynolds average equations governing the mean flow. These equations include the effect of the turbulence through the Reynolds stress $\overline{u_i' u_j'}$, where the line denotes average. Because of this additional stress, the Reynolds average equations involve more unknowns than equations and can not be solved directly. This closure problem implies that the Reynolds stress components have to be modeled and thereof be expressed in the mean flow variables. However, in the present thesis, the total flow is computed by solving the Navier–Stokes equations and no modeling is needed.

4.2. Spots in the asymptotic suction boundary layer

In the fifth paper, the development of turbulent spots in the asymptotic suction boundary layer is studied using DNS. In natural transition, the breakdown to turbulence typically starts in isolated regions initiated by disturbances present in the laminar flow. These turbulent spots grow in size as they propagate downstream and merge together to form a fully developed turbulent flow. Turbulent spots and their development in channel flows and boundary layers have been investigated extensively both experimentally (Riley & Gad-el-Hak 1985) and numerically (Mathew & Das 2000). But, until now, nothing has been reported on turbulent spots in the asymptotic suction boundary layer. However, numerical simulations of turbulent spots in the asymptotic suction boundary layer are fruitful as the temporal approach allows us to choose a shorter computational domain than the distance the spot actually propagates.

The turbulent spot is triggered by a localized disturbance that is introduced in the initial velocity field in the form of two counter-rotating vortex pairs, see figure 3.6. When it breaks down, the turbulence spreads in the streamwise and lateral directions as the spot propagates downstream. The growth of its height is, however, very small. Figures 4.1 and 4.2 show the turbulent spots in the asymptotic suction boundary layer at Reynolds number 500 and 800, respectively. The streamwise disturbance velocity in the wall-parallel plane at $y = 1$ and the (x, y)-plane along the centerline are visualized with dark and light regions displaying high and low values, respectively. The length of the planes is 300 while the width and height show the entire spanwise and wall-normal extend of the computational box, respectively. A corresponding visualization of a turbulent spot for Reynolds number 1200 is shown in figure 4.3, where the length of the planes is 200.

The turbulent spot takes a bullet-shaped form with a rounded leading edge and a straight trailing edge. This shape becomes more distinct for higher Reynolds numbers as the scales within the spot get smaller. The interior of the spot is occupied of turbulent streaky structures. The side views reveal that the leading edge develops an overhang over the laminar flow and this is typical for turbulent spots in boundary layers. Beneath this overhang, long streaks extend from the turbulent region close to the wall. Behind the trailing edge of the spot, shorter streaks persist followed by a calm wake with accelerated flow.

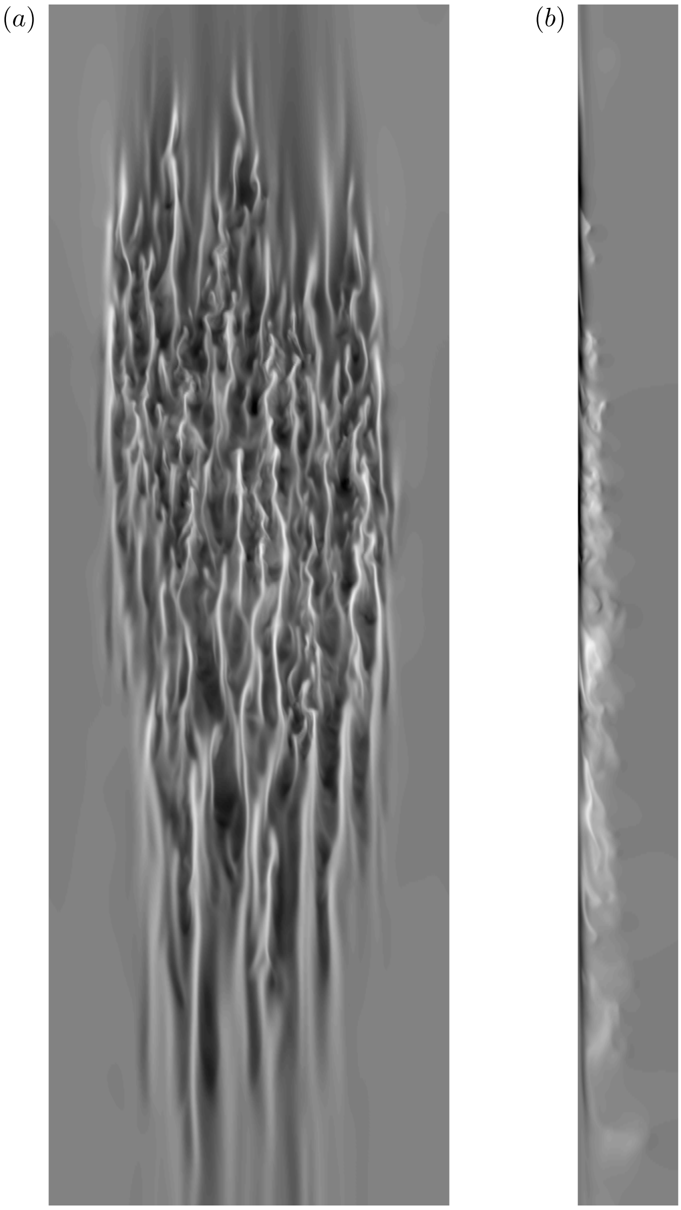

FIGURE 4.1. Numerical smoke visualization of a turbulent spot in the asymptotic suction boundary layer at $Re = 500$ and $t = 1100$. Flow is in downward direction and the length of the planes is 300. Dark and light regions show high and low streamwise disturbance velocity, respectively. (*a*) Top view at $y = 1$. (*b*) Side view through the middle of the spot at $z = 0$.

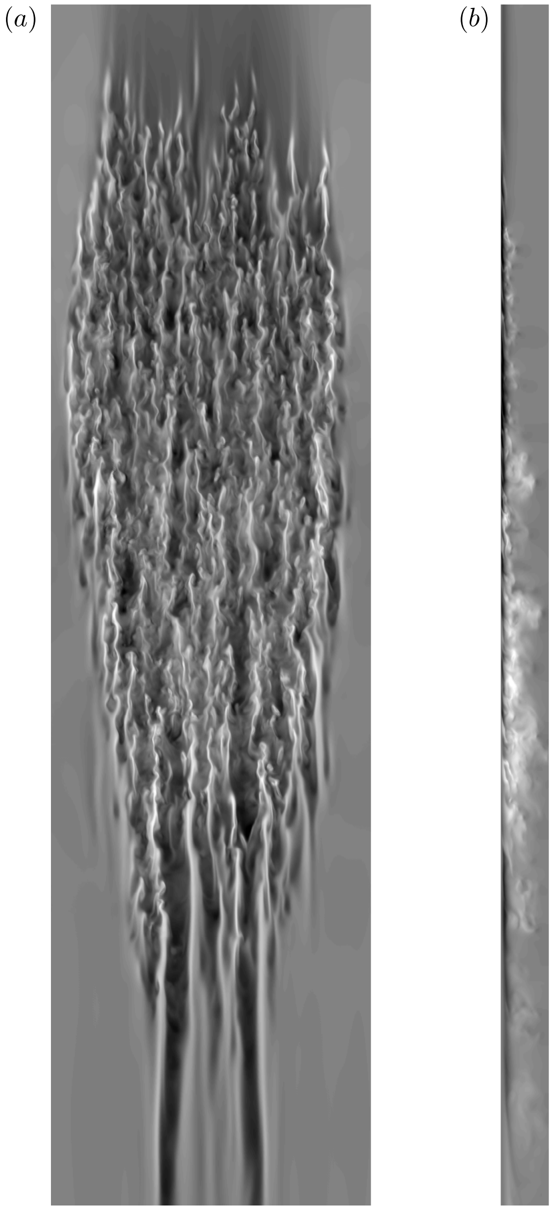

Figure 4.2. Numerical smoke visualization of a turbulent spot in the asymptotic suction boundary layer at $Re = 800$ and $t = 900$. Flow is in downward direction and the length of the planes is 300. Dark and light regions show high and low streamwise disturbance velocity, respectively. (*a*) Top view at $y = 1$. (*b*) Side view through the middle of the spot at $z = 0$.

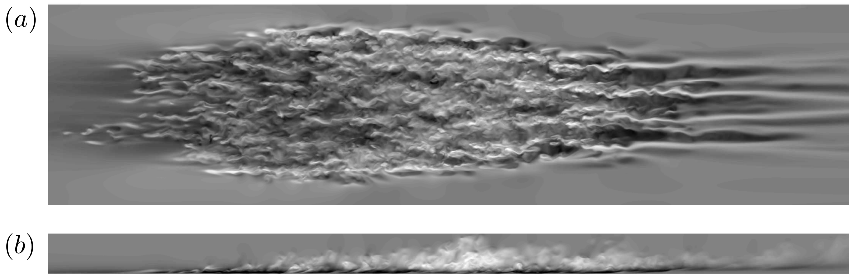

Figure 4.3. Numerical smoke visualization of a turbulent spot in the asymptotic suction boundary layer at $Re = 1200$ and $t = 500$. Flow is from left to right and the length of the planes is 200. Dark and light regions show high and low streamwise disturbance velocity, respectively. (a) Top view at $y = 1$. (b) Side view through the middle of the spot at $z = 0$.

The fully developed turbulent spot grows linearly both in length and width. The leading edge propagates at about 85-90 % of the free-stream velocity while the trailing edge velocity decreases from slightly bellow 70 % for $Re = 500$ to slightly bellow 50 % for $Re = 1200$. The half-width angle increases with increasing Reynolds number from about $2°$ for $Re = 500$ to about $4°$ for $Re = 1200$. However, it seems to level off to a constant value at high Reynolds numbers. At the time of writing this thesis, an ongoing experiment of turbulent spots in the asymptotic suction boundary layer at $Re = 500$ is performed in the MTL wind-tunnel at KTH Mechanics in Stockholm by Jens Fransson. His preliminary results indicate slightly larger spreading rates.

To summarize, the turbulent spot in the asymptotic suction boundary layer bears many similarities to spots in other flows. Its shape and spreading rates are reminiscent of the turbulent spot in boundary layers subjected to a favorable pressure gradient. In common with spots in plane Couette flow and plane Poiseuille flow, the spreading rates are dependent of the Reynolds number.

4.3. Turbulence statistics of the Blasius wall jet

In the sixth paper, the early turbulent evolution of the Blasius wall jet is studied. The investigation is an extension of the simulation presented in paper 3. The same forcing with two-dimensional waves and streamwise elongated streaks is done to trigger a natural transition mechanism. However, a four times larger computational domain is used, allowing the turbulent region of the wall jet to develop for a longer distance downstream. Statistics of mean flow and turbulent stresses are sampled for 2200 time units, corresponding to five months of non-stop simulations. The averaged data is then scaled with appropriate scalings for the inner boundary layer and the outer shear layer to identify self-similar behavior.

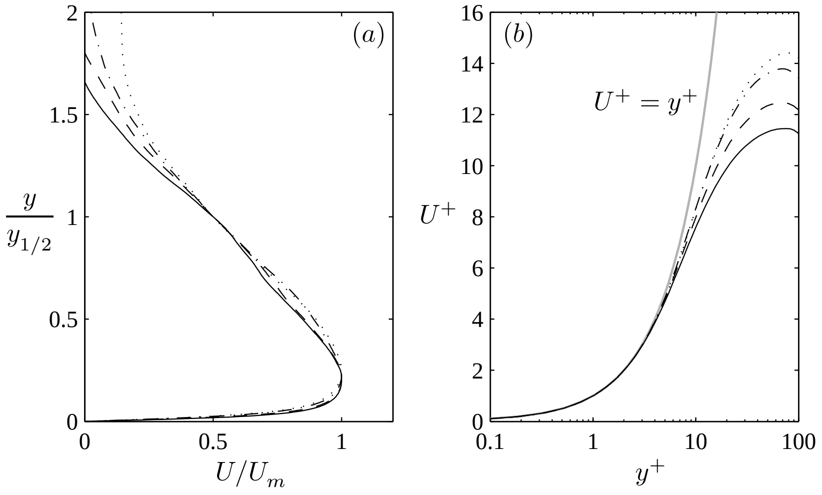

FIGURE 4.4. Mean streamwise velocity at $x = 170$ (solid line), 200 (dashed line), 250 (dashed-dotted line) and 300 (dotted line). (*a*) Outer scaling is used. (*b*) Inner scaling is used.

For the outer scaling, velocities are scaled with the local maximum velocity of the wall jet U_m and lengths are scaled with the half-width $y_{1/2}$, which is the distance from the wall where the velocity in the outer region reaches half the local maximum velocity. The streamwise mean velocity scaled with outer scaling is shown in figure 4.4(*a*). The profiles between $x = 200$ and 300 collapse reasonably well up to $y/y_{1/2} = 1$. Further away from the wall, the profiles deviate from each other owing to a secondary flow. This secondary flow originates from a start-up vortex that slowly convects downstream and then remains in the ambient flow in front of the fringe region, which seems to act like a wall on such large structures. External flows exist for wall jets in experimental facilities as well, but as the computational box is not as large as the surrounding space in an experiment, the problem is more prominent. It is possible to avoid the vortex by specifying the entrainment velocity at the upper boundary as was done by Dejoan & Leschziner (2005), who used a boundary condition based on the laminar free plane jet. However, it is chosen not to constrain the turbulent wall jet by prescribing an entrainment velocity based on laminar theory.

When using the inner scaling, velocities are scaled with the friction velocity $u_\tau = \sqrt{\nu |\partial U(y=0)/\partial y|}$ and lengths are scaled with the wall thickness $\eta = \nu / u_\tau$. Quantities scaled with the inner scaling are conventionally denoted with a plus (e.g. $y^+ = y/\eta$ and $uv^+ = \overline{u'v'}/u_\tau^2$). Using this notation, the half-width corresponds to about 300 plus units, a value that increases with Reynolds number. Figure 4.4(*b*) shows the near-wall region of the streamwise mean velocity scaled with inner scaling. Within the viscous sublayer, the profiles follow a linear law $U^+ = y^+$, shown as the gray line, up to about $y^+ = 4$. Further

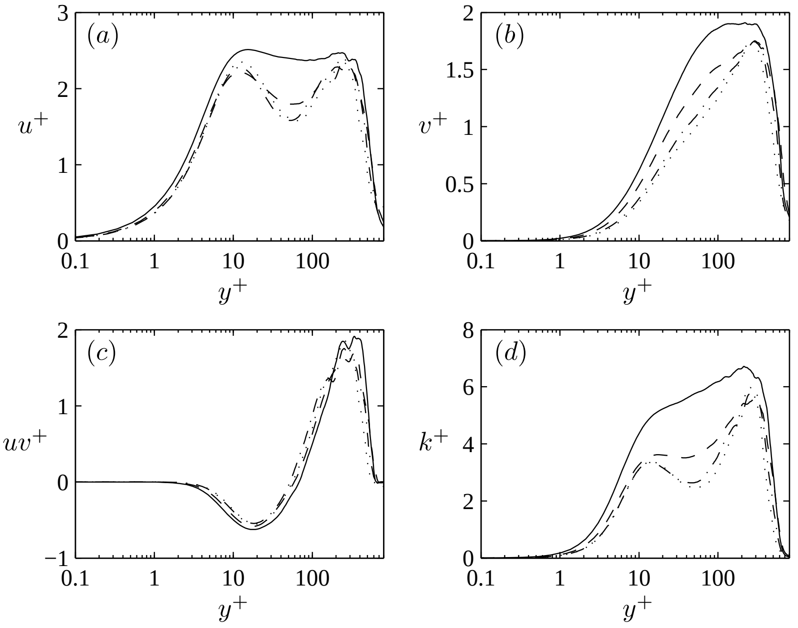

FIGURE 4.5. Profiles of (a) rms of u', (b) rms of v', (c) Reynolds shear stress and (d) turbulence kinetic energy. Lines as in figure 4.4.

away from the wall, the profiles start to deviate from the linear behavior, earlier than for a turbulent boundary layer that typically start to deviate for values $y^+ \geq 8$. Up to about $y^+ = 20$, the profiles at $x = 250$ and 300 collapse well.

Components of the Reynolds stress and the turbulent kinetic energy scaled with inner scaling are shown in figure 4.5 for the same streamwise positions as in figure 4.4. The profiles collapse reasonably well for the streamwise positions $x = 200$ to 300 indicating that the flow has started to exhibit a self-similar behavior. It can be noted that the collapse provided with inner scaling is much better than with outer scaling. The profile at the position $x = 170$ is, however, still close to the transitional region and deviates from the other profiles. The general shape of the profiles agree well with previous studies (e.g. Eriksson *et al.* 1998; Dejoan & Leschziner 2005). However, downstream of the position $x = 300$, the vortex present in the end of the computational domain causes the flow to depart from the self-similar behavior and profiles from this region are therefore not taken into account.

CHAPTER 5

Conclusions

The work presented in this thesis is motivated by the need of an increased fundamental understanding of the physics of wall-bounded flows. Investigations of the stability, transition mechanism and early turbulent evolution of wall-bounded flows have therefore been carried out. Three base flows have been considered, the Falkner–Skan boundary layer subjected to favorable, zero and adverse pressure gradients, boundary layers subjected to wall suction and the Blasius wall jet. The stability was investigated by means of linear stability equations valid both for the exponential and algebraic growth scenario. An adjoint-based optimization technique was used to optimize the algebraic growth of streaks. The exponential growth of waves was maximized in the sense that the envelope of the most amplified eigenmode has been calculated. The transition mechanism and turbulence were studied by direct numerical simulations.

In the first paper, the stability of the Falkner–Skan boundary layer subjected to favorable, zero and adverse pressure gradients is considered. The optimization of the algebraic growth was carried out over the initial streamwise location as well as the spanwise wavenumber and the angular frequency. It it found that the initial streamwise location, where the disturbance is introduced in the boundary layer, has a significant impact on the growth. The optimal location moves downstream with decreased pressure gradient of the base flow. In both the algebraic and exponential growth scenarios, the growth is found to increase with increased pressure gradient, although the effect is much more pronounced for the exponential growth. Furthermore, a unified transition prediction method incorporating the influences of pressure gradient and free-stream turbulence is suggested.

In the second paper, the algebraic growth of streaks in boundary layers subjected to wall suction is considered. It is found that the spatial analysis gives larger optimal growth in the asymptotic suction boundary layer than temporal theory. Furthermore, it is found that the optimal growth is larger for the semi suction boundary layer, where the suction begins a distance downstream of the leading edge, than for the asymptotic suction boundary layer. The upstream part of the boundary layer without suction is responsible for this increase of the growth as well as the decrease of the corresponding wavenumber. However, when the streamwise interval for which the optimization is carried out is prolonged, the differences reduce.

In the third paper, the Blasius wall jet, which was matched to the measured flow in an experimental wall-jet facility, is considered. Linear stability analysis with respect to the growth of two-dimensional waves and streamwise streaks was performed and compared to the experiments. The flow reveals a high instability to two-dimensional waves and non-modal streaks. Furthermore, the nonlinear interaction of introduced waves and streaks and the flow structures preceding the flow breakdown were investigated by means of direct numerical simulations. It is demonstrated that the streaks play an important role in the breakdown process, where their growth is transformed from algebraic to exponential as they become part of the secondary instability of the two-dimensional waves. The role of subharmonic waves and pairing of vortex rollers was also investigated. However, in the presence of streaks, pairing is suppressed and breakdown to turbulence is enhanced.

In the fourth paper, energy thresholds for transition to turbulence in the asymptotic suction boundary layer are considered. The development and breakdown of periodic disturbances were studied with direct numerical simulations. Transition triggered by streamwise vortices, oblique waves and random noise were investigated. It is found that the lowest energy threshold is provided by the oblique wave scenario for the considered Reynolds numbers (Re). The threshold energy is found to scale like $Re^{-2.6}$ for oblique transition and like $Re^{-2.1}$ for transition initiated by streamwise vortices and random noise. This indicates that oblique transition has the lowest energy threshold also for larger Reynolds numbers.

In the fifth paper, thresholds for transition of localized disturbances, their breakdown to turbulence and the development of turbulent spots in the asymptotic suction boundary layer are considered. The localized disturbance was introduced in the initial base flow and studied using direct numerical simulations. It is found that the threshold amplitude, defined as the maximum wall-normal disturbance velocity, scales like $Re^{-1.5}$ for $500 \leq Re \leq 1200$. For $Re \leq 367$, the localized disturbance decays after the initial transient growth. The turbulent spot is found to take a bullet-shaped form with a rounded leading edge and a straight trailing edge. Long streaks extend upstream evolving from the disturbed flow in an overhang region. It is found that the spot becomes more distinct and increases its spreading rate for higher Reynolds number.

In the sixth paper, the early turbulent evolution of the Blasius wall jet is considered. The direct numerical simulation is an extension of the work presented in paper 3 but a larger computational domain was used. The averaged data from turbulence statistics was scaled in both inner and outer scaling in order to identify self-similar behavior. Despite the low Reynolds number and the short computational domain, in comparison to available experiments, it was found that the turbulent flow exhibits a reasonable self-similar behavior, which is most pronounced with inner scaling in the near-wall region.

Acknowledgment

First of all, I would like to thank my supervisor, Professor Dan Henningson, for giving me the opportunity to work as his student and to develop my knowledge within the subject of fluid dynamics. He is always very helpful and brings joy into good as well as bad days at the office. In particular, I value his professional way to work and his personal way to be a friend.

I want to thank Doctor Jan Pralits, my previous colleague and office mate, for all the time he spent to help me to get started with the project. He was always very helpful and encouraging when ever I needed help.

I also want to thank Doctor Mattias Chevalier for the help with various modifications of the spectral code and Doctor Luca Brandt for the guidance with the direct numerical simulations. Furthermore, I would like to thank Associate Professor Ardeshir Hanifi who could sit for hours to help me with the stability codes.

I would like to thank my co-authors Valery Chernoray and Lennart Löfdahl at Chalmers, Niklas Davidsson at Luleå University, Martin Byström, Astrid Herbst and Dan Henningson at KTH Mechanics for nice collaborations.

Many thanks to my colleagues at KTH Mechanics for providing a very nice atmosphere at the Department. In particular I would like to thank Astrid Herbst, Carl-Gustav Unckel, Dan Henningson, Erik Stålberg, Espen Åkervik, Fredrik Lundell, Jan Pralits, Jens Fransson, Jérôme Hœpffner, Luca Brandt, Markus Högberg, Martin Byström, Martin Skote, Mattias Chevalier and I also want to thank the Department for providing the gym card and the opportunity to play indoor bandy.

This work has been funded by the Swedish Energy Agency (Energimyndigheten). The large direct numerical simulations were performed at the Center for Parallel Computers at KTH.

Finally, I want to thank my mother Doris and my father Robert for all the support that made this possible, my grandmother Gertrud, my grandfather Harry and all my friends. Special thanks are given to my lovely girlfriend Linda for all her love and support.

Bibliography

Abu-Ghannam, B. J. & Shaw, R. 1980 Natural transition of boundary layers - the effects of turbulence, pressure gradient, and flow history. *J. Mech. Eng. Sci.* **22**, 213–228.

Andersson, P., Berggren, M. & Henningson, D. S. 1999 Optimal disturbances and bypass transition in boundary layers. *Phys. Fluids* **11**, 134–150.

Bajura, R. A. & Catalano, M. R. 1975 Transition in a two-dimensional plane wall jet. *J. Fluid Mech.* **70**, 773–799.

Bajura, R. A. & Szewczyk, A. A. 1970 Experimental investigation of a laminar two-dimensional plane wall jet. *Phys. Fluids* **13**, 1653–1664.

Bech, K. H., Henningson, D. S. & Henkes, R. A. W. M. 1998 Linear and nonlinear development of localized disturbances in zero and adverse pressure gradient boundary-layers. *Phys. Fluids* **10**, 1405–1418.

Bernal, L. P. & Roshko, A. 1986 Streamwise vortex structure in plane mixing layers. *J. Fluid Mech.* **170**, 499–525.

Bertolotti, F. P., Herbert, T. & Spalart, P. R. 1992 Linear and nonlinear stability of the Blasius boundary layer. *J. Fluid Mech.* **242**, 441–474.

Boiko, A. V., Westin, K. J. A., Klingmann, B. G. B., Kozlov, V. V. & Alfredsson, P. H. 1994 Experiments in a boundary layer subjected to free stream turbulence. Part 2. The role of TS-waves in the transition process. *J. Fluid Mech.* **281**, 219–245.

Breuer, K. S. & Haritonidis, J. H. 1990 The evolution of a localized disturbance in a laminar boundary layer. Part 1. Weak disturbances. *J. Fluid Mech.* **220**, 569–594.

Breuer, K. S. & Landahl, M. T. 1990 The evolution of a localized disturbance in a laminar boundary layer. Part 2. Strong disturbances. *J. Fluid Mech.* **220**, 595–621.

Chun, D. H. & Schwarz, W. H. 1967 Stability of the plane incompressible viscous wall jet subjected to small disturbances. *Phys. Fluids* **10**, 911–915.

Corbett, P. & Bottaro, A. 2000 Optimal perturbations for boundary layers subject to stream-wise pressure gradient. *Phys. Fluids* **12**, 120–130.

Dejoan, A. & Leschziner, M. A. 2005 Large eddy simulation of a plane turbulent wall jet. *Phys. Fluids* **17**, 025102.

van Driest, E. R. & Blumer, C. B. 1963 Boundary layer transition: Freestream turbulence and pressure gradient effects. *AIAA J.* **1**, 1303–1306.

Dryden, H. L. 1959 Transition from laminar to turbulent flow. In *Turbulent flows and heat transfer* (ed. C. C. Lin), pp. 1–74. Princeton University Press.

Ellingsen, T. & Palm, E. 1975 Stability of linear flow. *Phys. Fluids* **18**, 487–488.

Eriksson, J. G., Karlsson, R. I. & Persson, J. 1998 An experimental study of a two-dimensional plane turbulent wall-jet. *Exps. Fluids* **25**, 50–60.

Fjørtoft, R. 1950 Application of integral theorems in deriving criteria for instability for laminar flows and for the baroclinic circular vortex. *Geofys. Publ., Oslo* **17**, 1–52.

Floryan, J. M. & Saric, W. S. 1979 Stability of Görtler vortices in boundary layers. *AIAA J.* **20**, 316–324.

Fransson, J. H. M. & Alfredsson, P. H. 2003 On the disturbance growth in an asymptotic suction boundary layer. *J. Fluid Mech.* **482**, 51–90.

Fransson, J. H. M. & Corbett, P. 2003 Optimal linear growth in the asymptotic suction boundary layer. *Eur. J. Mech. B/Fluids* **22**, 259–270.

Gogineni, S. & Shih, C. 1997 Experimental investigation of the unsteady structure of a transitional plane wall jet. *Exp. Fluids* **23**, 121–129.

Hall, P. 1983 The linear development of Görtler vortices in growing boundary layers. *J. Fluid Mech.* **130**, 41–58.

Hanifi, A. 1995 Local and non-local stability analysis and transition prediction of compressible boundary layer flows. PhD thesis, Royal Institute of Technology, Stockholm, Sweden.

Hein, S., Stolte, A. & Dallmann, U. C. 1999 Identification and analysis of nonlinear transition scenarios using NOLOT/PSE. *Z. Angew. Math. Mech.* **79**, S109–S112.

Henningson, D. S. 1996 Comment on "Transition in shear flows. Nonlinear normality versus non-normal linearity" [Phys. Fluids 7, 3060 (1995)]. *Phys. Fluids* **8**, 2257–2258.

Henningson, D. S., Lundbladh, A. & Johansson, A. V. 1993 A mechanism for bypass transition from localized disturbances in wall-bounded shear flows. *J. Fluid Mech.* **250**, 169–238.

Hocking, L. M. 1975 Non-linear instability of the asymptotic suction velocity profile. *Quart. J. Mech. Appl. Math.* **28**, 341–353.

van Ingen, J. L. 1956 Suggested semi-empirical method for the calculation of the boundary layer transition region. *Tech. Rep.* UTH-74. Dep. of Aero. Eng., University of Technology, Delft.

Klebanoff, P. S. 1971 Effect of freestream turbulence on the laminar boundary layer. *Bull. Am. Phys. Soc.* **10**, 1323.

Kosorygin, V. S. & Polyakov, N. P. 1990 Laminar boundary layers in turbulent flows. In *Laminar-Turbulent Transition* (eds. D. Arnal & R. Michel), pp. 573–578. Springer.

Landahl, M. T. 1980 A note on an algebraic instability of inviscid parallel shear flows. *J. Fluid Mech.* **98**, 243–251.

Lasheras, J. C., Cho, J. S. & Maxworthy, T. 1986 On the origin and evolution of streamwise vortical structures in a plane, free shear layer. *J. Fluid Mech.* **172**, 231–258.

Lorenz, E. N. 1963 The predictability of hydrodynamic flow. *Trans. NY Acad. Sci.* **25**, 409–432.

Lundbladh, A., Berlin, S., Skote, M., Hildings, C., Choi, J., Kim, J. & Henningson, D. S. 1999 An efficient spectral method for simulation of incompressible flow over a flat plate. *Tech. Rep.* KTH, Department of Mechanics, Stockholm.

Mack, L. M. 1977 Transition prediction and linear stability theory. In *AGARD-CP-224*, pp. 1–1 to 1–22. NATO, Paris.

Mathew, J. & Das, A. 2000 Direct numerical simulations of spots. *Current Science* **79**, 816–820.

Matsubara, M. & Alfredsson, P. H. 2001 Disturbance growth in boundary layers subjected to free-stream turbulence. *J. Fluid Mech.* **430**, 149–168.

Mele, P., Morganti, M., Scibilia, M. F. & Lasek, A. 1986 Behavior of wall jet in laminar-to-turbulent transition. *AIAA J.* **24**, 938–939.

Metcalfe, R. W., Orszag, S. A., Brachet, M. E., Menon, S. & Riley, J. J. 1987 Secondary instability of a temporally growing mixing layer. *J. Fluid Mech.* **184**, 207–243.

Nordström, J., Nordin, N. & Henningson, D. S. 1999 The fringe region technique and the Fourier method used in the direct numerical simulation of spatially evolving viscous flows. *SIAM J. Sci. Comput.* **20**, 1365–1393.

Orr, W. M. F. 1907 The stability or instability of the steady motions of a perfect liquid and of a viscous liquid. Part I: A perfect liquid. Part II: A viscous liquid. *Proc. R. Irish Acad. A* **27**, 9–138.

Pretsch, J. 1941 Die stabilität einer ebenen laminarströmung bei druckgefälle und druckanstieg. *Jb. dt. Luftfahrtforschung I* pp. 54–71.

Reyleigh, L. 1880 On the stability of certain fluid motions. *Proc. Math. Soc. Lond.* **11**, 57–70.

Reynolds, O. 1883 An experimental investigation of the circumstances which determine whether the motion of water shall be direct or sinuous, and of the law of resistance in parallel channels. *Phil. Trans. Royal Soc.* **174**, 935–982.

Riley, J. J. & Gad-el-Hak, M. 1985 The dynamics of turbulent spots. In *Fronties in Fluid Mechanics* (eds. S. H. Davis & J. L. Lumley), pp. 123–155. Springer.

Roach, P. E. & Brierley, D. H. 1992 The influence of a turbulent free-stream on zero pressure gradient transitional boundary layer development. I. Test cases T3A and T3B. In *Numerical Simulation of Unsteady Flows and Transition to Turbulence* (eds. O. Pironneau, W. Rodi, I. L. Ryhming, A. M. Savill & T. V. Truong), pp. 303–316. Cambridge University Press.

Schlichting, H. 1933 Berechnung der anfachung kleiner störungen bei der plattenströmung. *ZAMM* **13**, 171–174.

Schoppa, W., Hussain, F. & Metcalfe, R. W. 1995 A new mechanism of small-scale transition in a plane mixing layer: core dynamics of spanwise vortices. *J. Fluid Mech.* **298**, 23–80.

Schubauer, G. B. & Skramstad, H. F. 1947 Laminar boundary layer oscillations and stability of laminar flow. *J. Aero. Sci.* **14**, 69–78.

Smith, A. M. & Gamberoni, N. 1956 Transition, pressure gradient and stability theory. *Tech. Rep.* ES 26388. Douglas Aircraft Co., EL Segundo, Calif.

Sommerfeld, A. 1908 Ein beitrag zur hydrodynamischen erklärung der turbulenten flüssigkeitbewegungen. In *Atti del 4 Congr. Internat. dei Mat. III*, pp. 116–124. Roma.

SQUIRE, H. B. 1933 On the stability for three-dimensional disturbances of viscous fluid flow between parallel walls. *Proc. Roy. Soc. Lond. Ser. A* **142**, 621–628.

SUDER, K. L., O'BRIEN, J. E. & RESHOTKO, E. 1988 Experimental study of bypass transition in a boundary layer. *NASA TM* 100913.

TOLLMIEN, W. 1929 Über die entstehung der turbulenz. Nachr. Ges. Wiss Göttingen, 21–44, (English translation NACA TM 609, 1931).

WERNZ, S. & FASEL, H. F. 1996 Numerical investigation of unsteady phenomena in wall jets. *AIAA Paper* 96-0079.

WERNZ, S. & FASEL, H. F. 1997 Numerical investigation of forced transitional wall jets. *AIAA Paper* 97-2022.

WESTIN, K. J. A., BOIKO, A. V., KLINGMANN, B. G. B., KOZLOV, V. V. & ALFREDSSON, P. H. 1994 Experiments in a boundary layer subjected to free stream turbulence. Part 1. Boundary layer structure and receptivity. *J. Fluid Mech.* **281**, 193–218.

YANG, Z. Y. & VOKE, P. R. 1991 Numerical simulation of transition under turbulence. *Tech. Rep.* ME-FD/91.01. Dept. Mech. Eng. University of Surrey.

Part 2

Papers

Paper 1

Exponential vs algebraic growth and transition prediction in boundary layer flow

By Ori Levin and Dan S. Henningson

Department of Mechanics, KTH, SE-100 44 Stockholm, Sweden

Published in *Flow, Turbulence and Combustion* **70**, 183–210, 2003

For applications regarding transition prediction, wing design and control of boundary layers, the fundamental understanding of disturbance growth in the flat-plate boundary layer is an important issue. In the present work we investigate the energy growth of eigenmodes and non-modal optimal disturbances. We present a set of linear governing equations for the parabolic evolution of wavelike disturbances valid both for the exponential and algebraic growth scenario. The base flow is taken as the Falkner–Skan similarity solution with favorable, adverse and zero pressure gradients. The optimization is carried out over the initial streamwise position as well as the spanwise wave number and frequency. The exponential growth is maximized in the sense that the envelope of the most amplified eigenmode is calculated. In the case of algebraic growth, an adjoint-based optimization technique is used. We find that the optimal algebraic disturbance introduced at a certain downstream position gives rise to a larger growth than for the optimal disturbance introduced at the leading edge. The exponential and algebraic growth is compared and a unified transition-prediction method based on available experimental data is suggested.

---

1. Introduction

Fundamental understanding is important as a basis for engineering applications. In the aviation industry one wishes to decrease wing drag and lower operation costs for aircraft. One critical parameter is the streamwise transition position on the wing from laminar to turbulent flow. The fundamental understanding of the instabilities in the flat-plate boundary layer serve as a basis for the generation of tools for transition prediction, wing design and control of boundary layers.

The prediction of the stability of a given flow and the amplification of small disturbances have been of interest to the fluid dynamics community for more than a century. The traditional stability-analysis technique is to solve the eigenvalue problem of the Orr–Sommerfeld and Squire equations, which are the linearized stability equations based on the assumption of parallel flow with wavelike disturbances. The unstable eigenmodes are historically referred to as Tollmien–Schlichting (TS) waves, usually taking the form of exponentially growing two-dimensional waves.

The idea of solving the parabolic evolution of disturbances in non-parallel boundary layers was first introduced by Floryan & Saric (1979) and later also by Hall (1983) for steady Görtler vortices. Bertolotti *et al.* (1992) developed the method of parabolic evolution of eigenmodes in boundary layers and derived the parabolized stability equations (PSE). The method is computationally very fast and has been shown to be in excellent agreement with direct numerical simulations (DNS) of the Navier–Stokes equations and experiments.

In the transition community, the e^N-method is a well known transition-prediction tool and has been shown to fairly accurately predict transition for simple flows. It was developed independently by Smith & Gamberoni (1956) and van Ingen (1956) and empirically correlates the exponentially growing amplification of linear eigenmodes with the onset of transition. Transition takes place when the amplitude of the most amplified disturbance reaches e^N times its initial amplitude. The method does not account for the receptivity process. However, they reported, after analyzing data from a large number of low-disturbance experiments, that the N-factors between 8 and 11 fairly well described the onset and end of the transition region. They also concluded that those values decreased with increasing freestream turbulence. A modification of the e^N-method in order to account for freestream turbulence was proposed by Mack (1977). The freestream-turbulence level Tu was correlated to the N-factor by comparing the transition Reynolds number from experimental flat-plate boundary layer data collected by Dryden (1959) with parallel, linear stability theory for the Blasius boundary layer. Mack suggested the following relation for the N-factor at transition

$$N = -8.43 - 2.4 \ln Tu, \tag{1}$$

which he claims is valid in the range $0.1\,\% < Tu < 2\,\%$. For a freestream-turbulence level less than $0.1\,\%$, he mentioned that the dominant disturbance source is thought to be wind-tunnel noise rather than turbulence.

Exponential instability involving unstable eigenmodes is not the only transition scenario. For a sufficiently large disturbance amplitude, algebraic non-modal growth can lead to so-called bypass transition, not associated with exponential instabilities. At a moderate or high lever of freestream turbulence, many experiments have observed streaky structures, taking the form of elongated streamwise structures with narrow spanwise scales and much larger streamwise scales. This type of disturbance is historically denoted as the Klebanoff mode after the boundary-layer experiments of Klebanoff (1971). More recent experiments displaying streaky structures in boundary layers, subject to various levels of freestream turbulence, have been performed by e.g. Westin *et al.* (1994) and Matsubara & Alfredsson (2001). Ellingsen & Palm (1975) performed linear stability analysis of inviscid channel flow. They showed that finite three-dimensional disturbances without streamwise variation can lead to instability, even though the basic velocity does not possess any inflection point. The instability leads to an increase linearly with time of the streamwise disturbances, producing alternating low and high velocity streaks. Landahl (1980) demonstrated that all parallel inviscid shear flows can be unstable to three-dimensional disturbances, which lead to a growth of the disturbance energy at least as fast as linearly in time. The physical interpretation of the formation of the streaks is the lift-up effect, i.e. that fluid elements initially retain their horizontal momentum when displaced in the wall-normal direction, hence causing a streamwise disturbance. The combination of inviscid, algebraic growth and viscous dissipation has been known as transient growth (see Hultgren & Gustavsson 1981; Butler & Farrell 1992; Henningson *et al.* 1993; Reddy & Henningson 1993). In those papers, the optimal transient growth and associated disturbances were computed, in various parallel flows, by optimizing over the eigenmodes of the Orr–Sommerfeld operator.

Luchini (1996) considered steady spanwise periodic disturbances, with a spanwise scale much larger than the boundary layer thickness and much smaller than the streamwise scale. An eigenvalue problem in the Sturm–Liouville form was formulated for the Blasius boundary layer and it was concluded that there is a mode that possesses unbounded growth of the streamwise velocity. Tumin (2001) made an extension of Luchini's theory to the Falkner–Skan boundary layer and found that the unbounded growth may be suppressed by a favorable pressure gradient.

Andersson *et al.* (1999) and Luchini (2000) adopted an input-output methodology to calculate the optimal disturbance in the Blasius boundary layer, taking the non-parallel effects into account. The governing equations used are parabolic in the streamwise direction and were obtained from the linearized Navier–Stokes equations subject to the boundary-layer scalings. The disturbances were assumed to be slowly varying in the streamwise direction and periodic in the spanwise direction and time. An adjoint-based optimization technique was used to optimize the input disturbance at the leading edge giving rise to the largest disturbance energy gain at the final downstream position. By going to the limit of large Reynolds number (based on the final streamwise position), Luchini motivated the assumption that the optimal initial disturbance has a zero streamwise component, while the final downstream disturbance only consist of the streamwise component. That assumption simplifies the optimization procedure considerably. Andersson *et al.*and Luchini independently calculated the spanwise wave number $\beta = 0.45$ and a zero frequency for the optimal disturbance in the large-Reynolds-number limit giving rise to a growth $G = 0.0022 Re_l$. Their results agreed remarkably well with experimental data produced by Westin *et al.* (1994), irrespective of the absent optimization procedure in the experiments. Tumin & Reshotko (2003) made an extension of the model by Luchini to the case of compressible boundary layers. They also investigated the effect of different initial positions of the optimal disturbance.

Corbett & Bottaro (2000) used an direct-adjoint technique similar to the one used by Andersson *et al.*and Luchini to calculate optimal disturbances to the temporal problem for the Falkner–Skan boundary layer. The main advantage of the parallel-flow assumption, in contrast to the spatial approach, is that it permits the study of oblique disturbances with comparable streamwise and spanwise scales. It was found that optimal disturbances in flows subject to adverse pressure gradients experience greater amplifications and those in accelerated flows less amplification in comparison to the Blasius boundary layer. It was also found, as in the case for the Blasius boundary layer, that the most amplified disturbances are streamwise elongated structures.

Andersson *et al.* (1999) made an attempt at prediction of bypass-transition due to algebraic growth by correlating the transition Reynolds number Re_T and the freestream-turbulence level

$$\sqrt{Re_T}Tu = K, \tag{2}$$

where K should be constant for freestream-turbulence levels in the range $1\,\% < Tu < 5\,\%$. By comparison of different experimental studies the constant was chosen as $K = 12$.

Other empirical transition-prediction correlations involving the effects of freestream turbulence and streamwise pressure gradient have been developed. van Driest & Blumer (1963) postulated that transition occurs when the maximum vorticity Reynolds number reaches a critical value, to be correlated with the pressure gradient and freestream-turbulence level. In the case of zero pressure gradient their formula correlated with experiments agrees well with (2). Another example is a model by Abu-Ghannam & Shaw (1980), which gives the Reynolds number based on the momentum thickness θ, at the start and end of the transition region. The only inputs to the model are the freestream-turbulence level and the pressure gradient parameter $\lambda_\theta = (\theta^2/\nu)\partial U_0/\partial x$. More advanced transition prediction and studies of the transition phenomena itself can be made by numerical simulations such as the non-linear PSE technique (e.g. Hein *et al.* 1999).

In the present paper we first introduce governing equations valid for both linear exponential instability and algebraic instability analysis. We follow the work done by Andersson *et al.* (1999) in the algebraic-instability regime and calculate optimal disturbances in the large-Reynolds-number limit for flat-plate boundary layers with favorable, adverse and zero pressure gradients. The optimization is carried out over the initial streamwise position as well as the spanwise wave number and frequency. We present an energy growth for the optimal disturbance introduced at a certain downstream position, more than $50\,\%$ larger than for the optimal disturbance introduced at the leading edge. Furthermore, we calculate the exponential growth of the most amplified eigenmodes for the same base flows and Reynolds number. We conclude with comparing the two different instability scenarios and assess their impact on the

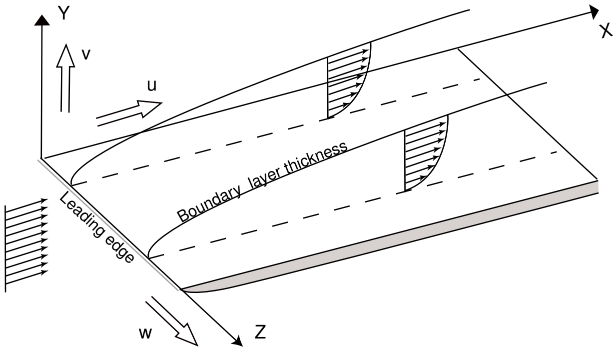

FIGURE 1. Flat-plate boundary layer flow.

transition Reynolds number by using a generalized version of (2) and the assumption that exponentially growing disturbances have a weak receptivity to freestream turbulence.

2. General Formulation

2.1. *Governing equations*

In this part we will discuss a set of equations that is valid for both algebraically and exponentially growing disturbances, even though the problems are associated with different scales. The well-known PSE technique (Bertolotti *et al.* 1992; Herbert 1997) uses the so called PSE-scaling (see table 1), which is suitable for exponentially growing eigenmodes. Here we follow the work by Andersson *et al.* (1999) and use a scaling appropriate for algebraically growing non-modal disturbances.

Consider an incompressible boundary layer over a flat plate as illustrated in figure 1. The scalings originate from the boundary-layer approximations and are also summarized in table 1. The streamwise coordinate x is scaled with the length scale l, which is a fixed distance from the leading edge. The wall-normal and spanwise coordinates y and z, respectively, are scaled with the boundary-layer parameter $\delta = \sqrt{\nu l/U_\infty}$, where ν is the kinematic viscosity of the fluid and U_∞ is the streamwise freestream velocity at the distance l from the leading edge. The streamwise velocity u is scaled with U_∞, while the wall-normal and spanwise velocities v and w, respectively, are scaled with $U_\infty \delta/l$. The pressure p is scaled with $\rho U_\infty^2 \delta^2/l^2$ and the time t is scaled with l/U_∞. The Reynolds numbers used here are defined as $Re_l = U_\infty l/\nu$ and $Re_\delta = U_\infty \delta/\nu$. It is useful to note the relations $l/\delta = Re_\delta = \sqrt{Re_l}$.

We want to study the linear stability of a high Reynolds number flow. The non-dimensional Navier–Stokes equations for an incompressible flow are linearized around a two-dimensional, steady base flow $\big(U(x,y), V(x,y), 0\big)$ to obtain the stability equations for the spatial evolution of three-dimensional, time-dependent disturbances $\big(u(x,y,z,t), v(x,y,z,t), w(x,y,z,t), p(x,y,z,t)\big)$.

Var.	x	y, z	t	$\hat{u}$	$\hat{v}, \hat{w}$	$\hat{p}$	α	β	ω
BL	l	δ	l/U_∞	U_∞	$U_\infty\delta/l$	$\rho U_\infty^2\delta^2/l^2$		$1/\delta$	U_∞/l
PSE	δ	δ	δ/U_∞	U_∞	U_∞	ρU_∞^2	$1/\delta$	$1/\delta$	U_∞/δ
Ratio	Re_δ	1	Re_δ	1	$1/Re_\delta$	$1/Re_\delta^2$		1	$1/Re_\delta$

Table 1. The boundary-layer and PSE-scalings of the variables and their ratio.

The base flow and the disturbances are scaled in the same way. The disturbances are taken to be periodic in the spanwise direction and time, which allows us to assume solutions of the form

$$f = \hat{f}(x, y) \exp\left[\mathrm{i}Re_\delta \int_{x_0}^{x} \alpha(x)\,\mathrm{d}x + \mathrm{i}\beta z - \mathrm{i}\omega t\right], \tag{3}$$

where f represents either one of the disturbances u, v, w or p. The complex streamwise wave number α captures the fast wavelike variation of the modes and is therefore scaled with $1/\delta$. α itself is assumed to vary slowly with x. Since x is scaled with l, the factor Re_δ appears in front of the integral. The x-dependence in the amplitude function $\hat{f}$ includes the weak variation of the disturbances. The real spanwise wave number β and angular frequency ω are scaled in a consistent way with z and t, respectively. Introducing the assumption (3) in the linearized Navier–Stokes equations and neglecting all third order terms in $1/Re_\delta$ or higher, we arrive at the parabolized stability equations in boundary-layer scalings

$$\hat{u}_x + \mathrm{i}Re_\delta\alpha\hat{u} + \hat{v}_y + \mathrm{i}\beta\hat{w} = 0, \tag{4a}$$

$$(U_x + \mathrm{i}Re_\delta\alpha U - \mathrm{i}\omega)\hat{u} + U\hat{u}_x + V\hat{u}_y + U_y\hat{v} + \frac{\hat{p}_x}{Re_\delta^2} + \frac{\mathrm{i}\alpha\hat{p}}{Re_\delta} = \hat{u}_{yy} - k^2\hat{u}, \tag{4b}$$

$$(V_y + \mathrm{i}Re_\delta\alpha U - \mathrm{i}\omega)\hat{v} + U\hat{v}_x + V_x\hat{u} + V\hat{v}_y + \hat{p}_y = \hat{v}_{yy} - k^2\hat{v}, \tag{4c}$$

$$(\mathrm{i}Re_\delta\alpha U - \mathrm{i}\omega)\hat{w} + U\hat{w}_x + V\hat{w}_y + \mathrm{i}\beta\hat{p} = \hat{w}_{yy} - k^2\hat{w}, \tag{4d}$$

where $k^2 = \alpha^2 + \beta^2$. Since we are considering both algebraically and exponentially growing disturbances, where the appropriate scales differ, the determination of which terms are of higher order needs a discussion. The boundary-layer and PSE-scalings of the variables and their ratio are presented in table 1. The last line in table 1 can also be interpreted as the relative difference in order between the algebraic and exponential disturbances.

Consider the algebraic instability problem. The order of magnitude of all amplitude functions, the spanwise wave number and angular frequency are the same. For algebraically growing disturbances, only weak streamwise variations are considered, captured by the amplitude functions themselves, so the streamwise wave number α is set to zero. After disregarding terms including α there is only one term of higher order kept in (4). That term is the $\hat{p}_x/Re_\delta^2$ term in the

Instability	$\mathcal{O}(1)$	$\mathcal{O}(Re_\delta)$	$\mathcal{O}(Re_\delta^2)$
algebraic	$\hat{u}, \hat{v}, \hat{w}, \hat{p}, \beta, \omega$		
exponential	$\hat{u}, \alpha, \beta$	$\hat{v}, \hat{w}, \omega$	$\hat{p}$

TABLE 2. Orders of the variables relative to the boundary-layer scalings.

streamwise momentum equation (4b). It is needed for the exponential instability problem, but is obviously $\mathcal{O}(1/Re_\delta^2)$ for the algebraic instability problem. Note that all the other terms are $\mathcal{O}(1)$ and there are no $\mathcal{O}(1/Re_\delta)$ terms left in the equations.

For the exponential instability problem we need to reconsider the orders of magnitude of the terms in (4). Note that we will be comparing the relative order between the terms within each equation and consider the two lowest orders as important for the problem. Now we include a fast oscillatory streamwise variation in the disturbances, implying that α is $\mathcal{O}(1)$ and ω is $\mathcal{O}(Re_\delta)$, since $\omega = \alpha c$ (c is the complex phase speed). A balance of terms in the continuity equation implies that $\hat{v}$ and $\hat{w}$ is $\mathcal{O}(Re_\delta)$. The total time derivative should balance the pressure gradient in the normal momentum equation (4c) and $\hat{p}$ changes to $\mathcal{O}(Re_\delta^2)$. The second, third, sixth and eighth term in the streamwise momentum equation (4b) are $\mathcal{O}(Re_\delta)$, the other terms are $\mathcal{O}(1)$. In the normal momentum equation (4c), the second, third and seventh term are $\mathcal{O}(Re_\delta^2)$, the other terms are $\mathcal{O}(Re_\delta)$ except the $V_x\hat{u}$ term, which is only $\mathcal{O}(1)$. Hence, that term is negligible for the exponential instability problem. In the spanwise momentum equation (4d) the first, second and fifth term are $\mathcal{O}(Re_\delta^2)$, while the rest of the terms are $\mathcal{O}(Re_\delta)$.

As a summary, the different orders of magnitude of the amplitude functions, wave numbers and angular frequency based on the scaling used are presented in table 2. We can conclude that all the terms in (4) are generally of the first or the second order except the $\hat{p}_x/Re_\delta^2$ term, in the streamwise momentum equation (4b), which is of the third order for the algebraic instability problem and the $V_x\hat{u}$ term, in the normal momentum equation (4c), which is of the third order for the exponential instability problem. Both of those terms, however, have to be included in a general formulation of the problem. Unfortunately, the $\hat{p}_x/Re_\delta^2$ term introduces numerical instability, setting a lower limit on the streamwise step size.

We are interested in solutions to (4) subject to no-slip conditions at the plate and vanishing at the wall-normal position y_{max} well outside the boundary layer. The boundary conditions in the wall-normal direction can then be written

$$\begin{aligned} \hat{u} = \hat{v} = \hat{w} = 0 \quad &\text{at} \quad y = 0, \\ \hat{u} = \hat{v} = \hat{w} = 0 \quad &\text{at} \quad y = y_{max}. \end{aligned} \tag{5}$$

The set of equations (4) is nearly parabolic in the streamwise coordinate and are marched forward from an initial position x_0 to a final position x_1. Given the initial conditions

$$\hat{u} = \hat{u}_0(y), \quad \hat{v} = \hat{v}_0(y), \quad \hat{w} = \hat{w}_0(y) \quad \text{at} \quad x = x_0, \tag{6}$$

the wave number β and the angular frequency ω, the initial-boundary-value problem (4–6) can be solved from x_0 to x_1 to obtain the downstream development of the disturbance. In addition, an additional equation for the streamwise wave number α is needed in the exponential instability problem, see Section 4.1

2.2. *Mathematical characteristics*

The large computational gain of the PSE technique is a result of the assumption that the disturbance can be decomposed into a rapidly varying wavelike component and a slowly varying amplitude function. The equations governing the evolution of the amplitude functions are parabolized and can be solved economically using a marching procedure. However, although there are no second streamwise derivatives left in the stability equations (4), still some ellipticity remains causing numerical stability problems. This is demonstrated by a rapid oscillation of the solution when the streamwise marching step becomes too small. The sources of ellipticity arise from the upstream propagation of acoustic waves and viscous diffusion. Haj-Hariri (1994) suggested the suppression of the upstream propagation of acoustic waves by either removing the streamwise derivative of the pressure or the streamwise velocity amplitude function in the streamwise momentum or continuity equation after analysis of disturbances with a fixed angular frequency in a parallel boundary layer. Li & Malik (1994, 1996) showed that numerical stability in the marching procedure is achieved by putting a requirement of the step size to be

$$\Delta x > \frac{1}{Re_\delta |\alpha_\mathrm{r}|}, \tag{7}$$

where the Reynolds number appears here due to the present difference in scaling of x and α. They also mentioned that dropping of $\hat{p}_x$ relaxes the step-size restriction. Andersson *et al.* (1998) made the equations well-posed and removed the step-size restriction by adding a term proportional to the truncation error to the first-order backward Euler scheme. They performed several numerical examples and showed a stable marching procedure for arbitrarily small step sizes. However, they pointed out, if the streamwise variation of the amplitude function becomes rapid, the error from the added term may become significant.

2.3. *Energy norm*

In investigations of spatial growth a commonly used measure of the disturbance energy at a specific streamwise position is defined by

$$E(x) = \int_0^{y_{max}} (Re_l|\hat{u}|^2 + |\hat{v}|^2 + |\hat{w}|^2)\,\mathrm{d}y\ \exp\left[-2Re_\delta \int_{x_0}^{x} \alpha_\mathrm{i}\,\mathrm{d}x\right]. \tag{8}$$

In order to cancel the influence of the difference in scaling and obtain similar weighting of the velocity components, the streamwise term in the energy is scaled with Re_l. Consequently, the streamwise term is $\mathcal{O}(Re_l)$ while the wall-normal and spanwise terms are $\mathcal{O}(1)$ for the algebraic instability problem, while they are of the same order for the exponential instability problem. The disturbance growth is defined by

$$G(x_0, x_1, \beta, \omega, Re_l) = \frac{E(x_1)}{E(x_0)}. \tag{9}$$

In order to compare the growth of the both instability problems in a convenient way and discuss transition prediction we need to introduce the N-factor defined as

$$N = \ln\sqrt{G} = \ln\sqrt{\frac{E(x_1)}{E(x_0)}}. \tag{10}$$

3. Algebraic Instability

3.1. *Linear scaling with Reynolds number*

As we will see in the next section, the spatial transient growth scales linearly with the Reynolds number in the large-Reynolds-number limit. This allows us to derive a transformation between the growth obtained for different parameter combinations. Let us define a Reynolds number independent growth as

$$\overline{G}(x_0, x_1, \beta, \omega) = \lim_{Re_l \to \infty} \frac{G(x_0, x_1, \beta, \omega, Re_l)}{Re_l}. \tag{11}$$

Consider the same physical problem scaled with two different length scales l and l' and the corresponding freestream velocities $U_\infty = U_\infty(l)$ and $U'_\infty = U_\infty(l')$. The dimensional quantities, denoted with a star, and the Reynolds numbers associated with the different scales can then be expressed as

$$\begin{gathered} x^* = xl = x'l', \quad \beta^* = \beta\sqrt{\frac{U_\infty}{\nu l}} = \beta'\sqrt{\frac{U'_\infty}{\nu l'}}, \\ \omega^* = \omega\frac{U_\infty}{l} = \omega'\frac{U'_\infty}{l'}, \quad Re_l = \frac{U_\infty l}{\nu}, \quad Re_{l'} = \frac{U'_\infty l'}{\nu}. \end{gathered} \tag{12}$$

Since the growth is independent of how we choose to scale the problem we have

$$G(x_0, x_1, \beta, \omega, Re_l) = G(x'_0, x'_1, \beta', \omega', Re_{l'}). \tag{13}$$

Introducing the scale ratios $c^2 = l/l'$ and $d^2 = U_\infty/U'_\infty$ and rewriting the right-hand side of (13) in the unprimed quantities using the relations in (12) yields

$$G(x_0, x_1, \beta, \omega, Re_l) = G(c^2 x_0, c^2 x_1, \frac{d}{c}\beta, \frac{d^2}{c^2}\omega, \frac{1}{c^2 d^2} Re_l). \tag{14}$$

Multiplying both sides of (14) by $c^2 d^2/Re_l$ and letting Reynolds number tend to infinity we obtain a transformation formula for the Reynolds-number-independent growth

$$c^2 d^2 \overline{G}(x_0, x_1, \beta, \omega) = \overline{G}(c^2 x_0, c^2 x_1, \frac{d}{c}\beta, \frac{d^2}{c^2}\omega). \tag{15}$$

Looking at the x-dependence in the growth, it is obvious that such a transformation is only possible when keeping the ratio x_0/x_1 constant.

3.2. *Optimal disturbances*

Now we consider solutions to (4) giving rise to disturbances with weak streamwise variations and α is set to zero. We are interested in maximizing the energy of the disturbance, given by (8), in the downstream position x_1 by optimizing the initial disturbance at x_0 with given initial energy. That is, we want to maximize the spatial transient growth defined by (9). Clearly, in the large-Reynolds-number limit, the maximum growth will, because of the difference in order between the terms, be obtained for initial disturbances with a zero streamwise component. Furthermore, provided that $\hat{u}_1$ is non-zero, even here because of the difference in order, $\hat{v}_1$ and $\hat{w}_1$ are neglected and the Reynolds-number-independent growth (11) can be simplified to

$$\overline{G} = \lim_{Re_l \to \infty} \frac{G}{Re_l} = \frac{\displaystyle\int_0^{y_{max}} |\hat{u}_1|^2 \, \mathrm{d}y}{\displaystyle\int_0^{y_{max}} (|\hat{v}_0|^2 + |\hat{w}_0|^2) \, \mathrm{d}y}. \tag{16}$$

Obviously, in the large-Reynolds-number limit, the optimal initial disturbance becomes independent of Re_l, which only appears as a proportional factor in the growth. If we introduce the norms

$$\|\hat{u}_1\|^2 = (\hat{u}_1, \hat{u}_1) = \int_0^{y_{max}} |\hat{u}_1|^2 \, \mathrm{d}y, \tag{17}$$

$$\|\boldsymbol{q}\|^2 = (\boldsymbol{q}, \boldsymbol{q}) = \int_0^{y_{max}} (|\hat{v}_0|^2 + |\hat{w}_0|^2) \, \mathrm{d}y, \tag{18}$$

where $\boldsymbol{q} = (\hat{v}_0, \hat{w}_0)^T$, the Reynolds-number-independent growth can be written as

$$\overline{G} = \frac{\|\hat{u}_1\|^2}{\|\boldsymbol{q}\|^2}. \tag{19}$$

Since the initial-boundary-value problem (4) is linear and homogeneous, we may adopt an input-output formulation

$$\hat{u}_1 = \mathcal{A}\boldsymbol{q}, \tag{20}$$

where $\mathcal{A}$ is a linear operator. The maximum Reynolds-number-independent growth may then be written

$$\overline{G}_{max} = \max_{\boldsymbol{q}\neq 0} \frac{\|\hat{u}_1\|^2}{\|\boldsymbol{q}\|^2} = \max_{\boldsymbol{q}\neq 0} \frac{(\mathcal{A}^*\mathcal{A}\boldsymbol{q},\boldsymbol{q})}{(\boldsymbol{q},\boldsymbol{q})}. \tag{21}$$

Here $\mathcal{A}^*$ denotes the adjoint operator to $\mathcal{A}$ with respect to the chosen inner product. The maximum of $(\mathcal{A}^*\mathcal{A}\boldsymbol{q},\boldsymbol{q})/(\boldsymbol{q},\boldsymbol{q})$ is attained for some vector $\boldsymbol{q}$. In view of some basic facts from operator theory, that vector is the eigenvector corresponding to the largest eigenvalue of the eigenvalue problem

$$\mathcal{A}^*\mathcal{A}\boldsymbol{q} = \lambda \boldsymbol{q}, \tag{22}$$

and $\overline{G}_{max}$ is the maximum eigenvalue λ_{max}, necessarily real and non-negative. The most natural attempt to calculate the optimal initial disturbance and its associated maximum Reynolds-number-independent growth is by power iterations

$$\boldsymbol{q}^{n+1} = \mathcal{A}^*\mathcal{A}\boldsymbol{q}^n, \tag{23}$$

where the initial disturbance is scaled to the given initial energy in each iteration.

3.3. *Adjoint equations*

In order to perform the power iterations we need to know the action of the adjoint operator $\mathcal{A}^*$ on some function $\psi_1(y)$. By definition of the adjoint operator $\mathcal{A}^*$, we have

$$(\psi_1, \mathcal{A}\boldsymbol{q}) = (\mathcal{A}^*\psi_1, \boldsymbol{q}). \tag{24}$$

If we denote $\mathcal{A}^*\psi_1 = \boldsymbol{\phi} = \big(\phi_2(y), \phi_3(y)\big)^T$, the inner products can explicitly be written

$$(\psi_1, \mathcal{A}\boldsymbol{q}) = \int_0^{y_{max}} \overline{\psi}_1 \hat{u}_1 \, \mathrm{d}y, \tag{25}$$

$$(\mathcal{A}^*\psi_1, \boldsymbol{q}) = \int_0^{y_{max}} (\overline{\phi}_2 \hat{v}_0 + \overline{\phi}_3 \hat{w}_0) \, \mathrm{d}y, \tag{26}$$

where the bar denotes complex conjugate. The following adjoint system is derived in the appendix

$$\begin{aligned}
&-v^*_y + \mathrm{i}\beta w^* = 0,\\
&-\mathrm{i}\omega u^* - U u^*_x - V_y u^* - V u^*_y + V_x v^* - p^*_x = u^*_{yy} - \beta^2 u^*,\\
&-\mathrm{i}\omega v^* - U v^*_x - U_x v^* - V v^*_y + U_y u^* - p^*_y = v^*_{yy} - \beta^2 v^*,\\
&-\mathrm{i}\omega w^* - U w^*_x - V w^*_y + \mathrm{i}\beta p^* = w^*_{yy} - \beta^2 w^*,
\end{aligned} \tag{27}$$

where $p^*(x,y)$, $u^*(x,y)$, $v^*(x,y)$ and $w^*(x,y)$ are the adjoint variables with boundary conditions

$$\begin{aligned}
&\overline{u}^* = \overline{v}^* = \overline{w}^* = 0 && \text{at} \quad y = 0,\\
&\overline{u}^* = \overline{w}^* = \overline{p}^* + 2V\overline{v}^* = 0 && \text{at} \quad y = y_{max}.
\end{aligned} \tag{28}$$

The individual values of $\overline{p}^*$ and $\overline{v}^*$ do not matter as long as the combination $\overline{p}^* + 2V\overline{v}^* = 0$ is fulfilled. The x-derivative in the parabolic set of equations (27) has opposite sign compared to (4) and is to be solved in the backward direction from the final position x_1 to the initial position x_0. Therefore the initial conditions are specified at x_1

$$\begin{aligned} &U_1\overline{u}_1^* + \overline{p}_1^* = \overline{\psi}_1(y) \quad && \text{at} \quad x = x_1, \\ &\overline{v}_1^* = \overline{w}_1^* = 0 && \text{at} \quad x = x_1. \end{aligned} \tag{29}$$

The action of the adjoint operator is then given by

$$\begin{aligned} &\overline{\phi}_2 = U_0(y)\overline{v}_0^*(y) \quad && \text{at} \quad x = x_0, \\ &\overline{\phi}_3 = U_0(y)\overline{w}_0^*(y) && \text{at} \quad x = x_0. \end{aligned} \tag{30}$$

3.4. *Optimization algorithm*

The adjoint-based optimization algorithm is very efficient and converges often within three or four iterations, indicating the existence of a well-separated dominating mode. The optimization problem in the large-Reynolds-number limit is defined by (21) and concerns the optimization of the initial disturbance $\boldsymbol{q}$ for given values of x_0, x_1, β and ω. It may be solved with the power iteration (23) and involves the following three steps:

1. Given a current guess of the initial condition $(\hat{v}_0^n, \hat{w}_0^n)$, initially arbitrary, solve equations (4) subject to the boundary conditions (5) and the initial conditions (6) with $\hat{u}_0 = 0$, $\hat{v}_0 = \hat{v}_0^n$ and $\hat{w}_0 = \hat{w}_0^n$.
2. Solve the adjoint equations (27) subject to the boundary conditions (28) and the initial conditions (29) with $\psi_1 = \hat{u}_1^n$ obtained from step 1.
3. Assign the new initial disturbance as the action of the adjoint operator (30) with v_0^* and w_0^* obtained from step 2 and where $\phi_2 = \hat{v}_0^{n+1}$ and $\phi_3 = \hat{w}_0^{n+1}$. After scaling the initial disturbance, making (18) to a given value, insert it into step 1 for the next iteration.

Terminate the iterations when $(G^{n+1} - G^n)/G^{n+1}$ falls below a small prescribed value.

The initial position can then be optimized with a simple polynomial optimization technique. Initially the optimal disturbances with associated growth are calculated for three initial positions. A second order polynomial is fitted to the points and the next guess of the optimal initial position is attained from the maximum of the polynomial. A new polynomial is fitted to the last three points and the procedure is proceeded until requested accuracy is achieved.

The numerical method solving the forward problem (4–6) and the backward problem (27–29) is based on a spectral collocation method involving Chebyshev polynomials. Details about the numerical scheme can be found in Andersson *et al.* (1999) and Hanifi *et al.* (1996). The numerical code is developed from the linear PSE code used by Pralits *et al.* (2002).

4. Exponential Instability

4.1. *Normalization condition*

Here we consider solutions to (4) giving rise to disturbances with strong streamwise variations and no terms are disregarded. As both the amplitude and phase function depend on x, one more equation is required. We also wish to satisfy the assumption that both the amplitude function and the wave number change slowly in the streamwise direction. We achieve this by specifying a normalization condition on the amplitude function

$$\int_0^{y_{max}} (Re_l \bar{\hat{u}} \hat{u}_x + \bar{\hat{v}} \hat{v}_x + \bar{\hat{w}} \hat{w}_x) \, \mathrm{d}y = 0, \tag{31}$$

where the bar again denotes complex conjugate. Other normalizations are possible and are presented in Bertolotti *et al.* (1992). The normalization condition specifies how much growth and sinusoidal variation is represented by the amplitude and phase function, respectively. The stability problem (4–6) and the normalization condition (31) have to be solved iteratively in each streamwise step. As mentioned in the previous section, details about the numerical scheme can be found in Andersson *et al.* (1999) and Hanifi *et al.* (1996) and the numerical code is developed from the linear PSE code used by Pralits *et al.* (2002). The initial conditions (6) are taken from the local theory as the least stable eigenfunction of Orr–Sommerfeld & Squire equations with corresponding eigenvalue $\alpha(x_0)$. Since the initial conditions then do not capture non-parallel effects there will be a region in the beginning of the domain that includes some errors. The size of those errors and the length of that region are dependent of how non-parallel the base flow is and will of course increase for lower Reynolds numbers.

Note that no optimization is made over the initial conditions as was done for the algebraically growing disturbances. Rather, the exponential growth is maximized in the sense that the envelope of the most amplified eigenmode is calculated. Within the PSE approximation it is difficult to incorporate the influence of mode non-normality. However an assessment of these effects for exponentially growing disturbances can be made by comparing to the work of Corbett & Bottaro (2000). They show that there is at most an additional factor of 10 contribution to the energy growth from those effects. This may add a value of one to our N-factor (10). However, the non-modal growth of TS-waves are due to the so called Orr-mechanism (Farrell 1988), which is based on initial conditions not too likely to occur in boundary layers in applications.

5. Results

5.1. *Base flow*

The linear stability analysis is done with the Falkner–Skan boundary layer as the base flow. Falkner–Skan similarity equation reads

$$f''' + ff'' + \beta_H(1 - f'^2) = 0, \tag{32}$$

subject to the boundary conditions

$$f(0) = f'(0) = 0, \quad f'(\infty) = 1, \tag{33}$$

where f is the non-dimensional stream function and the prime denotes derivatives with respect to the similarity variable η. The base flow can then be

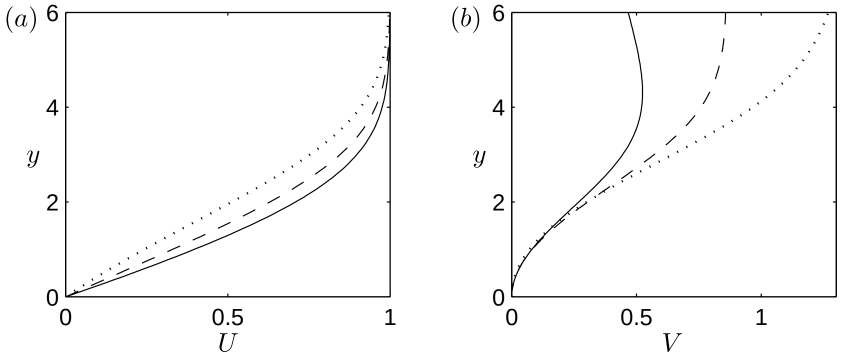

FIGURE 2. Base flow velocities from the Falkner–Skan similarity solution. Solid line: $\beta_H = 0.1$. Dashed line: $\beta_H = 0$. Dotted line: $\beta_H = -0.1$. (a) Streamwise velocity. (b) Wall-normal velocity.

written

$$U = U_e f', \quad V = \frac{1}{g}\big((1-\beta_H)\eta f' - f\big), \tag{34}$$

associated with the non-dimensional coordinates in the following way

$$y = g\eta, \quad U_e = x^{\frac{\beta_H}{2-\beta_H}}, \tag{35}$$

where $U_e = U_e(x)$ is the freestream velocity and

$$g = \sqrt{(2-\beta_H)\frac{x}{U_e}}. \tag{36}$$

The Hartree parameter β_H describes the freestream acceleration, as seen in (35), driven by the pressure gradient. In this work we have used three base flows with favorable, adverse and zero pressure gradients. The Hartree parameters are $\beta_H = 0.1$, $\beta_H = -0.1$ and $\beta_H = 0$, respectively. The streamwise and wall-normal base-flow velocities are shown in figure 2. Throughout this paper, figures showing results comparing the base flows have the same line type, with solid lines for the favorable pressure gradient, dotted lines for the adverse pressure gradient and dashed lines for the zero pressure gradient.

5.2. *Optimal disturbances and streaks*

We study the optimal algebraic growth (9) of disturbances in the large-Reynolds-number limit, and its dependence of the initial position x_0, spanwise wave number β and angular frequency ω. The final position is set to $x_1 = 1$, thus the dimensional final position is l and the Reynolds number there is set to $Re_l = 10^6$. When presenting results of the β and ω-dependency, the optimal initial position is used and the growth is represented in the N-factor (10).

Andersson *et al.* (1999) and Luchini (2000) used the leading edge as the initial position in their calculations. However, in base flows with non-zero

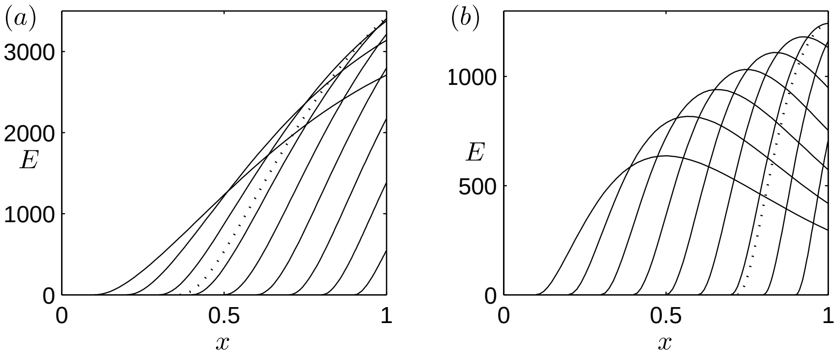

FIGURE 3. Energy growth along the plate in the Blasius boundary layer at $Re_l = 10^6$ for different initial positions, optimal case (dotted line). (*a*) $\beta = 0.5$ and $\omega = 0$. (*b*) $\beta = 1$ and $\omega = 5$.

pressure gradients it is not possible to perform accurate calculations starting very close to the leading edge due to the behavior of the similarity solution. Besides that problem we wish to investigate the impact of different x_0 on the growth. Figure 3(*a*) shows the energy growth along the plate for different initial positions for optimal disturbances with $\beta = 0.5$ and $\omega = 0$ in the Blasius boundary layer. The dotted line shows the optimal growth originating from the optimal initial position $x_0 = 0.36$. Disturbances introduced closer to the leading edge grow in a slower rate. On the other hand, disturbances introduced further downstream do not have distance enough to grow as much before the final position. An interpretation of the slower growth rate for disturbances introduced close to the leading edge is the influence of the boundary layer thickness on the lift-up effect. Upstream of the optimal initial position the boundary layer is not thick enough for the optimal distortion of fluid elements. Furthermore, the optimal disturbance introduced upstream will not have the optimal shape at a position further downstream. The growth rate seems to increase for disturbances introduced further downstream where the boundary layer is thicker.

Figure 3(*b*) again shows the energy growth in the Blasius boundary layer for different initial positions but for optimal disturbances with $\beta = 1$ and $\omega = 5$. Here it is seen that the viscous dissipation is more dominat and the energy soon starts to decay. The dotted line showing the optimal growth originates in this case from the initial position $x_0 = 0.72$. Since the adjoint-based optimization technique optimizes the initial disturbance with respect to the disturbance energy in the final position and we are interested in the maximum energy in the domain, the true optimum only results when the maximum energy appears in the final position. The optimization of the initial position not only gives

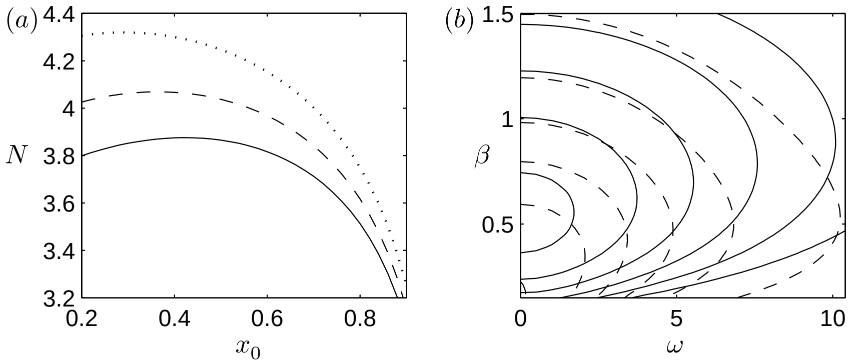

FIGURE 4. (a) N-factor vs x_0 at $Re_l = 10^6$ with $\beta = 0.5$ and $\omega = 0$. Lines as in figure 2. (b) Contours of constant N-factor (solid lines) with values, from right to left, 3 to 4 with contour spacing 0.2 and contours of constant optimum x_0 (dashed lines) with values, from left to right, 0.3 to 0.8 with contour spacing 0.1, for optimal disturbances in the Blasius boundary layer. $Re_l = 10^6$.

the optimal growth, it also ensures that the maximum energy is reached at the final position.

Figure 4(a) shows the x_0-dependence of the N-factor for optimal disturbances with $\beta = 0.5$ and $\omega = 0$ in the different base flows. The optimal initial position moves downstream with decreased pressure gradient. The particular values in this case are $x_0 = 0.29$ for the adverse-pressure-gradient base flow and $x_0 = 0.42$ for the favorable-pressure-gradient base flow. Contours of constant N-factor (solid lines) and constant optimal initial position (dashed lines) for optimal disturbances in the Blasius boundary layer can be seen in figure 4(b). The optimal initial position moves downstream with increasing spanwise wave number and angular frequency.

From now on the optimized initial position will be used and we turn our attention to the β and ω-dependency. First we investigate how the N-factor depends on β for the different base flows and the results are presented in figure 5(a). The optimal angular frequency $\omega = 0$ is used. The optimal β increases with decreased pressure gradient and the particular values are $\beta = 0.47$, $\beta = 0.53$ and $\beta = 0.58$. Secondly, figure 5(b) shows how the N-factors in the different base flows depend on ω. Here the optimal β-value for the respective flow case is used.

The results in figures 4(a) and 5(a) also show the effect of streamwise pressure gradient. The algebraic energy growth increases with increased streamwise pressure gradient of the base flow. That is consistent with the work by Tumin (2001), which used a slightly different spatial model, and the temporal stability analysis by Corbett & Bottaro (2000).

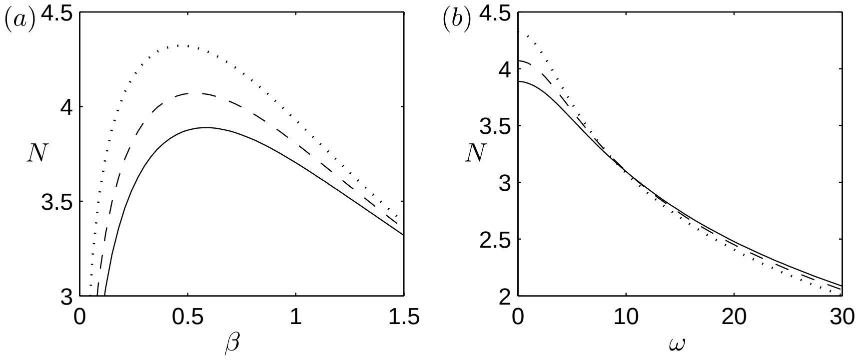

FIGURE 5. Lines as in figure 2. $Re_l = 10^6$. (a) N-factor vs β. $\omega = 0$. (b) N-factor vs ω. $\beta = 0.47, 0.53, 0.58$.

β_H	x_0	β	ω	N	G
0.1	0.45	0.58	0	3.9	$0.0024Re_l$
0	0.37	0.53	0	4.1	$0.0034Re_l$
-0.1	0.28	0.47	0	4.3	$0.0057Re_l$

TABLE 3. Optimal parameters for algebraically growing disturbances in the three base flows at $Re_l = 10^6$.

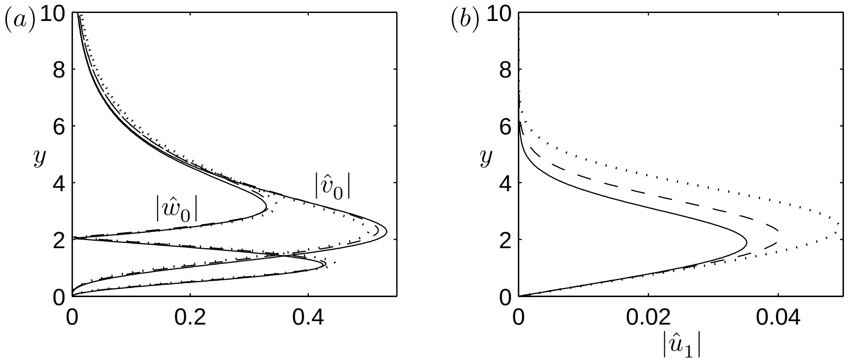

FIGURE 6. Lines as in figure 2. $Re_l = 10^6$. Parameters as in table 3. (a) Optimal initial disturbances. (b) Final disturbance.

The optimal x_0, β and ω and their corresponding growth in terms of N and G for the three base flows are summarized in table 3. The associated optimal initial disturbances are shown in figure 6(a) and when the spanwise periodic dependence is incorporated they take the form of vortices in the crossflow

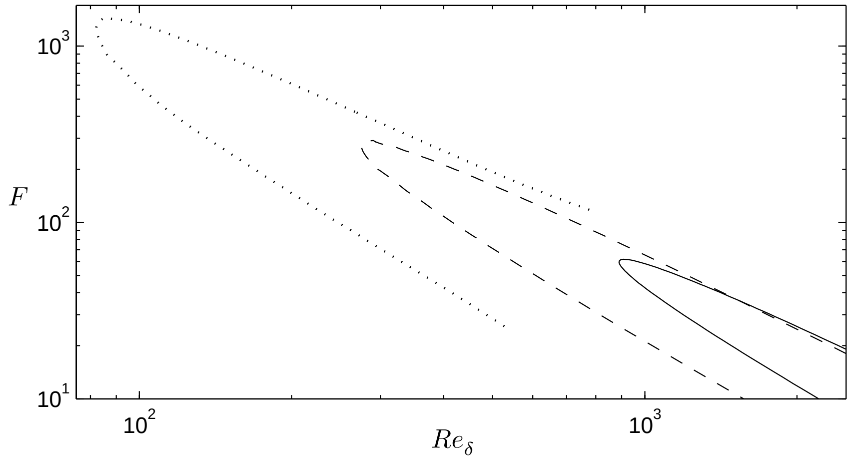

FIGURE 7. Lines as in figure 2. Neutral curves in the $Re_\delta - F$ plane for $\beta = 0$.

plane. Their shape, especially the normal scale, is rather insensitive to the change of pressure gradient in the base flow. The downstream response of the optimal disturbances, shown in figure 6(*b*), take the form of streamwise elongated streaks when the spanwise periodic dependence is incorporated.

5.3. *Tollmien–Schlichting waves*

We study the exponential growth (9) of modal disturbances, historically referred to as Tollmien–Schlichting waves, and its dependence of the spanwise wave number β and angular frequency ω. The Reynolds number is $Re_l = 10^6$. In the case of optimal disturbances we studied the dependence of the initial position of the disturbance. Here, the growth is maximized in the sense that the most amplified eigenmode is calculated within the unstable region of $x \in [0, 1]$. That means that x_0 is chosen as the lower-branch neutral point and x_1 is either equal to 1 or the upper-branch neutral point, if it appears for a lower value. However, since the initial condition does not capture non-parallel effects and introduces a region of errors, the equations are solved from an initial position sufficiently upstream of x_0 in order to remove those errors.

The disturbance is said to be unstable if the physical growth rate defined as

$$\sigma = \frac{1}{Re_\delta} \frac{1}{\sqrt{\hat{E}}} \frac{\partial \sqrt{\hat{E}}}{\partial x} - \alpha_{\mathrm{i}}, \tag{37}$$

where $\hat{E}$ is the amplitude function energy, is greater than zero and the neutral point is defined as the location where $\sigma = 0$. Figure 7 shows the neutral curves in the Re_δ–F plane, where $F = 10^6\omega/Re_l$ is the reduced frequency. The critical

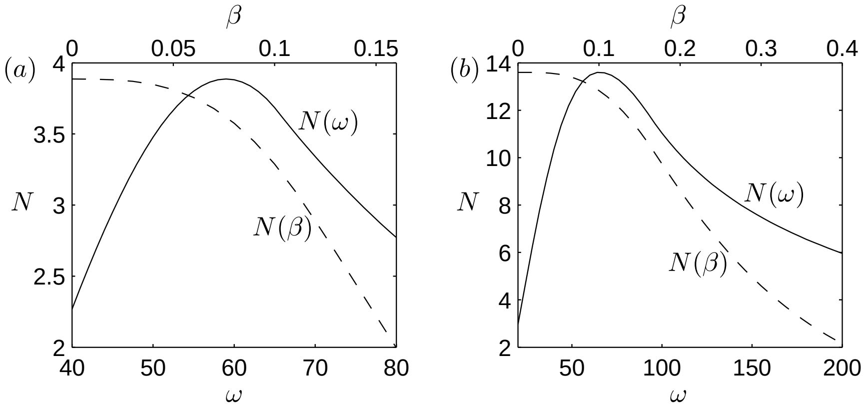

FIGURE 8. N-factor as function of ω (solid lines) and β (dashed lines) at $Re_l = 10^6$. (a) Blasius boundary layer. $N(\beta)$: $\omega = 59$, $N(\omega)$: $\beta = 0$ (b) Adverse-pressure-gradient base flow. $N(\beta)$: $\omega = 66$, $N(\omega)$: $\beta = 0$.

β_H	x_0	β	ω	N
0	0.31	0	59	3.9
-0.1	0.11	0	66	13.6

TABLE 4. Optimal parameters for exponentially growing disturbances for the zero and adverse-pressure-gradient base flows at $Re_l = 10^6$.

Reynolds numbers for the favorable, zero and adverse-pressure-gradient base flows are $Re_\delta = 889$, $Re_\delta = 275$ and $Re_\delta = 82$, respectively.

Since the favorable-pressure-gradient base flow is quite stable for exponentially growing disturbances, we will not investigate it further in this section. Instead we turn our attention to the β and ω-dependency of the two other base flows. Figures 8(a) and 8(b) show the results for the zero and adverse-pressure-gradient base flow, respectively. The solid lines show the N-factor as a function of ω and the optimal wave number $\beta = 0$ is used. The ω-labels are shown on the lower axis. The dashed lines show the N-factor as function of β and the optimal angular frequencies $\omega = 59$ and $\omega = 66$ in respective case are used. The β-labels are shown on the upper axis.

The optimal β and ω and their corresponding N-factors and lower-branch neutral points are summarized in table 4. The associated streamwise amplitude functions at x_0 and x_1, which is equal to 1 for the optimal cases, are shown in figures 9(a) and 9(b), respectively.

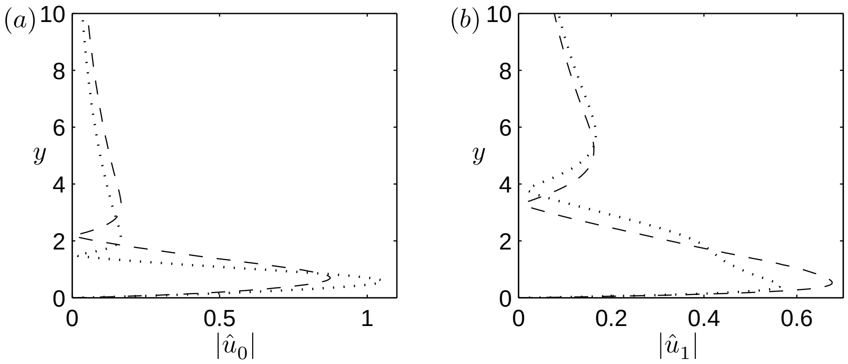

FIGURE 9. Lines as in figure 2. $Re_l = 10^6$. Parameters as in table 4. The most amplified streamwise amplitude functions at (*a*) x_0 and (*b*) x_1.

5.4. *Comparison of algebraic and exponential growth*

Now that we have studied the two different growth scenarios we compare the growth of optimal and modal disturbances. Figure 10(*a*) shows the envelope curves of the maximal algebraic and exponential N-factors vs Re_l. The algebraic growth in the large-Reynolds-number limit is proportional to Re_l and thus represented as the straight lines.

Figures 10(*b*), 10(*c*) and 10(*d*) show contours of constant N-factor in the ω-β plane at $Re_l = 10^6$ for the favorable, zero and adverse-pressure-gradient base flow, respectively. The locations of the peak values are indicated by crosses ($\times$) in the figures. In the case of the favorable-pressure-gradient base flow, only the algebraic growth appears, whereas for the Blasius boundary layer, the algebraic and exponential growth are comparable. For the adverse-pressure-gradient base flow on the other hand, the exponential growth is dominating. The parameters for the maximum growth of optimal and modal disturbances are summarized in tables 3 and 4, respectively.

5.5. *Transition prediction*

So far we have compared the growth of the disturbances and not their actual energy value. To draw any conclusions about when transition occurs, one has to know the initial disturbance energy, and thus know the receptivity process. Typical sources from which disturbances can enter the boundary layer are freestream turbulence, surface roughness, acoustic waves and vibrations. At low disturbance levels transition occurs at a N-factor between 8 and 11, depending of the definition of transition. At higher disturbance levels that number decreases. TS-wave receptivities to surface roughness, acoustic waves and vibrations are stronger than the receptivity to freestream turbulence, while streaks mainly are created through receptivity to freestream turbulence. Here

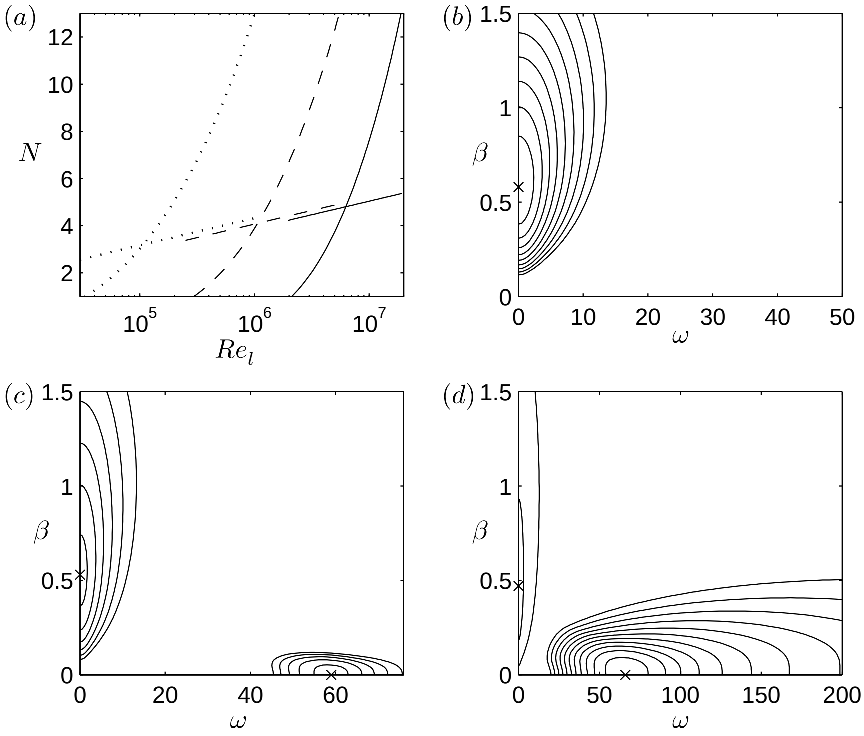

FIGURE 10. (*a*) Envelope curves of the maximal algebraic and exponential growth. Lines as in figure 2. $Re_l = 10^6$. (*b*) Contours of constant N-factor for the favorable-pressure-gradient base flow with contour spacing 0.1. The maximum growth has $N = 3.9$ at $\beta = 0.58$ and $\omega = 0$. (*c*) Blasius boundary layer with contour spacing 0.2. The maximum algebraic growth has $N = 4.1$ at $\beta = 0.53$ and $\omega = 0$ and the maximum exponential growth has $N = 3.9$ at $\beta = 0$ and $\omega = 59$. (*d*) Adverse-pressure-gradient base flow with contour spacing 1. The maximum algebraic growth has $N = 4.3$ at $\beta = 0.47$ and $\omega = 0$ and the maximum exponential growth has $N = 13.6$ at $\beta = 0$ and $\omega = 66$. $Re_l = 10^6$. Crosses (×) indicate the locations of the peak values.

we will concern ourself with receptivity to freestream turbulence. As is usual in linear transition prediction we incorporate the receptivity in the N-factor at transition.

Mack (1977) proposed a receptivity model (1) for the N-factor at transition associated with exponentially growing disturbances. The model is based on parallel, linear stability analysis for exponentially growing TS-waves in the Blasius

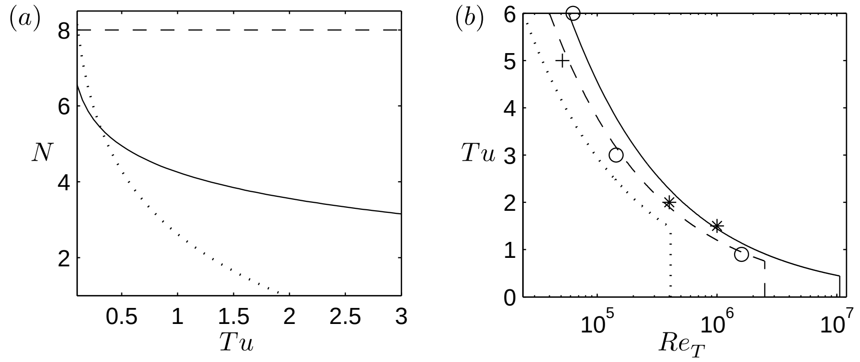

FIGURE 11. (*a*) Predicted N-factor at transition vs Tu given in percent for algebraic (solid line) and exponential (dashed line) growth. Dotted line: Model by Mack (1977). (*b*) Lines as in figure 2. Predicted transition contour in the Re_T-Tu plane. Tu is given in percent. The straight part of the lines corresponds to transition due to modal growth and the curved part to bypass transition. Experimental data for the Blasius boundary layer from Matsubara & Alfredsson (2001) ($*$) and Roach & Brierley (1992) ($\circ$). Numerical data from Yang & Voke (1991) ($+$).

boundary layer, correlated with experiments collected by Dryden (1959). The model, shown as the dotted line in figure 11(*a*), is misleading, however, since the transition process in these experiments most likely is a result of bypass transition of streaky structures, not TS-waves. A more appropriate model is that of Andersson *et al.* (1999). That model, equation (2), correlates the transition Reynolds number associated with bypass transition due to streamwise streaks, based on the maximum algebraic growth of optimal disturbances in the Blasius boundary layer. It is shown as the solid line in figure 11(*a*). Note that the model of Mack gives a lower N-value for transition than the model based on transient growth, something not supported by available experimental data. We will complement the transition model of Andersson *et al.* (1999) with the addition of base flows with various pressure gradients. The model is based on three assumptions.

1. We assume that the initial disturbance energy is proportional to the freestream-turbulence energy

$$E(x_0) = Tu^2, \tag{38}$$

for isotropic turbulence with the freestream-turbulence level defined as $Tu = \sqrt{\overline{u'^2}}/U_\infty$. Here u' is the fluctuating streamwise velocity in the freestream and the overbar denotes the temporal mean.

2. We assume that the initial disturbance grows with the optimal rate

$$E(x_1) = GE(x_0) = \overline{G} Re_l E(x_0). \tag{39}$$

3. We assume that transition occurs when the final energy reaches a specific value E_T, regardless of the pressure gradient of the base flow

$$E(x_1) = E_T. \tag{40}$$

Combining assumptions (38–40) yields the transition model

$$\sqrt{Re_T} Tu = \frac{k}{\sqrt{\overline{G}}}, \tag{41}$$

where k should be constant. Using the same correlation as Andersson *et al.* (1999) and the optimal Reynolds-number-independent growth in the Blasius boundary layer gives $k = 0.70$. Note that our model differs in the sense that we have used the growth from the optimal initial position and not the leading edge.

The influence of freestream turbulence on the generation of TS-waves is not conclusive. In fact, Boiko *et al.* (1994) made experiments on the behavior of controlled TS-waves, introduced by means of a vibrating ribbon, in a boundary layer subjected to $Tu = 1.5\,\%$. The measured amplification rates for the waves in the presence of the turbulence generating grid were smaller that for regular TS-waves, and damping set in further upstream than in the absence of the turbulence generating grid. Thus we make the simple assumption that transition resulting from exponentially growing disturbances occurs at $N = 8$, the dashed line in figure 11(a), irrespective of the freestream turbulence level.

Figure 11(b) shows the transition Reynolds number based on the results from the linear stability analysis and the transition model discussed above for freestream turbulence. The straight part of the lines represents the transition Reynolds number for exponentially growing modal disturbances and the curved part represents bypass transition. For high freestream turbulence levels, transition occurs as a result of the breakdown of streaky structures and for low freestream turbulence levels as a result of exponentially growing disturbances. The cross-over point occurs where the bypass transition model predicts a higher transition Reynolds number than for the exponentially growing disturbances. According to the model, bypass transition occurs in the Blasius boundary layer (dashed lines) for a freestream-turbulence level higher than 0.76 %. Similar results has been found in experiments. Suder *et al.* (1988) found in their experiment that the bypass mechanism prevailed for freestream-turbulence levels of 0.65 % and higher. Kosorygin & Polyakov (1990) suggested that TS-waves and streaks can co-exist and interact for freestream-turbulence levels up to approximately 0.7 %. However, our model does not account for the interaction between TS-waves and streaks.

6. Conclusions

The energy growth of eigenmodes and non-modal optimal disturbances has been investigated, by means of linear equations valid both for the exponential and algebraic growth scenarios, in the Falkner–Skan boundary layer with favorable, adverse and zero pressure gradients.

First, the algebraic growth of optimal disturbances in the large-Reynolds-number limit was studied. It was found that the initial streamwise position, where the disturbance is introduced in the boundary layer, has a significant impact on the growth. The optimal initial position moves downstream with increasing wave number and angular frequency of the disturbance and with decreasing pressure gradient of the base flow. Furthermore, the optimal spanwise wave number increases with decreased pressure gradient while the optimal angular frequency is equal to zero.

Second, the exponential growth of modal disturbances within the unstable region was studied. It was found that the optimal angular frequency increases with decreasing pressure gradient while the optimal spanwise wave number is equal to zero, as expected.

In both the algebraic and exponential growth scenarios, the growth increases with increasing pressure gradient, although the effect is much more pronounced for the exponential growth. Therefore, in a comparison of the two different growth scenarios at $Re_l = 10^6$, the algebraic growth is much larger for the favorable-pressure-gradient base flow and the exponential growth is much larger for the adverse-pressure-gradient base flow, while they are comparable for the Blasius boundary layer.

Finally, a unified transition-prediction method incorporating the influence of freestream turbulence was presented. It was shown that bypass transition due to streamwise streaks occurs for flows with a moderate to high level of freestream turbulence. The freestream-turbulence level for which bypass transition occurs decreases with decreased pressure gradient of the base flow.

Appendix: Derivation of the Adjoint Equations

In order to derive the adjoint equations for the algebraic optimization problem, we disregard terms including α and the $\hat{p}_x/Re_\delta^2$ term in the streamwise momentum equation. We rewrite the forward equations (4) in matrix form

$$\mathbf{A}\boldsymbol{f} + \mathbf{B}\boldsymbol{f}_y + \mathbf{C}\boldsymbol{f}_{yy} + \mathbf{D}\boldsymbol{f}_x = 0, \tag{42}$$

where the state vector $\boldsymbol{f} = (\hat{u}, \hat{v}, \hat{w}, \hat{p})^T$ and

$$\mathbf{A} = \begin{bmatrix} 0 & 0 & i\beta & 0 \\ U_x + \beta^2 - i\omega & U_y & 0 & 0 \\ V_x & V_y + \beta^2 - i\omega & 0 & 0 \\ 0 & 0 & \beta^2 - i\omega & i\beta \end{bmatrix},$$

$$\mathbf{B} = \begin{bmatrix} 0 & 1 & 0 & 0 \\ V & 0 & 0 & 0 \\ 0 & V & 0 & 1 \\ 0 & 0 & V & 0 \end{bmatrix},$$

$$\mathbf{C} = \begin{bmatrix} 0 & 0 & 0 & 0 \\ -1 & 0 & 0 & 0 \\ 0 & -1 & 0 & 0 \\ 0 & 0 & -1 & 0 \end{bmatrix},$$

$$\mathbf{D} = \begin{bmatrix} 1 & 0 & 0 & 0 \\ U & 0 & 0 & 0 \\ 0 & U & 0 & 0 \\ 0 & 0 & U & 0 \end{bmatrix}.$$

Let us define an inner product between two vectors $\boldsymbol{u}$ and $\boldsymbol{v}$ as follows

$$(\boldsymbol{u}, \boldsymbol{v}) = \int_{x_0}^{x_1}\int_{0}^{y_{max}} \boldsymbol{u}^* \boldsymbol{v} \, \mathrm{d}y \, \mathrm{d}x, \tag{43}$$

and the adjoint-state vector $\boldsymbol{g} = (p^*, u^*, v^*, w^*)^T$. The star on the adjoint-state variables is just traditional notation while a star on a vector or matrix denotes the conjugate transpose. Now we take the inner product between $\boldsymbol{g}$ and the left-hand side of the forward equation system (42) and move the derivatives from $\boldsymbol{f}$ to $\boldsymbol{g}$ by integration by parts

$$\begin{gathered} (\boldsymbol{g}, \mathbf{A}\boldsymbol{f} + \mathbf{B}\boldsymbol{f}_y + \mathbf{C}\boldsymbol{f}_{yy} + \mathbf{D}\boldsymbol{f}_x) = \\ \big((\mathbf{A}^* - \mathbf{B}_y^* - \mathbf{D}_x^*)\boldsymbol{g} - \mathbf{B}^*\boldsymbol{g}_y + \mathbf{C}^*\boldsymbol{g}_{yy} - \mathbf{D}^*\boldsymbol{g}_x, \boldsymbol{f}\big) + \\ \int_{x_0}^{x_1} \langle \mathbf{B}^*\boldsymbol{g}, \boldsymbol{f} \rangle \Big|_0^{y_{max}} \mathrm{d}x + \int_{x_0}^{x_1} \langle \mathbf{C}^*\boldsymbol{g}, \boldsymbol{f}_y \rangle \Big|_0^{y_{max}} \mathrm{d}x - \\ \int_{x_0}^{x_1} \langle \mathbf{C}^*\boldsymbol{g}_y, \boldsymbol{f} \rangle \Big|_0^{y_{max}} \mathrm{d}x + \int_{0}^{y_{max}} \langle \mathbf{B}^*\boldsymbol{g}, \boldsymbol{f} \rangle \Big|_{x_0}^{x_1} \mathrm{d}y. \end{gathered} \tag{44}$$

Since the left-hand side of the derivation (44) is equal to zero due to the state equations, the right-hand side also has to be zero. By setting each boundary term to zero we are ending up with a set of equations for the adjoint-state variables

$$(\mathbf{A}^* - \mathbf{B}_y^* - \mathbf{D}_x^*)\boldsymbol{g} - \mathbf{B}^*\boldsymbol{g}_y + \mathbf{C}^*\boldsymbol{g}_{yy} - \mathbf{D}^*\boldsymbol{g}_x = 0, \tag{45}$$

and the boundary terms can explicitly be written

$$\begin{gathered} \int_{x_0}^{x_1} \langle \mathbf{B}^*\boldsymbol{g}, \boldsymbol{f} \rangle \Big|_0^{y_{max}} \mathrm{d}x = \\ \int_{x_0}^{x_1} \big(V\overline{u}^*\hat{u} + (\overline{p}^* + V\overline{v}^*)\hat{v} + V\overline{w}^*\hat{w} + \overline{v}^*\hat{p}\big) \Big|_0^{y_{max}} \mathrm{d}x = 0, \end{gathered} \tag{46}$$

$$\int_{x_0}^{x_1} \langle \mathbf{C}^*\boldsymbol{g}, \boldsymbol{f}_y \rangle \Big|_0^{y_{max}} \mathrm{d}x = \int_{x_0}^{x_1} (-\overline{u}^*\hat{u}_y - \overline{v}^*\hat{v}_y - \overline{w}^*\hat{w}_y) \Big|_0^{y_{max}} \mathrm{d}x = 0, \tag{47}$$

$$\int_{x_0}^{x_1} \langle \mathbf{C}^*\boldsymbol{g}_y, \boldsymbol{f} \rangle \Big|_0^{y_{max}} \mathrm{d}x = (-\overline{u}_y^*\hat{u} - \overline{v}_y^*\hat{v} - \overline{w}_y^*\hat{w}) \Big|_0^{y_{max}} \mathrm{d}x = 0, \tag{48}$$

$$\int_0^{y_{max}} \langle \mathbf{D}^* \boldsymbol{g}, \boldsymbol{f} \rangle \Big|_{x_0}^{x_1} \mathrm{d}y =$$

$$\int_0^{y_{max}} \left((\overline{p}^* + U\overline{u}^*)\hat{u} + U\overline{v}^*\hat{v} + U\overline{w}^*\hat{w} \right) \Big|_{x_0}^{x_1} \mathrm{d}y = 0. \tag{49}$$

The necessary boundary conditions can be determined by the three first boundary terms (46–48)

$$\begin{array}{lll} \overline{u}^* = \overline{v}^* = \overline{w}^* = 0 & \text{at} & y = 0, \\ \overline{u}^* = \overline{w}^* = \overline{p}^* + 2V\overline{v}^* = 0 & \text{at} & y = y_{max}. \end{array} \tag{50}$$

Moreover, by identifying ψ_1 and Φ in the last boundary term (49) the initial conditions and the action of the adjoint operator can be stated

$$\begin{array}{l} U_1\overline{u}_1^* + \overline{p}_1^* = \overline{\psi}_1, \\ \overline{v}_1^* = \overline{w}_1^* = 0, \end{array} \tag{51}$$

$$\begin{array}{l} \overline{\phi}_2 = U_0\overline{v}_0^*, \\ \overline{\phi}_3 = U_0\overline{w}_0^*. \end{array} \tag{52}$$

References

Abu-Ghannam, B. & Shaw, R. 1980 Natural transition of boundary layers - the effects of turbulence, pressure gradient, and flow history. *J. Mech. Eng. Sci.* **22**, 213–228.

Andersson, P., Berggren, M. & Henningson, D. 1999 Optimal disturbances and bypass transition in boundary layers. *Phys. Fluids* **11**, 134–150.

Andersson, P., Henningson, D. & Hanifi, A. 1998 On a stabilization procedure for the parabolic stability equations. *J. Eng. Math.* **33**, 311–332.

Bertolotti, F. P., Herbert, T. & Spalart, P. R. 1992 Linear and nonlinear stability of the Blasius boundary layer. *J. Fluid Mech.* **242**, 441–474.

Boiko, A., Westin, K., Klingmann, B., Kozlov, V. & Alfredsson, P. 1994 Experiments in a boundary layer subjected to free stream turbulence. Part 2. The role of TS-waves in the transition process. *J. Fluid Mech.* **281**, 219–245.

Butler, K. & Farrell, V. 1992 Three-dimensional optimal pertubations in viscous shear flow. *Phys. Fluids A* **4**, 1637–1650.

Corbett, P. & Bottaro, A. 2000 Optimal pertubations for boundary layers subject to stream-wise pressure gradient. *Phys. Fluids* **12**, 120–130.

van Driest, E. & Blumer, C. 1963 Boundary layer transition: Freestream turbulence and pressure gradient effects. *AIAA J.* **1**, 1303–1306.

Dryden, H. 1959 Transition from laminar to turbulent flow. In *Turbulent flows and heat transfer* (ed. C. Lin), pp. 1–74. Princeton University Press.

Ellingsen, T. & Palm, E. 1975 Stability of linear flow. *Phys. Fluids* **18**, 487–488.

Farrell, B. 1988 Optimal exitation of pertubations in viscous shear flow. *Phys. Fluids* **31**, 2093–2102.

Floryan, J. & Saric, W. 1979 Stability of Görtler vortices in boundary layers. *AIAA J.* **20**, 316–324.

Haj-Hariri, H. 1994 Characteristics analysis of the parabolized stability equations. *Stud. Appl. Math.* **92**, 41–53.

Hall, P. 1983 The linear development of Görtler vortices in growing boundary layers. *J. Fluid Mech.* **130**, 41–58.

Hanifi, A., Schmid, P. & Henningson, D. 1996 Transient growth in compressible boundary layer flow. *Phys. Fluids* **8**, 826–837.

Hein, S., Stolte, A. & Dallmann, U. 1999 Identification and analysis of nonlinear transition scenarios using NOLOT/PSE. *Z. Angew. Math. Mech.* **79**, S109–S112.

Henningson, D., Lundbladh, A. & Johansson, A. 1993 A mechanism for bypass transition from localized disturbances in wall-bounded shear flows. *J. Fluid Mech.* **250**, 169–238.

Herbert, T. 1997 Parabolized stability equations. *Annu. Rev. Fluid Mech.* **29**, 245–283.

Hultgren, L. & Gustavsson, L. 1981 Algebraic growth of disturbances in a laminar boundary layer. *Phys. Fluids* **24**, 1000–1004.

van Ingen, J. 1956 Suggested semi-emperical method for the calculation of the boundary layer transition region. *Tech. Rep.* UTH-74. Dep. of Aero. Eng., University of Technology, Delft.

Klebanoff, P. 1971 Effect of freestream turbulence on the laminar boundary layer. *Bull. Am. Phys. Soc.* **10**, 1323.

Kosorygin, V. & Polyakov, N. 1990 Laminar boundary layers in turbulent flows. In *Laminar-Turbulent Transition* (eds. D. Arnal & R. Michel), pp. 573–578. Springer.

Landahl, M. 1980 A note on an algebraic instability of inviscid parallel shear flows. *J. Fluid Mech.* **98**, 243–251.

Li, F. & Malik, M. R. 1994 Mathematical nature of parabolized stability equations. In *4th IUTAM Symp. on Laminar-Turbulent transition, Sendi, Japan* (ed. R. Kobayashi), pp. 205–212. Springer.

Li, F. & Malik, M. R. 1996 On the nature of PSE approximation. *Theor. and Comp. Fluid Dyn.* **8**, 253–273.

Luchini, P. 1996 Reynolds-number-independent instability of the boundary layer over a flat surface. *J. Fluid Mech.* **327**, 101–115.

Luchini, P. 2000 Reynolds-number-independent instability of the boundary layer over a flat surface: optimal perturbations. *J. Fluid Mech.* **404**, 289–309.

Mack, L. 1977 Transition prediction and linear stability theory. In *AGARD-CP-224*, pp. 1–1 to 1–22. NATO, Paris.

Matsubara, M. & Alfredsson, P. 2001 Disturbance growth in boundary layers subjected to free-stream turbulence. *J. Fluid Mech.* **430**, 149–168.

Pralits, J., Hanifi, A. & Henningson, D. 2002 Adjoint-based optimization of steady suction for disturbance control in incompressible flows. *J. Fluid Mech.* **467**, 129–161.

Reddy, S. & Henningson, D. 1993 Energy growth in viscous channel flows. *J. Fluid Mech.* **252**, 209–238.

Roach, P. & Brierley, D. 1992 The influence of a turbulent free-stream on zero pressure gradient transitional boundary layer development. I. Test cases T3A and T3B. In *Numerical Simulation of Unsteady Flows and Transiton to Turbulence* (eds. O. Pironneau, W. Rodi, I. Ryhming, A. Savill & T. Truong), pp. 303–316. Cambridge University Press.

Smith, A. & Gamberoni, N. 1956 Transition, pressure gradient and stability theory. *Tech. Rep.* ES 26388. Douglas Aircraft Co., EL Segundo, Calif.

Suder, K., O'Brien, J. & Reshotko, E. 1988 Experimental study of bypass transition in a boundary layer. *NASA TM* 100913.

Tumin, A. 2001 A model of spatial algebraic growth in a boundary layer subjected to a streamwise pressure gradient. *Phys. Fluids* **13**, 1521–1523.

Tumin, A. & Reshotko, E. 2003 Optimal disturbances in compressible boundary layers. *AIAA Paper* 2003-0792.

Westin, K., Boiko, A., Klingmann, B., Kozlov, V. & Alfredsson, P. 1994 Experiments in a boundary layer subjected to free stream turbulence. Part 1. Boundary layer structure and receptivity. *J. Fluid Mech.* **281**, 193–218.

Yang, Z. Y. & Voke, P. R. 1991 Numerical simulation of transition under turbulence. *Tech. Rep.* ME-FD/91.01. Dept. Mech. Eng. University of Surrey.

Paper 2

Optimal disturbances in suction boundary layers

By Martin G. Byström, Ori Levin and Dan S. Henningson

Department of Mechanics, KTH, SE-100 44 Stockholm, Sweden

A well known optimization procedure is used to find the optimal disturbances in two different suction boundary layers within the spatial framework. The maximum algebraic growth in the asymptotic suction boundary layer is presented and compared to previous temporal results. Furthermore, the spatial approach allows a study of a developing boundary layer in which a region at the leading edge is left free from suction. This new flow, which emulates the base flow of a recent wind-tunnel experiment, is herein denoted a semi suction boundary layer. It is found that the optimal disturbances for these two suction boundary layers consist of streamwise vortices that develop into streamwise streaks, as previously found for a number of shear flows. For the semi suction boundary layer it is shown that the optimal spanwise scale is set in the suction-free region at the leading edge.

1. Introduction

The transition from laminar to turbulent flow is a critical process in any engineering application where the minimization of friction drag is a design objective. Transition prediction has traditionally been carried out by considering the unstable eigenmodes of the Orr–Sommerfeld equations, i.e. the exponentially growing Tollmien–Schlichting waves. However, under certain circumstances other transition scenarios are more likely. It is well known that elongated, streamwise-oriented structures of alternating low and high velocity develop in boundary layers subjected to high or moderate levels of free-stream turbulence. These structures are commonly referred to as streaks or Klebanoff modes after the experiments of Klebanoff (1971). Since then, a number of experimental studies have shown that these streaks grow algebraically in the downstream direction (Westin *et al.* 1994; Matsubara & Alfredsson 2001; Fransson *et al.* 2005). Due to secondary instabilities, they break down to turbulence when their amplitude reach a critical level (Andersson *et al.* 2001; Brandt & Henningson 2002; Hœpffner *et al.* 2005). The physical mechanism behind the formation of streaks was first explained by Landahl (1975, 1980). He argued that when a fluid element is lifted up in the wall-normal direction it will initially maintain its horizontal momentum. Hence, small perturbations in the wall-normal direction can cause large disturbances in the streamwise direction. This mechanism is commonly referred to as the *lift-up* effect. Ellingsen & Palm (1975) showed theoretically that three-dimensional disturbances can grow linearly with time in an inviscid flow without inflection point.

Among the first to calculate optimal perturbations numerically were Butler & Farrell (1992) and Reddy & Henningson (1993). Butler & Farrell (1992) considered the temporal development of linear, three-dimensional perturbations in a number of shear flows. They used a variational method to find the optimal perturbations, i.e. the perturbations that gain the most energy in a given time period. It was found that these perturbations resemble streamwise vortices that give rise to streamwise streaks. Corbett & Bottaro (2000, 2001*b*) calculated the optimal perturbation of the Falkner–Skan boundary layer and later the Falkner–Skan–Cooke boundary layer within the temporal framework.

The spatial framework is however more physically relevant than the temporal, it has also the advantage of allowing studies of non-parallel flows such as the developing Blasius boundary layer (BBL). Andersson *et al.* (1999) and Luchini (2000) separately calculated the optimal disturbance in the non-parallel BBL. The disturbance was introduced at the leading edge and it was found that the optimal disturbance consists of streamwise aligned vortex pairs developing into streaks. Levin & Henningson (2003) extended the work of Andersson *et al.* (1999) to the Falkner–Skan boundary layer. The disturbance was however not initiated at the leading edge, but at a downstream position optimized to give the highest possible growth.

One method to delay transition is to apply suction through the surface which the boundary layer develops over. The suction can be optimized to minimize the growth of different types of disturbances (Balakumar & Hall 1999; Pralits *et al.* 2002; Zuccher *et al.* 2004). Herein we will however study the algebraic disturbance growth in boundary layers where uniform suction is applied. When uniform suction is applied over a flat plate, the boundary layer will asymptotically approach the asymptotic suction boundary layer (ASBL), as outlined in Schlichting (1979). Fransson & Alfredsson (2003) made an experimental study on the algebraic growth of disturbances induced by free-stream turbulence in the ASBL. A small region at the leading edge was however free from suction, allowing a BBL to develop up to the point where the suction set in. Downstream of this point the flow evolved into the ASBL, which was reached within the upstream half of the measurement interval. In the present paper, we will denote this type of boundary layer, where suction is applied only over the downstream part of the interval, a semi suction boundary layer (SSBL). Fransson & Alfredsson (2003) compared the disturbance growth in the BBL and the SSBL. The disturbance energy was found to grow linearly in the downstream direction, but when suction was applied the growth ceased so that the present amplitude level was kept essentially constant. The suction also resulted in a twofold reduction of the boundary-layer thickness, despite of this the spanwise scale of the streaks was maintained. Fransson & Alfredsson (2003) argue that the initial spanwise scale is decided in the receptivity process, this would explain the similarity of scales since a BBL is present at the leading edge of the SSBL. Yoshioka *et al.* (2004) extended the work of Fransson & Alfredsson (2003) to a number of suction rates and free-stream turbulence levels. It was concluded that the wall suction suppresses the disturbance growth, for high suction rates the disturbance energy may even decay. The spanwise scale of the streaks decreases with increasing free-stream turbulence level but remains nearly constant in the downstream direction. Yoshioka *et al.* (2004) concluded that the disturbances initiated at the leading edge become mainly passive and are convected downstream by the flow. Fransson & Corbett (2003) used an adjoint-based optimization procedure (Corbett & Bottaro 2001*b*) to calculate the optimal perturbation in the ASBL within the temporal framework. The optimal velocity perturbation was found to be in good agreement with experimental data from Fransson & Alfredsson (2003), but there was some discrepancy between the optimal wavenumber and those experimentally observed.

In the present paper we calculate the optimal disturbances in the ASBL and the SSBL within the spatial context. The calculations are carried out with an adjoint-based optimization procedure implemented by Levin & Henningson (2003), valid in the large Reynolds-number limit for a viscous, incompressible flow. Furthermore, the spanwise wavenumber and angular frequency of the disturbance as well as the streamwise interval length are optimized. The current study was motivated by the wind-tunnel experiment by Fransson & Alfredsson (2003). Results from this experiment have previously been compared with the temporal study of the ASBL by Fransson & Corbett (2003). This comparison exposed some discrepancy with respect to the spanwise scale of the disturbances. The spatial approach used herein allows us to simulate the actual base flow of the experiments, i.e. the SSBL. A comparison of the optimal disturbances in the ASBL and the SSBL is then carried out to establish the effect of the differences between these two suction boundary layers.

2. General formulation

We study the algebraic growth in a flat plate boundary layer where suction is applied at the wall. As seen in figure 1, we denote the streamwise, wall-normal and spanwise coordinates x, y and z and the corresponding velocities u, v and w, respectively. The time is denoted t, the pressure p, the spanwise wavenumber and the angular frequency are denoted β and ω. The kinematic viscosity and the density of the fluid are denoted ν and ρ.

The base flow of the ASBL is given by a simple analytic expression, first derived by Griffith & Meredith (1936)

$$U = U_\infty \left(1 - \exp\left[\frac{V_w}{\nu} y\right]\right), \qquad V = V_w, \tag{1}$$

where U_∞ is the free-stream velocity and V_w is the suction velocity at the wall, which assumes a negative value when suction is applied. This velocity profile is

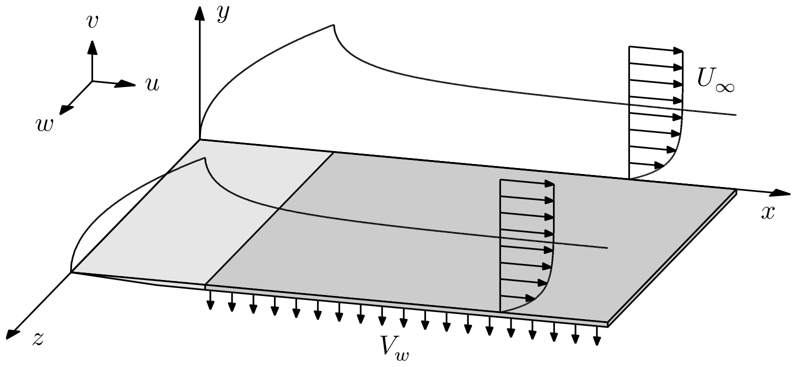

FIGURE 1. The semi suction boundary layer (SSBL).

an exact solution to both the full Navier–Stokes equations and the boundary-layer equations. The displacement thickness of the ASBL is constant since the base flow does not vary in the streamwise direction. The Reynolds number based on this constant displacement thickness can also be written as the ratio between the free-stream velocity and the suction velocity, from here on we will refer to this as the suction Reynolds number Re

$$\delta_1 = -\frac{\nu}{V_w}, \quad Re = \frac{U_\infty \delta_1}{\nu} = -\frac{U_\infty}{V_w}. \tag{2}$$

Herein we will use a scaling based on the constant displacement thickness of the ASBL to scale both mean flow and disturbances. This scaling, summarized in table 1, will be referred to as the ASBL scalings. From here on we will use the superscript * to distinguish non-scaled, physical quantities from those scaled in accordance with table 1. Using scaled quantities we may rewrite equation (1)

$$U = \frac{U^*}{U_\infty} = 1 - \exp\left[-\frac{y^*}{\delta_1}\right] = 1 - \exp\left[-y\right], \qquad V = \frac{V_w^*}{U_\infty} Re = V_w. \tag{3}$$

The base flow of the SSBL can be divided into two regions. In the first region, from the leading edge to the suction start, the base flow was obtained by solving the Blasius similarity equation. In the second region, downstream of the suction start, the base flow was obtained by numerically solving the boundary-layer equations. The streamwise velocity is subjected to homogeneous boundary conditions at the wall, the boundary condition for the wall-normal component is given by the suction velocity V_w. We scale the SSBL with the ASBL scalings given by table 1. The Reynolds number $Re = -U_\infty/V_w$ is however not physically relevant in the upstream part of the interval where no suction is applied. The BBL of this region has previously been studied by Andersson *et al.* (1999), Luchini (2000) and Levin & Henningson (2003). They used boundary-layer scalings and defined a Reynolds number $Re_l = U_\infty l/\nu$, where l is a fixed streamwise distance that is also used to scale x. In the SSBL,

variable:	x	y, z	t	u	v, w	p	β	ω
scaling:	$\delta_1 Re$	δ_1	$\dfrac{\delta_1 Re}{U_\infty}$	U_∞	$\dfrac{U_\infty}{Re}$	$\dfrac{\rho U_\infty^2}{Re^2}$	$\dfrac{1}{\delta_1}$	$\dfrac{U_\infty}{\delta_1 Re}$

Table 1. The ASBL scalings

the natural choice for l is the distance between the leading edge and the point where the suction starts. Writing the starting position of the suction, x_s, with the ASBL scalings from table 1

$$x_s = \frac{x_s^*}{\delta_1 Re} = \frac{l}{\delta_1 Re} = \frac{Re_l}{Re^2}, \tag{4}$$

we find that changing the starting position of the suction is equivalent to changing Re_l, given that Re is kept constant. In the study of the SSBL presented in § 3.1 we set x_s to unity in order to comply with the experiments by Fransson & Alfredsson (2003). Setting x_s to unity is equivalent to setting $Re_l = Re^2$, this is beneficiary since it means that quantities scaled with the ASBL scalings can be directly compared to quantities scaled with the boundary-layer scalings and vice versa. Further details on the base flow of the SSBL will be given in § 3.1.1.

For these two-dimensional steady base flows, the SSBL and the ASBL, we consider three-dimensional and time-dependent disturbances. The disturbances are taken to be periodic in the spanwise direction and in time. We consider algebraically growing disturbances with weak streamwise variation, the streamwise wavenumber is thus set to zero. Either one of the disturbances u, v, w or p can then be assumed to be of the form

$$f = \hat{f}(x, y) \exp\left[\mathrm{i}\beta z - \mathrm{i}\omega t\right]. \tag{5}$$

Introducing this assumption in the non-dimensional, linearized Navier–Stokes equations and neglecting terms of low order yields a parabolic set of disturbance equations as outlined in Levin & Henningson (2003). The disturbance is subjected to no-slip boundary conditions at the wall, the wall-normal disturbance can be set to zero since we consider suction through a material of low permeability. Together with boundary and initial conditions, the disturbance equations form an initial boundary-value problem that can be solved through downstream marching for a disturbance with given spanwise wavenumber and angular frequency.

The aim is to optimize the initial disturbance $(\hat{u}_0, \hat{v}_0, \hat{w}_0)$ at x_0, the beginning of the interval, in order to achieve maximum possible amplification of the disturbance energy at x_1, the end of the interval. We define the growth G over the interval $x_0 \leq x \leq x_1$ as the ratio between the disturbance energy E at the end and beginning of the interval.

$$G(x_0, x_s, x_1, \beta, \omega, Re) = \frac{E(x_1)}{E(x_0)}. \tag{6}$$

Observe that the growth in the ASBL will not depend on the suction start x_s since we assume that it is located sufficiently far upstream so that the ASBL has been reached at the start of the interval. The energy norm E is defined in the same way as stated in Andersson *et al.* (1999), Luchini (2000) and Levin & Henningson (2003). As outlined in these papers, in a high Reynolds-number flow the highest possible growth is achieved for an initial disturbance with a zero streamwise component, due to the difference in order between the streamwise component and the wall-normal and spanwise components. This difference in order also makes it possible to neglect the wall-normal and spanwise components at the end of the interval. It then follows that the growth scales quadratically with *Re* in the large Reynolds-number limit (Andersson *et al.* 1999; Luchini 2000; Levin & Henningson 2003).

Since the initial boundary-value problem is linear and homogeneous an input-output formulation can be adopted, such that the disturbance at the final position is a linear function of the initial disturbance. By introducing the adjoint equations, the optimal initial disturbance and the associated growth can be calculated through power iterations. The optimization procedure used herein to calculate the optimal disturbances in the SSBL and the ASBL was implemented by Levin & Henningson (2003). It is similar to the procedures that were used by Andersson *et al.* (1999) and Luchini (2000). A detailed description of this procedure can also be found in the textbook by Schmid & Henningson (2001).

3. Results

All results presented in this section have been subjected to convergence tests in order to ensure their accuracy. Furthermore, the height of the calculation box y_{max} was varied between 40 and 60 to make sure that the whole initial disturbance was captured.

3.1. *The semi suction boundary layer*

3.1.1. *Base flow*

In this section we study the SSBL in which a BBL develops from the leading edge to the point where the suction starts. Downstream of this point a uniform suction is applied, in this evolution region the flow evolves towards the ASBL. The streamwise distance needed for the flow to reach the ASBL is decided by the strength of the suction and the thickness of the BBL at the suction start. The SSBL emulates the base flow of an experiment carried out by Fransson & Alfredsson (2003). In this experiment, the boundary layer developed over a flat plate made of porous material so that suction could be applied. The leading edge was however made of an impermeable material, leaving this region free

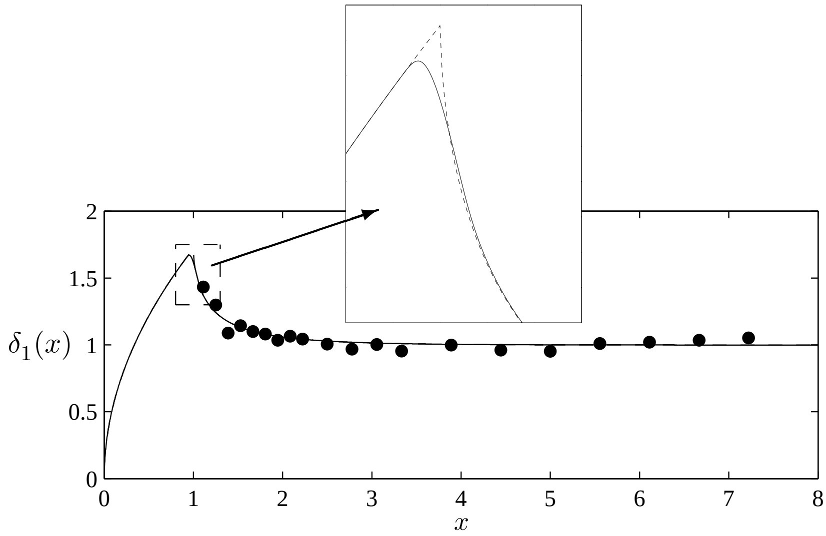

FIGURE 2. The displacement thickness $\delta_1(x)$ of the SSBL at $Re = 347$, scaled with the constant displacement thickness of the ASBL. Discontinuous flow (dashed line) and approximated continuous flow with smoothly applied suction (solid line). Experimental data from Fransson & Alfredsson (2003) (dots).

from suction. Fransson & Alfredsson (2003) set the suction Reynolds number to $Re = 347$ and started the suction 360 mm downstream of the leading edge, equivalent to setting $x_s = x_s^*/(\delta_1 Re)$ to unity. As outlined in § 2, this allows us to make direct comparisons with quantities scaled with the boundary-layer scalings. Herein we study the SSBL over nine streamwise intervals, all starting at $x_0 = 0$ and with suction from $x_s = 1$ to the end of the interval. The length of the interval is varied by changing the end position from $x_1 = 2$ to $x_1 = 10$ in steps of one.

Fransson & Alfredsson (2003) used a non-dimensional evolution equation to calculate the base flow of the evolution region between the BBL and the ASBL. The exact agreement with their results validated the numerical solver of the boundary-layer equations that was used in the present implementation. A small modification of the base flow was however made since the SSBL is discontinuous at $x_s = 1$ where the suction starts. In order to remove this discontinuity, we employ a strategy previously used by Zuccher *et al.* (2004) and Corbett & Bottaro (2001*a*), using a step function to smoothly increase the suction from zero at $x = 0.9$ to full suction at $x = 1.1$. The used step function (Berlin & Henningson 1999) has continuous derivatives of all orders and gives the same mass flux through the wall as the discontinuous flow. Figure 2 shows a comparison of the displacement thickness of the discontinuous flow and the modified continuous flow with smoothly applied suction. Despite the smooth

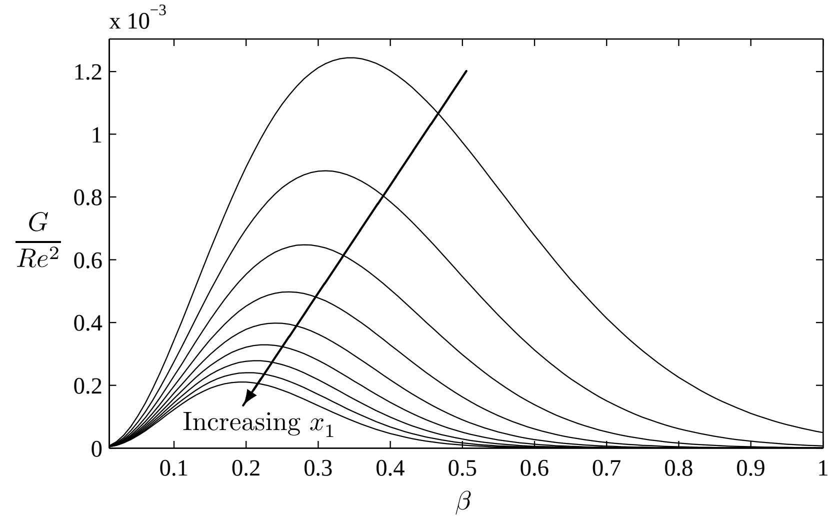

FIGURE 3. The growth G in the SSBL at $Re = 347$ as function of β for nine streamwise intervals ranging from $0 \leq x \leq 2$ to $0 \leq x \leq 10$ in steps of one.

application of the suction, the flow undergoes a significant transformation over a short streamwise distance, a finer grid was therefore used in the region where the suction starts. Experimental data from Fransson & Alfredsson (2003) is also included in figure 2, good agreement can be seen between the calculated and measured displacement thickness.

Another approximation was done in the treatment of the leading edge. The limit of the normal velocity of the BBL is infinity when x tends towards zero. However, here we follow the work of Andersson *et al.* (1999) and set the normal velocity to zero and the streamwise velocity to unity at the initial point of the calculation interval.

3.1.2. *Optimal disturbances*

The influence of the spanwise wavenumber β and the angular frequency ω on the energy growth in the SSBL was studied for the nine streamwise intervals defined in § 3.1.1. Apart from when the ω-dependence is studied, ω is set to zero for all calculations presented in this section.

Figure 3 shows the growth as function of β for all nine streamwise intervals. We gather that the optimal growth occurs at different β for each respective interval, i.e. for each streamwise interval there is an optimal β that gives the largest possible growth at the end of that interval. This optimal β and the corresponding optimal growth decrease as the interval is prolonged. The optimal spanwise wavenumbers and the corresponding optimal growth are summarized in table 2, § 3.2.

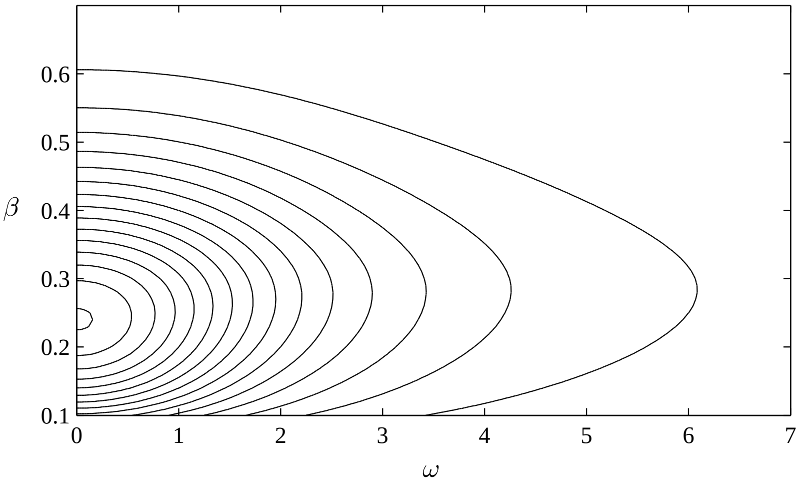

FIGURE 4. Contours of constant growth G in the SSBL at $Re = 347$ in the (ω, β)-plane for the streamwise interval $0 \leq x \leq 6$.

The ω-dependence is exposed in figure 4, which shows contours of constant growth in the (ω, β)-plane for the streamwise interval $0 \leq x \leq 6$. From the figure we conclude that the optimal ω is zero, this conclusion was found to be true for all the streamwise intervals studied here. This is in agreement with what has been found for the BBL by Luchini (2000) and the Falkner–Skan boundary layer by Levin & Henningson (2003).

The growth as function of the streamwise coordinate x is shown in figure 5 for all nine streamwise intervals. The optimal β of each respective interval was used in these calculations and ω was set to zero. The optimization procedure used herein optimizes the growth at the end of the streamwise interval. The optimal growth is thus the largest possible growth at the end of the streamwise interval but does not necessarily constitute the largest growth in the interval. As seen in figure 5 each curve has a maximum upstream of their respective end position and these maxima exceed the optimal growth for all intervals. The maxima are located in the suction part of the SSBL, except for the shortest interval $(0 \leq x \leq 2)$, which has the maximum located at the starting point of the suction, i.e. at the end of the BBL. When the endpoint of the interval was moved further upstream, towards the starting point of the suction, it was found that the maximum remains located at this point. Due to the smooth application of the suction (see § 3.1.1), the maximum growth is reached slightly upstream of $x_s = 1$. It is however reasonable to assume that the maximum growth will be reached at exactly $x_s = 1$ in the discontinuous flow. The optimal interval for the SSBL thus ends at the point where the suction starts. In this interval, where no suction is applied, the base flow is simply the BBL for which

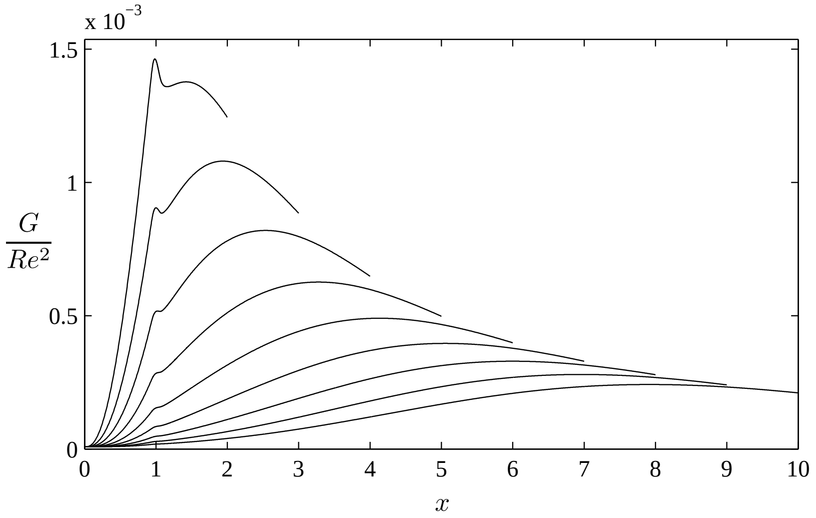

FIGURE 5. The growth G in the SSBL at $Re = 347$ as function of x for nine streamwise intervals ranging from $0 \leq x \leq 2$ to $0 \leq x \leq 10$ in steps of one. The optimal β of each respective interval was used, ω was set to zero.

it is well known that the optimal spanwise wavenumber is $\beta = 0.45$ (Andersson *et al.* 1999; Luchini 2000).

Figure 6 shows the optimal disturbances in the SSBL for the streamwise intervals $0 \leq x \leq 2$ (solid line), $0 \leq x \leq 6$ (dashed line) and $0 \leq x \leq 10$ (dotted line). For each respective interval the optimal β was used and ω was set to zero. Figures 6(*a*–*b*) show the optimal disturbance while figure 6(*c*) shows the downstream response of the optimal disturbance at the final position. The downstream response takes the form of a streamwise elongated streak when the spanwise periodic dependence is considered. The amplitude of the streak is larger for short intervals than for long, but the shape of the streak remains similar and the profile maximum is located at about the same wall-normal distance from the wall, where the SSBL reaches approximately three quarters of the free-stream velocity. From this we conclude that there is an optimal shape, a streak located at a certain wall-normal position, that gives the highest disturbance energy at the end of the interval.

The optimal disturbance, i.e. the wall-normal and spanwise components shown in figures 6(*a*–*b*), takes the form of streamwise aligned vortex pairs when the spanwise periodic dependence is considered. We also observe that the profile maxima move upward when the streamwise interval is prolonged. Thus, the vortex cores of the initial disturbance move upward and the vortices grow in size, as seen in figure 7. An explanation for this is that the suction will draw the disturbance towards the wall as it evolves downstream. From figure 6(*c*)

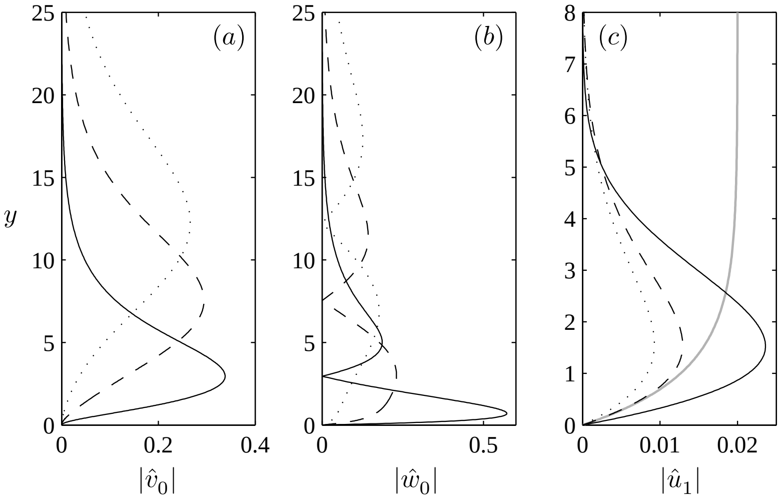

FIGURE 6. The optimal disturbance in the SSBL at $Re = 347$ and for the streamwise intervals $0 \leq x \leq 2$ (solid line), $0 \leq x \leq 6$ (dashed line) and $0 \leq x \leq 10$ (dotted line). (*a*–*b*) The wall-normal component $\hat{v}_0$ and the spanwise component $\hat{w}_0$ of the optimal disturbance. (*c*) The downstream response of the optimal disturbance, streamwise component $\hat{u}_1$. Observe that the scaling of $\hat{u}$ differs a factor Re from the scaling of $\hat{v}$ and $\hat{w}$, see § 2. The grey line shows the ASBL, scaled down to fit the figure. The ASBL has been reached (within graphical accuracy) at the end of the streamwise intervals examined here.

we saw that the downstream response of the optimal disturbance is a streak located at a certain optimal wall-normal position. The cores of the vortices, i.e. the optimal disturbance, must be located some distance higher in the wall-normal direction in order to allow the suction to draw the disturbance down to this optimal wall-normal position as it evolves over the interval. This effect is stronger for longer streamwise intervals where the suction will act on the disturbance over a longer distance. The vortex cores must therefore be located higher for a long interval than for a short in order for the disturbance to reach the optimal wall-normal coordinate at the end of the interval.

3.2. *A comparison with the asymptotic suction boundary layer*

In this section we study the energy growth of the optimal disturbance in the ASBL and make a comparison between the SSBL and the ASBL. We study the ASBL over the same streamwise intervals that were used for the SSBL, although the suction is here applied over the whole interval. Since the base flow of the ASBL does not vary in the streamwise direction (see § 2), it is however arbitrary

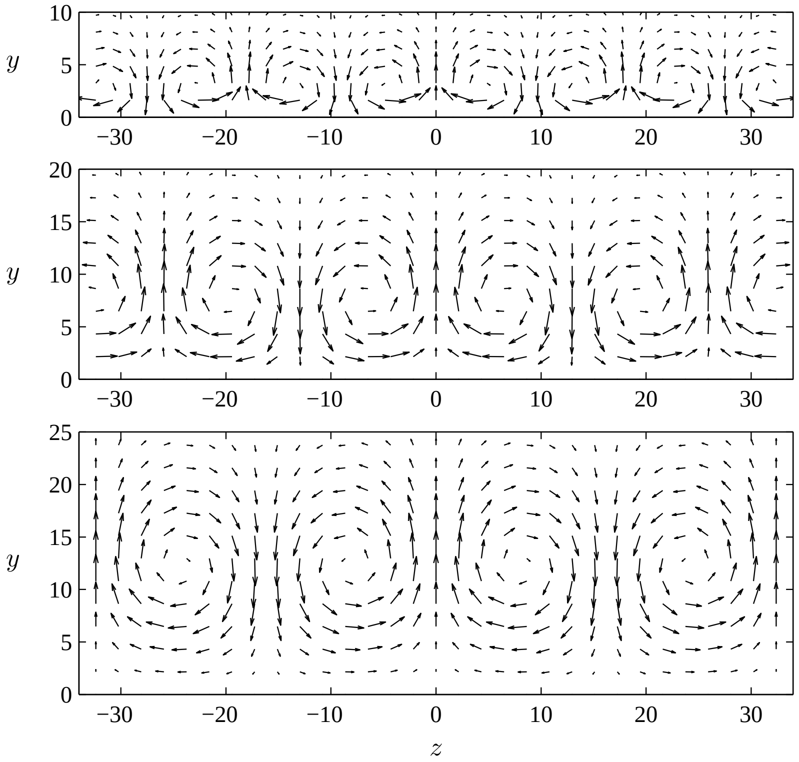

FIGURE 7. The optimal disturbance in the SSBL at $Re = 347$ for the streamwise intervals $0 \leq x \leq 2$ (upper row), $0 \leq x \leq 6$ (middle row) and $0 \leq x \leq 10$ (bottom row).

which interval we study as long as we keep the length constant. The Reynolds number Re was set to 347, as in the study of the SSBL.

The optimal disturbance in the ASBL takes the form of streamwise aligned vortex pairs that give rise to streamwise elongated streaks. This is in agreement with the results from the temporal study of the ASBL by Fransson & Corbett (2003). The dependence on the spanwise wavenumber β resembles that found for the SSBL (see table 2) and the optimal angular frequency ω was found to be zero irrespective of the interval length. Figure 8 shows the growth as function of the streamwise coordinate for all nine streamwise intervals, the optimal β for each respective interval was used in these calculations and ω was set to zero. For all the intervals the optimal growth is exceeded by maxima upstream of the endpoints. An optimization of the endpoint of the streamwise interval was therefore carried out, it was found that the largest possible growth of $G = 0.11 \cdot 10^{-2} Re^2$ occurs when $x_1 = 0.89$ and $\beta = 0.52$, the dashed line in figure 8. This result can be compared with the temporal study of the ASBL by Fransson & Corbett (2003). They found that the optimal disturbance, with

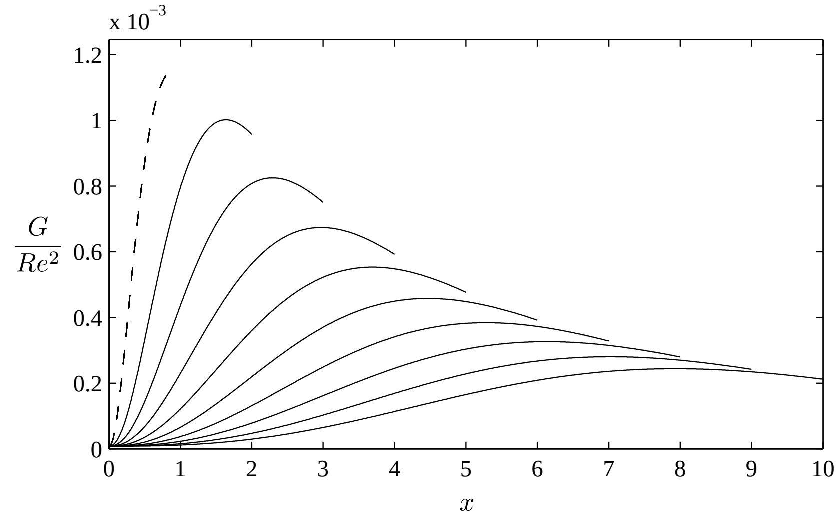

FIGURE 8. The growth G in the ASBL as function of x at $Re = 347$ for nine streamwise intervals ranging from $0 \leq x \leq 2$ to $0 \leq x \leq 10$ in steps of one (solid lines) and for the optimal interval $0 \leq x \leq 0.89$ (dashed line). The optimal β of each respective interval was used in these calculations and ω was set to zero.

$\beta = 0.53$, gives rise to a growth of $G = 0.99 \cdot 10^{-3} Re^2$ over the optimal temporal interval. The spatial growth presented here is 16 % higher than this temporal result. Biau & Bottaro (2004), who carried out a study on optimal disturbances in the plane Poiseuille flow, also found that spatial analysis gives higher growth than the temporal analysis. The plane Poiseuille flow was implemented herein and the growth calculated for the optimal wavenumber and interval given by Biau & Bottaro (2004). The result matched that of Biau & Bottaro (2004) and thus validated the used optimization procedure.

It is interesting to compare the optimal disturbance in the SSBL with that in the ASBL since it will expose how the differences in the base flow at the beginning of the interval affect the disturbance as it evolves downstream. One would expect that the differences between the disturbances will go towards zero as the streamwise interval is prolonged since the base flow of the SSBL approaches that of the ASBL.

The left column of figure 9 shows the growth as function of the spanwise wavenumber β for both the SSBL (solid line) and the ASBL (dashed line) while the right column shows the growth as function of the streamwise coordinate x. The angular frequency ω was set to zero and the optimal β was used when the growth as function of x was calculated. Three different streamwise intervals were used, $0 \leq x \leq 2$, $0 \leq x \leq 6$ and $0 \leq x \leq 10$. For the shortest interval, shown in the upper row, the SSBL gives a 30 % higher optimal growth than the

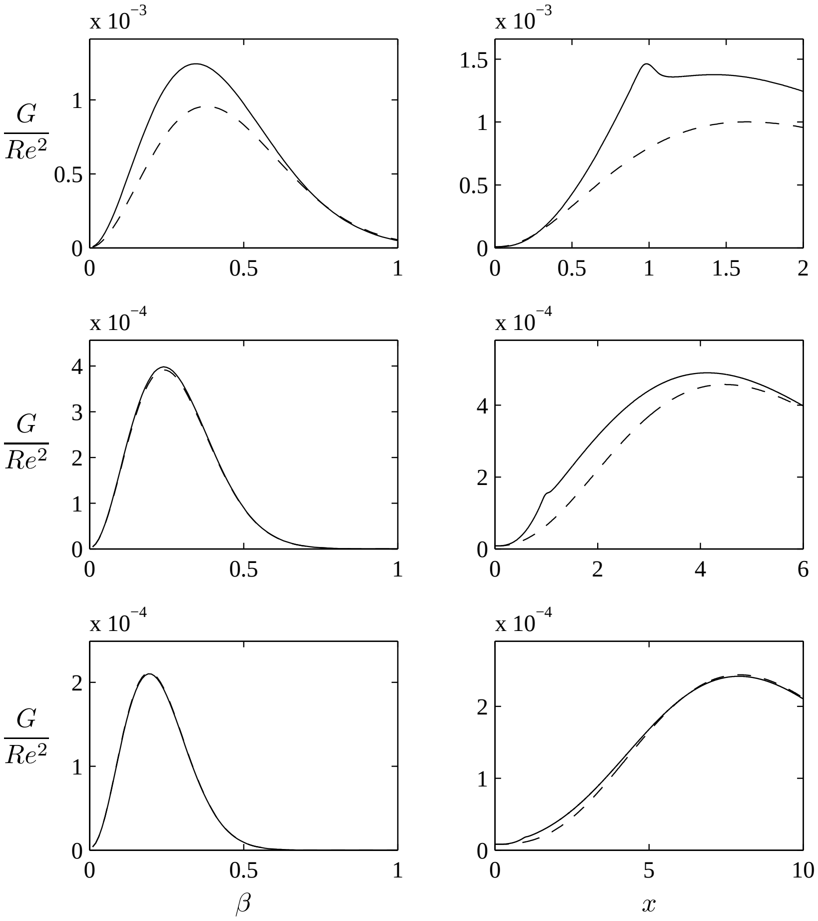

FIGURE 9. Left column: the growth G as function of β. Right column: the growth of the disturbance with optimal β as function of x. The SSBL (solid line) and the ASBL (dashed line) at $Re = 347$. The upper, middle and bottom row shows the growth in the streamwise intervals $0 \leq x \leq 2$, $0 \leq x \leq 6$ and $0 \leq x \leq 10$, respectively.

ASBL. The optimal growth also occurs at a lower spanwise wavenumber for the SSBL than for the ASBL. Studying the growth as function of x, we gather that the reason for the large difference in growth is the contribution from the BBL at the beginning of the SSBL. The middle row shows the interval $0 \leq x \leq 6$, for this interval the curves lie much closer, but the SSBL still gives a slightly higher optimal growth than the ASBL. The optimal spanwise wavenumber is however the same. The contribution from the BBL is also much smaller, this explains why the optimal growth in the SSBL ends up so much closer to that in

x_1	2	3	4	5	6	7	8	9	10
β_{ASBL}	0.38	0.32	0.29	0.26	0.24	0.23	0.21	0.20	0.19
β_{SSBL}	0.35	0.31	0.28	0.26	0.24	0.23	0.21	0.20	0.19
$G_{\text{ASBL}}/Re^2 \cdot 10^2$	0.096	0.075	0.059	0.048	0.039	0.033	0.028	0.024	0.021
$G_{\text{SSBL}}/Re^2 \cdot 10^2$	0.12	0.088	0.065	0.050	0.040	0.033	0.028	0.024	0.021

Table 2. The optimal growth and spanwise wavenumber in the ASBL and the SSBL at $Re = 347$ for nine streamwise intervals of different length.

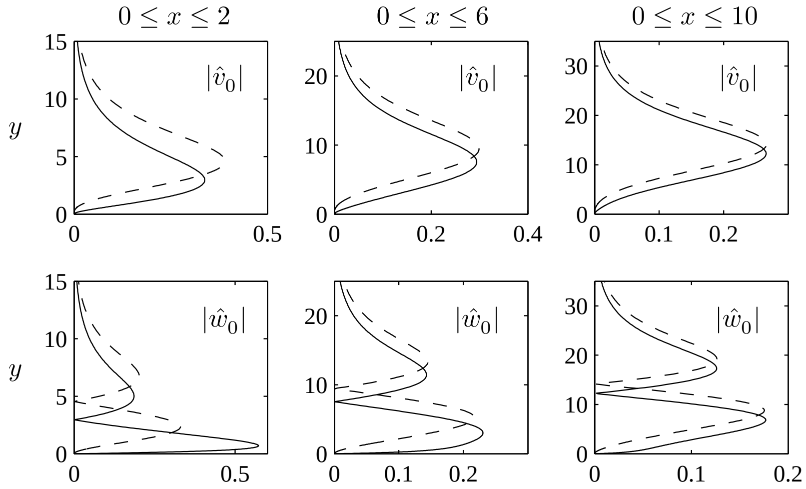

Figure 10. The optimal disturbance in the SSBL (solid line) and the ASBL (dashed line) at $Re = 347$. The upper and bottom row shows respectively the wall-normal component $\hat{v}_0$ and the spanwise component $\hat{w}_0$.

the ASBL. Finally we examine the long streamwise interval $0 \le x \le 10$, shown in the bottom row of figure 9. The curves collapse when we study the growth as function of the spanwise wavenumber, but a small difference can still be seen at the beginning of the streamwise interval. A more detailed comparison is done in table 2, which states the optimal spanwise wavenumber and corresponding optimal growth for all streamwise intervals. We conclude that the optimal growth and spanwise wavenumber in the SSBL go towards those in the ASBL when the streamwise interval is prolonged.

In figure 10 we compare the optimal disturbance in the SSBL (solid lines) and the ASBL (dashed lines). The upper row shows the wall-normal component $\hat{v}_0$ while the bottom row shows the spanwise component $\hat{w}_0$. The left, middle and right columns show the disturbances in the streamwise intervals $0 \le x \le 2$,

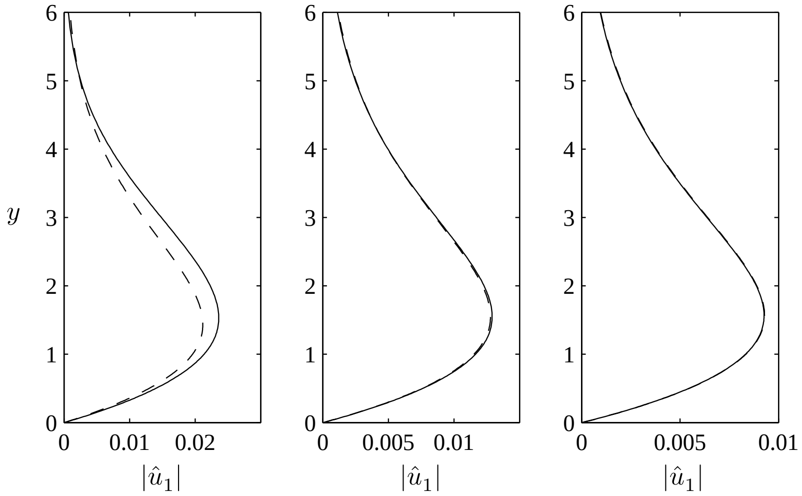

FIGURE 11. The downstream response $\hat{u}_1$ of the optimal disturbance in the SSBL (solid line) and the ASBL (dashed line) at $Re = 347$.

$0 \leq x \leq 6$ and $0 \leq x \leq 10$, respectively. This figure reveals that there are significant differences between the optimal disturbance in the SSBL and the optimal disturbance in the ASBL. For the shortest streamwise interval, the shapes of the disturbance profiles differ, especially for the $\hat{w}$ component which is larger close to the wall in the SSBL than in the ASBL. For the longer intervals, the disturbances assume more or less the same shape, but the profile maxima are still located slightly higher in the ASBL than in the SSBL. This is due to the fact that the suction acts on the disturbance over a longer distance in the ASBL where the suction is applied over the whole interval. When the $\hat{v}$ and $\hat{w}$ components in the longest interval are plotted at $x = 1$ (not shown here), the disturbances in the ASBL and the SSBL almost collapse.

The optimal disturbance evolves downstream to the final position of the interval, shown in figure 11. The differences are now much smaller and only clearly visible for the shortest interval. There is no significant difference in the wall-normal distribution or shape of the disturbances, we conclude that for long intervals the downstream response of the optimal disturbance in the SSBL and the ASBL have the same shape and wall-normal distribution.

3.3. *Comparison with experimental results*

As previously mentioned, Fransson & Alfredsson (2003) made an experimental study on the development and growth of disturbances induced into the SSBL by free-stream turbulence. The suction Reynolds numbers was $Re = 347$, the same Reynolds number has been used for the calculation of optimal disturbances in the present work. Fransson & Alfredsson (2003) found that the spanwise wavenumber of the streaks depends on the level of the free-stream turbulence. Three grids were used to achieve different levels of turbulence; 1.4 %, 2.2 % and 4.0 %. For these turbulence levels the measured spanwise wavenumbers were $\beta = 0.33$, $\beta = 0.41$ and $\beta = 0.47$, respectively. In comparison, the optimal wavenumber in the ASBL is $\beta = 0.53$ (Fransson & Corbett 2003) with temporal analysis and $\beta = 0.52$ with the spatial analysis presented herein. Fransson & Corbett (2003) argue that the experimentally measured spanwise wavenumber approach the optimal wavenumber as the free-stream turbulence level is increased. Their reasoning is that a high level of free-stream turbulence will provide enough energy over the whole range of scales to allow the boundary layer to amplify the disturbance with a wavenumber close to that of the optimal disturbance. There is however a discrepancy between the optimal and the measured wavenumber, even for the highest turbulence level.

Fransson & Alfredsson (2003) furthermore report that the spanwise scale of the streaks is maintained when suction is applied compared with the no-suction case. According to Fransson & Alfredsson (2003), the initial spanwise scale is probably set by the receptivity process in the BBL at the leading edge of the SSBL. Yoshioka *et al.* (2004) found that the spanwise scale of the streaks remains nearly constant in the downstream direction and concluded that the disturbances initiated at the leading edge become mainly passive and are convected downstream by the flow. To summarize, the experimental findings seem to indicate that the spanwise scale is set at the leading edge of the SSBL, where the base flow is unaffected by the suction. The results presented herein strengthen this hypothesis, since they show that the maximum disturbance growth in the SSBL is achieved over the BBL at the leading edge. The optimal spanwise wavenumber in the SSBL is therefore the same as that in the BBL, $\beta = 0.45$ (Andersson *et al.* 1999; Luchini 2000). This is quite close to the experimentally observed wavenumber at the highest turbulence level, $\beta = 0.47$ (Fransson & Alfredsson 2003). The downstream response to the optimal disturbance, shown in figure 11, was also compared to experimental data from Fransson & Alfredsson (2003). Good agreement was found, as previously reported by Fransson & Corbett (2003). There are however important differences between the calculation of optimal disturbances presented herein and the experimental conditions. In the calculation of the optimal disturbance we assume that the disturbance enter the boundary layer at the initial point of the streamwise interval and then evolves downstream without any influence from the outside disturbance environment. In the experiment the boundary layer is subjected to continuous forcing from the free-stream turbulence over the entire streamwise interval. It is also possible that non-linear effects that are not accounted for in the calculation of the optimal disturbances occur in the receptivity process.

4. Conclusions

The energy growth of optimal disturbances was studied by means of linearized equations for the semi suction boundary layer (SSBL) and the asymptotic suction boundary layer (ASBL). The suction Reynolds number was set to 347.

First the algebraic growth in the SSBL was studied. It was found that the optimal disturbance consists of streamwise aligned vortex pairs that give rise to streamwise streaks. This disturbance gives rise to the highest possible growth when the streamwise interval ends at the point where the suction starts. The base flow of this optimal interval is the BBL, the optimal spanwise wavenumber in the SSBL is therefore the same as that in the BBL, $\beta = 0.45$ (Andersson *et al.* 1999; Luchini 2000). When the interval is prolonged beyond the starting point of the suction, the optimal spanwise wavenumber decreases, the optimal angular frequency is however zero irrespective of the interval length. Furthermore, it was found that the vortices, i.e. the optimal disturbance, grow as the interval is prolonged and that the cores of the vortices move upward in the wall-normal direction. This effect is due to the suction which draws the disturbance down towards the wall. The vortex cores must therefore be located higher initially in a long interval where the suction will act on the disturbance over a longer distance.

Second, the optimal disturbance in the ASBL was studied and a comparison with the SSBL was made. The optimal disturbance in the ASBL closely resembles that in the SSBL. The cores of the vortices, i.e. the optimal disturbance, are however located higher in the ASBL due to the fact that the suction acts on the disturbance over the whole streamwise interval. This difference vanishes as the disturbance evolves in the streamwise direction, the downstream response is therefore the same over long intervals. Furthermore, it was found that for short intervals the SSBL gives a significantly higher growth due to the contribution from the BBL. The optimal spanwise wavenumber was also lower for the SSBL than for the ASBL for these intervals. As the streamwise interval was prolonged the optimal growth and spanwise wavenumber in the SSBL approached those in the ASBL.

Finally, a comparison was made with experimental results from Fransson & Alfredsson (2003) and Yoshioka *et al.* (2004). This comparison showed that both the experimental findings and the results presented herein support the theory that the spanwise scale of the disturbances is set in the BBL at the leading edge of the SSBL.

Acknowledgements

The authors thank Doctor J. H. M. Fransson who provided many insightful comments, from which this work has greatly benefitted. We are indebted to Doctor P. Corbett, Professor A. Bottaro and Doctor J. H. M. Fransson who generously shared their code for temporal analysis of optimal disturbances.

References

Andersson, P., Berggren, M. & Henningson, D. S. 1999 Optimal disturbances and bypass transition in boundary layers. *Phys. Fluids* **11**, 134–150.

Andersson, P., Brandt, L., Bottaro, A. & Henningson, D. S. 2001 On the breakdown of boundary layer streaks. *J. Fluid Mech.* **428**, 29–60.

Balakumar, P. & Hall, P. 1999 Optimum suction distribution for transition control. *Theoret. Comput. Fluid Dyn.* **13**, 1–19.

Berlin, S. & Henningson, D. S. 1999 A nonlinear mechanism for receptivity of free-stream disturbances. *Phys. Fluids* **11**, 3749–3760.

Biau, D. & Bottaro, A. 2004 Transient growth and minimal defects: Two possible initial paths of transition to turbulence in plane shear flows. *Phys. Fluids* **16**, 3515–3529.

Brandt, L. & Henningson, D. S. 2002 Transition of streamwise streaks in zero-pressure-gradient boundary layers. *J. Fluid Mech.* **472**, 229–261.

Butler, K. M. & Farrell, V. F. 1992 Three-dimensional optimal perturbations in viscous shear flow. *Phys. Fluids A* **4**, 1637–1650.

Corbett, P. & Bottaro, A. 2000 Optimal perturbations for boundary layers subject to stream-wise pressure gradient. *Phys. Fluids* **12**, 120–130.

Corbett, P. & Bottaro, A. 2001*a* Optimal control of nonmodal disturbances in boundary layers. *Theoret. Comput. Fluid Dyn.* **15**, 65–81.

Corbett, P. & Bottaro, A. 2001*b* Optimal linear growth in swept boundary layers. *J. Fluid Mech.* **435**, 1–23.

Ellingsen, T. & Palm, E. 1975 Stability of linear flow. *Phys. Fluids* **18**, 487–488.

Fransson, J. H. M. & Alfredsson, P. H. 2003 On the disturbance growth in an asymptotic suction boundary layer. *J. Fluid Mech.* **482**, 51–90.

Fransson, J. H. M. & Corbett, P. 2003 Optimal linear growth in the asymptotic suction boundary layer. *Eur. J. Mech. B/Fluids* **22**, 259–270.

Fransson, J. H. M., Matsubara, M. & Alfredsson, P. H. 2005 Transition induced by free-stream turbulence. *J. Fluid Mech.* **527**, 1–25.

Griffith, A. A. & Meredith, F. W. 1936 The possible improvement in aircraft performance due to boundary layer suction. *Tech. Rep.* 2315. Rep. Aero. Res. Coun.

Hœpffner, J., Brandt, L. & Henningson, D. S. 2005 Transient growth on boundary layer streaks. *J. Fluid Mech.* **537**, 91–100.

Klebanoff, P. S. 1971 Effect of freestream turbulence on the laminar boundary layer. *Bull. Am. Phys. Soc.* **10**, 1323.

Landahl, M. T. 1975 Wave breakdown and turbulence. *SIAM J. Appl. Maths* **28**, 735–756.

Landahl, M. T. 1980 A note on an algebraic instability of inviscid parallel shear flows. *J. Fluid Mech.* **98**, 243–251.

Levin, O. & Henningson, D. S. 2003 Exponential vs algebraic growth and transition prediction in boundary layer flow. *Flow, Turb. Combust.* **70**, 183–210.

Luchini, P. 2000 Reynolds-number-independent instability of the boundary layer over a flat surface: optimal perturbations. *J. Fluid Mech.* **404**, 289–309.

Matsubara, M. & Alfredsson, P. H. 2001 Disturbance growth in boundary layers subjected to free-stream turbulence. *J. Fluid Mech.* **430**, 149–168.

Pralits, J. O., Hanifi, A. & Henningson, D. S. 2002 Adjoint-based optimization of steady suction for disturbance control in incompressible flows. *J. Fluid Mech.* **467**, 129–161.

Reddy, S. C. & Henningson, D. S. 1993 Energy growth in viscous channel flows. *J. Fluid Mech.* **252**, 209–238.

Schlichting, H. 1979 *Boundary-Layer Theory*, 7th edn. Mc-Graw-Hill.

Schmid, P. J. & Henningson, D. S. 2001 *Stability and transition in shear flows*. Springer.

Westin, K. J. A., Boiko, A. V., Klingmann, B. G. B., Kozlov, V. V. & Alfredsson, P. H. 1994 Experiments in a boundary layer subjected to free stream turbulence. Part 1. Boundary layer structure and receptivity. *J. Fluid Mech.* **281**, 193–218.

Yoshioka, S., Fransson, J. H. M. & Alfredsson, P. H. 2004 Free stream turbulence induced disturbances in boundary layers with wall suction. *Phys. Fluids* **16**, 3530–3539.

Zuccher, S., Luchini, P. & Bottaro, A. 2004 Algebraic growth in a Blasius boundary layer: optimal and robust control by mean suction in the nonlinear regime. *J. Fluid Mech.* **513**, 135–160.

Paper 3

A study of the Blasius wall jet

By Ori Levin[1], Valery G. Chernoray[2], Lennart Löfdahl[2] and Dan S. Henningson[1]

[1]Department of Mechanics, Royal Institute of Technology, SE-100 44 Stockholm, Sweden

[2]Thermo and Fluid Dynamics, Chalmers University of Technology, SE-412 96 Göteborg, Sweden

Published in *Journal of Fluid Mechanics* **539**, 313–347, 2005

A plane wall-jet flow is numerically investigated and compared to experiments. The measured base flow is matched to a boundary-layer solution developing from a coupled Blasius boundary layer and Blasius shear layer. Linear stability analysis is performed, revealing high instability of two-dimensional eigenmodes and non-modal streaks. The nonlinear stage of laminar-flow breakdown is studied with three-dimensional direct numerical simulations and experimentally visualized. In the direct numerical simulation, an investigation of the nonlinear interaction between two-dimensional waves and streaks is made. The role of subharmonic waves and pairing of vortex rollers is also investigated. It is demonstrated that the streaks play an important role in the breakdown process, where their growth is transformed from algebraic to exponential as they become part of the secondary instability of the two-dimensional waves. In the presence of streaks, pairing is suppressed and breakdown to turbulence is enhanced.

---

1. Introduction

1.1. *The wall jet*

A wall jet may generally be considered as a flow field that is produced by the injection of a high-velocity fluid in a thin layer close to a surface. The ambient fluid may be either quiescent or moving at a certain velocity, which typically is lower than the velocity of the injected jet. Such flows are of great interest to engineers, for instance in film cooling of gas turbine blades and combustion chambers, in defrosters for automobiles, and in boundary-layer control of airfoils and flaps. Fundamentally, a wall jet may, in principle, be treated as a two-layer flow with an inner region that reaches, in the normal direction, up to the point of maximum velocity and an outer region above. The inner region is most similar to a wall boundary layer and the outer region has a flow pattern that is closely related to a free shear layer. The major characteristics of these layers are different, and in a wall jet, the interaction between these regions forms a complex flow field.

Two-dimensional wall jets have been considered since the mid 1950s and in a classical work by Glauert (1956), it was found that a similarity solution exists for the laminar wall jet. This solution was obtained explicitly and is valid far downstream from the position of the fluid injection. Glauert's solution has provided a good basis for a number of subsequent stability investigations.

1.2. *Two-dimensional behaviour*

The temporal linear stability of the Glauert wall jet was examined theoretically by Chun & Schwarz (1967) by solving the Orr–Sommerfeld equation. Bajura & Szewczyk (1970) performed hot-wire measurements in an air wall jet and confirmed the existence of the Glauert wall jet. Furthermore, the stability of the flow to natural disturbances was studied and the streamwise velocity fluctuation was found to exhibit two large peaks, one peak on each side of the wall jet core. The amplification rate of the outer peak was found to be larger, and hence, the instability of the wall jet is controlled by the outer region. The results are in qualitative agreement with the linear stability theory by Chun & Schwarz (1967). The dominance of the outer region was also reported by Bajura & Catalano (1975), who investigated the whole transition process of a water wall jet. By using flow visualization, they observed the following five stages in natural transition: (i) formation of discrete vortices in the outer region; (ii) vortex pairing in the outer region, resulting in a doubling of the disturbance wavelength, coupled with the possible pairing of vortex-like motions in the inner region; (iii) lift-off of the wall jet into the ambient fluid; (iv) onset of turbulent motion; (v) re-laminarization of the upstream flow, until the next vortex pairing.

By solving the Orr–Sommerfeld equation, Mele *et al.* (1986) clarified the existence of two unstable modes in the wall jet. One mode, unstable at low disturbance frequencies, shows the highest amplitude close to the inflection point in the outer region of the wall jet, while the other mode, unstable at higher frequencies, attains the highest amplitude close to the wall. They concluded that the inviscid instability in the outer region governs the large-scale disturbances while the viscous instability governs the small-scale disturbances close to the wall. Tumin & Aizatulin (1997) numerically investigated the instability and receptivity of a laminar wall jet and concluded that the high-frequency viscous mode can be exited more easily by periodic blowing and suction through the wall than the low-frequency inviscid mode. Cohen *et al.* (1992) found a new family of laminar self-similar solutions describing the mean flow of an incompressible two-dimensional wall jet subjected to steady wall blowing or suction. By applying linear stability theory in the temporal framework for the family of solutions, it was shown that blowing stabilizes the inviscid mode while destabilizing the viscous one. The opposite effect was found when suction is applied. These self-similar profiles were later confirmed experimentally by Amitay &

Cohen (1993). Amitay & Cohen (1997) investigated the interaction of the two different modes in the wall jet subject to steady wall blowing or suction.

In a low-disturbance environment, the initial stage of the transition process is indeed defined by two-dimensional eigenmodes growing in the outer layer. Two-dimensional direct numerical simulations (DNS) have been successfully employed and the transitional process has been studied (e.g. Gogineni *et al.* 1999; Seidel & Fasel 2001) for forced laminar wall jets. The simulations demonstrate good agreement with the supporting experiments, at least for the initial stages of transition, where the three-dimensional activity was relatively weak. Seidel & Fasel (2001) adopted a two-dimensional DNS-solver to analyse the effect of periodical forcing by a blowing and suction slot on a laminar wall jet over a heated flat plate. For very low disturbance amplitudes, the simulations show a good agreement with linear stability theory. For an increased amplitude, a strong nonlinear distortion of the mean flow was observed. In particular, the skin friction is reduced markedly, the local maximum velocity is decreased and the wall heat transfer is increased. It was shown that the large structures, generated by the forcing, are the main cause for the strong mean flow distortion of both velocity and temperature. The wall heat transfer was found to increase as large structures entrain cold fluid from the ambient fluid and hot fluid is convected away from the wall.

1.3. *Three-dimensional behaviour*

Gogineni *et al.* (1993, 1999) and Gogineni & Shih (1997) investigated a laminar wall jet undergoing transition using particle image velocimetry (PIV). Their results show that the transition process is dominated by formation and development of discrete vortices in both the inner and outer regions and the interaction between them. Three-dimensionality initiated in the outer region spreads to the inner region and the emergence of large three-dimensional structures inside the shear layer triggers the complete breakdown of the flow. The importance of the three-dimensional effects on the transition process has also been numerically demonstrated. Wernz & Fasel (1996, 1997) performed DNS to study the transition process of the wall jet both for two-dimensional and three-dimensional disturbances and found that when forcing of high-amplitude disturbances is introduced, mushroom-shaped structures are ejected from the wall jet into the ambient fluid. Visbal *et al.* (1998) investigated the breakdown process in a finite-aspect-ratio wall jet by means of DNS and high-resolution experimental measurements. In the simulation, the experimental base flow was matched to a parabolic profile at the nozzle outlet. In the spanwise direction, an incoming sidewall boundary layer was simulated using a hyperbolic tangent distribution. Two-dimensional forcing was applied by varying the whole base-flow amplitude. They observed a rapid spanwise breakdown of the two-dimensional rollers into streamwise vortices and streaks that start near the sidewalls and propagate toward the midspan of the wall jet.

The primary instability in inflectional base flows such as free shear layers and wall jets is a strong inviscid exponential instability resulting in the roll-up of waves into strong spanwise vortices. These two-dimensional vortices can experience two different types of secondary instability. For low initial three-dimensional excitation, the secondary instability is subharmonic and associated with vortex pairing, like that observed by Bajura & Catalano (1975). If the initial three-dimensional excitation is large enough, a three-dimensional secondary instability is predominant, which changes the path to turbulence.

It is well-known that in a free shear layer, the development of two-dimensional motion is coupled with secondary streamwise coherent structures, see Ho & Huerre (1984), Bernal & Roshko (1986) and Lasheras *et al.* (1986). The three-dimensional instabilities manifest themselves mainly as counter-rotating streamwise vortices and are formed in the braids between the coherent two-dimensional rollers. Numerical studies support these results, see Metcalfe *et al.* (1987) and Balaras *et al.* (2001). The location of the formation of the three-dimensionalities is strongly dependent on the location of the origin and the magnitude of the upstream three-dimensional perturbations. In fact, the observed three-dimensional small scales may destroy the two-dimensional large-scale structures for the case of a high level of random initial disturbances, as is clearly shown by Balaras *et al.* (2001).

1.4. *Outline of the paper*

The wall jet constitutes an excellent flow case for studying how a free shear layer and a wall-bounded flow interacts through a detailed investigation of the interplay between two- and three-dimensional structures in the flow breakdown to turbulence. For stability investigations of a high-Reynolds-number wall jet, a description of the laminar base flow is required, and here this flow is analysed using the boundary-layer equations. For the case of a non-interacting boundary layer and top shear layer, a simple solution exists that consists of a coupling of the Blasius boundary layer and the Blasius shear layer. Hereinafter, a wall jet of this type and its downstream development is referred to as a *Blasius wall jet*.

In this work, we perform linear stability calculations and highly resolved three-dimensional DNS of the Blasius wall jet and compare the results to experiments. It is discovered that in the experimental wall jet, apart from the two-dimensional waves, almost stationary streaks occur. The streaks interact with the waves and seed the secondary instability. As a result, the breakdown process happens fast, resulting in a short laminar part of the wall jet. Such longitudinal structures are likely to exist in various applications, especially when the wall jet is created through contractions where vorticity is amplified. In § 2, the equipment and methodology of the experiment are described. In § 3, the numerical techniques used are presented and in § 4, the results obtained are presented. Firstly, the measured base flow is matched to the boundary-layer solution. Results from the linear stability calculations for both eigenmodes and

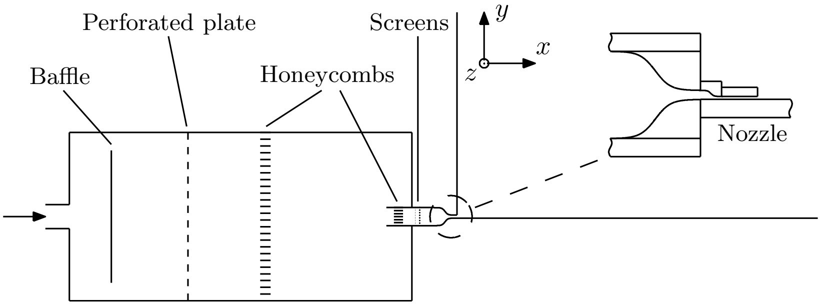

FIGURE 1. Wall-jet facility.

non-modal streaks are presented and compared with the experiment. Finally, the nonlinear breakdown process is highlighted by the experiment and examined more closely by analysing the DNS data. The role of subharmonic waves and pairing is also investigated.

2. Experimental methods

2.1. *Experimental set-up*

All experiments were conducted at Chalmers University of Technology in a wall-jet facility, which is schematically shown in figure 1. The wall jet is formed by the injection of air through a slot and develops over a large horizontal flat plate of 2.1 m in length and 3.2 m in width. This plate is made of wood and coated with a thin plastic laminate. The height of the slot used is 3 mm and the width is 500 mm. A coordinate system is defined in figure 1 with the x-axis streamwise, y-axis normal to the wall and the z-axis in the spanwise direction. Equipped with a vertical back wall of 1.2 m height, located just above the inlet and sidewalls of the same height, the current wall jet can be considered to operate in quiescent surroundings, since the facility is located in a large hall ($15 \times 15 \times 8\,\mathrm{m}^3$) with negligible room draught.

Air is supplied by a centrifugal fan to the settling chamber, which is equipped with flow straightening devices; namely, a baffle, perforated plate, honeycombs and screens. After the settling chamber, the flow enters two smooth contractions of total ratio 36:1. The measured turbulence level of the outlet flow is sufficiently low, less than 0.05 % in the frequency range from 10 Hz to 10 kHz. During the measurements, the velocity in the middle of the nozzle, U_0, is checked by a Pitot–Prandtl tube. The manometer used, FSO510, is also equipped with sensors for temperature and absolute pressure readings.

The streamwise velocity component of the wall-jet flow field is measured by a hot wire, which is monitored by a DANTEC constant-temperature anemometer. A tungsten single-wire boundary-layer probe with a wire diameter and length of $5\,\mu$m and 0.7 mm, respectively, is operated at an overheat ratio of 1:8.

The hot wire is calibrated in the jet outlet versus the Prandtl tube. Details on the experimental procedure as well as on the measurement equipment used can be found in Chernoray *et al.* (2005). Typically, the calibration resulted in an error of less than 0.5 % for all points in the calibration range. The hot-wire position traversing mechanism is computer controlled and can be completely automated for long experimental runs through the definition of a geometrical mesh of measurement points. Equipped with servo-motors it can sustain an absolute coordinate system with an accuracy of $10\,\mu$m in the horizontal directions, and $5\,\mu$m in the wall-normal direction. The acquisition system is the IOTech Wavebook 516 sampling module with expansion unit, enabling 16 bit 1 MHz sample and hold with full analogue and digital triggering options. The software used to control the sampling and saving of data files is linked into a program for automated, triggered flow measurements using the traverse system and a pre-defined mesh of sampling points. The distance between the hot wire and the wall is measured using an 'electro-optical' method and is checked before every experimental run. To employ this method, a strip of electrically conductive foil is glued onto the surface and when one probe prong touches the surface an electric circuit is closed. The distance between the wire and the wall when the prong touches the surface is measured optically in this position. It should be pointed out that the wall-distance measurements are performed before the hot-wire calibration.

2.2. *Artificial disturbances*

To use the advantages of a controlled experiment and to study the development of two-dimensional waves and stationary longitudinal streaks in detail, disturbances are introduced in the flow artificially.

Time-periodic two-dimensional waves are excited by a loudspeaker situated about two metres downstream of the nozzle outlet. The signal for the loudspeaker of controlled frequency and amplitude is generated by an analogue output board in a computer and an external amplifier unit. The frequency of the artificial disturbances is chosen to be 1221 Hz, which is close to the natural flow frequency and detuned off 50 Hz of the power network. The measurement of the linear instability waves is performed in a region starting at about one hydrodynamic wavelength downstream of the nozzle outlet and prior to the downstream distance where significant nonlinear interactions occur. Such recommendations can be found in the review by Ho & Huerre (1984) for shear layers and are based mostly on the fact that instability waves are influenced by the solid edge in a near-field region. It is also recommended that the acoustic wavelength should be large enough for the assurance of the wave two-dimensionality, and this length is about 0.3 m for the mentioned frequency of 1221 Hz. Before the experiment, the two-dimensionality of the base flow and that of the excited waves is carefully checked through measurements and visualizations. To obtain the amplitude and phase information of the signal, fast Fourier transform

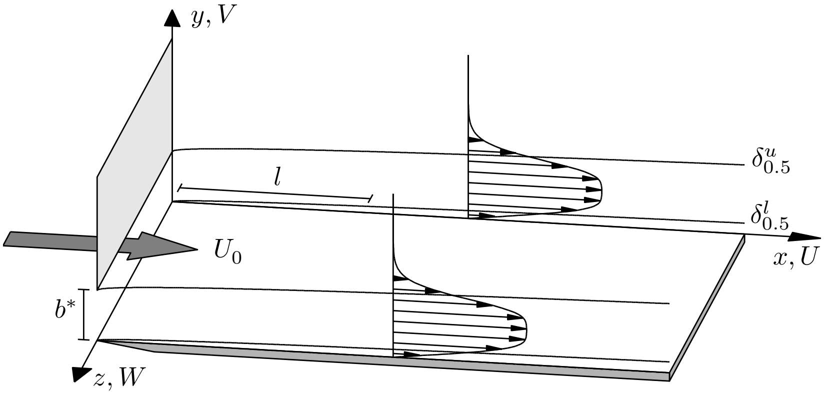

FIGURE 2. Plane wall-jet flow.

(FFT) is applied to the velocity time traces, see Chernoray *et al.* (2005) for details.

Stationary longitudinal streaks are introduced in the flow by fine roughness elements of controlled geometry and a typical height of 40 μm. The roughness elements are positioned at the orifice of the wall jet onto the inner surface of the top lip of the nozzle. To introduce a streaky pattern of a single spanwise scale, typically an array of five uniformly distributed roughness elements is used. It is decided to introduce five different streak scales, and accordingly five groups of humps are positioned on the nozzle. As a result, nearly sinusoidal mean flow modulation is obtained after a short distance downstream of the nozzle outlet. The evaluation of the streaks is performed by measurements of (y, z)-velocity planes of two or three spanwise wavelengths. A cross-sectional plane for each scale is taken with constant steps in the y-direction of 0.15 mm and 0.5 mm in the z-direction, and the corresponding number of points for each plane is 20 in the wall-normal extent and from 12 to 30 in the spanwise extent, depending on the spanwise streak scale. Subsequently, the undisturbed base flow is subtracted and the remaining stationary disturbance is decomposed into spanwise modes using FFT.

During the measurements, the output signal from the anemometer is amplified and digitized; post-processing is done using the software package Matlab.

3. Numerical solution methods

3.1. *Scaling*

Consider an incompressible wall jet over a flat plate as illustrated in figure 2. Through a slot with height b^*, fluid with exit velocity U_0 is blown tangentially along a wall. The scalings are originating from the boundary-layer approximations. The streamwise coordinate x is scaled with the length scale l, which is a fixed distance from the slot. The wall-normal and spanwise coordinates y

and z, respectively, are scaled with the boundary-layer parameter $\delta = \sqrt{\nu l/U_0}$, where ν is the kinematic viscosity of the fluid. The streamwise velocity U is scaled with U_0, while the wall-normal and spanwise velocities V and W, respectively, are scaled with $U_0\delta/l$. The pressure P is scaled with $\rho U_0^2\delta^2/l^2$, where ρ is the density of the fluid, and the time t is scaled with l/U_0. The Reynolds numbers used here are defined as $Re_l = U_0 l/\nu$ and $Re_\delta = U_0\delta/\nu$. It is useful to note the relations $l/\delta = Re_\delta = \sqrt{Re_l}$.

3.2. *Linear disturbance equations*

The well-known technique based on the parabolized stability equations (PSE) (Bertolotti *et al.* 1992; Herbert 1997) deals with the spatial evolution of exponentially growing eigenmodes. These equations are scaled with a suitable scaling for modal waves, e.g. the streamwise and normal disturbance velocities are assumed to be of the same order. However, in the last decade there has been an increasing interest in the algebraically growing non-modal Klebanoff modes (Klebanoff 1971; Westin *et al.* 1994; Andersson *et al.* 1999; Luchini 2000). The two growth scenarios are associated with different scales. The governing equations for non-modal disturbances are scaled with the boundary-layer scalings (see Andersson *et al.* 1999). Here we summarize a set of stability equations valid for both algebraically and exponentially growing disturbances, given by Levin & Henningson (2003). For further details, see that investigation.

We want to study the linear stability of a high-Reynolds-number flow. The non-dimensional Navier–Stokes equations for an incompressible flow are linearized around a two-dimensional, steady base flow ($U(x,y)$, $V(x,y)$, 0) to obtain the stability equations for the spatial evolution of three-dimensional time-dependent disturbances ($u(x,y,z,t)$, $v(x,y,z,t)$, $w(x,y,z,t)$, $p(x,y,z,t)$). The disturbances, that are scaled as the base flow, are taken to be periodic in the spanwise direction and time. This allows us to assume solutions of the form

$$f = \hat{f}(x,y)\exp\left(\mathrm{i}Re_\delta\int_{x_0}^{x}\alpha(x)\,\mathrm{d}x + \mathrm{i}\beta z - \mathrm{i}\omega t\right), \tag{1}$$

where f represents either one of the disturbances u, v, w or p. The complex streamwise wavenumber α captures the fast wavelike variation of the modes and is therefore scaled with $1/\delta$, but α itself is assumed to vary slowly with x. The x-dependence in the amplitude function $\hat{f}$ includes the weak variation of the disturbances. The real spanwise wavenumber β and the real disturbance angular frequency ω are scaled in a consistent way with z and t, respectively. Introducing (1) in the linearized Navier–Stokes equations and neglecting third-order terms in $1/Re_\delta$ or higher, we arrive at the parabolized stability equations in boundary-layer scalings

$$\hat{u}_x + \mathrm{i}Re_\delta \alpha \hat{u} + \hat{v}_y + \mathrm{i}\beta \hat{w} = 0, \tag{2a}$$

$$(U_x + \mathrm{i}Re_\delta \alpha U - \mathrm{i}\omega)\hat{u} + U\hat{u}_x + V\hat{u}_y + U_y\hat{v} + \frac{\hat{p}_x}{Re_\delta^2} + \frac{\mathrm{i}\alpha\hat{p}}{Re_\delta} = \hat{u}_{yy} - k^2\hat{u}, \tag{2b}$$

$$(V_y + \mathrm{i}Re_\delta \alpha U - \mathrm{i}\omega)\hat{v} + U\hat{v}_x + V_x\hat{u} + V\hat{v}_y + \hat{p}_y = \hat{v}_{yy} - k^2\hat{v}, \tag{2c}$$

$$(\mathrm{i}Re_\delta \alpha U - \mathrm{i}\omega)\hat{w} + U\hat{w}_x + V\hat{w}_y + \mathrm{i}\beta\hat{p} = \hat{w}_{yy} - k^2\hat{w}, \tag{2d}$$

where $k^2 = \alpha^2 + \beta^2$. All the terms are generally of the first or the second order except the $\hat{p}_x/Re_\delta^2$-term, in (2b), which is of the third order for the algebraic instability problem and the $V_x\hat{u}$-term, in (2c), which is of the third order for the exponential instability problem. Both of these terms, however, have to be included in a general formulation of the problem. Unfortunately, the $\hat{p}_x/Re_\delta^2$-term introduces numerical instability, setting a lower limit of the streamwise step size (Li & Malik 1994), as is the case for all PSE-formulations.

We are interested in solutions subject to no-slip conditions at the plate and vanishing at the wall-normal position y_{max} well outside the wall jet. The boundary conditions in the wall-normal direction can then be written

$$\left.\begin{array}{lll} \hat{u} = \hat{v} = \hat{w} = 0 & \text{at} & y = 0, \\ \hat{u} = \hat{v} = \hat{w} = 0 & \text{at} & y = y_{max}. \end{array}\right\} \tag{3}$$

The set of equations is nearly parabolic in the streamwise coordinate and is marched forward from an initial position x_0 to a final position x_1. Given the initial conditions

$$\hat{u} = \hat{u}_0(y), \quad \hat{v} = \hat{v}_0(y), \quad \hat{w} = \hat{w}_0(y) \quad \text{at} \quad x = x_0, \tag{4}$$

the wavenumber β and the angular frequency ω, the initial-boundary-value problem is solved from x_0 to x_1 to obtain the downstream development of the disturbance.

The disturbance growth is generally measured by the average change in the kinetic energy of the fluid. In spatially evolving investigations, a commonly used quantity to represent this change is the disturbance energy defined as

$$E(x, \beta, \omega, Re_l) = \int_0^{y_{max}} (Re_l|u|^2 + |v|^2 + |w|^2)\,\mathrm{d}y = \hat{E}\mathrm{e}^\theta, \tag{5}$$

where

$$\hat{E} = \int_0^{y_{max}} (Re_l|\hat{u}|^2 + |\hat{v}|^2 + |\hat{w}|^2)\,\mathrm{d}y, \quad \theta = -2Re_\delta \int_{x_0}^{x} \alpha_\mathrm{i}\,\mathrm{d}x. \tag{6}$$

3.2.1. *Exponential growth*

Here we consider solutions to (2)–(4) associated with wavelike disturbances, i.e. where α in the phase function in (6) is order unity. As both the amplitude and phase functions depend on x, one more equation is required. We require that both the amplitude function and the wavenumber α change slowly in the streamwise direction, and specify a normalization condition on the amplitude function

$$\int_0^{y_{max}} (Re_l \overline{\hat{u}}\hat{u}_x + \overline{\hat{v}}\hat{v}_x + \overline{\hat{w}}\hat{w}_x)\,\mathrm{d}y = 0, \tag{7}$$

where the bar denotes complex conjugate. Other conditions are possible and are presented in the paper by Bertolotti *et al.* (1992). The normalization condition specifies how much growth and sinusoidal variation are represented by the amplitude and phase function, respectively. The stability problem (2)–(4) and (7) have to be solved iteratively in each streamwise step. The numerical method solving the stability equations is based on a spectral collocation method involving Chebyshev polynomials. Details about the numerical scheme can be found in Andersson *et al.* (1999) and Hanifi *et al.* (1996). The initial condition (4) is taken as the least stable eigenfunction of Orr–Sommerfeld and Squire equations with corresponding eigenvalue $\alpha(x_0)$. Since the initial condition do not capture non-parallel effects there will be a region in the beginning of the domain that includes some errors (e.g. see figure 9). The size of these errors and the length of this region are dependent of the type of base flow and how non-parallel it is.

3.2.2. *Optimal disturbances*

Now we consider solutions to (2)–(4) with $\alpha = 0$, giving rise to disturbances with weak streamwise variations. We are interested in maximizing the disturbance energy (5), at the downstream position x_1, by optimizing the initial disturbance at x_0 with given initial energy. That is, we want to maximize the disturbance growth defined by

$$G(x_0, x_1, \beta, \omega, Re_l) = \frac{E(x_1)}{E(x_0)}. \tag{8}$$

When going to the limit of large Reynolds number, the maximum growth will, because of the difference in order between the terms in the disturbance energy (5), be obtained for initial disturbances with a zero streamwise velocity component. Furthermore, provided that $\hat{u}_1$ is non-zero, $\hat{v}_1$ and $\hat{w}_1$ can be neglected and the Reynolds-number-independent growth can be simplified to

$$\overline{G} = \lim_{Re_l \to \infty} \frac{G}{Re_l} = \frac{\displaystyle\int_0^{y_{max}} |\hat{u}_1|^2\,\mathrm{d}y}{\displaystyle\int_0^{y_{max}} (|\hat{v}_0|^2 + |\hat{w}_0|^2)\,\mathrm{d}y} = \frac{(\hat{u}_1, \hat{u}_1)_u}{(\boldsymbol{q}, \boldsymbol{q})_q}. \tag{9}$$

The last identity defines the appropriate inner products, where $\boldsymbol{q} = (\hat{v}_0, \hat{w}_0)^T$. The optimization problem in the large-Reynolds-number limit is defined by maximizing (9) and concerns the optimization of the initial disturbance $\boldsymbol{q}$ for given values of x_0, x_1, β and ω. Details about the derivation of the optimization procedure can be found in the Appendix and in Levin & Henningson (2003) and details about the numerical scheme is given in Andersson *et al.* (1999) and Hanifi *et al.* (1996). The numerical method solving the forward problem

(2)–(4) and the backward problem (30)–(32) is based on a spectral collocation method involving Chebyshev polynomials.

3.3. *DNS techniques*

3.3.1. *Numerical methods*

The numerical code (see Lundbladh *et al.* 1999) uses spectral methods to solve the three-dimensional time-dependent incompressible Navier–Stokes equations. The discretization in the streamwise and spanwise directions make use of Fourier series expansions, which enforces periodic solutions. The discretization in the normal direction is represented with Chebyshev polynomial series. A pseudospectral treatment of the nonlinear terms is used. The time advancement used is a second-order Crank–Nicolson method for the linear terms and a four-step low-storage third-order Runge–Kutta method for the nonlinear terms. Aliasing errors arising from the evaluation of the pseudospectrally convective terms are removed by dealiasing by padding and truncation using the 3/2-rule when the FFTs are calculated in the wall-parallel planes. In the normal direction, it has been found that increasing the resolution is more efficient than the use of dealiasing.

Flows such as boundary layers and wall jets are spatially growing and to fulfil the necessary periodic boundary condition in the streamwise direction, required by the spectral discretization, a fringe region (see Nordström *et al.* 1999) is added in the downstream end of the computational domain. In this region, the function $\lambda(x)$ is smoothly raised from zero and the flow is forced to a desired solution $\boldsymbol{v}$ in the following manner

$$\frac{\partial \boldsymbol{u}}{\partial t} = NS(\boldsymbol{u}) + \lambda(x)(\boldsymbol{v} - \boldsymbol{u}) + \boldsymbol{g}, \tag{10}$$

$$\boldsymbol{\nabla} \cdot \boldsymbol{u} = 0, \tag{11}$$

where $\boldsymbol{u}$ is the solution vector and $NS(\boldsymbol{u})$ the right-hand side of the (unforced) momentum equations. Both $\boldsymbol{g}$, which is a disturbance forcing, and $\boldsymbol{v}$ may depend on the three spatial coordinates and time. The forcing vector $\boldsymbol{v}$ is smoothly changed (blended) from the undisturbed wall-jet solution of the boundary-layer equations at the beginning of the fringe region to the prescribed inflow velocity vector, which is the Blasius wall jet shown in figure 3(a). In the case of forcing a disturbance in the flow, it is also added to the forcing vector in the end of the fringe region. The fringe function is conveniently written as

$$\lambda(x) = \lambda_{max} \left[S\left(\frac{x - x_{start}}{\Delta_{rise}}\right) - S\left(\frac{x - x_{end}}{\Delta_{fall}} + 1\right)\right], \tag{12}$$

where λ_{max} is the maximum strength of the damping, x_{start} and x_{end} are the start and end of the fringe region, respectively, and Δ_{rise} and Δ_{fall} are the rise and fall distance of the damping function. $S(\xi)$ is a smooth step function with

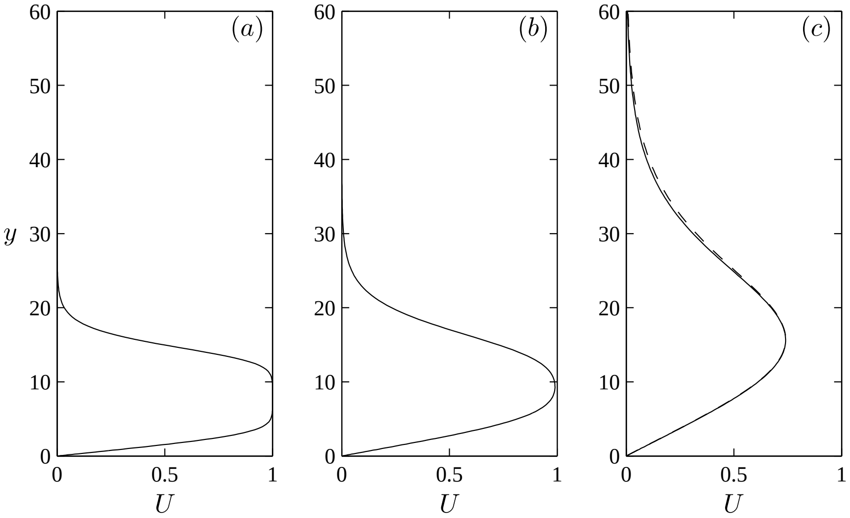

FIGURE 3. Streamwise development of the Blasius wall jet calculated with the boundary-layer equations. (*a*) $x = 1$, (*b*) 3.14, (*c*) 20. Far downstream, the solution approaches a Glauert similarity solution evolving from a different virtual origin. The Glauert solution (— — —) is shown for comparison in (*c*).

continuous derivatives of all orders defined by

$$S(\xi) = \begin{cases} 0, & \xi \leqslant 0, \\ 1\Big/\left[1 + \exp\left(\dfrac{1}{\xi - 1} + \dfrac{1}{\xi}\right)\right], & 0 < \xi < 1, \\ 1, & \xi \geqslant 1. \end{cases} \tag{13}$$

This method damps disturbances flowing out of the physical region and smoothly transforms the flow to the desired inflow state, with a minimal upstream influence (Nordström *et al.* 1999).

At the wall, a no-slip boundary condition is set and at the free-stream position y_{max}, the generalized boundary condition is applied in Fourier space with different coefficients for each wavenumber. It is non-local in physical space and takes the form

$$\frac{\partial \hat{\boldsymbol{u}}}{\partial y} + k\hat{\boldsymbol{u}} = \frac{\partial \hat{\boldsymbol{v}}_0}{\partial y} + k\hat{\boldsymbol{v}}_0, \tag{14}$$

where $\hat{\boldsymbol{u}}$ is the Fourier transform of $\boldsymbol{u}$. Here, $\boldsymbol{v}_0$ denotes the blended wall-jet solution of the boundary-layer equations taken as the initial condition and $\hat{\boldsymbol{v}}_0$ its Fourier transform. In the spanwise direction, periodic boundary condition is set.

3.3.2. *Disturbance generation and numerical parameters*

The present numerical implementation provides several possibilities for disturbance generation. Disturbances can be included in the desired solution $\boldsymbol{v}$, thereby forcing them in the fringe region, by a body force $\boldsymbol{g}$ and by blowing and suction at the wall through non-homogeneous boundary conditions.

To study the instability and interaction of time-periodic two-dimensional waves $\boldsymbol{v}_w$ and stationary longitudinal streaks $\boldsymbol{v}_s$, the velocity fields are added to the blended Blasius wall-jet solution $\boldsymbol{v}_0$ to give a forcing vector of the form $\boldsymbol{v} = \boldsymbol{v}_0 + \boldsymbol{v}_w + \boldsymbol{v}_s$. The waves and streaks can then be forced in the fringe region. The two-dimensional waves $\boldsymbol{v}_w = (u, v, 0)$ are taken from solutions of the parabolized stability equations (2) with $\beta = 0$. The vector, which can be derived from (1) takes the form

$$\boldsymbol{v}_w = \boldsymbol{f}_c \cos\omega t + \boldsymbol{f}_s \sin\omega t, \tag{15}$$

where

$$\boldsymbol{f}_c = (\hat{\boldsymbol{f}}_\mathrm{r}\cos a_\mathrm{r} - \hat{\boldsymbol{f}}_\mathrm{i}\sin a_\mathrm{r})\mathrm{e}^{-a_\mathrm{i}}, \quad \boldsymbol{f}_s = (\hat{\boldsymbol{f}}_\mathrm{r}\sin a_\mathrm{r} + \hat{\boldsymbol{f}}_\mathrm{i}\cos a_\mathrm{r})\mathrm{e}^{-a_\mathrm{i}} \tag{16}$$

and

$$a_\mathrm{r} = \int_{x_0}^{x} \alpha_\mathrm{r}\,\mathrm{d}x, \quad a_\mathrm{i} = \int_{x_0}^{x} \alpha_\mathrm{i}\,\mathrm{d}x, \tag{17}$$

where the subscripts $_\mathrm{r}$ and $_\mathrm{i}$ denote real and imaginary part, respectively. The spanwise periodic streaks are taken from optimized solutions of the stability equations (2) with $\omega = 0$ and $\alpha = 0$. The forcing vector takes the form

$$\boldsymbol{v}_s = (\hat{u}_\mathrm{r}\cos\beta z,\ \hat{v}_\mathrm{r}\cos\beta z,\ -\hat{w}_\mathrm{i}\sin\beta z). \tag{18}$$

The size of the computational box used for the simulations presented in this paper is $(xl \times yl \times zl) = (3.09 \times 206 \times 29.8)$. The width of the box is set to fit one spanwise wavelength of the forced streaks. The Reynolds number at the initial location of the box where $x = 1$ is $Re_\delta = 173$. The resolution is $(nx \times ny \times nz) = (540 \times 541 \times 64)$, which is about 18.7 million points. Dealiasing is activated in the streamwise and spanwise directions. This increases the computational resolution in the simulation with a factor of 2.25 (1.5 in each direction). A shared memory parallelization is implemented in the numerical code. The current study uses 16 nodes, each with two processors. With a wall clock time of 60 h, a typical simulation calculates about one time unit. The parameters for the fringe region are $x_{start} = 3.49$, $x_{end} = 4.09$, $\Delta_{rise} = 0.199$, $\Delta_{fall} = 0.0996$ and $\lambda_{max} = 1.0$.

The waves and streaks are forced in the fringe region in a similar manner as done by Brandt & Henningson (2002), who made use of the same spectral code to study the transition of streamwise streaks in the Blasius boundary layer. The forcing is turned on smoothly in both space and time. The steamwise amplitudes of the waves and streaks are prescribed at the end of the fringe region to 0.001 and 0.03, respectively.

When only two-dimensional waves are forced in the fringe region, random noise is added to the initial field in order to introduce three-dimensionality to the flow. The noise is in the form of Stokes modes, i.e. eigenmodes of the flow operator without the convective term. These modes fulfil the equation of continuity and the boundary condition of vanishing velocity at the wall. While the simulation is running, no more forcing of three-dimensional noise is required since a small level of noise passes through the fringe region. However, the fringe region damps incoming disturbances to an energy level below about 10^{-7}.

4. Results

4.1. *Matching the base flow*

Most of the numerical studies of wall jets have concerned the similarity solution of Glauert (1956), which is an asymptotic solution. However, a consideration of the near field of the wall jet in this investigation shows that the flow has not achieved the self-similar Glauert profile. To investigate the flow close to the slot at a rather high Reynolds number, it is necessary to find another base flow more suitable to match with the experiment.

Consider a top-hat profile through a slot with height b located at $x = 0$, see figure 2. Immediately downstream of the slot, a boundary layer develops at the wall and a shear layer develops in the upper part of the top-hat profile, independently of each other. Further downstream, the boundary layer and the shear layer begin interacting and the local maximum velocity slows down. Our solution consists of a coupling of the Blasius boundary layer and the Blasius shear layer as an initial condition to the boundary-layer equations. The two solutions, which are both similarity solutions to the Blasius equation with different boundary conditions, are discussed in Schlichting (1979). In the boundary-layer scalings, Blasius similarity equation reads

$$2f''' + ff'' = 0, \tag{19}$$

where $f(\eta)$ is the non-dimensional streamfunction and the prime denotes derivatives with respect to the similarity variable η. The base flow can then be written

$$U = f', \quad V = \tfrac{1}{2}(\eta f' - f). \tag{20}$$

For the boundary layer, the similarity variable η_b relates to the non-dimensional coordinates as $y = \sqrt{x}\eta_b$ and the boundary conditions read

$$\eta_b = 0: \quad f = 0, \quad f' = 0; \qquad \eta_b \to +\infty: \quad f' = 1. \tag{21}$$

The shear layer has the displaced similarity variable $\eta_s = \eta_b - b$ and is subject to the boundary conditions

$$\eta_s \to -\infty: \quad f = \eta_s - 2V_b, \quad f' = 1; \qquad \eta_s \to +\infty: \quad f' = 0, \tag{22}$$

where V_b denotes the normal component of the free-stream velocity taken from the boundary-layer similarity solution, to fulfil continuity in the normal velocity throughout the wall jet. The two similarity solutions are connected to each other at the location $x = 1$ and form the boundary-layer and shear-layer regions in the Blasius wall jet. The downstream development is computed with the boundary-layer equations. Figure 3 shows the Blasius wall jet and

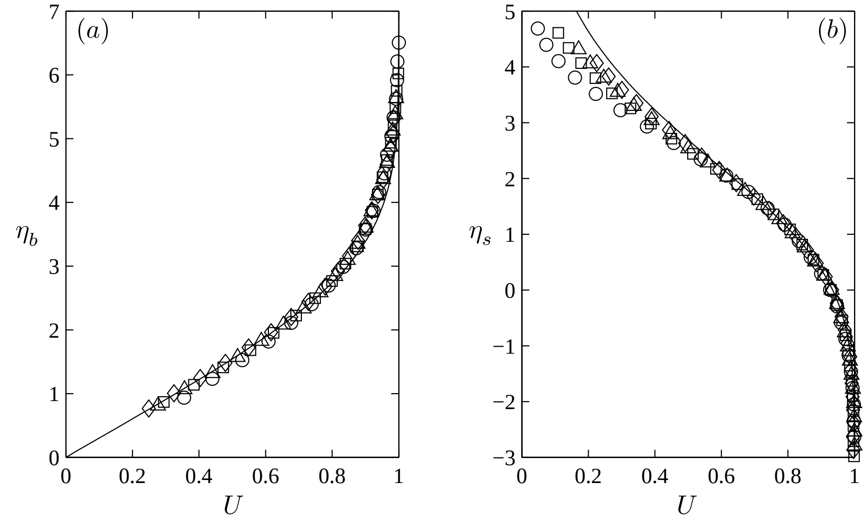

FIGURE 4. Comparison of the computed base flow (—) for $Re_\delta = 173$ with experimental results at 1 mm (○), 6 mm (□), 11 mm (△) and 16 mm (◇) downstream of the nozzle outlet. The experimental data are scaled with the local boundary-layer parameter δ and local maximum velocity U_m and fitted to the computed similarity solutions with $l = 29$ mm and $b^* = 2.06$ mm. (*a*) Boundary-layer region. (*b*) Shear-layer region.

its streamwise development calculated with the boundary-layer equations. The location in figure 3(*a*) corresponds to the initial condition at $x = 1$. Figure 3(*b*) shows the location $x = 3.14$, where the interaction of the boundary layer and the shear layer has just begun and the maximum velocity is $U_m = 0.99U_0$. Far downstream at the location $x = 20$ (figure 3*c*), the flow approaches the Glauert (1956) solution shown as the dashed line.

In the experiment, thin boundary layers are already formed in the nozzle. Therefore, the virtual slot is placed a distance l upstream of the nozzle outlet with a virtual slot height b^*, different from the height of the experimental nozzle opening. In order to match the theoretical base flow to the experiment, l, which is taken as the streamwise scale, and b^* have to be chosen. To do so, the boundary-layer and shear-layer regions of the measured wall jet are scaled with local scalings and compared to the Blasius boundary and shear-layer similarity solutions, see figure 4. The experimental data are taken from 1 mm, 6 mm, 11 mm and 16 mm downstream of the nozzle outlet. The streamwise locations and their corresponding dimensional distances downstream of the experimental nozzle outlet used for the measurements are summarized in table 1. The maximum outlet velocity is $U_0 = 15.4\,\mathrm{m\,s^{-1}}$, corresponding to the Reynolds number $Re_\delta = 173$. The best matching is achieved for $l = 29$ mm and $b^* = 2.06$ mm

x:	1.0	1.03	1.21	1.38	1.55	2.0	3.14	20.0
$x^* - l$ (mm):	0	1	6	11	16	29	62	551

Table 1. Streamwise locations with the corresponding dimensional distances downstream of the experimental nozzle outlet.

corresponding to the non-dimensional virtual slot height $b = 12.3$. The normal scale is $\delta = \sqrt{\nu l/U_0} = 0.168\,\text{mm}$.

The Blasius wall jet can be made independent of the slot height b, downstream of the point of interaction of the shear layer and the boundary layer, by introducing the coordinates

$$\zeta = \frac{y}{b}, \quad \xi = \frac{x}{b^2}. \tag{23}$$

If we rescale the downstream distance measured from the experimental nozzle opening with the virtual slot height, locations downstream of the point of interaction may be written

$$\frac{x^* - l}{b^*} = Re_\delta \left(b\xi - \frac{1}{b} \right), \tag{24}$$

where the star denotes dimensional variables. Inserting the value of the slot height used for our Blasius wall jet, the value of the right-hand side of (24) is $1.55 Re_\delta$ at the location shown in figure 3(c). Hence, given the top-hat profile blowing out from a slot, the Glauert wall jet is reachable only many slot height distances downstream of the slot in the case when the flow Reynolds number is high. As the flow Reynolds number decreases, the distance required to approach this solution also decreases. However, given a different initial condition at the slot such as a plane Poiseuille flow, the Glauert wall jet may be reached earlier. Bajura & Szewczyk (1970) experimentally obtain a very good agreement to the Glauert wall jet 18 slot heights downstream of the nozzle outlet for a jet-exit Reynolds number of 377 based on the slot height. Similar results were obtained by Cohen *et al.* (1992) 30 slot heights downstream of the nozzle for a Reynolds number of 725. For comparison, the Reynolds number $Re_\delta = 173$ in this investigation corresponds to 2120 based on the virtual slot height b^*, and 3080 based on the height of the experimental nozzle opening.

It can be seen in figure 4 that the agreement between the experiment and the theory in the lower part of the boundary-layer region, shown in figure 4(a), and in particular the upper part of the shear-layer region, shown in figure 4(b), is not perfect. The experimental data are however, approaching the theoretical solution further downstream. A slight difference in the upper part of the boundary-layer region remains as the flow evolves downstream. The agreement between the experiment and the theory near the jet core in the shear-layer region is excellent. The main reason for the disagreement in the upper part of the wall jet is the influence of the nozzle. A jump of the boundary condition

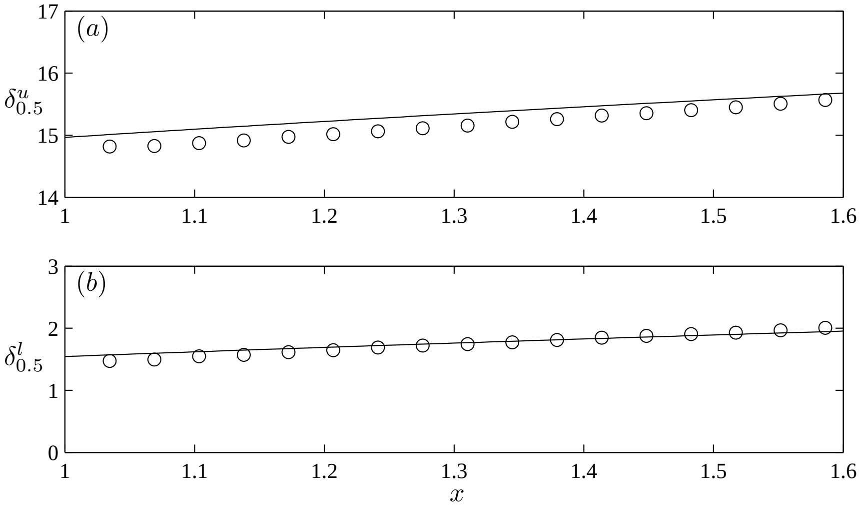

FIGURE 5. Comparison of the computed base flow (—) for $Re_\delta = 173$ with experimental results (○). The graphs show (*a*) the upper and (*b*) lower jet half-widths $\delta^u_{0.5}$ and $\delta^l_{0.5}$, respectively.

occurs on the top lip of the nozzle as the flow leaves and a kink in the experimental velocity data can be observed. With increased downstream distance, the influence of the nozzle disappears and the agreement becomes better.

Figures 5(*a*) and 5(*b*) show the streamwise development of the upper and lower jet half-widths $\delta^u_{0.5}$ and $\delta^l_{0.5}$, respectively, which are the distances from the wall where the velocity reaches half the local maximum velocity. The experimental data are measured with 1 mm steps to 17 mm downstream of the nozzle outlet. The whole scaled flow is shown in figure 6 for four downstream locations $x = 1.03, 1.21, 1.38, 1.55$ and the measured upper and lower jet half-widths are indicated with crosses.

4.2. *Linear stability analysis*

In this section, the stability of the computed base flow at $Re_\delta = 173$ is investigated by means of the linear parabolized stability equations and the results are compared with the measurements. The instability with respect to two-dimensional eigenmodes and non-modal streaks is investigated.

4.2.1. *Two-dimensional waves*

The natural spectra of the streamwise velocity component measured in the position of maximum disturbance in the wall-normal direction is shown, at $x = 1.38$ (− − −) and $x = 1.55$ (—), in figure 7(*a*). The reduced frequency is defined as $F = 10^6\omega/Re_l$. It is clear that under natural conditions, the

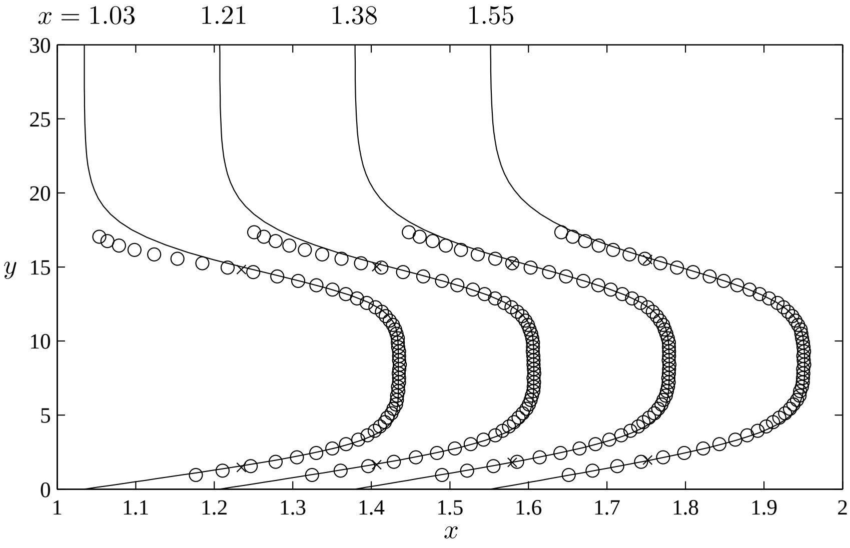

FIGURE 6. Comparison of the computed base flow (—) for $Re_\delta = 173$ with experimental results (○) at 1 mm, 6 mm, 11 mm and 16 mm downstream of the nozzle outlet (the non-dimensional locations are indicated in the figure). ×, upper and lower jet half-widths.

wall jet operates in unforced mode and a broad band of frequencies amplifies. The root mean square of the broadband disturbance amplitude at $x = 1.55$ is approximately 0.5 % of the jet exit velocity. This allows us to consider the flow to be laminar down to this location under natural conditions. Figure 7(b) shows the computed physical growth rate, defined as

$$\sigma(x) = \frac{1}{Re_\delta}\frac{1}{\sqrt{\hat{E}}}\frac{\partial\sqrt{\hat{E}}}{\partial x} - \alpha_\mathrm{i}, \tag{25}$$

versus the reduced frequency. It is clearly visible that in the stability calculations, as well as in the experiment, the most amplified frequency decreases with increased streamwise location. The most amplified frequency of the Blasius shear layer predicted with inviscid stability theory by Monkewitz & Huerre (1982) is about 480, which is very close to the peak observed for the location $x = 1$ in figure 7(b). This suggests that the wall jet operates in the shear-layer mode.

Subsequently, the flow is artificially forced in the experiment and characteristics of the instability waves under controlled conditions are studied. The frequency of the artificial disturbances is 1221 Hz corresponding to $\omega = 14.4$, or $F = 482$. This is close to the natural dominating flow frequency, leading to breakdown. In figure 7(c), the forced spectrum, for a relatively large forcing

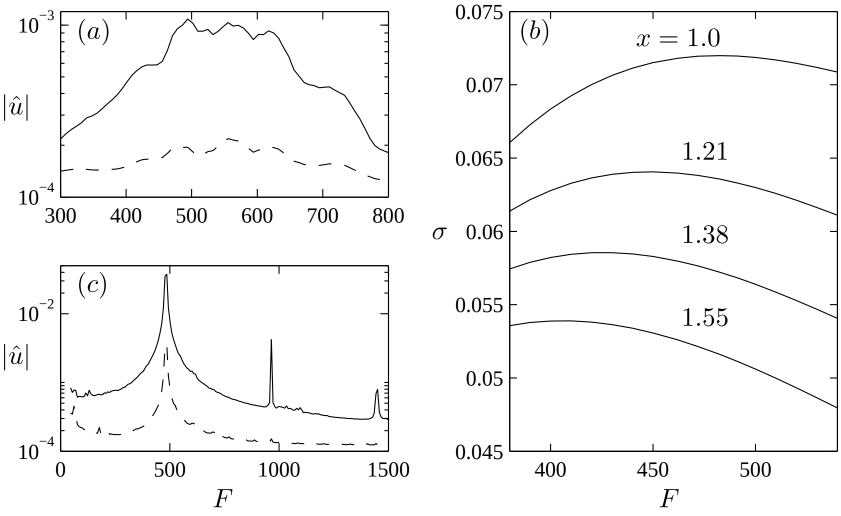

FIGURE 7. Frequency spectra at $x = 1.38$ (– – –) and $x = 1.55$ (—) for natural case (*a*) and forced by a loudspeaker at 1221 Hz ($F = 482$) with amplitude 4 % at $x = 1.55$ (*c*). (*b*) Computed growth rates σ for $Re_\delta = 173$ at different streamwise locations corresponding to 0 mm, 6 mm, 11 mm and 16 mm downstream of the nozzle outlet (the non-dimensional locations are indicated in the figure).

amplitude (4 % at $x = 1.55$) is shown for the same streamwise locations as the natural spectrum. At the location $x = 1.55$, nonlinear effects start to be apparent and peaks of higher harmonics of the main frequency can be seen in the spectra. The first superharmonic has about 10 % of the main harmonic amplitude. The forcing of the flow leads to a strong coherence of the disturbance around the excitation frequency, as can also be seen for free shear layers.

Since the Blasius wall jet is a composition of both a boundary layer and a free shear layer, we should expect the possibility of two co-existing unstable eigenmodes, one associated with the viscous instability of the boundary layer in the inner region and the other with the inviscid instability of the shear layer in the outer region. Mele *et al.* (1986), among others, elaborated the role of these two instability modes of the Glauert wall jet. For the low Reynolds number specified in the current investigation, the PSE-approach does not detect the inner mode, instead it converges to the outer mode. In order to study the inner mode, the Orr–Sommerfeld equation is solved. Thereby, a comparison of the PSE-technique with the parallel theory can also be done. Such comparisons have been made by Bertolotti *et al.* (1992) for the Blasius boundary layer.

Figure 8 shows the streamwise component of Orr–Sommerfeld eigenfunctions at $x = 1$ for $F = 482$ and $Re_\delta = 173$. The inner mode is shown as the

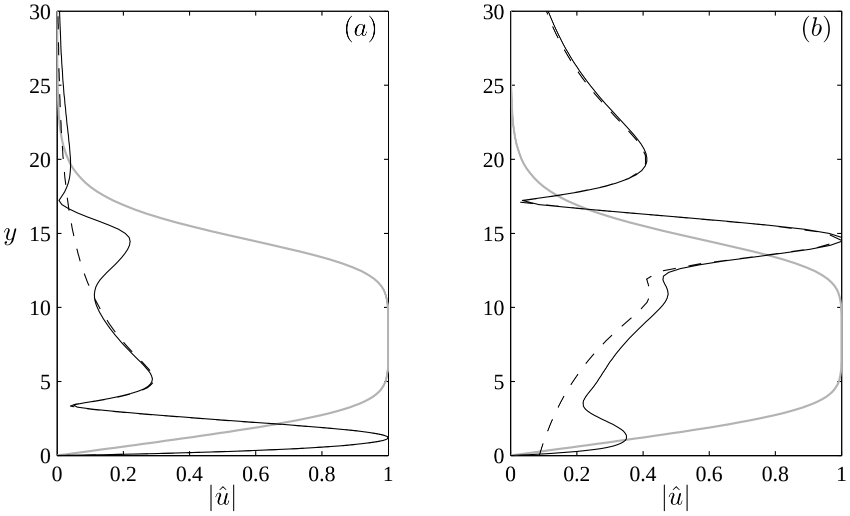

FIGURE 8. Streamwise component of Orr–Sommerfeld eigenfunctions at $x = 1$ for $F = 482$ and $Re_\delta = 173$. The grey line shows the Blasius wall jet. (*a*) Inner mode (—) compared with the corresponding mode of the Blasius boundary layer (– – –). (*b*) Outer mode (—) compared with the corresponding mode of the Blasius shear layer (– – –).

solid line in figure 8(*a*) while the dashed line shows the corresponding mode of the Blasius boundary layer. As expected, the agreement between the profiles of the two modes is perfect in the inner region close to the wall, whereas two additional small peaks persist in the outer region of the wall-jet mode. In figure 8(*b*), the comparison between the outer mode and the corresponding mode of the Blasius shear layer is shown. Here, as expected, the profiles of the modes agree perfectly in the outer region, whereas the wall-jet mode has a small peak in the inner region. However, the agreement between the inner and outer modes of the Blasius wall jet with the corresponding modes of the Blasius boundary layer and Blasius shear layer, respectively, decreases further downstream as the boundary-layer region and the shear-layer region of the Blasius wall jet begin to interact.

At the given Reynolds number and frequency, the outer mode is the only unstable mode of the Blasius wall jet. The critical Reynolds number for the Blasius wall jet is 2.15, this is when the outer mode becomes unstable at $F = 23\,000$. The corresponding critical Reynolds number for the Blasius shear layer is zero. The inner mode becomes unstable at a significantly higher Reynolds number of 272 at $F = 260$. The corresponding critical Reynolds number for the Blasius boundary layer is 302 at $F = 230$. As a comparison, it can be

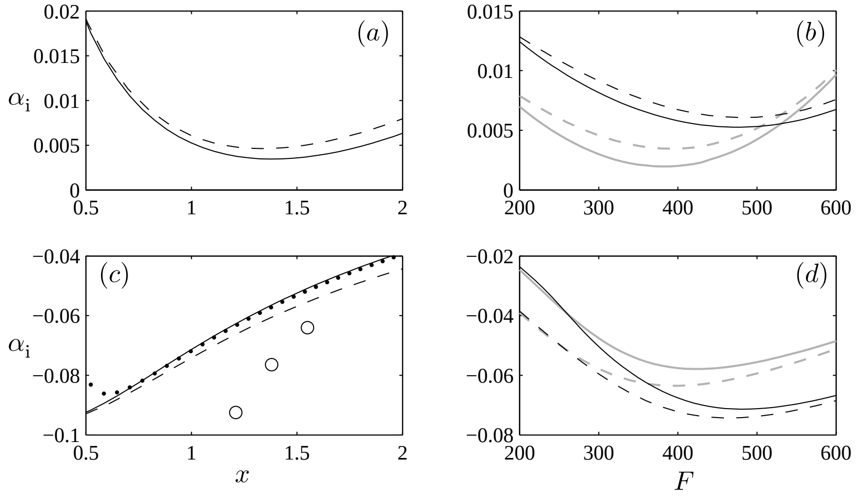

FIGURE 9. Imaginary part of Orr–Sommerfeld eigenvalues for $Re_\delta = 173$. (a, c) Streamwise dependency for $F = 482$. The dotted line in (c) shows a comparison with the PSE-solution. A comparison with the Orr–Sommerfeld solution of the interpolated experimental base flow is also made (○) for $x = 1.21, 1.38, 1.55$. (b, d) Frequency dependency at $x = 1$ (black lines) and $x = 1.38$ (grey lines). (a, b) Inner mode (—) compared with the corresponding mode of the Blasius boundary layer (– – –). (c, d) Outer mode (—) compared with the corresponding mode of the Blasius shear layer (– – –).

mentioned that the critical Reynolds number for the Glauert wall jet is 13.6 at $F = 9600$.

Figure 9 shows the imaginary part of Orr–Sommerfeld eigenvalues for $Re_\delta = 173$. The inner and outer modes of the Blasius wall jet are shown as solid lines while dashed lines show the corresponding modes of the Blasius boundary layer and the Blasius shear layer, respectively. The streamwise dependency for $F = 482$ is shown in figure 9(a, c). The inner mode of the Blasius wall jet, shown in figure 9(a), is stable, but not as stable as the corresponding mode of the Blasius boundary layer. The outer mode, shown in figure 9(c), is unstable, but the corresponding mode of the Blasius shear layer is slightly more unstable. In both cases, the difference increases downstream. In figure 9(c), a comparison with the PSE-solution is made. The dots represent each streamwise step of the computation, which is seen to converge at about $x = 0.7$. Downstream of this location the agreement with parallel theory is excellent, indicating that non-parallel effects are small. The local theory seems to slightly under predict the amplification rate. In order to elaborate the effect of the base-flow disagreement on the stability characteristics, the Orr–Sommerfeld equation is solved for the

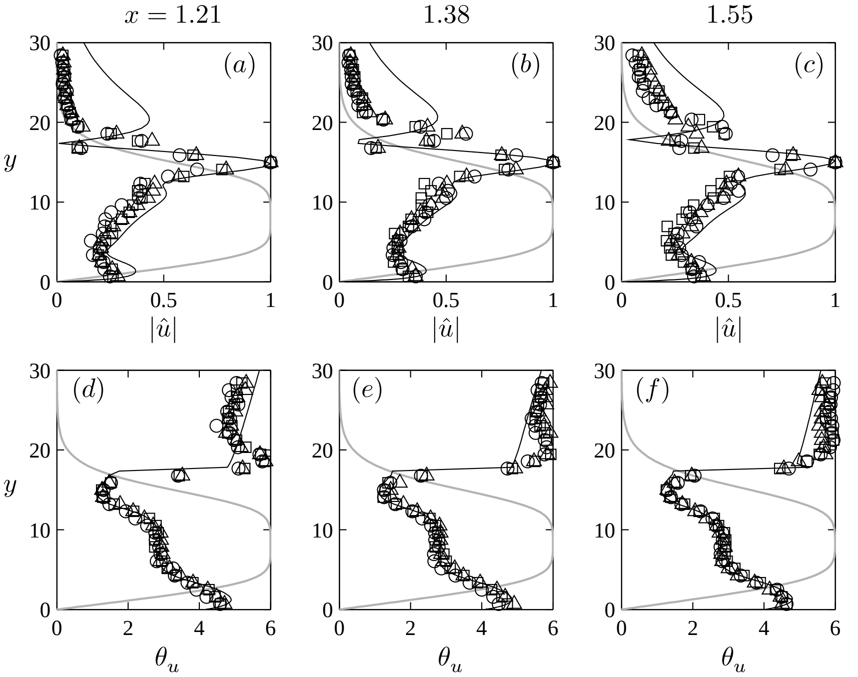

FIGURE 10. Comparison of the computed (—) u-velocity amplitude, normalized with its maximum value, and phase distribution θ_u, for $Re_\delta = 173$ and $F = 482$ with experimental results at $x = 1.21, 1.38, 1.55$. The disturbances are triggered by a loudspeaker at 1221 Hz and have the amplitudes 0.3 % (○), 1.1 % (□) and 1.7 % (△) at $x = 1.55$. The grey line shows the computed Blasius wall jet.

experimental base flow. First, the experimental base flow is interpolated and extrapolated with continuous first and second derivatives. The imaginary part of the streamwise wavenumber at $x = 1.21, 1.38, 1.55$, from these calculations, is shown as the circles in figure 9(*c*). It reveals a large difference in amplification rate which is due to the disagreement between the shear-layer regions in the measured and the theoretical base flows. The frequency dependency at $x = 1$ (black lines) and $x = 1.38$ (grey lines) of the inner and outer modes is shown in figure 9(*b*) and 9(*d*), respectively.

Figure 10 shows the amplitude and phase distribution at three downstream locations $x = 1.21, 1.38, 1.55$ for the three different forcing amplitudes 0.3 % (○), 1.1 % (□) and 1.7 % (△) compared with the computed PSE-results (—). The three experimental amplitude values are measured at the streamwise location $x = 1.55$. It can be noted that the agreement between the experiment and the linear stability computation is acceptable apart from the upper part of the shear-layer region. The deviation there is most probably because the waves in

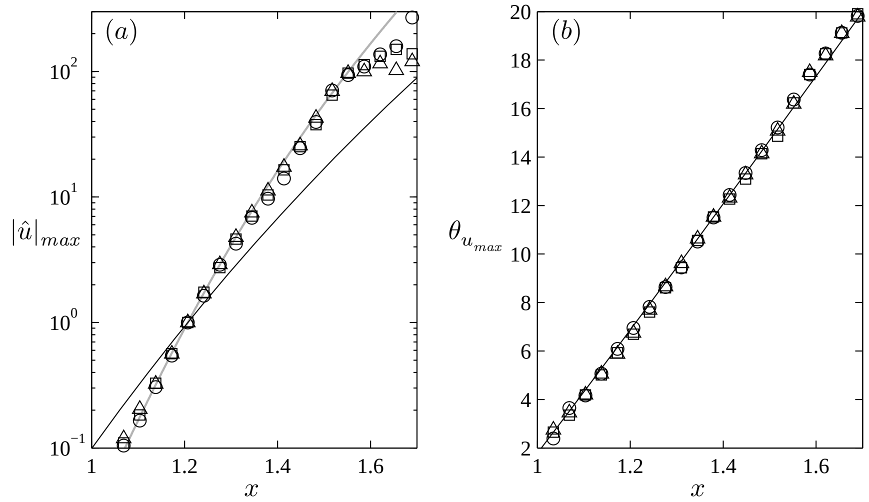

FIGURE 11. Comparison of the computed (—) maximum u-velocity amplitude (a) and phase (b) amplification for $Re_\delta = 173$ and $F = 482$ with experimental results. The disturbances are triggered by a loudspeaker at 1221 Hz and have the amplitudes 0.3 % (○), 1.1 % (□) and 1.7 % (△) at $x = 1.55$. The grey line shows the amplification calculated with the Orr–Sommerfeld equation applied to the interpolated experimental base flow.

the experiment are not fully developed eigenmodes this close to the nozzle outlet. Solving the Orr–Sommerfeld equations for the interpolated experimental base flow reveals that the difference in the base flow does not affect the shape of the eigenmodes much. However, the agreement between the outer part of the measured and computed amplitude distributions improves downstream. The disturbance has a typical shape and the peak in the shear-layer region is in antiphase to the peak near the wall in the boundary-layer region.

The downstream development of the disturbances is demonstrated in figure 11(a) and 11(b), where the maximum u-velocity amplitude and phase, respectively, are shown versus the streamwise coordinate. The three cases of forcing are compared with the computation and the same symbols are used as in figure 10. The demonstrated amplitude data is normalized with the amplitude at the location $x = 1.21$, and the disturbance phase θ_u is shown in radians. The agreement in the results between the different forcing amplitudes in figures 10 and 11 indicates the linearity of the disturbance. Both the disturbance distribution and the amplification agree very well for the different forcing amplitudes. An indication of the nonlinear effects appear just after the location $x = 1.55$ where it shows up as lower amplification for the larger forcing amplitudes. The agreement of the amplification between the measured data and the PSE-results showed as the black solid line in figure 11(a) is not satisfactory. This difference of the slopes of the amplitude curves implies a 40 % higher growth rate in the experiment, approximately. To investigate how the base flow difference affects the amplification, the Orr–Sommerfeld equation is applied to the interpolated experimental base flow. The amplification, interpolated from the eigenvalues at $x = 1.03, 1.21, 1.38, 1.55$, is shown as the grey line in figure 11(a) and the agreement to the measured data is very good. This clearly shows that the difference between the computed and experimental base flow is responsible for the disagreement in amplification between the measured data and the stability calculations.

4.2.2. *Stationary longitudinal streaks*

The exponentially growing disturbances studied in the previous section are the dominating instabilities of flows having a point of inflection. This is true for wall jets as well as for free shear layers operated in a low-disturbance environment. On the other hand, numerous studies of wall-bounded shear flows show that three-dimensional disturbances of a different type may dominate in the breakdown process, especially when the flow is highly disturbed, see e.g. Westin *et al.* (1994). The dominating role of the longitudinal disturbances has been clarified recently by Balaras *et al.* (2001) for highly disturbed free shear layers. As was mentioned in § 1, intermediate states when both two- and three-dimensional disturbances exist are also possible for free shear layers. A similar behaviour is expected for wall jets. In the current experiment, streaks appear naturally from existing irregularities and amplification of vorticity in the contraction. Since such longitudinal structures are also likely to exist in various applications, this is a motivation to study the growth of streamwise streaks.

In the experiment, stationary longitudinal streaks are introduced in the flow by periodically distributed roughness elements that are positioned on the top lip of the orifice. In separate runs, five spanwise scales are generated corresponding to β from 0.175 to 0.574 by the roughness elements of corresponding width from 3 to 1 mm. In figure 12(a), the spectral decomposition of the maximum streak amplitude for the three largest spanwise scales, $\beta = 0.264$ (○), $\beta = 0.218$ (□) and $\beta = 0.176$ (△), at the streamwise location $x = 1.55$, is shown. The other two smallest scales are decaying in the experiment. One of the introduced scales, $\beta = 0.218$, leads to the disturbance with the largest amplitude and is optimal in this sense. Streaks of approximately this scale are also visible for roughness-unforced flow in the nonlinear stage (see figure 14). These streaks are, however, not stationary, contrary to the forced streaks, they move slowly back and forth.

An idea of how the steady perturbations are selected in the wall-jet flow is directly obtained by considering a plot of the maximized disturbance growth G_{max} versus the streamwise wavenumber. In figure 12(b), the computed optimal growth for $\omega = 0$, $x_0 = 0.403$ and $x_1 = 1.55$ is shown as a function of

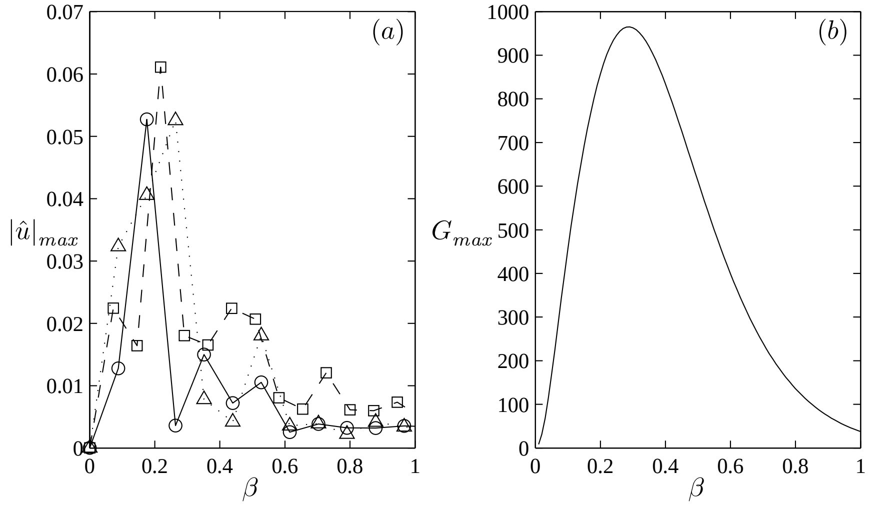

FIGURE 12. (*a*) FFT of three spanwise wavelengths behind arrays of evenly distributed roughness elements with width (half wavelength) 3 mm (○), 2.5 mm (□) and 2 mm (△) from measured streamwise disturbances at $x_1 = 1.55$. (*b*) Computed optimal growth for $\omega = 0$, $x_0 = 0.403$ and $x_1 = 1.55$. $Re_l = 173^2$ is used as the scale factor.

the spanwise wavenumber. The spanwise scale that grows the most is approximately $\beta = 0.29$. In calculations with fixed x_1, the optimal spanwise wavenumber decreases with decreased x_0. However, for practical reasons, to obtain an initial disturbance in the subsequently described DNS, the initial position is set equal to the starting position of the fringe region. From the comparison of the computed and experimental optimal spanwise scales in figure 12, it can be observed that the computed scale is somewhat smaller, however, it is close to that one observed in the experiment.

The optimal disturbance consists of streamwise vortices developing into streamwise streaks. The resulting disturbance from the computation at $x = 1$, for $\beta = 0.211$, $\omega = 0$, $x_0 = 0.403$ and $x_1 = 1.55$, is shown to the left-hand side in figure 13, where one spanwise wavelength of the disturbance is depicted. In figure 13(*a*), the cross-flow velocity components are represented with arrows, and in figure 13(*b*) the streamwise velocity is shown as contours. Positive values of disturbance velocity are shown by solid lines and the dashed lines represent negative values. At the spanwise location $z = 0$, high-momentum fluid is moved up from the jet core, producing a high-velocity streak in the shear-layer region. An opposite motion is observed at the edges of the plot, half a wavelength away, where low-momentum fluid is moved down from the upper velocity field and low-velocity streaks are formed in the shear-layer region. Additionally, in the boundary-layer region, a weak low-velocity streak is formed below the

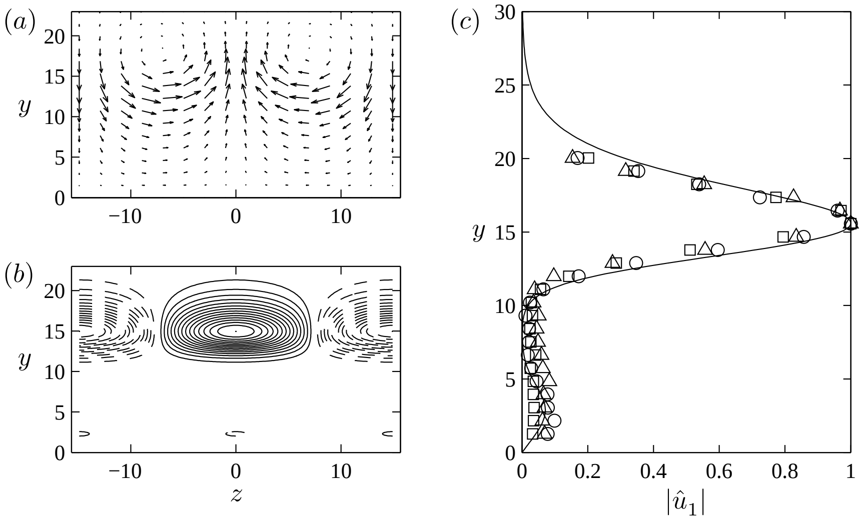

FIGURE 13. Downstream response of the computed optimal disturbance for $\beta = 0.211$, $\omega = 0$, $x_0 = 0.403$ and $x_1 = 1.55$. (a, b) The cross-flow plane at $x = 1$. Arrows represent cross-flow velocity components (a) and contours show constant positive (—) and negative (− − −) streamwise velocity (b). (c) Computed final streamwise amplitude velocity distribution (—), normalized with its maximum value, compared with experimental results for $\beta = 0.176$ (○), $\beta = 0.218$ (□) and $\beta = 0.264$ (△).

high-velocity streak at $z = 0$, since the upward motion of fluid there carries low-momentum fluid from the wall region. In a similar way, weak high-velocity streaks are formed in the boundary-layer region on the sides. Thus, the more complicated overall character of the disturbance as compared to, for example, the flat-plate boundary layer is explained by rather simple mechanisms, which in general are similar in the single-shear flow of the flat plate and in the wall jet studied here. In figure 13(c), the computed normalized streamwise amplitude distribution at $x_1 = 1.55$ is compared with the measured results. The downstream response at the location x_1 is insensitive to the choice of spanwise wavenumber and initial position. The similarity between the amplitude functions for the three largest scales in the experiment is also evident in figure 13(c). Since the initial condition in the experiment is not the optimal one, we cannot expect to find the calculated disturbance amplitude. However, as long as the initial streamwise vortex in the experiment has a projection on the optimal disturbance, we can expect the final computed velocity disturbance to agree with the measured one, as is shown in figure 13(c). This agreement and the fact that the computation contains an optimization procedure while the experiment does not, indicate that a fundamental mode is triggered in the flow. This has also been observed by, for example, Andersson *et al.* (1999) and Westin *et al.* (1994) in the flat-plate boundary layer. These non-modal growth mechanisms are referred to as algebraic growth. In the present work, disturbances are triggered by the surface roughness, however, free-stream turbulence is also a possible triggering mechanism, see, for example, Westin *et al.* (1994) for the flat-plate boundary layer results.

4.3. *Towards transition to turbulence*

In this section, the transition process of the wall jet is studied. Two-dimensional eigenmodes with the fundamental frequency and non-modal streaks are forced into the flow.

4.3.1. *Overview of the transition process*

The importance of the three-dimensional effects during flow breakdown is clearly demonstrated by the performed flow visualizations, which are shown in figure 14. Two-dimensional waves are excited by the loudspeaker and can be observed to develop parallel to the nozzle edge. A laser sheet is pulsing, synchronized with the wave frequency while smoke is provided into the inlet of the facility driving fan. With this technique, the flow modulation can be visualized only in the top shear layer, where the difference in the smoke concentration is clear. No special forcing is applied to generate three-dimensional disturbances, as they appear naturally from existing irregularities. Nevertheless, well-defined and nearly uniform streamwise vortices and streaks are visibly, forming in the flow. As can be seen in figure 14(a), initially the waves are dominating, while the streaks are rather weak. Further downstream, the streaky structures become dominating. In figure 14(b), the braid region of the wave is shown, which corresponds approximately to the mid streamwise location in figure 14(a). In the braids, the streaks are well pronounced and they attain a typical mushroom shape. Also, moving the visualization plane further from the wall, regions can be reached where streak tips exist, while waves do not. In fact, the current visualization demonstrates a very similar phenomenon as was observed by Bernal & Roshko (1986) and Lasheras *et al.* (1986) in free shear layers. The streaks in the present case are generated by irregularities in the facility. It is clear that disturbances associated with the streaks are amplified from their upstream origin as the flow develops.

4.3.2. *Spectral analysis*

In the previous section, we saw that the role of the initial conditions for the development of the wall jet is essential. To investigate the process of the breakdown in this flow carefully and understand the nonlinear interactions involved, a direct numerical simulation is necessary. A numerical study conducted in a highly controlled environment is free from various uncontrollable parameters, which make the numerical results more straightforward to interpret than these

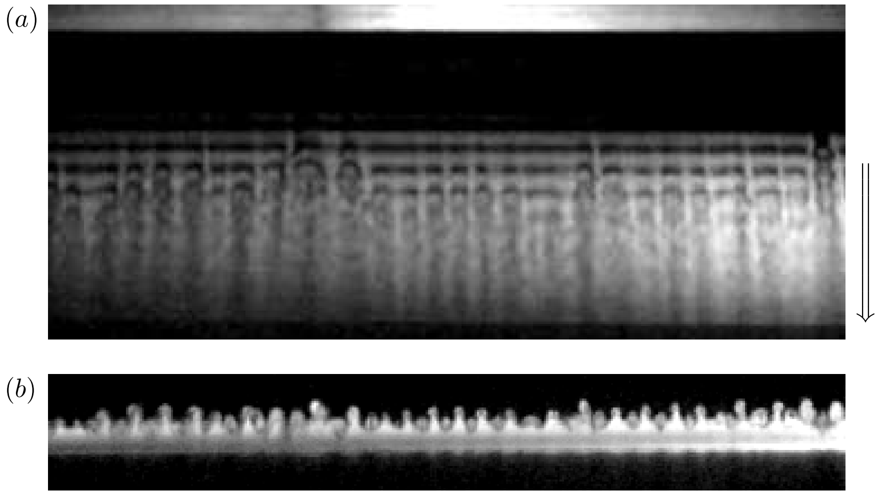

Figure 14. Visualization of the nonlinear structures in the wall jet. (*a*) Light sheet is placed parallel to the wall at about 5 mm from it ($y = 30$). The flow direction is down. (*b*) Light sheet is perpendicular to the flow and placed at about 40 mm ($x = 2.3$) downstream of the nozzle outlet.

obtained from the experiment. Two instability modes, the two-dimensional waves and the streamwise streaks are observed to trigger the breakdown of the wall jet to turbulence. These disturbances are excited in the DNS in a controlled manner, as described in § 3.3.2, and the forcing functions are taken from the previously obtained linear stability calculations (see figures 10 and 13). The amplitudes of the waves and streaks are prescribed in the beginning of the computational box to 0.1 % and 3 % of the wall-jet core velocity, respectively. The amplitudes are chosen to obtain a similar transition scenario as in the experimental wall jet seen in figure 14.

The streamwise development of the initially generated modes and the thereafter exited modes of nonlinear interaction can be seen by looking at the development of the Fourier components shown in figure 15. For the Fourier transform, 16 evenly distributed velocity fields in time, within two fundamental time periods, starting from $t = 10.95$ are used. Eight modes are used in the spanwise direction. The velocity fields are Fourier transformed in time and in the spanwise direction and the notation (ω_1, β_1), where ω_1 and β_1 are the frequency and spanwise wavenumber, each normalized with the corresponding fundamental frequency and wavenumber, is used. Thus, the waves and the streaks are represented by $(1, 0)$ and $(0, 1)$, respectively, and are shown as black solid lines in figure 15. Without nonlinear interactions, the instability modes should amplify in agreement with the linear theory and this is observed

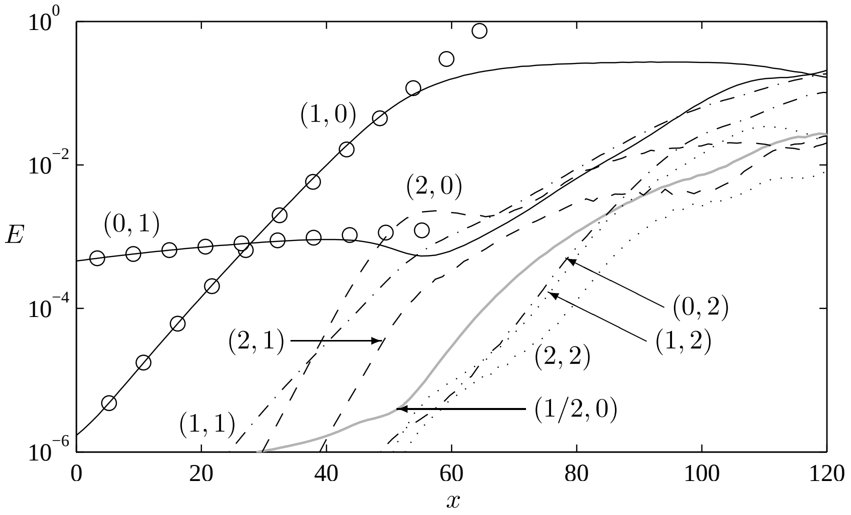

FIGURE 15. Energy in different Fourier modes (ω_1, β_1) from the DNS. The initially excited modes (waves and streaks) are shown by black solid lines, the nonlinearly generated modes are shown by dashed and dotted lines. The modes are indicated in the figure. The pairing mode grows up from numerical noise and is displayed by the thick grey line. Results from the PSE ($\circ$) are shown for comparison.

in the beginning of the computational box, where the waves grow exponentially and the streaks have an algebraic growth. The results from the PSE ($\circ$) are shown for comparison and the agreement is excellent. The waves grow according to the linear theory for surprisingly large amplitudes while the nonlinear interactions for the streaks are encountered earlier. It is evident that close to the slot, the two-dimensional effects are dominating over the stronger forced stationary streaks. At about $x = 1.3$ to $x = 1.4$, nonlinear effects start to be apparent when energy is transferred to the modes $(1, 1)$, $(2, 0)$ and $(2, 1)$. Further downstream, the streak mode $(0, 1)$ is decaying and a dip in the energy can be observed at approximately $x = 1.55$. At this location, the time-periodic mode $(1, 0)$ starts to saturate and an abrupt change of the breakdown process happens, namely, an exponential growth of the streak mode.

There are two possible secondary instabilities on two-dimensional vortices generated by inflectional shear-flow instabilities, a subharmonic one leading to vortex pairing, and a three-dimensional one leading to spanwise modulation of the vortices (see e.g. Metcalfe *et al.* 1987). In low-disturbance environments, the predominant secondary instability is associated with vortex pairing. If the initial three-dimensional excitation is large enough, the three-dimensional secondary instability is predominant, resulting in the growth of a spanwise modulation of the vortices. This results in a suppression of the vortex pairing, and is what can be observed in the current numerical simulation. We have seen that the exponentially growing two-dimensional waves break down owing to what appears to be a three-dimensional secondary instability triggered by the presence of the streaks. In order to asses whether the pairing mode $(1/2, 0)$ is present in the simulation, the energy content in this subharmonic frequency is evaluated and shown as the grey line in figure 15. However, since this mode is not forced (in the fringe region), but only grows out of numerical noise, its amplitude is small. Upstream of the location where nonlinear interactions set in, the amplification rate of the subharmonic mode is about half of the fundamental one. This is consistent with linear theory (see figure 9*d*), indicating that an eigenmode with the subharmonic frequency $F = 241$ is born. At about $x = 1.55$, the amplification rate doubles as a result of nonlinear effects. However, the energy content in this mode stays at least one magnitude below the exponentially growing streak mode.

4.3.3. *Flow structures*

From the performed numerical simulation, structures appearing in the flow can be visualized and contribute to an increased understanding of the transition process, complementing the above discussion. In figure 16, positive isosurfaces of the instantaneous streamwise and normal velocity are displayed in light and medium grey, respectively, at $t = 12.70$. Vortical structures can be identified in the flow by plotting regions where the second largest eigenvalue λ_2 of the Hessian of the pressure assumes negative values (Jeong *et al.* 1997). The vortical structures in figure 16 are represented by dark grey isosurfaces displaying a constant negative value of λ_2. At the instantaneous moment shown in the figure, the waves are most pronounced in the beginning of the box, where the waves have already started to saturate. Counterclockwise rotating rollers are moving with the wave troughs in the outer shear layer, of which one is visible at about $x = 1.7$. Slightly downstream of each shear-layer roll-up, clockwise rotating rollers in the boundary layer exist, one of these is visible at about $x = 1.8$. Associated with the boundary-layer rollers are small regions of separated flow. Between the rollers in the outer shear layer and in the boundary layer, inclined regions of upward flow feed the next downstream wave crest. The presence of the streaks deforms the rollers in the spanwise direction. (This is also visualized in figure 20, where only the vortical structures are shown for different instants within one fundamental period.) At about $x = 1.9$, in figure 16, the high-velocity streak becomes dominant and is lifted up from the shear-layer region forming a mushroom-shaped structure. Such structures were also observed by, for example, Wernz & Fasel (1996, 1997) and Gogineni & Shih (1997).

Figure 17 shows six cross-flow slices from the instantaneous flow field presented in figure 16. The arrows represent the cross-flow velocity while the black solid lines show contours of positive streamwise velocity. Contours of negative

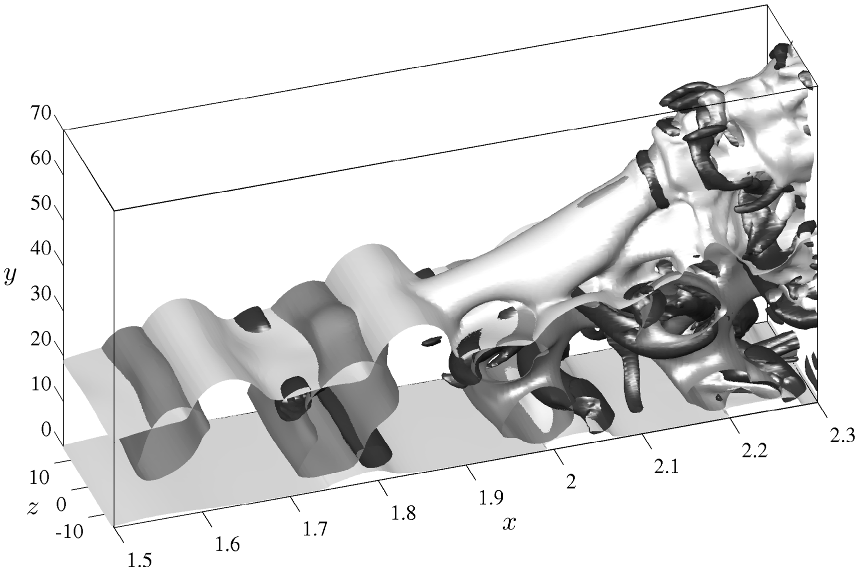

FIGURE 16. Isosurfaces of streamwise velocity (light grey), normal velocity (medium grey) and λ_2 (dark grey) at an instant of $t = 12.70$. The waves and streaks are forced with initial amplitudes 0.1 % and 3 %, respectively, in the Blasius wall jet for $Re_\delta = 173$. The levels of the isosurfaces are 0.1, 0.1 and -0.015, respectively.

or zero streamwise velocity are shown by dotted lines. The thick grey lines show the core of vortical structures at the same level of λ_2 as in figure 16. The first slice, shown in figure 17(*a*), is a cut through the boundary-layer roller at $x = 1.8$ and the region of inclined upward flow. A small region of separated flow exists close to the wall. The streak is visible in the outer shear layer where it shows up as a bump in the streamwise velocity contours. This bump is more pronounced in the next slice, depicted in figure 17(*b*), which shows a cut through the downward flow at $x = 1.9$. In the slice at $x = 2.0$, shown in figure 17(*c*), most of the flow is moving upward and the lift-up of the streak in the ambient flow results in a mushroom-shaped structure. Another small separation bubble can be seen at the wall. The mushroom leg, where the upward motion is strongest, is formed by the combined effect of the upward wave motion and the high-velocity streak. In the top of the upward motion, a vortex pair is forming the mushroom hat. The vortex pair in the mushroom hat separates from its leg and continues upwards through the otherwise mainly downward motion in figure 17(*d*), which shows the slice at $x = 2.1$. The breakdown to turbulence is associated with this upper vortex pair. In the slice at $x = 2.2$, shown in figure 17(*e*), it can be seen that the outer part of the wall jet

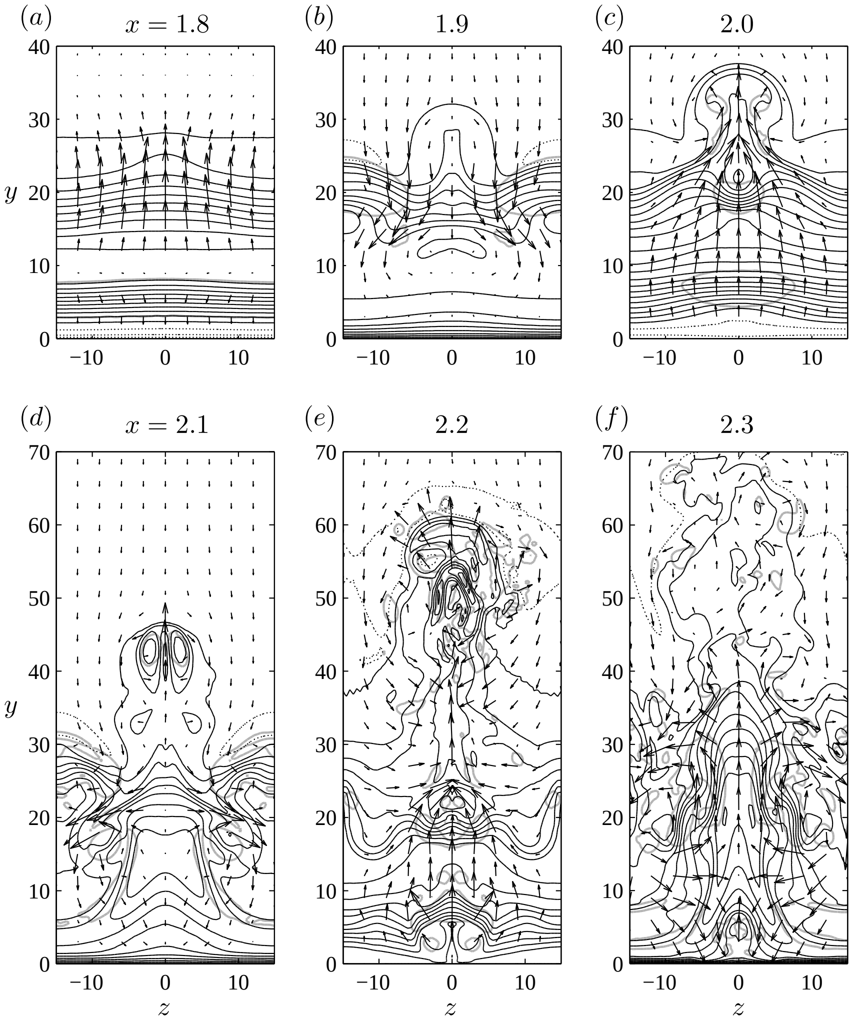

FIGURE 17. Cross-flow planes from the instantaneous data shown in figure 16. Arrows represent the cross-flow velocity while the streamwise velocity is displayed by contours with line increment 0.1. Positive values are displayed by solid lines and negative or zero values by dotted lines. Thick grey lines show the core of vortical structures where $\lambda_2 = -0.015$.

is turbulent while the inner part remains organized. However, the turbulence spreads towards the wall further downstream and the flow undergoes transition to a fully turbulent wall jet. Figure 17(f) shows the slice at $x = 2.3$ where the flow is almost fully turbulent.

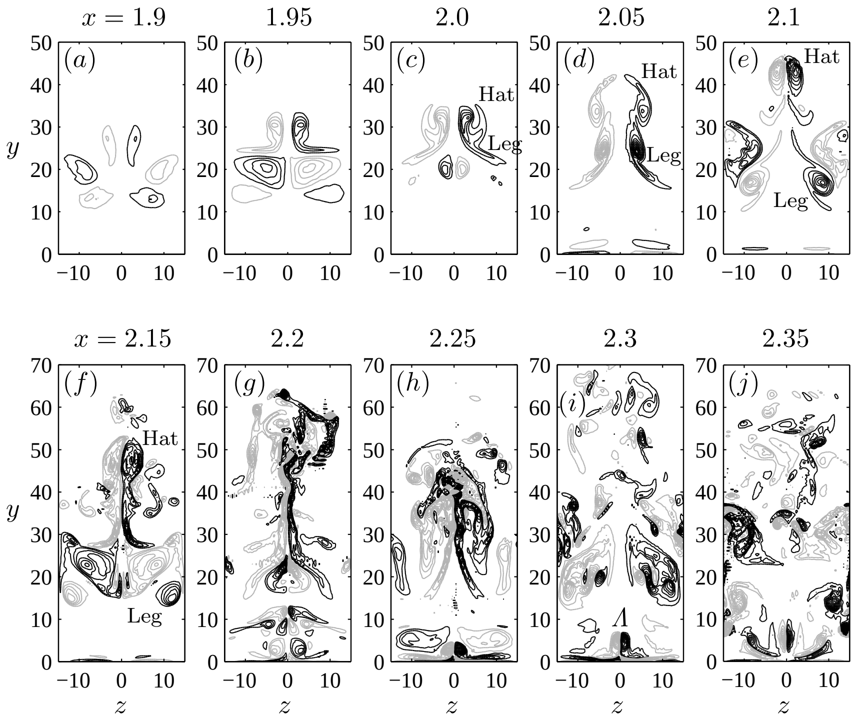

FIGURE 18. Contours of streamwise vorticity in cross-flow planes from the instantaneous data shown in figure 16. The streamwise positions are indicated in the figure. Black lines show positive values and grey lines negative values, the line increment is 0.1, but the zero contour is not displayed.

Figure 18 allows us to follow the streamwise vorticity in the instantaneous flow field, shown in figure 16, through 12 cross-flow slices. The slices are evenly distributed in space from $x = 1.9$ to $x = 2.35$ and black solid lines show contours of positive streamwise vorticity while contours of negative values are displayed by grey solid lines. The line increment is 0.1, but the zero contour is not shown. In figure 18(c), the streamwise vorticity associated with the mushroom-shaped structure in figure 17(c) can be seen. The hat and the leg of the mushroom-shaped structure are indicated in the figure. Further downstream, in figure 18(e), the hat can be found in the upper part, while the leg splits up and moves with the downward flow towards the edges of the slice. In the slice, shown in figure 18(f), the first signs of breakdown to turbulence can be seen above the mushroom hat. In the slices, shown in figures 18(g)–18(j), the turbulence spreads downward. However, the flow close to the wall is still organized. Through these slides a Λ-structure in the boundary layer at the wall can be identified and is indicated with Λ in figure 18(i). Such structures

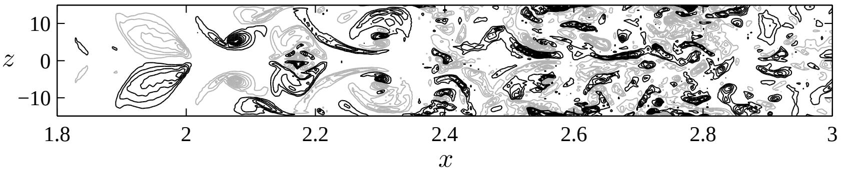

FIGURE 19. Contours of streamwise vorticity in the horizontal plane at $y = 20$ from the instantaneous data shown in figure 16. Black lines show positive values and grey lines negative values, the line increment is 0.1, but the zero contour is not displayed.

are typical for Klebanoff transition in boundary layers (e.g. Bake *et al.* 2002). Figure 19 shows the streamwise vorticity in a slice parallel to the wall at $y = 20$. It covers a longer region and further demonstrates the three-dimensional flow behaviour and the breakdown to turbulence.

Figure 20 shows the time development of the vortical structures in one fundamental disturbance period starting from $t = 13.31$. The vortex visualization uses instantaneous data from the DNS at six evenly distributed instants. Vortex rollers are moving downstream in the outer shear layer and in the boundary layer. The high-velocity streak in the outer shear layer deforms the roll-up and gives it a bent shape. The corresponding low-velocity streak in the boundary layer induces a bent shape in the opposite direction to the vortex roller in the boundary layer. The interaction between these counter-rotating rollers contributes to the three-dimensional modification of the boundary-layer roller. At the left-hand side of figure 20(b), the curved rollers can be seen. Between the rollers, the flow is pushed upward and forward and inclined rib vortices are created. The rib vortices extend from above the shear-layer roller to beneath the previous one, see figure 20(c). Such rib vortices have been observed in many experimental and computational studies of mixing layers (e.g. Bernal & Roshko 1986; Lasheras *et al.* 1986; Metcalfe *et al.* 1987; Schoppa *et al.* 1995). The rib vortices are close together at the tails and wider apart at the tips. At about $x = 2.0$, in figure 20(d), the upward flow is pushing the rib vortices upward, where they are forming the hat of the mushroom-shaped structure. The tails of the rib vortices, at about $x = 1.9$, keep the normal position. The tails of the previous rib vortices separate around the upcoming rib vortices. Figure 20(d) shows the instant exactly two fundamental periods after the instantaneous data shown in figures 16–19. The separated legs of the previous rib vortices forms a Ω-shaped vortex ring around the upcoming rib vortices, see figure 20(e). In front of this vortex ring another counter-rotating vortex ring is created (at about $x = 2.1$ in figure 20f). The vortex ring formation precedes the breakdown to turbulence. In the end of the lower part of the box, in figure 20(c), where the flow is not yet turbulent, the Λ-structure between the wall and the roller in the boundary layer can be seen.

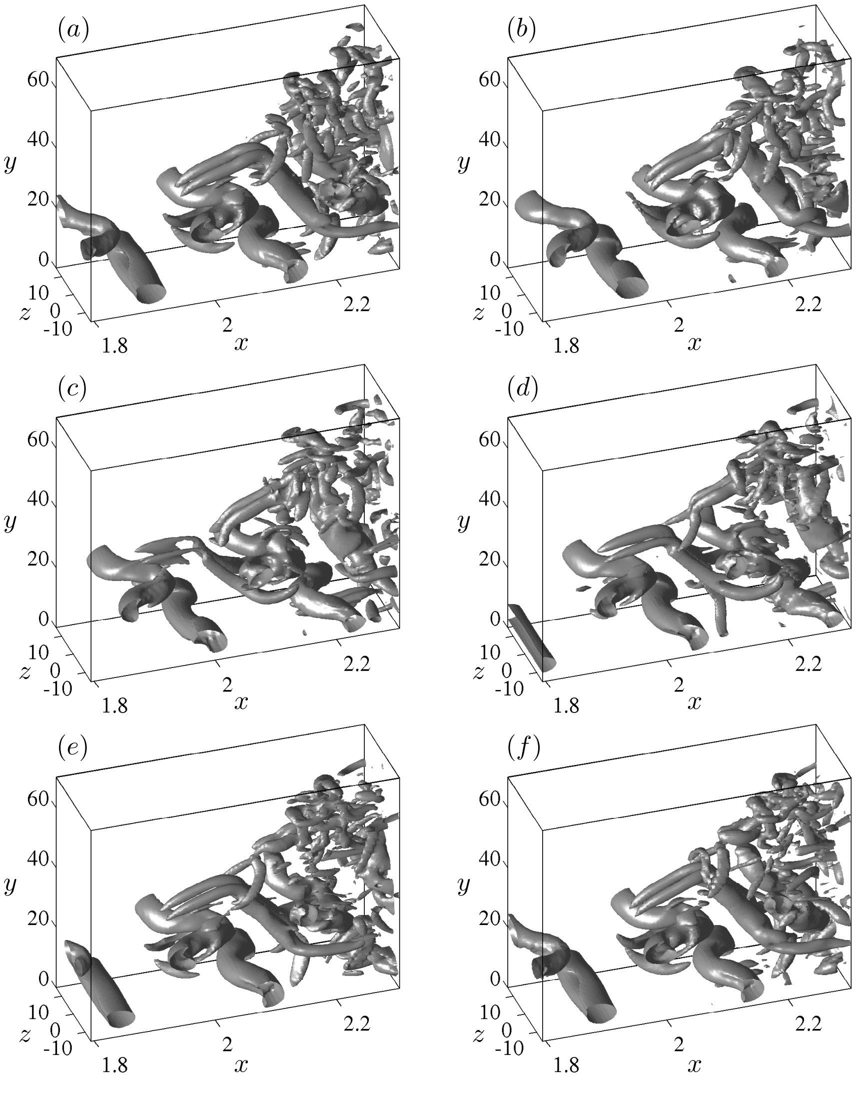

FIGURE 20. Vortex visualization (isosurfaces of $\lambda_2 = -0.015$) using instantaneous data from the DNS at six instants within one fundamental disturbance period T: (*a*) $t = 0$, (*b*) $t = 0.2T$, (*c*) $t = 0.4T$, (*d*) $t = 0.6T$, (*e*) $t = 0.8T$, (*f*) $t = T$.

The coincidence of the numerical visualization with the experimental visualizations of figure 14 is clear; namely, it is seen that in the outer region of the wall jet, the large-amplitude streak structures dominate the late stage of flow breakdown. Both in the computations and in the experiments, a staggered formation of streaks can be observed. The strong three-dimensionality is formed only a certain distance from the nozzle outlet.

4.4. *Subharmonic waves and pairing*

In this section, the role of the subharmonic waves is investigated. Two additional simulations are performed, one with the streaks, the fundamental and subharmonic waves forced in the flow and the other with only the fundamental and subharmonic waves and noise in the initial field.

Free mixing layers are known to undergo pairing of the fundamental vortex rollers preceding the breakdown to turbulence (Ho & Huerre 1984; Metcalfe *et al.* 1987; Moser & Rogers 1993; Rogers & Moser 1993; Schoppa *et al.* 1995). Further downstream in the turbulent flow region, spanwise coherent structures may also be observed, where they coexist with fine-scale motion (Konrad 1976). The pairing originates from a subharmonic wave displacing one vortex to the low-velocity region and the next to the high-velocity region. The vortex travelling in the high-velocity region overtakes the slower-moving vortex in the low-velocity region, and pairing appears. The relative phasing of the fundamental and subharmonic disturbances influences the development of the pairing. The three-dimensional modification of the spanwise rollers has been studied numerically by Moser & Rogers (1993), Rogers & Moser (1993) and Schoppa *et al.* (1995) and experimentally by Tung & Kleis (1996). Pairing is found to inhibit the growth of infinitesimal three-dimensional disturbances, and to trigger the transition to turbulence in highly three-dimensional flows. If the amplitude of the initial three-dimensional disturbances is large enough, transition occurs before the pairing takes place. Vortex pairing has also been observed in wall jets (e.g. Bajura & Catalano 1975; Wernz & Fasel 1996).

In order to determine the role of pairing in the Blasius wall jet, the subharmonic disturbance is studied. The Orr–Sommerfeld mode with half the frequency of the fundamental one is forced in the DNS, as described in § 3.3.2. Figure 21 shows the spanwise vorticity in the (x, y)-plane at $z = 14.9$ from instantaneous data at $t = 12.70$ for three different forcing cases. Black solid lines show contours of positive spanwise vorticity while contours of negative values are displayed by grey solid lines. The line increment is 0.1, but the zero contour is not shown. In Case 1, shown in figure 21(a), streaks and fundamental waves are forced (the simulation described in § 4.3). In Case 2, shown in figure 21(b), subharmonic waves are forced in addition to the streaks and the fundamental waves. In Case 3, shown in figure 21(c), only fundamental and subharmonic waves are forced. In the absence of the three-dimensional streak, a low level of noise is added to the initial field to introduce three-dimensionality to the flow. The pairing mode is weak in Case 1, as is also seen in the energy content of the corresponding Fourier mode $(1/2, 0)$ in figure 15. In this case pairing does not occur. In Case 2 and 3, the pairing mode is stronger and can be seen as the staggered pattern of the vortex rollers in the outer shear

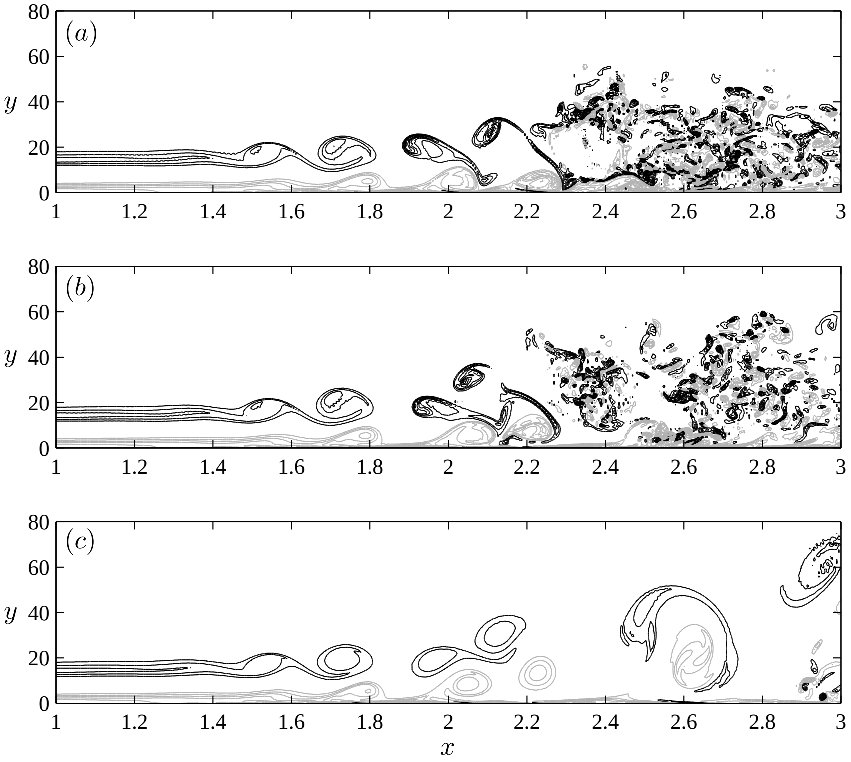

FIGURE 21. Contours of spanwise vorticity in the (x, y)-plane at $z = 14.9$. Black lines show positive values and grey lines negative values, the line increment is 0.1, but the zero contour is not displayed. (*a*) Streaks and fundamental waves are forced, same instantaneous data as in figure 16. (*b*) Streaks, fundamental and subharmonic waves are forced. (*c*) Fundamental and subharmonic waves are forced.

layer. However, in Case 2, pairing does not occur before the breakdown to turbulence. In Case 3, pairing occurs between rollers in the outer shear layer as well as in the boundary layer. Signs of breakdown are first seen in the vortex pair close to the wall in the very end of the box. It can be noted that the vorticity is stronger and breakdown to turbulence is enhanced in the presence of the streak. Figure 22(*a*–*c*) shows the spanwise vorticity in a cross-flow slice at $x = 2.1$ for the corresponding flow cases. From this figure the difference in the three-dimensional modification becomes clear.

5. Summary and conclusion

The dynamics of a plane wall jet is studied using both calculations and experiments. It is found that a laminar wall jet can be successfully described by the

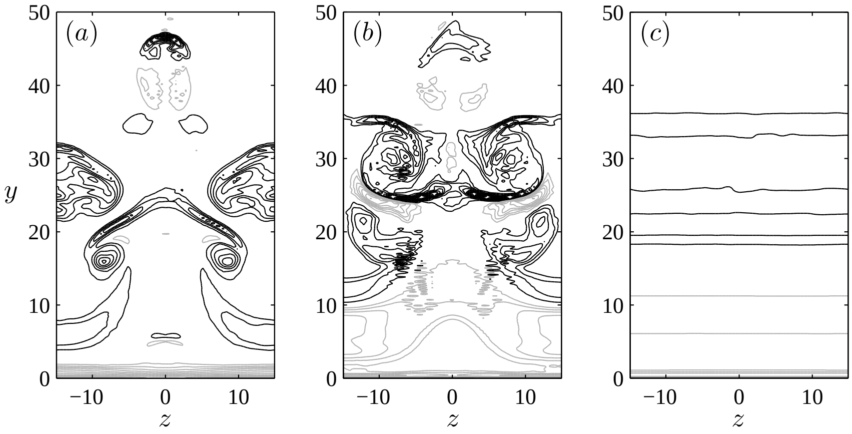

Figure 22. Contours of spanwise vorticity in the cross-flow plane at $x = 2.1$ from the instantaneous data shown in figure 21. Black lines show positive values and grey lines negative values, the line increment is 0.1, but the zero contour is not displayed. (*a*) Streaks and fundamental waves are forced. (*b*) Streaks, fundamental and subharmonic waves are forced. (*c*) Fundamental and subharmonic waves are forced.

solution of the boundary-layer equations. The so-called Blasius wall jet, which is matched to the experimental data, is valid in the region just downstream of the nozzle in contrast to the well-known Glauert similarity solution valid further downstream. Comparison of the results of linear stability calculations with experiments shows that the theory is able to predict the most amplified frequency of the periodical waves and the most amplified scale of the streaks. However, the difference in the upper part of the base flow causes an underprediction of the calculated modal amplification. Orr–Sommerfeld calculations demonstrate that the interaction of the two layers of the Blasius wall jet is affecting the stability of both layers. Because of this interaction, the shear-layer part of the jet is stabilized and the boundary-layer part is destabilized. Critical Reynolds numbers are affected in the same manner. The stabilization effect increases with increased interaction between the layers. The local stability approach is shown to work rather well.

In the experiment, streamwise streaks appear naturally in the flow. Linear stability analysis demonstrates a rather large growth of non-modal streaks and this mechanism is responsible for the generation of initial three-dimensionality of the wall jet. Additional support of this conclusion is the excellent agreement between the calculated and measured amplitude functions of the streak. An optimal, most amplified scale exists for the stationary streaks both in the calculations and in the experiment. The calculations indicate that the optimal disturbance represents streamwise vortices, which cause the formation of streaks by the so-called lift-up effect. The mechanism of non-modal growth may affect the selection of scales in the secondary instability of spanwise vortex rollers and thereby the three-dimensional modification preceding flow breakdown.

The nonlinear stage of the laminar flow breakdown is studied with DNS and is experimentally visualized. Three-dimensional simulations with coherent forcing are performed and they clearly demonstrate that growing streaks are important for the breakdown process. It is found that the forcing of streamwise streaks feed into the three-dimensional secondary instability preceding the flow breakdown. As a result, the three-dimensionalities in the flow are enhanced and the other possible secondary instability of the flow, namely the subharmonic pairing of the spanwise vortices, is suppressed. The transition mechanisms can be described by the following stages. (i) Spanwise rollers are formed in the wave troughs in the outer shear layer and move downstream. In the boundary layer close to the wall beneath the wave crests, counter-rotating rollers are formed. (ii) In the presence of streaks, the shear-layer rollers are sinuously modified in the spanwise direction with the boundary-layer rollers deforming in the opposite direction. (iii) Vortex ribs are formed in the braids of the waves, extending from the top of the shear-layer roller to the bottom of the previous one. (iv) The vortex ribs follow the upward flow between two neighbouring shear-layer rollers and are associated with mushroom-shaped structures ejected from the wall jet into the ambient flow. (v) The tail legs of the vortex ribs, generated one fundamental period earlier, separate and form a vortex ring around the upcoming vortex ribs and additional counter-rotating vortex rings are created preceding breakdown to turbulence.

Both the experiment and the DNS reveal that the flow history is extremely important for the transition scenario. In the experiment, the flow is subjected to disturbances already in the apparatus (settling chamber, contraction and nozzle). In the simulations, different forcings of the upstream disturbances lead to different transition scenarios. In order to determine the role of pairing in the Blasius wall jet, the subharmonic disturbance is studied. In total three different forced simulations are performed. (i) Streaks and fundamental waves. (ii) Streaks, fundamental and subharmonic waves. (iii) Fundamental and subharmonic waves and noise. When the subharmonic disturbance is not forced in the flow, the pairing mode is weak and pairing does not occur. When the subharmonic disturbance is forced, the pairing mode is stronger and can be seen as the staggered pattern of the vortex rollers in the outer shear layer. However, pairing does not occur before the breakdown to turbulence in the presence of streaks. It can also be concluded that vorticity is stronger and breakdown to turbulence is enhanced in the presence of streaks.

This work was funded by the Swedish Energy Agency (Energimyndigheten). The direct numerical simulations was performed at the Center for Parallel Computers at KTH. Many thanks to Mattias Chevalier for the help with various modifications of the spectral code and to Professor Victor Kozlov for the help with the smoke visualizations and for the loan of the laser. Maria Litvinenko has taken part in the experimental measurements which we gratefully acknowledge.

Appendix. Optimization procedure

In this Appendix, the optimization procedure for the optimal disturbances in the algebraic instability problem is derived. We adopt an input–output formulation of the initial-boundary-value problem (2)–(4)

$$\hat{u}_1 = \mathcal{A}\boldsymbol{q}, \tag{26}$$

where $\mathcal{A}$ is a linear operator. The maximum Reynolds-number-independent growth may then be written

$$\overline{G}_{max} = \max_{\boldsymbol{q}\neq 0} \frac{(\hat{u}_1, \hat{u}_1)_u}{(\boldsymbol{q},\boldsymbol{q})_q} = \max_{\boldsymbol{q}\neq 0} \frac{(\mathcal{A}^*\mathcal{A}\boldsymbol{q},\boldsymbol{q})_q}{(\boldsymbol{q},\boldsymbol{q})_q}. \tag{27}$$

Here, $\mathcal{A}^*$ denotes the adjoint operator to $\mathcal{A}$ with respect to the chosen inner product. The maximum of $(\mathcal{A}^*\mathcal{A}\boldsymbol{q},\boldsymbol{q})/(\boldsymbol{q},\boldsymbol{q})$ is attained for some vector $\boldsymbol{q}$, which is the eigenvector corresponding to the largest eigenvalue of the eigenvalue problem

$$\mathcal{A}^*\mathcal{A}\boldsymbol{q} = \lambda\boldsymbol{q}, \tag{28}$$

where $\overline{G}_{max}$ is the maximum eigenvalue λ_{max}, necessarily real and non-negative. The most natural attempt to calculate the optimal initial disturbance and its associated maximum Reynolds-number-independent growth is by power iterations

$$\boldsymbol{q}^{n+1} = \mathcal{A}^*\mathcal{A}\boldsymbol{q}^n, \tag{29}$$

where the initial disturbance is scaled to the given initial energy in each iteration. To be able to perform the power iterations, we need to know the action of the adjoint operator on $\hat{u}_1$. The following adjoint system can be derived from (2)–(4) with $\alpha = 0$ and $\hat{p}_x = 0$, by integration by parts

$$-v^*_y + \mathrm{i}\beta w^* = 0, \tag{30a}$$

$$-\mathrm{i}\omega u^* - Uu^*_x - V_y u^* - Vu^*_y + V_x v^* - p^*_x = u^*_{yy} - \beta^2 u^*, \tag{30b}$$

$$-\mathrm{i}\omega v^* - Uv^*_x - U_x v^* - Vv^*_y + U_y u^* - p^*_y = v^*_{yy} - \beta^2 v^*, \tag{30c}$$

$$-\mathrm{i}\omega w^* - Uw^*_x - Vw^*_y + \mathrm{i}\beta p^* = w^*_{yy} - \beta^2 w^*, \tag{30d}$$

where $p^*(x,y)$, $u^*(x,y)$, $v^*(x,y)$ and $w^*(x,y)$ are the adjoint variables with boundary conditions

$$\left.\begin{array}{lll} \overline{u}^* = \overline{v}^* = \overline{w}^* = 0 & \text{at} & y = 0, \\ \overline{u}^* = \overline{w}^* = \overline{p}^* + 2V\overline{v}^* = 0 & \text{at} & y = y_{max}. \end{array}\right\} \tag{31}$$

The x-derivative in the parabolic set of equations (30) has opposite sign compared to (2) and the problem has to be solved in the backward direction from the final position x_1 to the initial position x_0. Therefore, the initial condition is specified at x_1

$$\left.\begin{array}{lll} U_1 u^*_1 + p^*_1 = \hat{u}_1(y) & \text{at} & x = x_1, \\ v^*_1 = w^*_1 = 0 & \text{at} & x = x_1. \end{array}\right\} \tag{32}$$

The action of the adjoint operator is given by

$$\left.\begin{aligned} \hat{v}_0 &= U_0(y)v_0^*(y) \quad \text{at} \quad x = x_0, \\ \hat{w}_0 &= U_0(y)w_0^*(y) \quad \text{at} \quad x = x_0. \end{aligned}\right\} \tag{33}$$

The adjoint-based optimization algorithm is very efficient and converges often within three to four iterations, indicating the existence of a well-separated dominating mode.

References

Amitay, M. & Cohen, J. 1993 The mean flow of a laminar wall-jet subjected to blowing or suction. *Phys. Fluids A* **5**, 2053–2057.

Amitay, M. & Cohen, J. 1997 Instability of a two-dimensional plane wall jet subjected to blowing or suction. *J. Fluid Mech.* **344**, 67–94.

Andersson, P., Berggren, M. & Henningson, D. S. 1999 Optimal disturbances and bypass transition in boundary layers. *Phys. Fluids* **11**, 134–150.

Bajura, R. A. & Catalano, M. R. 1975 Transition in a two-dimensional plane wall jet. *J. Fluid Mech.* **70**, 773–799.

Bajura, R. A. & Szewczyk, A. A. 1970 Experimental investigation of a laminar two-dimensional plane wall jet. *Phys. Fluids* **13**, 1653–1664.

Bake, S., Meyer, D. G. W. & Rist, U. 2002 Turbulence mechanism in Klebanoff transition: a quantitative comparison of experiment and direct numerical simulation. *J. Fluid Mech.* **459**, 217–243.

Balaras, E., Piomelli, U. & Wallace, J. M. 2001 Self-similar states in turbulent mixing layers. *J. Fluid Mech.* **446**, 1–24.

Bernal, L. P. & Roshko, A. 1986 Streamwise vortex structure in plane mixing layers. *J. Fluid Mech.* **170**, 499–525.

Bertolotti, F. P., Herbert, T. & Spalart, P. R. 1992 Linear and nonlinear stability of the Blasius boundary layer. *J. Fluid Mech.* **242**, 441–474.

Brandt, L. & Henningson, D. S. 2002 Transition of streamwise streaks in zero-pressure-gradient boundary layers. *J. Fluid Mech.* **472**, 229–261.

Chernoray, V. G., Kozlov, V. V., Pratt, P. R. & Löfdahl, L. 2005 Hot wire visualizations of breakdown to turbulence in complex flows. In *Proc. of EUCASS conf.*, pp. 2.11–2.16. Moscow, Russia.

Chun, D. H. & Schwarz, W. H. 1967 Stability of the plane incompressible viscous wall jet subjected to small disturbances. *Phys. Fluids* **10**, 911–915.

Cohen, J., Amitay, M. & Bayly, B. J. 1992 Laminar-turbulent transition of wall-jet flows subjected to blowing and suction. *Phys. Fluids A* **4**, 283–289.

Glauert, M. B. 1956 The wall jet. *J. Fluid Mech.* **1**, 625–643.

Gogineni, S. & Shih, C. 1997 Experimental investigation of the unsteady structure of a transitional plane wall jet. *Exp. Fluids* **23**, 121–129.

Gogineni, S., Shih, C. & Krothapalli, A. 1993 PIV study of a two-dimensional transitional wall jet. *AIAA Paper* 93-2913.

Gogineni, S., Visbal, M. & Shih, C. 1999 Phase-resolved PIV measurements in a transitional plane wall jet: a numerical comparison. *Exp. Fluids* **27**, 126–136.

Hanifi, A., Schmid, P. J. & Henningson, D. S. 1996 Transient growth in compressible boundary layer flow. *Phys. Fluids* **8**, 826–837.

Herbert, T. 1997 Parabolized stability equations. *Annu. Rev. Fluid Mech.* **29**, 245–283.

Ho, C. & Huerre, P. 1984 Perturbed free shear layers. *Annu. Rev. Fluid Mech.* **16**, 365–424.

Jeong, J., Hussain, F., Schoppa, W. & Kim, J. 1997 Coherent structures near the wall in a turbulent channel flow. *J. Fluid Mech.* **332**, 185–214.

Klebanoff, P. S. 1971 Effect of freestream turbulence on the laminar boundary layer. *Bull. Am. Phys. Soc.* **10**, 1323.

Konrad, J. H. 1976 An experimental investigation of mixing in two-dimensional turbulent shear flows with applications to diffusion-limited chemical reactions. *Intern. Rep.* CIT-8-PU, California Institute of Technology.

Lasheras, J. C., Cho, J. S. & Maxworthy, T. 1986 On the origin and evolution of streamwise vortical structures in a plane, free shear layer. *J. Fluid Mech.* **172**, 231–258.

Levin, O. & Henningson, D. S. 2003 Exponential vs algebraic growth and transition prediction in boundary layer flow. *Flow, Turb. Combust.* **70**, 183–210.

Li, F. & Malik, M. R. 1994 Mathematical nature of parabolized stability equations. In *4th IUTAM Symp. on Laminar–Turbulent transition, Sendai, Japan* (ed. R. Kobayashi), pp. 205–212. Springer.

Luchini, P. 2000 Reynolds-number-independent instability of the boundary layer over a flat surface: optimal perturbations. *J. Fluid Mech.* **404**, 289–309.

Lundbladh, A., Berlin, S., Skote, M., Hildings, C., Choi, J., Kim, J. & Henningson, D. S. 1999 An efficient spectral method for simulation of incompressible flow over a flat plate. *Tech. Rep.* KTH, Department of Mechanics, Stockholm.

Mele, P., Morganti, M., Scibilia, M. F. & Lasek, A. 1986 Behavior of wall jet in laminar-to-turbulent transition. *AIAA J.* **24**, 938–939.

Metcalfe, R. W., Orszag, S. A., Brachet, M. E., Menon, S. & Riley, J. J. 1987 Secondary instability of a temporally growing mixing layer. *J. Fluid Mech.* **184**, 207–243.

Monkewitz, P. A. & Huerre, P. 1982 Influence of the velocity ratio on the spatial instability of mixing layers. *Phys. Fluids* **25**, 1137–1143.

Moser, R. D. & Rogers, M. M. 1993 The three-dimensional evolution of a plane mixing layer: pairing and transition to turbulence. *J. Fluid Mech.* **247**, 275–320.

Nordström, J., Nordin, N. & Henningson, D. S. 1999 The fringe region technique and the Fourier method used in the direct numerical simulation of spatially evolving viscous flows. *SIAM J. Sci. Comput.* **20**, 1365–1393.

Rogers, M. M. & Moser, R. D. 1993 Spanwise scale selection in plane mixing layers. *J. Fluid Mech.* **247**, 321–337.

Schlichting, H. 1979 *Boundary-Layer Theory*, 7th edn. Mc-Graw-Hill.

Schoppa, W., Hussain, F. & Metcalfe, R. W. 1995 A new mechanism of small-scale transition in a plane mixing layer: core dynamics of spanwise vortices. *J. Fluid Mech.* **298**, 23–80.

Seidel, J. & Fasel, H. F. 2001 Numerical investigations of heat transfer mechanisms in the forced laminar wall jet. *J. Fluid Mech.* **442**, 191–215.

Tumin, A. & Aizatulin, L. 1997 Instability and receptivity of laminar wall jets. *Theoret. Comput. Fluid Dyn.* **9**, 33–45.

Tung, S. & Kleis, S. J. 1996 Initial streamwise vorticity formation in a two-stream mixing layer. *J. Fluid Mech.* **319**, 251–279.

Visbal, M. R., Gaitonde, D. V. & Gogineni, S. P. 1998 Direct numerical simulation of a forced transitional plane wall jet. *AIAA Paper* 98-2643.

Wernz, S. & Fasel, H. F. 1996 Numerical investigation of unsteady phenomena in wall jets. *AIAA Paper* 96-0079.

Wernz, S. & Fasel, H. F. 1997 Numerical investigation of forced transitional wall jets. *AIAA Paper* 97-2022.

Westin, K. J. A., Boiko, A. V., Klingmann, B. G. B., Kozlov, V. V. & Alfredsson, P. H. 1994 Experiments in a boundary layer subjected to free stream turbulence. Part 1. Boundary layer structure and receptivity. *J. Fluid Mech.* **281**, 193–218.

Paper 4

Transition thresholds in the asymptotic suction boundary layer

By Ori Levin[1], E. Niklas Davidsson[2] and Dan S. Henningson[1]

[1]KTH Mechanics, SE-100 44 Stockholm, Sweden
[2]Division of Fluid Mechanics, Luleå University of Technology, SE-971 87 Luleå, Sweden

Physics of Fluids, In press.

Energy thresholds for transition to turbulence in an asymptotic suction boundary layer is calculated by means of temporal direct numerical simulations. The temporal assumption limits the analysis to periodic disturbances with horizontal wavenumbers determined by the computational box size. Three well known transition scenarios are investigated: oblique transition, the growth and breakdown of streaks triggered by streamwise vortices, and the development of random noise. Linear disturbance simulations and stability diagnostics are also performed for a base flow consisting of the suction boundary layer and a streak. The scenarios are found to trigger transition by similar mechanisms as obtained for other flows. Transition at the lowest initial energy is provided by the oblique wave scenario for the considered Reynolds numbers 500, 800 and 1200. The Reynolds number dependence on the energy thresholds are determined for each scenario. The threshold scales like $Re^{-2.6}$ for oblique transition and like $Re^{-2.1}$ for transition initiated by streamwise vortices and random noise, indicating that oblique transition has the lowest energy threshold also for larger Reynolds numbers.

1. Introduction

1.1. *Earlier work on suction and bypass transition*

One of the principal interests in fluid mechanics is the reduction of energy losses in various flow systems, where the boundary layer plays an important part. This can be achieved by laminar flow control (LFC), i.e. methods of delaying/prohibiting transition to turbulence. One such method is wall suction, which utilizes porous surfaces to remove flow from the boundary layer. Early interest by the aircraft industry was mostly aimed at steady uniform suction, which stabilizes the boundary layer mainly by altering the mean flow. For an aircraft, typically 50 % of the drag comes from skin friction (Thibert *et al.* 1990). Keeping a boundary layer laminar will decrease this quantity to a fraction of its turbulent value. Beyond the LFC-application, uniform suction can be used to damp out existing turbulence. The large amount of suction required will however introduce a sharp velocity gradient near the wall and as a result increased skin friction. The energy cost for relaminarization is typically one order of magnitude larger than required for LFC (Joslin 1998). Rioual *et al.* (1996) investigated the power balance of a flat plate used as an airfoil. Uniform suction was found to reduce the wake drag and an optimum for the suction velocity was obtained, leading to a reduction of power consumption.

In order to obtain the stabilizing effects on the boundary layer, one must assure that the chosen material is able to provide continuous suction. MacManus & Eaton (2000) investigated the flow instabilities caused by suction through discrete holes and found a relation between the perforation diameter and the displacement thickness of the boundary layer $d/\delta_1 \simeq 0.6$ below which the non-uniform effects will not provoke transition. Roberts & Floryan (2001) considered non-uniform suction by linear instability calculations and the non-uniformities were shown to trigger streamwise vortices, whose growth rate scales linearly with the Reynolds number of the flow.

Optimal distribution of steady suction (with respect to minimizing the disturbance energy) along various geometries have been investigated in different ways. Thibert *et al.* (1990) computed transition locations on a wing versus different mean suction rates and found that linearly decreasing suction rate gives the best result. Optimization techniques has also been incorporated to control different types of disturbances in various boundary layers (Balakumar & Hall 1999; Pralits *et al.* 2002; Zuccher *et al.* 2004). The results have in common that the suction distribution has a peak near the start of the control volume and decays thereafter, however in somewhat different ways.

The present work focuses on the application of steady uniform suction for which recent experimental studies have been carried out in the MTL wind tunnel at KTH Mechanics (Stockholm) by Fransson & Alfredsson (2003). In that work, measurements on Tollmien–Schlichting (TS) wave propagation as well as the influence of free-stream turbulence (FST) were carried out. An interesting result is that the FST-induced disturbances reach a constant level inside the boundary layer as suction is applied. For the given Reynolds number and turbulence grids, it was also shown that transition is prevented as the suction is turned on. Yoshioka *et al.* (2004) investigated the FST scenario further in a parametric study based on the fact that for the asymptotic suction boundary layer (ASBL), the boundary layer thickness and its associated Reynolds number can be changed independently. They found that the spanwise spacing of the obtained streamwise elongated disturbances (streaks) is maintained in the suction area, indicating that due to the suppression of the disturbance growth, the streaks mainly become passive disturbances convected downstream with the flow.

As far as the classical scenario with exponential growth of two-dimensional TS-waves is concerned, experiments and theory match well. For bypass transition, however, the experimentally observed differences between boundary layers with and without suction are not completely understood. Fransson & Corbett (2003) report a weakening of optimal linear energy growth, compared to the Blasius boundary layer (BBL), which nevertheless still is of the same order of magnitude. Roberts & Floryan (2001) observed that the application of uniform suction significantly stabilizes TS-waves but has a negligible effect on streamwise vortices.

Considering bypass transition in general, it is well known that transient growth is the dominating mechanism for flat-plate boundary-layer experiments with high levels of FST present. Flow visualizations by Matsubara & Alfredsson (2001) clearly indicate the route to transition: streaks form inside the boundary layer, become unstable and develop turbulent spots. Numerical flow visualizations showing the same qualitative results have also been done (Brandt *et al.* 2004), where the inflow FST was obtained by superposition of modes of the continuous spectrum of the Orr–Sommerfeld and Squire operators. Westin *et al.* (1994) among others observed that the obtained disturbance level inside the boundary layer grows as $x^{1/2}$. Fransson & Alfredsson (2003) reproduced this result and showed that, as earlier mentioned, uniform suction is able to stop the growth. Andersson *et al.* (1999) calculated the optimal scales for streamwise streaks in the BBL and predicted that the spanwise spacing of these optimal streaks also grows as $x^{1/2}$. They confirmed the disturbance growth found by Westin *et al.* (1994) when the growth of the optimal spanwise streak spacing was incorporated.

Theoretical insight of how perturbations can enter a boundary layer is further provided by the so called oblique-transition model. This concept was originally introduced by Schmid & Henninson (1992) for incompressible flows and by Fasel *et al.* (1993) for compressible flows. Schmid & Henningson showed, by numerical simulations on plane Poiseuille flow, how the interaction of disturbances consisting of a pair of oblique waves can lead to transition. For the flat-plate boundary layer, this scenario was first tested numerically by Berlin *et al.* (1994), and extended in the context of FST by Berlin *et al.* (1999). The numerical results are also confirmed by experimental studies of the various flows; see Elofsson & Alfredsson (1998) and Berlin *et al.* (1999) for plane Poiseuille flow and the flat-plate boundary layer, respectively. For the ASBL, or any boundary layer involving suction, this scenario is however not investigated to the authors knowledge.

Disturbances as streamwise vortices and oblique waves in shear flows may lead to transition to turbulence. However, for transition to occur at subcritical Reynolds numbers, a finite initial energy of the disturbance is required. The threshold energy is defined to be the minimum initial disturbance energy that leads to transition. Comparing the threshold energies gives a measure of the probability that a particular transition scenario occurs in a disturbed shear flow. Such investigations have been done in previous numerical works for plane Couette and Poiseuille flows (Kreiss *et al.* 1994; Lundbladh *et al.* 1994; Reddy *et al.* 1998) and a temporal growing Blasius boundary layer (Schmid *et al.* 1996).

1.2. *Present work*

In the present paper, we study bypass transition in the asymptotic limit of the suction boundary layer (i.e. where the flow over a flat plate with suction has obtained a constant boundary layer thickness) by temporal direct numerical simulations (DNS). The investigation is limited to periodic disturbances with specified horizontal wavenumbers. Three transition scenarios are investigated:

- The Streamwise Vortices scenario (SV), where the initial flow field consists of two counter-rotating streamwise vortices. These vortices produce streaks by the lift-up effect as time proceeds. Transition can take place if the streak amplitude becomes large enough for secondary instabilities to operate on it.
- The Oblique Waves scenario (OW), where the initial flow field consists of two superposed oblique waves traveling with opposite angles to the free-stream direction. These waves interact nonlinearly to create streamwise vortices. This is essentially a different and quicker way of triggering growth of streaks, which in turn are subjected to secondary instabilities.
- The Noise scenario (N), where the initial flow field consists of three-dimensional random noise added to the base flow.

Natural transition, or growth of TS-waves, is not considered in this investigation. The asymptotic suction boundary layer is very stable to such disturbances and a critical Reynolds number of 54370 is reported by Hocking (1975). The likelihood of a certain scenario to appear in practice depends on the actual disturbance environment, the receptivity of the flow and the required disturbance energy and time for transition to occur. We aim at determining *upper* bounds on the required energy, and also look at the time when the transition takes place.

The paper is outlined as follows: In § 2, the numerical methods are considered. Here we describe the numerical code, base flow, how to create the primary disturbances and which parameters are used for the simulations. In § 3, a linear disturbance simulation is performed for the streaky base flow. Then the results from the DNS are presented in terms of flow visualizations and spectral energy evolution. Finally, the transition times and the energy thresholds of the three scenarios is presented. The obtained results are summarized in § 4.

2. Numerical details

2.1. *Base flow and scaling*

Consider a boundary layer over a wall where x, y and z denote the streamwise, wall-normal and spanwise coordinates, respectively. The corresponding velocity components are $\boldsymbol{U} = (U, V, W)$. Lengths are made nondimensional by the displacement thickness δ_1 and velocities are made nondimensional by the free-stream velocity, U_∞. The time t is scaled with δ_1/U_∞. The Reynolds number is defined as $Re = U_\infty \delta_1/\nu$, where ν is the kinematic viscosity of the fluid. When uniform wall-normal suction, with velocity $-V_0$, is applied at the wall, the flow will evolve to the asymptotic suction profile after some evolution region (Fransson & Alfredsson 2003). The ASBL is an analytical solution to the Navier–Stokes equations and can be written as

$$\boldsymbol{U}_0 = (1 - \exp(-y), -V_0, 0). \tag{1}$$

The analytical solution allows the displacement thickness to be calculated exactly, $\delta_1 = \nu/V_0^*$ and the Reynolds number to be expressed as the velocity ratio, $Re = U_\infty/V_0^*$, where $-V_0^*$ is the dimensional suction velocity.

2.2. *DNS techniques*

The numerical code (Lundbladh *et al.* 1999) uses spectral methods to solve the three-dimensional time-dependent incompressible Navier–Stokes equations. The discretization in the streamwise and spanwise directions make use of Fourier series expansions, which enforces periodic solutions. The discretization in the normal direction is represented with Chebyshev series. A pseudospectral treatment of the nonlinear terms is used. The time advancement used is a second-order Crank–Nicolson method for the linear terms and a four-step low-storage third-order Runge–Kutta method for the nonlinear terms. Aliasing errors arising from the evaluation of the pseudospectrally convective terms are removed by dealiasing by padding and truncation using the 3/2-rule when the FFTs are calculated in the wall-parallel planes. In the normal direction, it has been found that increasing the resolution is more efficient than the use of dealiasing. The code can be run in both a temporal and a spatial mode. In the latter case, a fringe region (Nordström *et al.* 1999) is added to the downstream end of the physical domain, in which the outgoing flow is forced to its initial state. When studying parallel flows, such as the ASBL with periodic disturbances, the advantage of a temporal simulation can be used.

The numerical code does not allow for non-zero mean mass flow through the lower and upper boundaries. However, the normal suction in the ASBL can be moved from the boundary condition to the governing equations. Hence, instead of solving the Navier–Stokes equations for V with the boundary condition $V = -V_0$, the same solution can be obtained by solving for $V - V_0$ with the boundary condition $V = 0$. In the code, the velocity-vorticity formulation of the Navier–Stokes equations is solved. The equations for the normal velocity can be written

$$\frac{\partial \phi}{\partial t} = h_V + \frac{1}{Re}\nabla^2 \phi, \tag{2}$$

$$\nabla^2 V = \phi, \tag{3}$$

where

$$h_V = \left(\frac{\partial^2}{\partial x^2} + \frac{\partial^2}{\partial z^2}\right) H_2 - \frac{\partial}{\partial y}\left(\frac{\partial H_1}{\partial x} + \frac{\partial H_3}{\partial z}\right), \tag{4}$$

$$H_1 = V\vartheta - W\eta, \quad H_2 = W\chi - U\vartheta, \quad H_3 = U\eta - V\chi. \tag{5}$$

Here $\boldsymbol{\omega} = (\chi, \eta, \vartheta)$ denote the vorticity components. The equation for the normal vorticity can be written

$$\frac{\partial \eta}{\partial t} = h_\eta + \frac{1}{Re}\nabla^2 \eta, \tag{6}$$

where

$$h_\eta = \frac{\partial H_1}{\partial z} - \frac{\partial H_3}{\partial x}. \tag{7}$$

Once V and η have been obtained, U and W can be calculated from the incompressibility constraint and the definition of the normal vorticity. In order to solve the equations with the ASBL as a base flow, the normal velocity component in (5) is modified as follows

$$H_1 = (V - V_0)\vartheta - W\eta, \quad H_3 = U\eta - (V - V_0)\chi, \tag{8}$$

where the suction velocity is specified as

$$V_0 = \frac{1}{Re}. \tag{9}$$

The above system of equations is closed by specifying boundary conditions at the edges of the computational box. At the wall, no-slip boundary condition is used, i.e.

$$\boldsymbol{U} = 0, \tag{10}$$

and at the upper boundary at the free-stream position $y = y_L$, generalized boundary condition is applied in Fourier space with different coefficients for each wavenumber. It is non-local in physical space and takes the following form

$$\frac{\partial \hat{\boldsymbol{U}}}{\partial y} + k\hat{\boldsymbol{U}} = \frac{\partial \hat{\boldsymbol{U}}_0}{\partial y} + k\hat{\boldsymbol{U}}_0, \tag{11}$$

where hats denote Fourier transform and k is the modulus of the horizontal wavenumbers ($k^2 = \alpha^2 + \beta^2$). The condition (11) represents a potential flow solution decaying away from the upper edge of the computational box. This condition decreases the required box height by damping the higher frequencies rather than forcing the disturbance velocities to a rapid decay. In the horizontal directions, periodic boundary conditions are used.

2.3. *Disturbance generation and numerical parameters*

The present numerical implementation provides several possibilities for disturbance generation. Disturbances can be included in the flow by a body force, by blowing and suction at the wall through non-homogeneous boundary conditions and by adding them in the initial velocity field. Streamwise vortices and oblique waves are representative disturbances that lead to transient growth and bypass transition to turbulence (Schmid & Henninson 1992; Elofsson & Alfredsson 1998; Reddy *et al.* 1998; Berlin *et al.* 1999; Elofsson *et al.* 1999). They are added in the form $\hat{\boldsymbol{u}}(y)\exp(\mathrm{i}\alpha x + \mathrm{i}\beta z) + \mathrm{cc}$ to the ASBL in the initial velocity field. The amplitude function $\hat{\boldsymbol{u}}(y)$ of the initial disturbance, with

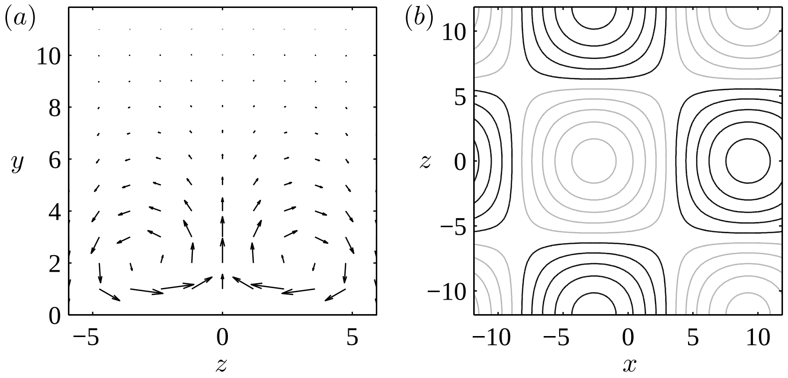

FIGURE 1. Initial optimal disturbances in the ASBL for $Re = 800$. (*a*) Cross-flow plane of the optimal streamwise vortices. (*b*) Contours of normal disturbance velocity of the oblique waves in a horizontal plane at $y = 1.6$.

given horizontal wavenumbers (α, β), is optimized to obtain the highest energy gain over a specified time period. The optimization code uses a direct-adjoint technique applied to the linear disturbance equations in the temporal frame and was originally implemented by Corbett & Bottaro (2000) that studied the algebraic growth in boundary layers subject to different streamwise pressure gradients. The optimization code was later extended to include the ASBL by Fransson & Corbett (2003). For the simulations in the present work, the streamwise vortices are optimized for $(\alpha, \beta) = (0, 0.53)$, which is the global optimal wavenumbers for $Re = 800$ found by Fransson and Corbett. The time period, which the growth is optimized for, is chosen to be 300. The oblique wave is optimized for $(\alpha, \beta) = (0.265, 0.265)$ over a time period of 75 and is introduced in the initial velocity field both for (α, β) and $(\alpha, -\beta)$. From this initial condition, the nonlinear interaction between the waves will produce streaks with wavenumbers $(\alpha, \beta) = (0, 0.53)$. Figure 1 shows the initial optimal streamwise vortices and oblique waves for $Re = 800$. The thresholds are expressed in terms of the energy density of the initial disturbance. The energy density of a disturbance (u, v, w) is given by

$$E = \frac{1}{2\mathscr{V}} \int (u^2 + v^2 + w^2) \,\mathrm{d}\mathscr{V}, \tag{12}$$

where $\mathscr{V}$ is the volume of one periodic box. Apart from the optimal disturbance, random noise is added to the initial velocity field. The noise is in the form of Stokes modes, i.e. eigenmodes of the flow operator without the convective term. These modes fulfill the equation of continuity and the boundary condition of vanishing velocity at the wall. The total energy density of the noise is set to 0.01 % of the energy density of the primary disturbance.

Scenario	*Re*	Resolution	Box size
(SV)	500	$40 \times 61 \times 64$	$11.86 \times 10 \times 11.86$
	800	$40 \times 81 \times 80$	$11.86 \times 10 \times 11.86$
	1200	$48 \times 109 \times 96$	$11.86 \times 10 \times 11.86$
(OW)	500	$80 \times 91 \times 128$	$23.71 \times 10 \times 23.71$
	800	$96 \times 109 \times 144$	$23.71 \times 10 \times 23.71$
	1200	$108 \times 129 \times 180$	$23.71 \times 10 \times 23.71$
(N)	500	$40 \times 81 \times 80$	$11.86 \times 10 \times 11.86$
	800	$40 \times 81 \times 80$	$11.86 \times 10 \times 11.86$
	1200	$48 \times 109 \times 96$	$11.86 \times 10 \times 11.86$

TABLE 1. Grid resolution and box size used for the three transition scenarios given in the order streamwise, wall-normal and spanwise direction, respectively.

The horizontal lengths of the box for scenario (SV) are $2\pi/\beta$, which corresponds to one spanwise wavelength of the optimal disturbance. In scenario (OW) the horizontal lengths of the box are doubled to fit one streamwise and spanwise period of the oblique waves. The height of the box is 10 for all simulations. Both the box height and the resolutions are carefully tested by convergence tests of the transition time and flow structures with varied box height and resolution. Dealiasing is activated in the streamwise and spanwise directions. That increases the computational resolution in the simulations with a factor of 2.25 (1.5 in each direction). The size of the computational box and the resolution used for the simulations are listed in table 1.

3. Results

3.1. *Streamwise wavelength of secondary instability*

The streak, seen as a primary disturbance, grows out of the optimal streamwise vortices introduced in the initial field as time proceeds. When the streak amplitude increases beyond a certain critical value, secondary disturbances become unstable and start to grow. The most amplified wavelength of the secondary instability is dependent of the shape and amplitude of the primary streak disturbance. To be able to quantify the size of the primary disturbance, Andersson *et al.* (2001) introduced a definition of the streak amplitude. It is defined as half the difference between the maximum and minimum of the streamwise velocity deviation, hence

$$A = \frac{1}{2}\left[\max_{y,z}(U - U_0) - \min_{y,z}(U - U_0)\right]. \tag{13}$$

Figure 2 shows a cross-flow plane of an undisturbed streak obtained from a simulation for scenario (SV) with $Re = 800$ and $E_0 = 3 \cdot 10^{-5}$, without noise in the initial field. The figure shows contours of streamwise disturbance velocity

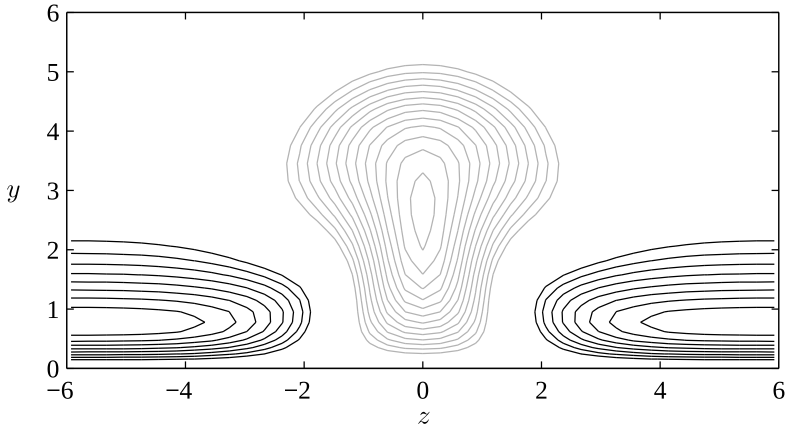

FIGURE 2. Primary streak disturbance (without noise) at $t = 400$ for scenario (SV) with $Re = 800$ and $E_0 = 3 \cdot 10^{-5}$. Contours of streamwise disturbance velocity are shown in a cross-flow plane. Black and grey lines show positive (high-speed streak) and negative (low-speed streak) values, respectively. The line spacing is 0.025 but the zero contour is not displayed.

at $t = 400$. In absence of noise, no secondary disturbances exist to set off secondary instability and the flow stays laminar.

When a secondary disturbance grows on a streak, the length of the periodic box will affect its wavelength. Thus, one can either perform the simulations with a very long box to let the simulation decide the wavelength of the secondary instability, or select the box length to match one streamwise wavelength of the secondary disturbance. The latter alternative is used in this paper, where many simulations are required to find the energy thresholds. That constrains the investigation to disturbances with wavenumbers that fit the periodic box. The first alternative is however tested in one simulation for scenario (SV) to determine the naturally preferred instability wavelength. In that simulation, which is performed for $Re = 800$ and $E_0 = 3 \cdot 10^{-5}$, the length of the box is $40\pi/\beta$ and the resolution is $480 \times 51 \times 40$. The obtained flow at $t = 400$ in a part of the box is shown in figure 3, where contours of the streamwise disturbance velocity is drawn. At the given time, the streak is clearly unstable to secondary disturbances and eleven streamwise waves with varying length are present in the box. The shorter waves grow more than the longer waves and can thus be considered to be more unstable. The corresponding streamwise wavenumber is approximately $\alpha = 0.4$. However, that value is likely to vary slightly with Reynolds number, initial energy density of the primary disturbance and the noise.

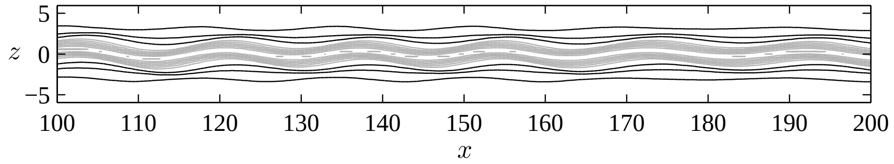

Figure 3. Natural secondary instability of a streak at $t = 400$ for scenario (SV) with $Re = 800$ and $E_0 = 3 \cdot 10^{-5}$. Contours of streamwise disturbance velocity are shown in a horizontal plane at $y = 1.6$. Black and grey lines show positive and negative values, respectively. The line spacing is 0.05 but the zero contour is not displayed.

An additional method of finding the most amplified streamwise wavelength is used. By determining the linear impulse response (Brandt *et al.* 2003) for the base flow with a pure streak extracted from scenario (SV) without noise, as the streak shown in figure 2, the growth rate versus the streamwise wavenumber can be calculated. The method solves the disturbance equations in time and space, linearized around the streaky base flow at a fixed time instant. The assumption of constant streak amplitude is justified since the secondary instability is inviscid in nature and therefore leads to a fast growth in comparison to the growth of the streak itself. The base flow is spanwise periodic and symmetric with respect to the (x, y)-plane. As a consequence, it admits two classes of normal modes: a sinuous mode and a varicose mode. The initial condition representing the impulse response for the secondary disturbance triggers two counter-rotating streamwise vortex pairs. It has been used previously by Henningson *et al.* (1993) and Bech *et al.* (1998) and potentially excites both the sinuous and varicose modes. As time proceeds, the disturbance rides on the streaky base flow and evolves into a dispersive wave packet.

The linear impulse response is calculated for the streak in the time interval 200-600 with steps of 100. Spatio-temporal diagnostic tools are used in order to evaluate the simulation results for growth rates in the asymptotic limit where the disturbances are considered to grow exponentially. The growth rates are denoted ω_i and σ, where the former is strictly temporal and the latter is the spatio-temporal counterpart as observed while traveling with the group velocity v_g. For further details on how these quantities are evaluated, the reader is referred to Delbende & Chomaz (1998) and Delbende *et al.* (1998). Figures 4(a) and 4(b) show the obtained sinuous type growth rates for the different streak time instants versus the streamwise wavenumber and the group velocity, respectively. The varicose mode attains about half the growth rate and is not displayed here. According to Delbende *et al.* (1998), the overall maximum of both type of growth rates will coincide. This quantity, denoted σ^{max}, is summarized in table 2 for the different time instants, together with its corresponding streamwise wavenumber α^{max} and group velocity v_g^{max}. Further

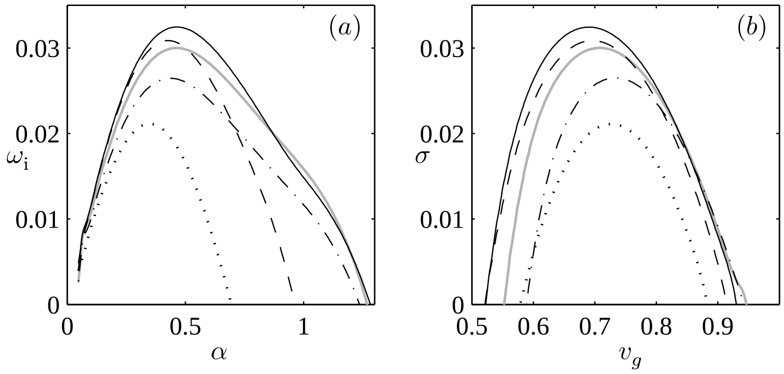

FIGURE 4. Linear impulse response for a streak with $Re = 800$ and $E_0 = 3 \cdot 10^{-5}$. Streaks extracted for $t = 200$ (dotted line), 300 (dashed line), 400 (solid line), 500 (grey line) and 600 (dash-dotted line). (*a*) Temporal growth rate $\omega_{\rm i}$ versus streamwise wavenumber α. (*b*) Spatio-temporal growth rate σ versus group velocity v_g.

t	A	α^{max}	σ^{max}	v_g^-	v_g^{max}	v_g^+
200	0.33	0.35	0.021	0.58	0.73	0.88
300	0.36	0.42	0.031	0.52	0.70	0.91
400	0.35	0.47	0.033	0.52	0.69	0.93
500	0.33	0.46	0.030	0.55	0.71	0.95
600	0.32	0.43	0.027	0.59	0.73	0.94

TABLE 2. Comparison of linear impulse response for the streak at different time instants. The data complements figure 4.

information in table 2 is the amplitude of the streak defined as in (13) and the trailing-edge and leading-edge velocities of the wave packet, where $\sigma = 0$, denoted v_g^- and v_g^+, respectively. The instability of the wave packet riding on the streak is clearly convective. The group velocities of the trailing and leading edge are around 52 % and 95 % of the free-stream velocity, respectively. Brandt *et al.* (2003) found a trailing-edge velocity of about 67 % for the wave packet riding on a streak with $A = 0.36$ in the BBL, while the leading-edge velocity was found to be about the same as for the ASBL. The overall largest growth rate is obtained for $\alpha^{max} = 0.47$ for the streak at $t = 400$. Andersson *et al.* (2001) studied the secondary instability and breakdown of streamwise steaks in the BBL. They found that the growth rate and streamwise wavenumber increase with the streak amplitude. The critical amplitude of the streak, beyond which streamwise traveling waves are excited, was found to be about 26 % of the free-stream velocity. The results for the ASBL show the same general behavior. That explains why the waves in the long-box simulation is longer, with a corresponding smaller value of the streamwise wavenumber. The longest waves start to grow at a smaller streak amplitude and thus have longer time to develop. As waves with different lengths start to grow at different streak amplitudes and hence at different time instants, it is difficult to judge which streamwise wavenumber that dominates the secondary instability. With that in consideration and the fact that the maximum growth rates are rather insensitive to the streamwise wavenumber, the box length is set equal to the box width throughout this investigation.

3.2. *Simulations of transition*

3.2.1. *Transition thresholds*

As mentioned in the introduction, the ASBL is stable to infinitesimal disturbances below a critical Reynolds number of 54370 (Hocking 1975). However, a transient disturbance growth may occur for much lower Reynolds numbers. If the initial energy of the disturbance exceeds a certain threshold value transition occurs. The energy threshold of the primary disturbance typically decreases with Reynolds number. Previous investigations have mainly been concerned with determining the negative exponent γ, relating to the initial amplitude of the primary disturbance as $A_0 \propto Re^{\gamma}$. In this representation, the scenario with the smallest exponent will most easily become turbulent when sufficiently large Reynolds numbers are considered. Trefethen *et al.* (1993) used simple models to feed transient growth by nonlinearities and conjectured that for the Navier–Stokes equations, γ must be ≤ -1. Later Baggett & Trefethen (1997) reviewed several mathematical models of transition in parallel shear flows collected from different research groups, and found the exponents $-3 \leq \gamma \leq -1$ depending on model and base flow. However, they conclude that for actual flows in pipes and channels, the range is more likely $-2 \leq \gamma < -1$. Most investigations dealing with this relationship focus on plane channel flows. Kreiss *et al.* (1994) obtained through DNS the threshold exponent $\gamma = -1$, for transition in plane Couette flow initiated by streamwise vortices. Numerical studies by Lundbladh *et al.* (1994) indicate that for scenario (SV), the exponent is $-7/4$ for plane Poiseuille flow, while for scenario (OW), the exponents are $\gamma = -5/4$ and $-7/4$ for plane Couette and plane Poiseuille flow, respectively. Reddy *et al.* (1998) approximately confirm these values. The quoted numerical simulations are limited to Reynolds numbers less than 5000. Chapman (2002) used an asymptotic ($Re \to \infty$) analysis of the Navier–Stokes equations to study the threshold exponents for transition in plane Couette and plane Poiseuille flow initiated by streamwise vortices and oblique waves. He finds the exponents to be different than in the above mentioned works (Lundbladh *et al.* 1994; Reddy *et al.* 1998). Chapman explains this difference by the fact that the asymptotic values are only reached for very large Reynolds numbers, of order 10^6, where the scaling laws of the transient growth is different than for the Reynolds numbers used in the numerical simulations. Recent experiments on pipe flow by Hof *et al.* (2003)

indicate that the required disturbance amplitude to cause transition scales as Re^{-1}.

For boundary layer flows, little work aimed in this direction is found, mainly because of difficulties to define such a relationship as the local Reynolds number changes with the boundary layer thickness. However, tools for transition prediction in boundary layers have been developed for half a century. Andersson *et al.* (1999) proposed a relation for bypass transition prediction in the BBL. The relation states that the Reynolds number (based on the boundary layer thickness) at transition scales as -1 with the level of FST. It is based on transient growth theory together with the assumption that the initial disturbance energy is proportional to the FST energy. Levin & Henningson (2003) later generalized the relation to the Falkner–Skan boundary layer. Fransson *et al.* (2005) experimentally showed a very good correlation to the relation in the BBL.

In a parallel boundary layer such as the ASBL, the Reynolds number based on the boundary layer thickness is constant and therefore the procedure to find the threshold energy is straightforward. When a simulation is found to reach transition, another one is simply carried out with smaller initial energy until the accuracy is considered sufficient. It is also of interest to determine the time (t_T) when transition occurs. There are several methods of determining if transition has taken place. For example, it can be defined by the appearance of sharp peaks of some flow quantity like the velocity components, energy density or wall shear stress. In the present work, the Reynolds number based on the mean friction velocity, Re_τ, provides a well-defined measure. Transition is defined to appear when the friction velocity Reynolds number exceeds a certain critical value that is chosen, based on the results, to be 26, 38 and 50 for Reynolds number 500, 800 and 1200, respectively. However, at low Reynolds numbers and large initial energies of the primary disturbance, this definition breaks down for scenario (SV) and (OW). This is because the initial disturbance produces a larger mean friction velocity than the turbulence itself. Examples of the evolution of the friction velocity Reynolds number are shown in figure 5, where transition takes place at the rapid growth of the friction velocity Reynolds number around $t = 800$.

Before presenting the results, two things need to be mentioned about these simulations. Firstly, we register transition as the process when the fluid goes into the turbulent state. However, the simulations are not continued to ensure that turbulence is sustained over time. Secondly, random noise is added to the primary disturbance in the (SV) and (OW) simulations. This is especially important in scenario (SV) where we need to break the symmetry of the streak, which otherwise would decay (Gustavsson 1991). Increasing the energy level of the noise makes the flow more unstable and transition appears earlier as shown in figure 5(a). Figure 5(b) shows that distributing the energy of the noise differently affects the course of events somewhat as well, despite the low initial energy compared to that of the primary disturbance. In this investigation, one

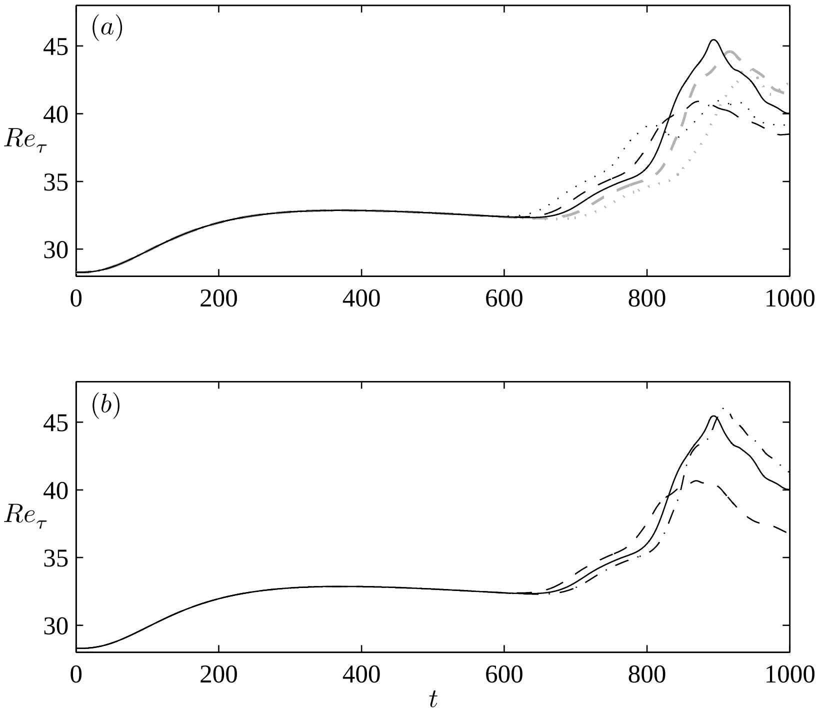

FIGURE 5. Effect of noise on the friction velocity Reynolds number Re_τ for scenario (SV) with $Re = 800$ and $E_0 = 3{\cdot}10^{-5}$. (*a*) Constant seed number and various initial energy density quota between noise and primary disturbance. Black lines: Solid 0.01 %, dashed 0.02 %, dotted 0.05 %. Grey lines: dashed 0.005 %, dotted 0.002 %. (*b*) Various seed numbers, keeping initial energy quotient set to 0.01 %.

noise setup is used, thus our obtained energy threshold must be considered as an upper bound, since more optimal disturbance configurations that would lead to transition for lower initial energies may exist.

3.2.2. *Transition initiated by streamwise vortices*

In the simulations of scenario (SV), the initial condition consists of optimal streamwise vortices (see figure 1*a*) and a small amount of random noise to set off secondary instability. The size and resolution of the box for the three simulated Reynolds numbers 500, 800 and 1200 are specified in table 1. The flow pattern of the simulation for $Re = 800$ and $E_0 = 3 \cdot 10^{-5}$ is shown in figure 6, where lines of constant streamwise disturbance velocity are plotted in a horizontal plane at $y = 1.6$. At the start of this simulation, the initiated streamwise vortices evolve into streaks by the lift-up effect. Figure 6(*a*) shows

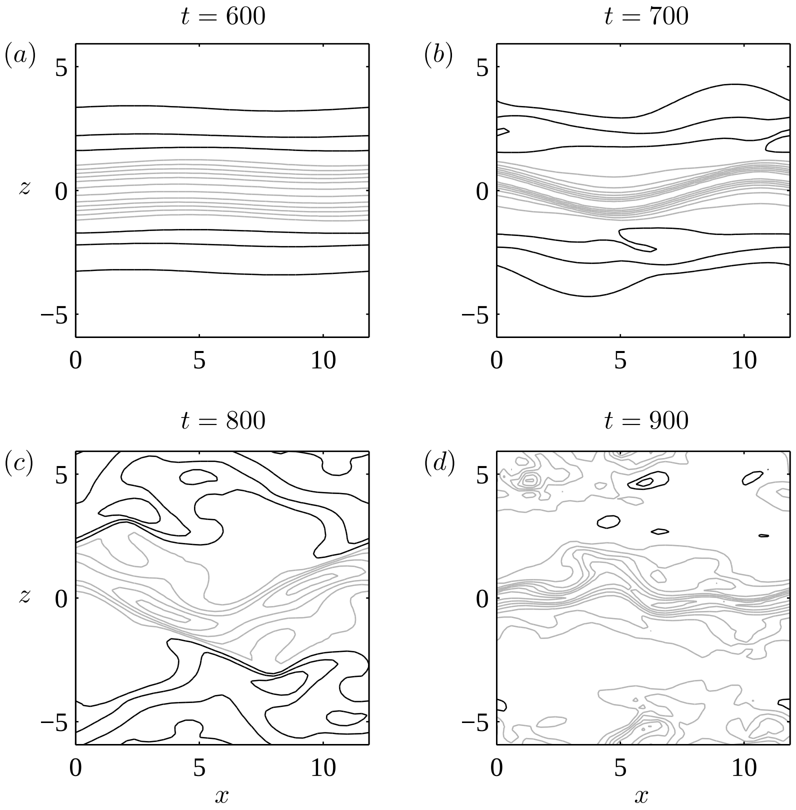

FIGURE 6. Flow pattern close to transition for scenario (SV) with $Re = 800$ and $E_0 = 3 \cdot 10^{-5}$. Contours of streamwise disturbance velocity are shown in a horizontal plane at $y = 1.6$ at time instants 600 (*a*), 700 (*b*), 800 (*c*) and 900 (*d*). Black and grey lines show positive and negative values, respectively. The line spacing is 0.05 but the zero contour is not displayed.

the resulting streak at $t = 600$. Grey lines demonstrate negative disturbance velocity, i.e. the low speed streak positioned around $z = 0$. At $t = 700$, shown in figure 6(*b*), a secondary instability has developed that deforms the streak in a sinuous manner with a streamwise wavelength equal to the box length. Figure 6(*c*) shows the state at $t = 800$, which is close to the breakdown to turbulence. According to our definition, the transition time in this case is 820. The solid line in figure 5(*a*) shows the evolution of Re_τ for this simulation. For the undisturbed base flow $Re_\tau = \sqrt{Re}$, which is also very close to the initial value in the figure. This quantity shows a rather slow increase as the streaks form and grow in amplitude, followed by a rapid growth as the streaks break

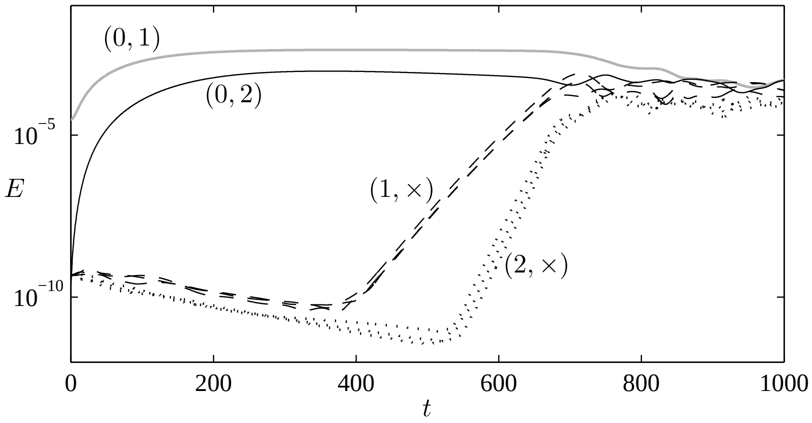

FIGURE 7. Energy content in Fourier modes (α_1, β_1) for scenario (SV) with $Re = 800$ and $E_0 = 3 \cdot 10^{-5}$. The initially excited mode $(0, 1)$ is shown by the grey solid line, while the nonlinearly generated modes are shown by black lines. The modes are indicated in the figure and × denotes 0, 1 or 2.

down and transition occurs. The early turbulent state succeeding breakdown is shown in figure 6(*d*), which shows the flow pattern at $t = 900$.

Further insight into the transition process is provided by the energy evolution of the Fourier components, shown in figure 7. The velocity field is Fourier transformed in the horizontal directions and (α_1, β_1) denotes the streamwise and spanwise wavenumbers, respectively, each normalized with the corresponding fundamental wavenumbers. The initial energy is fed into streamwise vortices $(0, 1)$ shown as the grey line in figure 7. This mode grows algebraically as transient growth place energy into the streamwise velocity component (the streak). The superharmonic streak mode $(0, 2)$ also experience an algebraic growth although the energy content in this mode is at least one decade smaller. At about $t = 400$, the streak reaches its largest amplitude. At the same time, the secondary instability is triggered and the modes $(1, 0\text{-}2)$ show an exponential growth. At later instants higher harmonics start to grow exponentially; the modes $(2, 0\text{-}2)$ are shown in the figure. Transition is obtained as the energy content of these modes are of the same order as that for the streak.

3.2.3. *Transition initiated by oblique waves*

In the simulations of scenario (OW), the initial condition consists of two optimal oblique waves (see figure 1*b*) oriented 45 degrees angle to the free-stream direction, one in the positive spanwise direction and the other in the negative. The same random noise as for scenario (SV) is added to the initial field. The size and resolution of the box for the simulations are given in table 1. Contours of constant streamwise disturbance velocity in a horizontal plane at $y = 1.6$

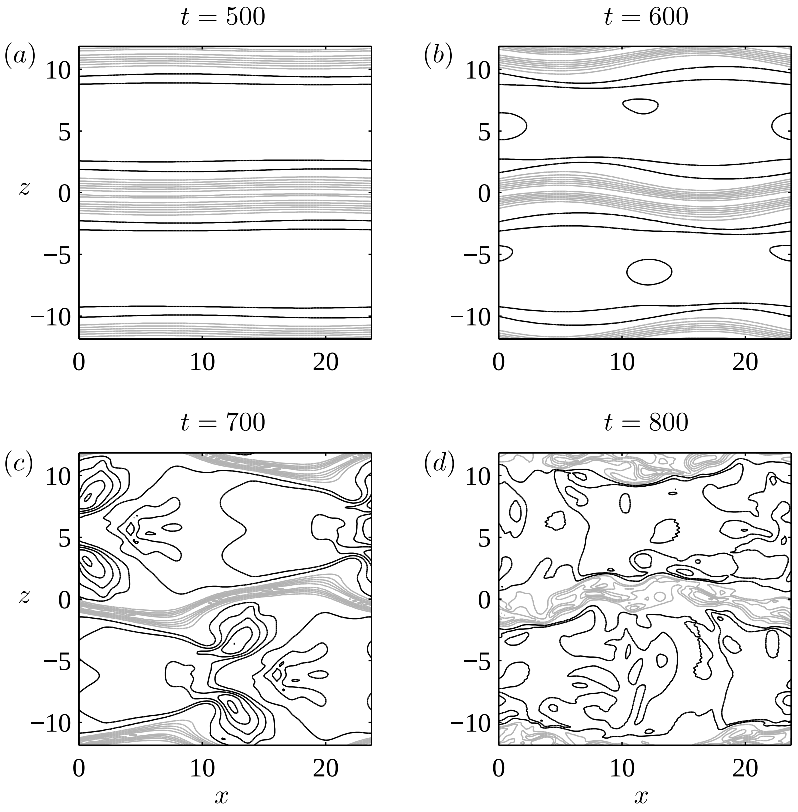

FIGURE 8. Flow pattern close to transition for scenario (OW) with $Re = 800$ and $E_0 = 1 \cdot 10^{-5}$. Contours of streamwise disturbance velocity are shown in a horizontal plane at $y = 1.6$ at time instants 500 (*a*), 600 (*b*), 700 (*c*) and 800 (*d*). Black and grey lines show positive and negative values, respectively. The line spacing is 0.05 but the zero contour is not displayed.

are shown in figure 8 from the simulation for $Re = 800$ and $E_0 = 1 \cdot 10^{-5}$. At the start of this scenario, the initiated pair of oblique waves interact with each other and streamwise vortices with half the spanwise wavelength are created. The streamwise vortices again evolve into streaks due to the lift-up effect. Figure 8(*a*) shows two spanwise periods of streaks at $t = 500$. In the presence of the oblique modes, the secondary instability is of the varicose type with horizontal wavelengths equal to these of the oblique waves, and thus also of the horizontal box dimension. At $t = 600$, shown in figure 8(*b*), the secondary instability has developed and deforms the streaks. Figure 8(*c*) shows the flow pattern at $t = 700$ close to the transition time, which with our definition becomes 731.

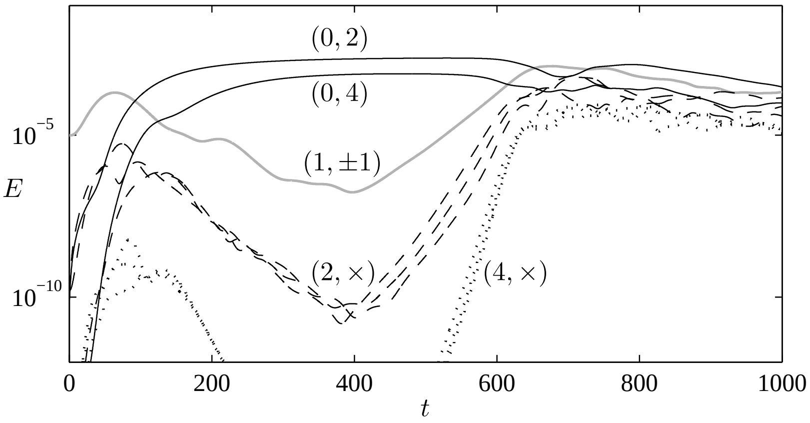

FIGURE 9. Energy content in Fourier modes (α_1, β_1) for scenario (OW) with $Re = 800$ and $E_0 = 1 \cdot 10^{-5}$. The initially excited modes $(1, \pm 1)$ are shown by the grey solid line, while the nonlinearly generated modes are shown by black lines. The modes are indicated in the figure and × denotes 0, 2 or 4.

The early turbulent state succeeding breakdown is shown in figure 8(*d*), which shows the flow pattern at $t = 800$.

Figure 9 shows the energy evolution of the Fourier components. The initial energy is fed into the oblique wave modes $(1, \pm 1)$ shown as the grey line in the figure. These modes grow initially due to linear transient effects, but start decaying rather quickly as the energy is nonlinearly redistributed into the streamwise vortices $(0, 2)$. These vortices produce streamwise streaks with spanwise wavenumber 0.53 as for scenario (SV). From this point, scenarios (OW) and (SV) are similar in behavior since both contain the instability and breakdown of streaks. However, when the streak amplitude is large enough for the secondary instability to set in, at $t \approx 400$, the oblique wave modes $(1, \pm 1)$ still contain a considerable amount of energy. Since the oblique modes are associated with a varicose or symmetric streak instability this will have the opposite spanwise symmetry compared to the sinuous or antisymmetric secondary instability found in scenario (SV). As a consequence, these wavelengths become twice as large compared to the streak breakdown in scenario (SV).

3.2.4. *Threshold energy*

In addition to scenarios (SV) and (OW), a corresponding investigation for scenario (N) is performed. In these simulations, the initial disturbance consists of noise only. This noise is the same as for the other simulations, but with a considerably higher level of initial energy density, which is required for breakdown to turbulence to occur. The size and resolution for scenario (N) are reported in table 1. Figure 10 shows the energy evolution of the Fourier components in the

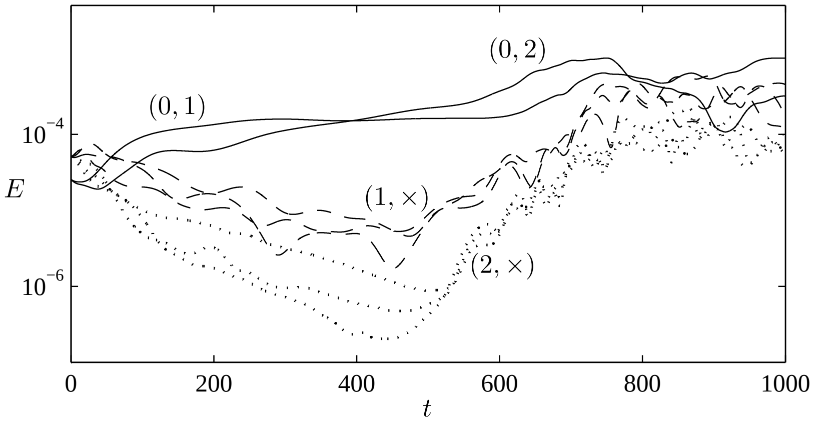

FIGURE 10. Energy content in Fourier modes (α_1, β_1) for scenario (N) with $Re = 800$ and $E_0 = 3.2 \cdot 10^{-4}$. The modes are indicated in the figure and × denotes 0, 1 or 2.

simulation with $Re = 800$ and $E_0 = 3.2 \cdot 10^{-4}$. The initial energy is distributed in the modes with $|\alpha_1| \leq 2$ and $|\beta_1| \leq 2$. The streak modes $(0, 1)$ and $(0, 2)$ grow algebraically while the other modes shown in the figure decay until about $t = 500$, when secondary instabilities are triggered. Transition occurs as the energy content of these modes are of the same order as for the streak modes. For our definition of the transition time, this appears at $t = 729$. The transition mechanism for scenario (N) seems to be the same as for scenario (SV). Streaks are produced of the random noise and breakdown occurs as a result of a secondary streak instability.

In order to compare the threshold energies for the three scenarios, the time of transition t_T for each initial energy density E_0 of the simulations are summarized in figure 11. The lines connecting the data are extrapolated towards $t_T \to \infty$ for the lowest obtained energy that leads to breakdown before $t = 2000$ of each case. The figure shows how the time of transition decreases as the initial energy of the primary disturbance increases. This trend is less significant for scenario (N) where rather high energies are required to obtain transition. The most competitive initial disturbance, of the ones considered herein, in terms of transition at low energy/short time is the pair of oblique waves. Scenario (N), on the other hand, requires 1-2 orders of magnitude larger energy.

The energy thresholds for transition, extracted from figure 11 (where the lines approach the time 2000), are plotted for their respective Reynolds number in figure 12. The solid lines represent least square fits of the formula $E_0 \propto Re^{2\gamma}$, and the determined proportionality constants and exponents are given inside the plot. The exponents for scenarios (SV) and (N) are with the present accuracy, equal. However, with increased accuracy, the exponent for scenario (SV) becomes slightly lower than for scenario (N). As mentioned

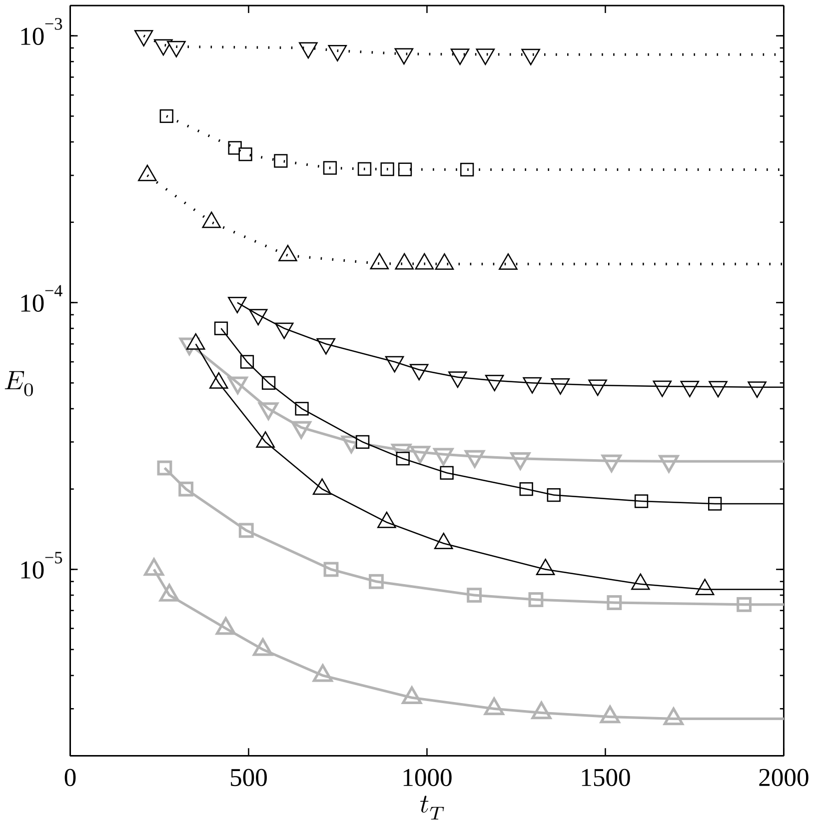

FIGURE 11. Transition time as a function of initial energy density. Black lines (SV), grey lines (OW) and dotted lines (N) for Reynolds number 500 ($\bigtriangledown$), 800 ($\square$) and 1200 ($\triangle$).

above, scenario (N) essentially seem to be another way to trigger streaks. Thus it is not surprising that the exponents are adjacent. Since random noise is not the optimal disturbance distribution to create streaks, a higher initial energy is required for transition to occur. The steepest slope is obtained for scenario (OW), which thereby will have the highest potential to trigger transition also for larger Reynolds numbers than considered here. This is in agreement with previous investigations of plane Couette flow (Lundbladh *et al.* 1994).

4. Conclusions

In the present study, several scenarios of bypass transition are investigated for the asymptotic suction boundary layer (ASBL). This flow is strictly parallel in the sense of constant thickness of the boundary layer, which allows for direct numerical simulations in the temporal regime. However, the temporal assumption limits the analysis to periodic disturbances with horizontal wavenumbers

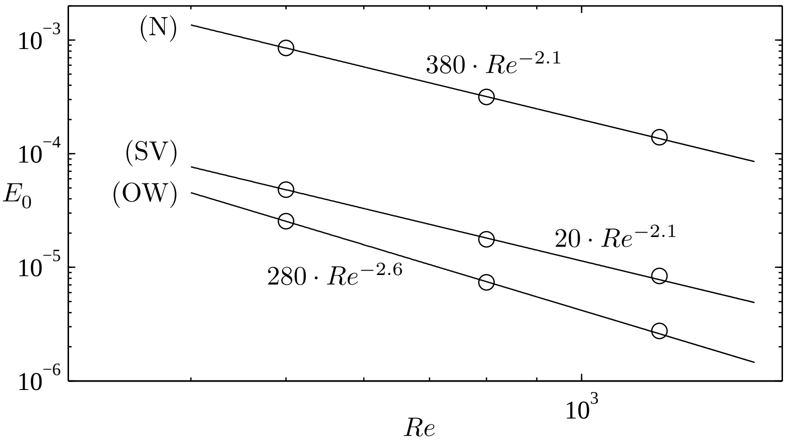

FIGURE 12. Threshold energy density for the three scenarios, streamwise vortices (SV), oblique waves (OW) and random three-dimensional noise (N). The circles correspond to data from the DNS. The lines are fits to the data with their corresponding functions indicated beside.

determined by the computational box size. The work aims at finding energy thresholds for generic disturbances that are known to lead to transition with low initial energies and not for the most likely disturbances that may be present in the flow. Furthermore, the receptivity of the flow is not considered. Three scenarios are considered: growth and breakdown of streaks initiated by streamwise vortices (SV), oblique transition where an oblique wave pair (OW) is used to trigger the streamwise vortices, and three-dimensional random noise (N). These scenarios are well established and thoroughly investigated for other flows (Kreiss *et al.* 1994; Lundbladh *et al.* 1994; Reddy *et al.* 1998; Chapman 2002). The different stages of transition are identified and found to be in accordance with previous work on channel flows and boundary layers.

For scenario (SV), simulations of secondary disturbances are performed in order to study the influence of the box length. The result is a wave packet with a trailing-edge velocity of 0.52, to be compared with 0.67 for the Blasius boundary layer (BBL) (Brandt *et al.* 2003). The leading-edge velocity is 0.95, which is similar to what is found for the BBL. Growth rates are also calculated, which become largest for the sinuous instability mode with a streamwise wavenumber comparable to the spanwise wavenumber of the streak.

The obtained threshold energies for the three transition scenarios scale with Reynolds number as $Re^{-2.6}$ (OW), $Re^{-2.1}$ (SV) and $Re^{-2.1}$ (N). These values correspond to slightly below -1 when considering disturbance amplitudes, which agree reasonably well with numerical investigations for other flows. For the present accuracy, the exponents for scenarios (SV) and (N) are equal. The reason may be that the underlying transition mechanisms are identical, since noise also gives rise to transient growth of streaks. However, the required initial energy of the noise for transition to occur is higher since the noise is far from the optimal configuration to trigger streaks. It is important, when considering the likelihood of these scenarios to appear in practice, to consider the initial energy of the disturbance required to achieve transition. For the investigated domain of Reynolds numbers, oblique transition clearly posses the largest potential to transform this flow into the turbulent state. It also has the steepest threshold curve, indicating that this scenario will dominate even more as the Reynolds number is increased.

A similar study was made by Schmid *et al.* (1996) by simulations of a temporally growing BBL for the initial Reynolds number 500. Their lowest threshold is obtained for scenario (OW) and the value is $\simeq 8 \cdot 10^{-7}$, to be compared to $2.7 \cdot 10^{-5}$ obtained from our curve fits. For scenario (SV) the roles are opposite but the energies are larger. Keeping in mind that a temporal simulation of the BBL does not represent the fully physical situation, these results indicate that perhaps the physics of the ASBL makes this boundary layer more resistant to the initial nonlinear redistribution necessary to obtain the growing streaks out of the oblique waves. Such investigations are left for future studies, however.

The authors are grateful to Luca Brandt for helping us with the calculations of the linear impulse response. We are also thankful to Peter Corbett, Alessandro Bottaro and Jens Fransson for letting us use their disturbance optimization code. Use of computational resources at High Performance Computing Center North (HPC2N) is also gratefully acknowledged. This work has been financed through the program of Energy Related Fluid Mechanics operated by the Swedish Energy Agency.

References

Andersson, P., Berggren, M. & Henningson, D. S. 1999 Optimal disturbances and bypass transition in boundary layers. *Phys. Fluids* **11**, 134–150.

Andersson, P., Brandt, L., Bottaro, A. & Henningson, D. S. 2001 On the breakdown of boundary layer streaks. *J. Fluid Mech.* **428**, 29–60.

Baggett, J. S. & Trefethen, L. N. 1997 Low-dimensional models of subcritical transition to turbulence. *Phys. Fluids* **9**, 1043–1053.

Balakumar, P. & Hall, P. 1999 Optimum suction distribution for transition control. *Theoret. Comput. Fluid Dyn.* **13**, 1–19.

Bech, K. H., Henningson, D. S. & Henkes, R. A. W. M. 1998 Linear and nonlinear development of localized disturbances in zero and adverse pressure gradient boundary-layers. *Phys. Fluids* **10**, 1405–1418.

Berlin, S., Lundbladh, A. & Henningson, D. S. 1994 Spatial simulations of oblique transition in a boundary layer. *Phys. Fluids* **6**, 1949–1951.

Berlin, S., Wiegel, M. & Henningson, D. S. 1999 Numerical and experimental investigations of oblique boundary layer transition. *J. Fluid Mech.* **393**, 23–57.

Brandt, L., Cossu, C., Chomaz, J.-M., Huerre, P. & Henningson, D. S. 2003 On the convectively unstable nature of optimal streaks in boundary layers. *J. Fluid Mech.* **485**, 221–242.

Brandt, L., Schlatter, P. & Henningson, D. S. 2004 Transition in boundary layers subject to free-stream turbulence. *J. Fluid Mech.* **517**, 167–198.

Chapman, S. J. 2002 Subcritical transition in channel flows. *J. Fluid Mech.* **451**, 35–97.

Corbett, P. & Bottaro, A. 2000 Optimal perturbations for boundary layers subject to stream-wise pressure gradient. *Phys. Fluids* **12**, 120–130.

Delbende, I. & Chomaz, J.-M. 1998 Nonlinear convective/absolute instabilities in parallel two-dimensional wakes. *Phys. Fluids* **10**, 2724–2736.

Delbende, I., Chomaz, J.-M. & Huerre, P. 1998 Absolute and convective instabilities in the Batchelor vortex: a numerical study of the linear impulse response. *J. Fluid Mech.* **355**, 229–254.

Elofsson, P. A. & Alfredsson, P. H. 1998 An experimental study of oblique transition in plane Poiseuille flow. *J. Fluid Mech.* **358**, 177–202.

Elofsson, P. A., Kawakami, M. & Alfredsson, P. H. 1999 Experiments on the stability of streamwise streaks in plane Poiseuille flow. *Phys. Fluids* **11**, 915–930.

Fasel, H. F., Thumm, A. & Bestek, H. 1993 Direct numerical simulation of transition in supersonic boundary layers: oblique breakdown. In *Transitional and Turbulent Compressible Flows* (eds. L. D. Kral & T. A. Zang), vol. 151, pp. 77–92. ASME FED.

Fransson, J. H. M. & Alfredsson, P. H. 2003 On the disturbance growth in an asymptotic suction boundary layer. *J. Fluid Mech.* **482**, 51–90.

Fransson, J. H. M. & Corbett, P. 2003 Optimal linear growth in the asymptotic suction boundary layer. *Eur. J. Mech. B/Fluids* **22**, 259–270.

Fransson, J. H. M., Matsubara, M. & Alfredsson, P. H. 2005 Transition induced by free-stream turbulence. *J. Fluid Mech.* **527**, 1–25.

Gustavsson, L. H. 1991 Energy growth of three-dimensional disturbances in plane Poiseuille flow. *J. Fluid Mech.* **224**, 241–260.

Henningson, D. S., Lundbladh, A. & Johansson, A. V. 1993 A mechanism for bypass transition from localized disturbances in wall-bounded shear flows. *J. Fluid Mech.* **250**, 169–238.

Hocking, L. M. 1975 Non-linear instability of the asymptotic suction velocity profile. *Quart. J. Mech. Appl. Math.* **28**, 341–353.

Hof, B., Juel, A. & Mullin, T. 2003 Scaling of the turbulence transition threshold in a pipe. *Phys. Rev. Lett.* **91**, 244502.

Joslin, R. D. 1998 Aircraft laminar flow control. *Annu. Rev. Fluid Mech.* **30**, 1–29.

Kreiss, G., Lundbladh, A. & Henningson, D. S. 1994 Bounds for threshold amplitudes in subcritical shear flows. *J. Fluid Mech.* **270**, 175–198.

Levin, O. & Henningson, D. S. 2003 Exponential vs algebraic growth and transition prediction in boundary layer flow. *Flow, Turb. Combust.* **70**, 183–210.

Lundbladh, A., Berlin, S., Skote, M., Hildings, C., Choi, J., Kim, J. &

Henningson, D. S. 1999 An efficient spectral method for simulation of incompressible flow over a flat plate. *Tech. Rep.* KTH, Department of Mechanics, Stockholm.

Lundbladh, A., Henningson, D. S. & Reddy, S. C. 1994 Threshold amplitudes for transition in channel flows. In *Transition, Turbulence, and Combustion* (eds. M. Y. Hussaini, T. B. Gatski & T. L. Jackson), vol. 1, pp. 309–318. Kluwer Academic Publishers.

MacManus, D. G. & Eaton, J. A. 2000 Flow physics of discrete boundary layer suction-measurements and predictions. *J. Fluid Mech.* **417**, 47–75.

Matsubara, M. & Alfredsson, P. H. 2001 Disturbance growth in boundary layers subjected to free-stream turbulence. *J. Fluid Mech.* **430**, 149–168.

Nordström, J., Nordin, N. & Henningson, D. S. 1999 The fringe region technique and the Fourier method used in the direct numerical simulation of spatially evolving viscous flows. *SIAM J. Sci. Comput.* **20**, 1365–1393.

Pralits, J. O., Hanifi, A. & Henningson, D. S. 2002 Adjoint-based optimization of steady suction for disturbance control in incompressible flows. *J. Fluid Mech.* **467**, 129–161.

Reddy, S. C., Schmid, P. J., Baggett, J. S. & Henningson, D. S. 1998 On stability of streamwise streaks and transition thresholds in plane channel flows. *J. Fluid Mech.* **365**, 269–303.

Rioual, J.-L., Nelson, P. A., Hackenberg, P. & Tutty, O. R. 1996 Optimum drag balance for boundary-layer suction. *J. Aircraft* **33**, 435–438.

Roberts, P. J. D. & Floryan, J. M. 2001 Boundary layer instability induced by surface suction. *Phys. Fluids* **13**, 2543–2552.

Schmid, P. J. & Henninson, D. S. 1992 A new mechanism for rapid transition involving a pair of oblique waves. *Phys. Fluids A* **4**, 1986–1989.

Schmid, P. J., Reddy, S. C. & Henningson, D. S. 1996 Transition thresholds in boundary layer and channel flow. In *Advances in turbulence VI* (eds. S. Gavrilakis, L. Machiels & P. A. Monkewitz), pp. 381–384. Kluwer Academic Publishers.

Thibert, J. J., Reneaux, J. & Schmitt, V. 1990 ONERA activities in drag reduction. In *17^{th} Congr. Int. Counc. Aeron. Sci.*, pp. 1053–1064. ICAS.

Trefethen, L. N., Trefethen, A. E., Reddy, S. C. & Driscoll, T. A. 1993 Hydrodynamic stability without eigenvalues. *Science* **261**, 578–584.

Westin, K. J. A., Boiko, A. V., Klingmann, B. G. B., Kozlov, V. V. & Alfredsson, P. H. 1994 Experiments in a boundary layer subjected to free stream turbulence. Part 1. Boundary layer structure and receptivity. *J. Fluid Mech.* **281**, 193–218.

Yoshioka, S., Fransson, J. H. M. & Alfredsson, P. H. 2004 Free stream turbulence induced disturbances in boundary layers with wall suction. *Phys. Fluids* **16**, 3530–3539.

Zuccher, S., Luchini, P. & Bottaro, A. 2004 Algebraic growth in a Blasius boundary layer: optimal and robust control by mean suction in the nonlinear regime. *J. Fluid Mech.* **513**, 135–160.

Paper 5

Turbulent spots in the asymptotic suction boundary layer

By Ori Levin

KTH Mechanics, SE-100 44 Stockholm, Sweden

Amplitude thresholds for transition of localized disturbances, their breakdown to turbulence and the development of turbulent spots in the asymptotic suction boundary layer are studied using direct numerical simulations. A parametric study of the horizontal scales of the initial disturbance is performed and the disturbance that lead to the highest growth under the conditions investigated are used in the simulations. It is found that the threshold amplitude scales like $Re^{-1.5}$ for $500 \leq Re \leq 1200$, based on the free-stream velocity and the displacement thickness. For $Re \leq 367$, the localized disturbance does not lead to a turbulent spot. The localized disturbance develops into a hairpin vortex. When it breaks down to a turbulent spot, it happens through the development of hairpin vortex heads and spiral vortices. The shape and spreading rate of the turbulent spot are determined for $Re = 500$, 800 and 1200. Flow visualizations reveal that the turbulent spot takes a bullet-shaped form that becomes more distinct for higher Reynolds numbers. Long streaks extend in front of the spot and in its wake, a calm region exists. The spreading rate of the turbulent spot is found to increase with increasing Reynolds number.

1. Introduction

In natural transition, the breakdown to turbulence typically starts in isolated regions initiated by disturbances present in the laminar flow. These turbulent spots grow in size as they propagate downstream and merge together to form a fully developed turbulent flow. Turbulent spots were first observed by Emmons (1951) in shallow water flowing down an inclined plate. Since then, turbulent spots and their development have been investigated extensively in channel flows and boundary layers.

The early experimental work of turbulent spots in boundary layers has been reviewed by Riley & Gad-el-Hak (1985). Flow visualizations of Elder (1960) and Cantwell *et al.* (1978) reveal that the turbulent spot in the boundary layer over a flat plate takes the form of an arrowhead with its tip pointing in the downstream direction. The leading edge develops an overhang over the laminar boundary layer. Behind the spot, a nonturbulent region with streaks can be seen. The laminar flow in the wake of the turbulent spot turns out to be more stable and has been termed a calmed region. The leading and trailing edges propagate at about 90 % and 50 % of the free-stream velocity, respectively, while the lateral spreading is at a half-width angle of about 10° regardless of Reynolds number (Wygnanski *et al.* 1976). As the spot propagates downstream, its height increases at a rate similar to the growth of a turbulent boundary layer. Wygnanski *et al.* (1979) observed oblique wave packets swept at an angle of about 40° near the wingtips of the spot. Whether these waves packets play an important role in the lateral spreading or merely act as passive attendants to the spot has been debated.

The evolution of turbulent spots in boundary layers with pressure gradients has also been investigated. Katz *et al.* (1990) observed that the rate of growth of the spot is significantly inhibited by a favourable pressure gradient. The familiar arrowhead shape of the spot gave way to a rounded triangular shape with the trailing interface being straight and perpendicular to the free-stream direction. They did not observe wave packets and attributed this to the stability of the laminar flow. With an adverse pressure gradient, the trend is the opposite as observed by Seifert & Wygnanski (1995). The rate of growth of turbulent spots, especially the lateral growth, is enhanced by an adverse pressure gradient as well as the interaction of the spot with the wave packet trailing it.

There are very few simulations of turbulent spots in boundary layers. The first direct numerical simulation (DNS) of a spot that was taken far enough in time to make comparisons with experiments was performed by Henningson *et al.* (1987) for a temporally growing Blasius boundary layer. Later Singer (1996) looked more into details of the substructures within a young turbulent spot by means of DNS of a spatially growing Blasius boundary layer. In these simulations, the spot assumed the well-known shape of an arrowhead with its characteristic overhang of the leading edge but wave packets were not observed.

In plane Poiseuille flow, the spot develops the shape of a reverse arrowhead as can be seen in flow visualizations by Carlson *et al.* (1982) and Alavyoon *et al.* (1986). Oblique waves can be seen at the wingtips and streaks extend in the interior of the spot throughout its length. A further investigation of the oblique waves were done by Henningson & Alfredsson (1987). In contrary to spots in the flat-plate boundary layer, the spreading rates in the streamwise and spanwise directions are found to depend on the Reynolds number (Alavyoon *et al.* 1986). The only simulation of a turbulent spot in plane Poiseuille flow was performed by Henningson & Kim (1991). Their obtained spot had a very similar shape to that observed in laboratory flows and oblique waves existed at the wingtips.

For turbulent spots in plane Couette flow, the simulations of Lundbladh & Johansson (1991) preceded the experiments of Tillmark & Alfredsson (1992) and Dauchot & Daviaud (1995). In both the simulations and the experiments, the spot assumed an elliptical shape that evolved towards a circular shape as it propagated downstream. Moreover, the lateral spreading rate increased with increasing Reynolds number for low Reynolds numbers but levelled off to a constant rate at high Reynolds numbers corresponding to a half-width angle of 13° in the simulations and 11° in the experiments of Tillmark &

Alfredsson (1992). In the experiments, waves with the wave crests aligned in the streamwise direction were observed at the spanwise edges of the spots. These waves were not observed in the simulations.

There have been many investigations of turbulent spots in wall-bounded flows, mostly experimental studies but also simulations (Mathew & Das 2000). But nothing has been reported on turbulent spots in the asymptotic suction boundary layer (ASBL). Boundary layers subjected to suction at the wall are interesting flow cases with applications in the area of control (Joslin 1998; Balakumar & Hall 1999; Pralits *et al.* 2002; Zuccher *et al.* 2004). The ASBL is stable to infinitesimal disturbances below a critical Reynolds number of 54370, based on the free-stream velocity and the displacement thickness (Hocking 1975). However, a transient disturbance growth may occur for much lower Reynolds numbers (Fransson & Alfredsson 2003; Fransson & Corbett 2003; Yoshioka *et al.* 2004). Levin *et al.* (2005) reported breakdown to turbulence in the ASBL at a Reynolds number of 500. At the time of writing this paper, experiments of turbulent spots in the ASBL are, however, performed in the MTL wind-tunnel at KTH Mechanics in Stockholm by Jens Fransson.

In the present study, threshold amplitudes of localized disturbances, their breakdown and the development of turbulent spots in the ASBL are carried out by means of DNS. In § 2, the numerical method is presented as well as a parametric study of the localized disturbance. In § 3, the results are organized as follows: amplitude thresholds are presented in § 3.1, vortical structures within a transitional localized disturbance are visualized in § 3.2 and the development of turbulent spots is investigated in § 3.3. Finally, conclusions are drawn in § 4.

2. Numerical details

2.1. *Base flow and scaling*

Consider a boundary layer over an infinite wall with permeable properties and with suction applied under it, see figure 1. The coordinates in the streamwise, wall-normal and spanwise directions are denoted x, y and z, respectively. The corresponding velocity components are $\boldsymbol{U} = (U, V, W)$. Lengths are scaled by the displacement thickness δ_1 and velocities are scaled by the free-stream velocity U_∞. The units of time t are δ_1/U_∞. The Reynolds number is defined as $Re = U_\infty \delta_1/\nu$, where ν is the kinematic viscosity of the fluid. When uniform wall-normal suction, with velocity $-V_0$, is applied at the wall, the boundary layer thickness, shown as the dashed lines in figure 1, becomes constant over the wall. This asymptotic suction profile can be experimentally obtained after some evolution region (Fransson & Alfredsson 2003). The ASBL is an analytical solution to the Navier–Stokes equations. It was first derived by Griffith & Meredith (1936) and can be written as

$$\boldsymbol{U}_0 = (1 - \exp(-y), -V_0, 0). \tag{1}$$

The analytical solution allows the displacement thickness to be calculated exactly, $\delta_1 = \nu/V_0^*$ and the Reynolds number to be expressed as the velocity ratio,

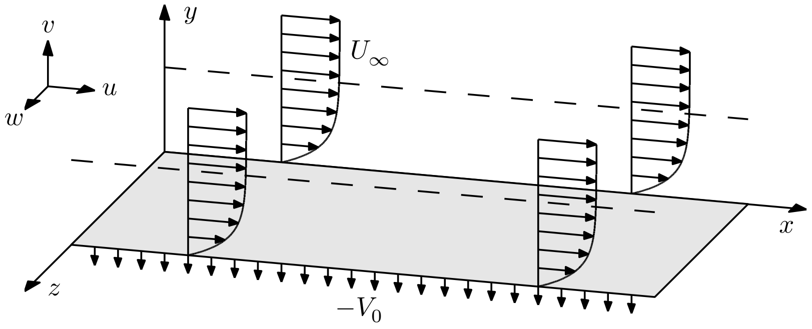

Figure 1. The asymptotic suction boundary layer.

$Re = U_\infty/V_0^*$, where $-V_0^*$ is the dimensional suction velocity. This also implies that the displacement thickness and the Reynolds number can be prescribed independently.

2.2. *DNS techniques*

The numerical code (see Lundbladh *et al.* 1999) uses spectral methods to solve the three-dimensional time-dependent incompressible Navier–Stokes equations. The discretization in the streamwise and spanwise directions makes use of Fourier series expansions, which enforce periodic solutions. The discretization in the wall-normal direction is represented with Chebyshev polynomial series. A pseudospectral treatment of the nonlinear terms is used. The time advancement is a second-order Crank–Nicolson method for the linear terms and a four-step low-storage third-order Runge–Kutta method for the nonlinear terms. Aliasing errors arising from the evaluation of the pseudospectrally convective terms are removed by dealiasing by padding and truncation using the 3/2-rule when the FFTs are calculated in the wall-parallel planes. In the wall-normal direction, it has been found that increasing the resolution is more efficient than the use of dealiasing. The code can be used both for temporal and spatial simulations. In the latter case a fringe region (Nordström *et al.* 1999) is added to the downstream end of the physical domain, in which the outgoing flow is forced to its initial state. However, when studying parallel flows, such as the ASBL with a localized disturbance, the advantage of a temporal simulation can be used.

The numerical code does not allow for uniform flow through the lower and upper boundaries. However, the wall-normal suction in the ASBL can be moved from the boundary conditions to the governing equations (see Levin *et al.* 2005). Hence, instead of solving the Navier–Stokes equations for V with the boundary condition $V = -V_0$, the same solution can be obtained by solving for $V - V_0$ with the boundary condition $V = 0$.

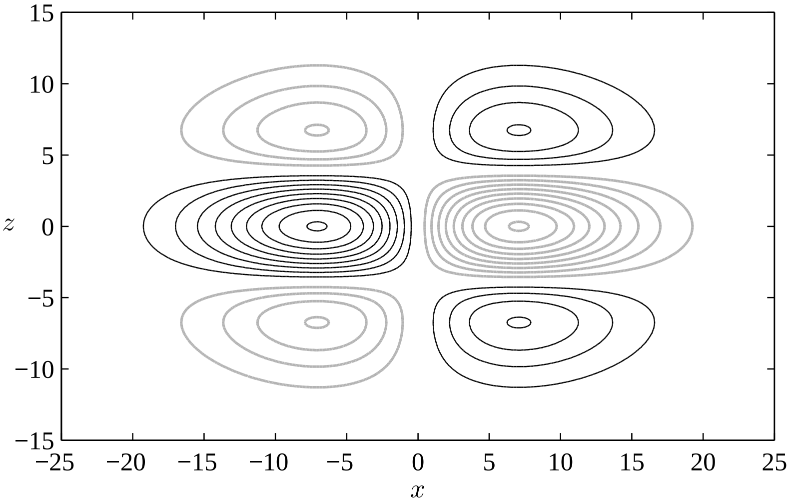

FIGURE 2. Contours of wall-normal velocity, at $y = 1$, of a localized disturbance consisting of two counter-rotating vortex pairs with the scales $l_x = 10$, $l_y = 1.0$ and $l_z = 5.5$. Black and grey lines display positive and negative values, respectively.

At the wall, no-slip boundary conditions are specified and at the upper edge of the computational box, a generalized boundary condition is applied in Fourier space with different coefficients for each wavenumber. The condition represents a potential-flow solution decaying away from the upper edge of the computational box and decreases the required box height by damping the higher frequencies rather than forcing the disturbance velocities to a rapid decay. In the horizontal directions, periodic boundary conditions are used.

2.3. *Disturbance generation and numerical parameters*

The present numerical implementation provides several possibilities for disturbance generation. Disturbances can be included in the flow by a body force, by blowing and suction at the wall through non-homogeneous boundary conditions and by adding them in the initial velocity field. In order to produce a turbulent spot, a localized disturbance is superposed to the ASBL in the initial velocity field. The type of disturbance is centred around a pair of oblique waves, in the streamwise-spanwise wavenumber plane, consisting of two counter-rotating vortex pairs, see figure 2. This type of initial disturbance has been used in earlier studies of transient growth and transition in channel flows (Henningson *et al.* 1993) and boundary layers (Breuer & Haritonidis 1990; Breuer & Landahl 1990; Bech *et al.* 1998). In terms of a stream function, it is defined by

$$\psi = A\bar{x}\bar{y}^3\bar{z}\exp\left(-\bar{x}^2 - \bar{y}^2 - \bar{z}^2\right), \tag{2}$$

Re	A	$L_x \times L_y \times L_z$	$N_x \times N_y \times N_z$	End time	Note
500	0.08	$100 \times 15 \times 40$	$200 \times 101 \times 160$	200	Res. check
800	0.05	$100 \times 15 \times 40$	$320 \times 161 \times 256$	200	Res. check
1200	0.03	$100 \times 15 \times 40$	$480 \times 241 \times 384$	200	Res. check

Table 1. Flow and box parameters for resolution checks.

where $\bar{x} = x/l_x$, $\bar{y} = y/l_y$ and $\bar{z} = z/l_z$. The velocity components are given by $(u, v, w) = (0, -\psi_z, \psi_y)$ and normalized so that the amplitude A is given by the maximum absolute value of the wall-normal disturbance velocity. The energy of the disturbance is defined by

$$E = \frac{1}{2} \int (u^2 + v^2 + w^2)\, \mathrm{d}x\, \mathrm{d}y\, \mathrm{d}z. \tag{3}$$

When studying the development of turbulent spots, apart from the localized disturbance, random noise is added to the initial velocity field in order to break up symmetries. The noise is in the form of Stokes modes, i.e. eigenmodes of the flow operator without the convective term. These modes fulfil the equation of continuity and the boundary condition of vanishing velocity at the wall. The introduced noise level is specified with its energy density, thus the total energy of the noise divided by the volume of the box.

Amplitude thresholds for transition and the development of turbulent spots are investigated for three Reynolds numbers, $Re = 500$, 800 and 1200. For each Reynolds number, the resolution is carefully checked for a small test case. Dealiasing is activated in the streamwise and spanwise directions. The amplitude of the localized disturbance, which has the scales given in figure 2, is about twice as large as the threshold value for the corresponding Reynolds number, resulting in breakdown to a turbulent spot well before the termination time of 200. When evaluating the resolution convergence, the disturbance energy, extreme values of velocity and vorticity components and visual examinations of flow structures are taken into account. The resolutions given in table 1 are decided to be in use after being compared to both coarser and finer grids not given here. As can be seen in table 1, the resolution in each direction is linearly scaled with the Reynolds number. Moreover, when the box size is increased, the resolution is increased correspondingly to insure the same number of modes per length unit in each direction. To summarise the above, the number of modes is at least given by $(N_x \times N_y \times N_z) = (Re/250 \cdot L_x \times Re/75 \cdot L_y + 1 \times Re/125 \cdot L_z)$, where L_x, L_y and L_z denote the length, height and width of the box, respectively. When searching for the critical Reynolds number, the resolution for $Re = 500$ is used.

Apart from the resolution checks, the size of the box is examined for a few cases. It is found that the needed box height decreases with increased Reynolds number. One reason for this can be the fact that lower initial amplitudes of the wall-normal disturbance velocity are used for higher Reynolds numbers. The interaction distance between mirror spots in the spanwise direction is short, resulting in low sensitivity of the box width. On the other hand, the interaction distance in the streamwise direction is longer. The interaction takes the form of bonding between streaks at the front and trail of mirror spots. For each simulation, the box size is set to fit one spot and avoid interactions between mirror spots during the time simulated.

2.4. *Study of horizontal scales of localized disturbances*

The influence of the streamwise and spanwise length scales of the localized disturbance is studied. The wall-normal scale is $l_y = 1$ while the horizontal scales l_x and l_z are varied. The Reynolds number is $Re = 500$ and the size of the computational box used for this parametric study is $(L_x \times L_y \times L_z) = (100 \times 15 \times 50)$. In a first attempt to study how the horizontal scales of the initial disturbance affect the development of a turbulent spot, the amplitude of the initial disturbance is kept constant to $A = 0.07$. As a result, the energy of the initial disturbance increases as the horizontal scales increase. This give rise to stronger breakdown and larger turbulent spots. When the scales are increased further, the localized disturbance break down to several turbulent spots and this is not requested. The next approach is to keep the initial energy of the disturbance constant, while varying the horizontal scales. The streamwise scale is varied from 7 to 11 with steps of 1 and the spanwise scale is varied form 4 to 7 with steps of 0.5. The energy level is set to the value that the disturbance with horizontal scales $l_x = l_z = 7$ assumes with the amplitude $A = 0.07$. Figure 3 shows contours of constant initial disturbance amplitude as dotted lines and contours of constant disturbance energy at time 200 as the solid lines. Among the simulated cases, $l_x = 10$ and $l_z = 5.5$ give rise to the maximum disturbance energy at time 200. The energy evolution until this instant is somewhat different for the various cases and no clear trend can be distinguished apart from the initial transient growth. When evaluating the disturbance energy at $t = 30$, 40 and 50, the maximum moves out from the considered scales towards longer and more narrow initial disturbances. However, these narrow localized disturbances do not lead to transition despite their large initial amplitude.

Breuer & Haritonidis (1990) compared the numerical results for a weak localized disturbance with experiments, where the disturbance was caused by the impulsive motion of a membrane at the wall and received good qualitative agreement of the initial evolution. Henningson *et al.* (1993) investigated the effects caused by turning the localized disturbance an angle around the y-axis and found that a non-zero angle gives rise to larger initial growth. In a preliminary study to the present work, it was found that a disturbance with 20 degrees angle to the free-stream direction results in lower threshold amplitudes. However, in the present study, we focus on localized disturbances aligned with the free-stream direction and that can be experimentally reproduced with the down-up motion of a membrane at the wall.

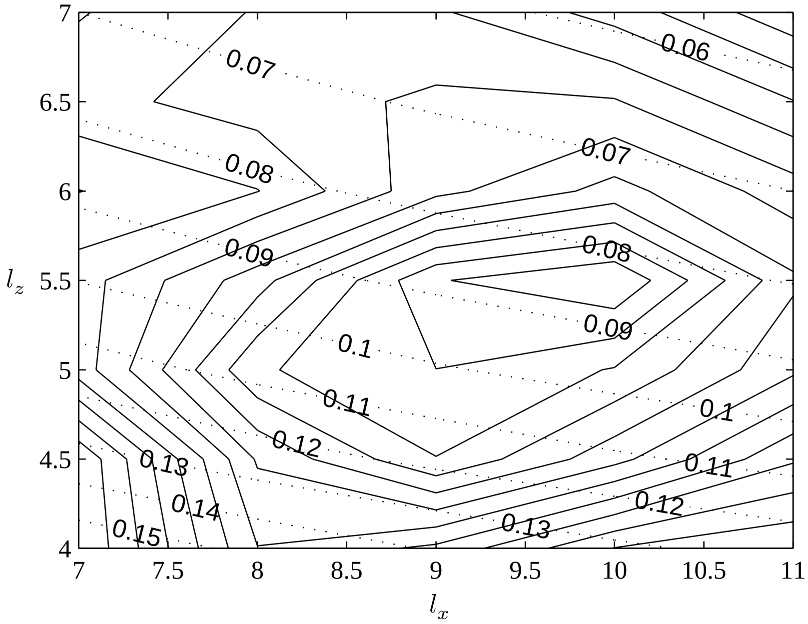

FIGURE 3. Study of horizontal scales of the localized disturbance. Contours of A (dotted lines) and disturbance energy at time 200 (solid lines). The energy contours show values from 46 to 58 with steps of 1.

3. Results

3.1. *Transition thresholds for localized disturbances*

In this section, the threshold amplitudes for transition from a localized disturbance to a turbulent spot are investigated by a numerous of direct numerical simulations. If the initial amplitude of the disturbance exceeds a certain threshold value, A_T, transition occurs. Previous investigations have mainly been concerned with determining the negative exponent γ, relating to the initial amplitude of the primary disturbance as $A_T \propto Re^{\gamma}$. Trefethen *et al.* (1993) used simple models to feed transient growth by nonlinearities and conjectured that for the Navier–Stokes equations, γ must be ≤ -1. Later Baggett & Trefethen (1997) reviewed several mathematical models of transition in parallel shear flows collected from different research groups, and found the exponents $-3 \leq \gamma \leq -1$ depending on model and base flow. However, they conclude that for actual flows in pipes and channels, the range is more likely $-2 \leq \gamma < -1$. Most investigations dealing with this relationship focus on plane channel flows (Kreiss *et al.* 1994; Lundbladh *et al.* 1994; Dauchot & Daviaud 1995; Reddy *et al.* 1998). However, Levin *et al.* (2005) investigated transition thresholds for periodic disturbances in the ASBL at the same Reynolds number as considered in the present work. They found that the threshold amplitude scales

Re	A	$L_x \times L_y \times L_z$	$N_x \times N_y \times N_z$	End time	Note
360	0.1	$200 \times 30 \times 64$	$400 \times 201 \times 256$	1000	No trans.
366	0.1	$200 \times 30 \times 64$	$400 \times 201 \times 256$	1000	No trans.
367	0.1	$200 \times 30 \times 64$	$400 \times 201 \times 256$	1000	No trans.
368	0.1	$200 \times 30 \times 64$	$400 \times 201 \times 256$	1000	Transition
370	0.1	$200 \times 30 \times 64$	$400 \times 201 \times 256$	1000	Transition
380	0.1	$200 \times 30 \times 64$	$400 \times 201 \times 256$	1000	Transition
500	0.05	$150 \times 15 \times 40$	$300 \times 101 \times 160$	300	Transition
500	0.048	$200 \times 15 \times 40$	$400 \times 101 \times 160$	500	Transition
500	0.046	$300 \times 19 \times 60$	$600 \times 129 \times 240$	1000	Transition
500	0.045	$300 \times 19 \times 60$	$600 \times 129 \times 240$	1000	Transition
500	0.044	$300 \times 19 \times 60$	$600 \times 129 \times 240$	1000	No trans.
800	0.025	$200 \times 15 \times 40$	$640 \times 161 \times 256$	500	Transition
800	0.023	$200 \times 15 \times 40$	$640 \times 161 \times 256$	500	Transition
800	0.022	$300 \times 15 \times 40$	$960 \times 161 \times 256$	602	Transition
800	0.0215	$300 \times 15 \times 40$	$960 \times 161 \times 256$	1000	Transition
800	0.021	$300 \times 15 \times 40$	$960 \times 161 \times 256$	1000	No trans.
800	0.0205	$300 \times 15 \times 40$	$960 \times 161 \times 256$	1000	No trans.
1200	0.015	$200 \times 10 \times 40$	$960 \times 161 \times 384$	500	Transition
1200	0.013	$300 \times 10 \times 40$	$1440 \times 161 \times 384$	1000	Transition
1200	0.012	$300 \times 10 \times 40$	$1440 \times 161 \times 384$	1000	Transition
1200	0.011	$300 \times 10 \times 40$	$1440 \times 161 \times 384$	1000	No trans.

Table 2. Flow and box parameters for threshold simulations.

like $Re^{-1.3}$ for oblique transition and like $Re^{-1.05}$ for transition initiated by streamwise vortices and random noise.

For growing boundary layers, little work aimed in this direction is found, mainly because of difficulties to define such a relationship as the local Reynolds number changes with the boundary layer thickness. However, tools for transition prediction in boundary layers have been developed for half a century. Andersson *et al.* (1999) proposed a relation for bypass transition prediction in the Blasius boundary layer where the level of free-stream turbulence that lead to transition scales like Re^{-1}. A very good correlation to this result was experimentally obtained by Fransson *et al.* (2005).

On the other hand, for a parallel boundary layer such as the ASBL, where the Reynolds number based on the boundary layer thickness is constant, the procedure to find the threshold amplitude is straightforward. Simulations are carried out with varied initial amplitudes of the localized disturbance at the Reynolds numbers 500, 800 and 1200. Some of the simulations in the search for the threshold amplitudes are summarized in table 2. When evaluating whether transition occurs or not, the disturbance energy, extreme values of velocity and vorticity components and visual examinations of the flow field are taken

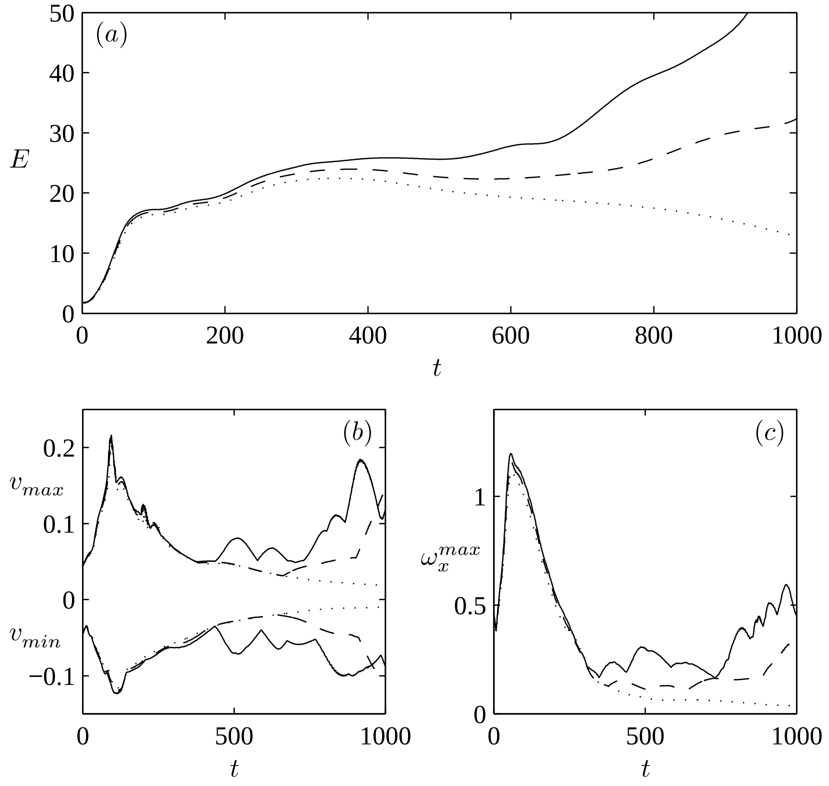

FIGURE 4. Evolution of disturbance energy (*a*), minimum and maximum wall-normal disturbance velocity (*b*) and maximum streamwise vorticity (*c*) at $Re = 500$ and $A = 0.046$ (solid line), 0.045 (dashed line) and 0.044 (dotted line).

into account. Figure 4 shows the evolution of disturbance energy (figure 4*a*), minimum and maximum wall-normal disturbance velocity (figure 4*b*) and maximum streamwise vorticity (figure 4*c*) for three initial amplitudes close to the threshold value at $Re = 500$. In this case, transition occurs for the amplitudes $A = 0.045$ and 0.046 but not for 0.044 for which the disturbance energy and flow extreme values decay after the initial transient growth.

The circles in figure 5 summarizes the amplitude thresholds taken as the lowest amplitudes for which transition is attained in the DNS before $t = 1000$ for the three Reynolds numbers. The solid line is the least square fit of Re^{γ} to the data and for this range of Reynolds numbers, the threshold amplitude is found to scale as $Re^{-1.5}$. In this investigation, only one localized disturbance is introduced in the flow, thus the obtained amplitude thresholds must be considered as an upper bound, since more optimal disturbance configurations that would lead to transition for lower initial amplitudes may exist. Furthermore,

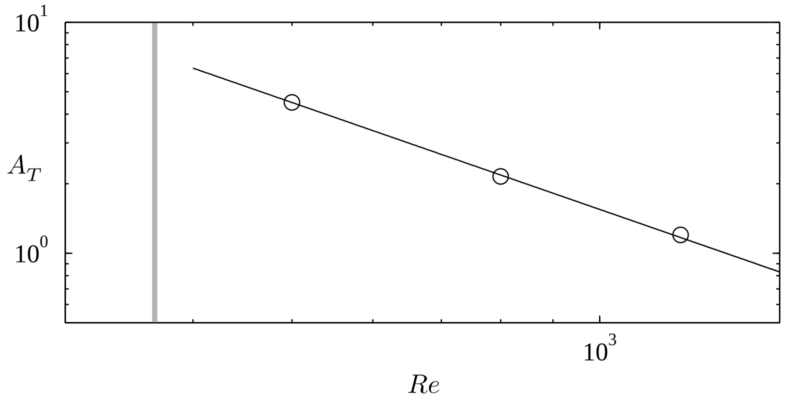

FIGURE 5. Threshold amplitude as function of Reynolds number. The circles correspond to the lowest amplitudes from the DNS that lead to transition. The black line is a least square fit to the data corresponding to $A_T = 6.36 \cdot 10^4 Re^{-1.54}$. The grey line indicates the critical Reynolds number of 367.

no conclusions of the asymptotic behaviour ($Re \rightarrow \infty$) can be drawn. In fact, Chapman (2002) used an asymptotic analysis of the Navier–Stokes equations to study threshold exponents for transition in plane Couette flow and plane Poiseuille flow and found discrepancies to available results from numerical simulations. He explains this difference by the fact that the asymptotic values are only reached for very large Reynolds numbers, of order 10^6, where the scaling laws of the transient growth is different than for the Reynolds numbers used in the numerical simulations.

An attempt of finding the critical Reynolds number for transition initiated of the localized disturbance is also carried out. Simulations are performed with an initial amplitude of the localized disturbance of 0.1 and varied Reynolds numbers, see table 2. This amplitude is considered to be sufficiently large to represent the search for a critical Reynolds number after evaluation of simulations with larger amplitudes. The resolution for these simulations is the same as used for $Re = 500$. Relaxation of the localized disturbance appears for $Re = 367$ or below. This value is indicated in figure 5 as the thick grey line.

3.2. *Breakdown to a turbulent spot*

In this section, the breakdown mechanism of a localized disturbance is discussed and visualized by vortical structures. The turbulent spot is an assemblage of many small-scale streaky structures and hairpin vortices (Perry *et al.* 1981; Sankaran *et al.* 1988; Singer & Joslin 1994; Schröder & Kompenhans 2004). These hairpin vortices evolve at the trailing edge of the young spot and increase the region of turbulence in the streamwise and spanwise directions as the spot grow. The spot appears to grow through the birth of new structures

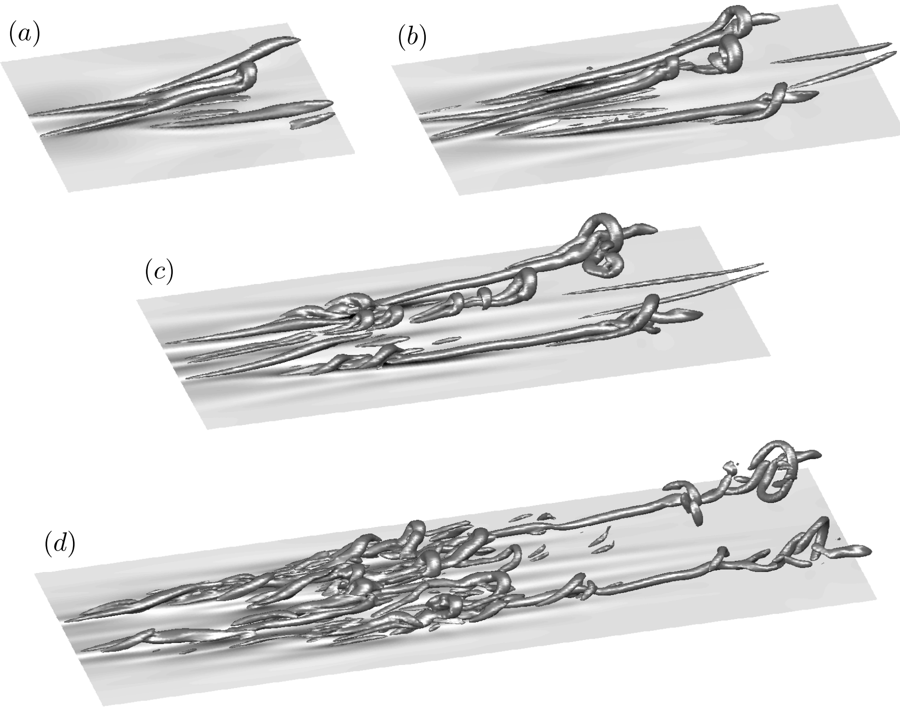

FIGURE 6. Visualizations of vortical structures ($\lambda_2 = -0.002$) and wall-shear stress (with dark regions displaying high shear) for the breakdown of a localized disturbance with $A = 0.06$ at $Re = 500$. (*a*) $t = 80$, (*b*) 140, (*c*) 200 and (*d*) 300.

rather than the growth or spreading of the substructures themselves. Vortical structures can be identified in the flow by plotting regions where the second largest eigenvalue λ_2 of the Hessian of the pressure assumes negative values (Jeong *et al.* 1997). Figure 6 shows a sequence of the early development of the localized disturbance with $A = 0.06$ at $Re = 500$. The initial disturbance develops into a hairpin vortex aligned with the streamwise direction, see figure 6(*a*) that shows the instant at $t = 80$. Its legs are close to the wall at the trailing edge of the disturbance while the head is located higher up and further downstream. Between the legs, an upward motion is present. On each side of the head, counter-rotating structures can be seen. As can be seen in figure 6(*b*), which shows the instant at $t = 140$, the head is detached as a result of vortex stretching and a new head is formed in its place. At the same time, spiral vortices appear at the counter-rotating structures on each side. The head detachment continues as the time proceeds and at $t = 200$, six hairpin heads can

Re	A	$L_x \times L_y \times L_z$	$N_x \times N_y \times N_z$	End time	Note
500	0.06	$400 \times 25 \times 100$	$800 \times 181 \times 400$	1200	Spot
800	0.03	$400 \times 12 \times 80$	$1280 \times 129 \times 512$	950	Spot
1200	0.02	$300 \times 10 \times 80$	$1440 \times 161 \times 768$	510	Spot

TABLE 3. Flow and box parameters for simulations of turbulent spots.

be distinguished along the centreline in figure 6(*c*). At $t = 300$, the flow pattern has become complex with many hairpin and spiral vortices characterising a young turbulent spot.

3.3. *Development of turbulent spots*

In this section, turbulent spots are visualized and the spreading angles and propagation velocities of the leading and trailing edges are evaluated. Table 3 summarizes the parameters for the three performed simulations. Apart from the localized disturbance, random noise is added to the initial velocity field in order to break up symmetries. The level of the noise is prescribed with its energy density, which has the value 10^{-7} for all three simulations.

As the spot propagates downstream, it grows in size. However, the wall-normal spreading is very small. Figure 7 shows the turbulent spot at $t = 950$ for the Reynolds number 500. The streamwise disturbance velocity is visualized with dark and light regions displaying high and low values, respectively. The wall-parallel plane at $y = 1$ is shown in figure 7(*a*) and the (x, y)-plane along the centreline ($z = 0$) is shown in figure 7(*b*). A corresponding visualization of a turbulent spot at $t = 950$ for Reynolds number 800 is shown in figure 8. For both figures, the length of the planes is 300 while the width and height show the entire spanwise and wall-normal extend of the computational box, respectively. From the visualizations it can be interpreted that the turbulent spot takes a bullet-shaped form with a rounded leading edge and a straight trailing edge. This shape becomes more distinct for higher Reynolds numbers as the scales within the spot get smaller. The interior of the spot is occupied of turbulent streaky structures. The side views reveal that the leading edge develops an overhang over the laminar flow and this is typical for turbulent spots in boundary layers. Beneath this overhang, long streaks extend from the turbulent region close to the wall. These streaks evolve from the influence of the disturbed flow in the overhang region. Behind the trailing edge of the spot, shorter streaks persist and they evolve from the relaminarization of turbulent structures propagating in a slower rate than the trailing edge itself. In the wake of the spot, the flow is accelerated close to the wall resulting in a calm region similar to what can be seen behind turbulent spots in boundary layers without wall suction. As expected for such a stable base flow, no evidence of waves surrounding the spot can be seen.

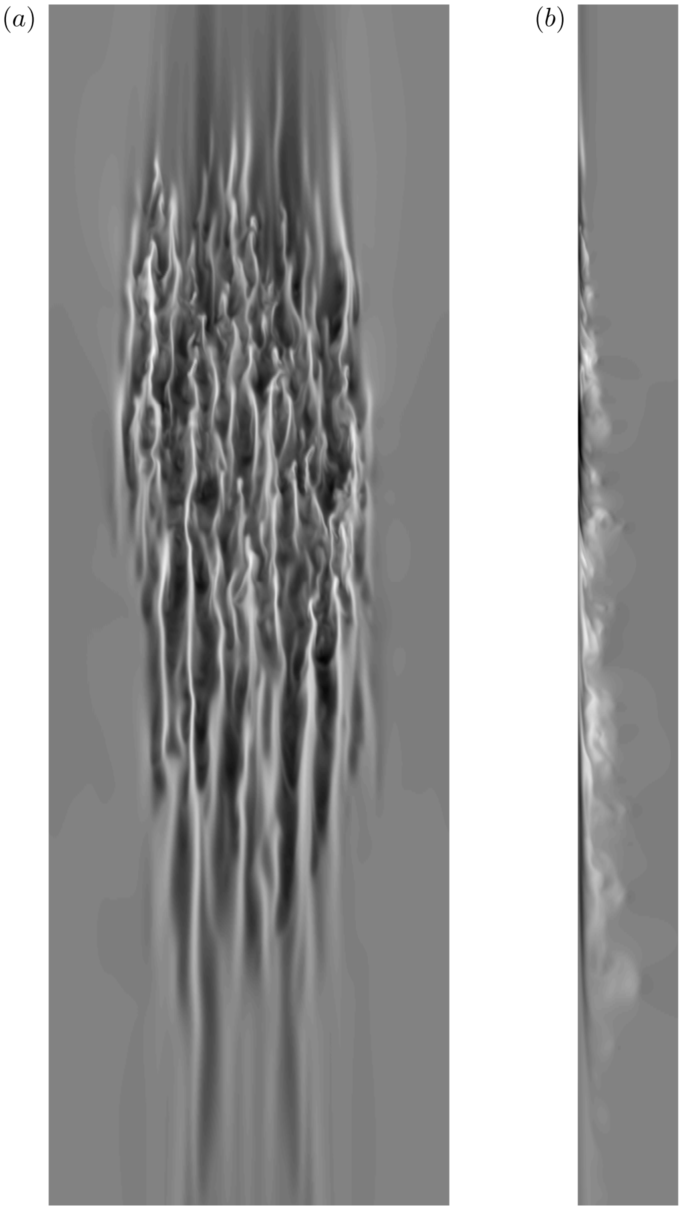

FIGURE 7. Visualization of a turbulent spot at $Re = 500$ and $t = 950$. Flow is in downward direction and the length of the planes is 300. Dark and light regions show high and low streamwise disturbance velocity, respectively. (*a*) Top view at $y = 1$. (*b*) Side view through the middle of the spot at $z = 0$.

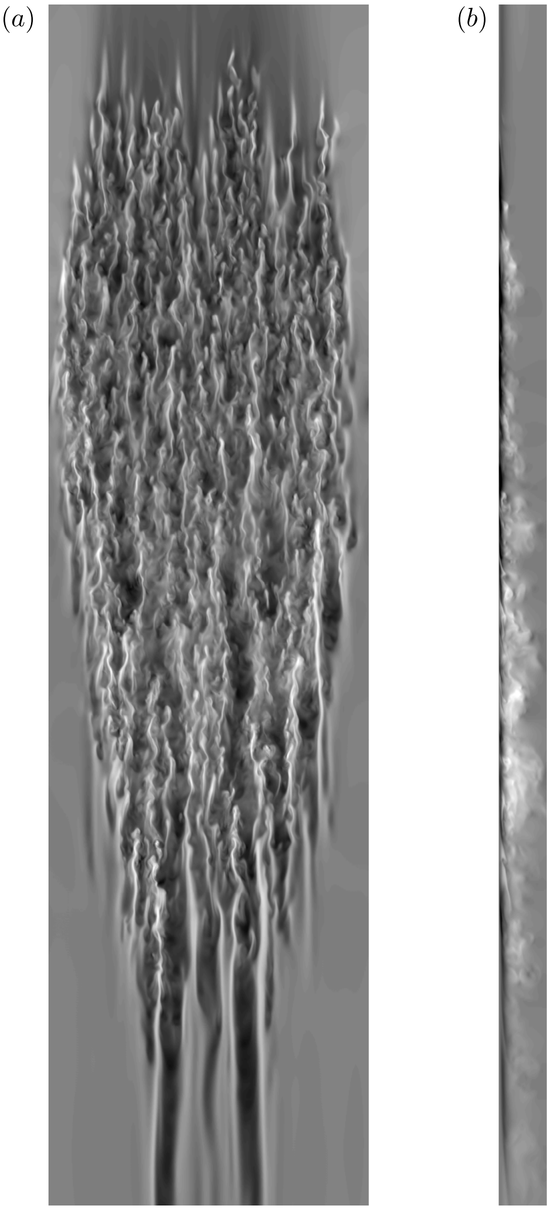

FIGURE 8. Visualization of a turbulent spot at $Re = 800$ and $t = 950$. Flow is in downward direction and the length of the planes is 300. Dark and light regions show high and low streamwise disturbance velocity, respectively. (*a*) Top view at $y = 1$. (*b*) Side view through the middle of the spot at $z = 0$.

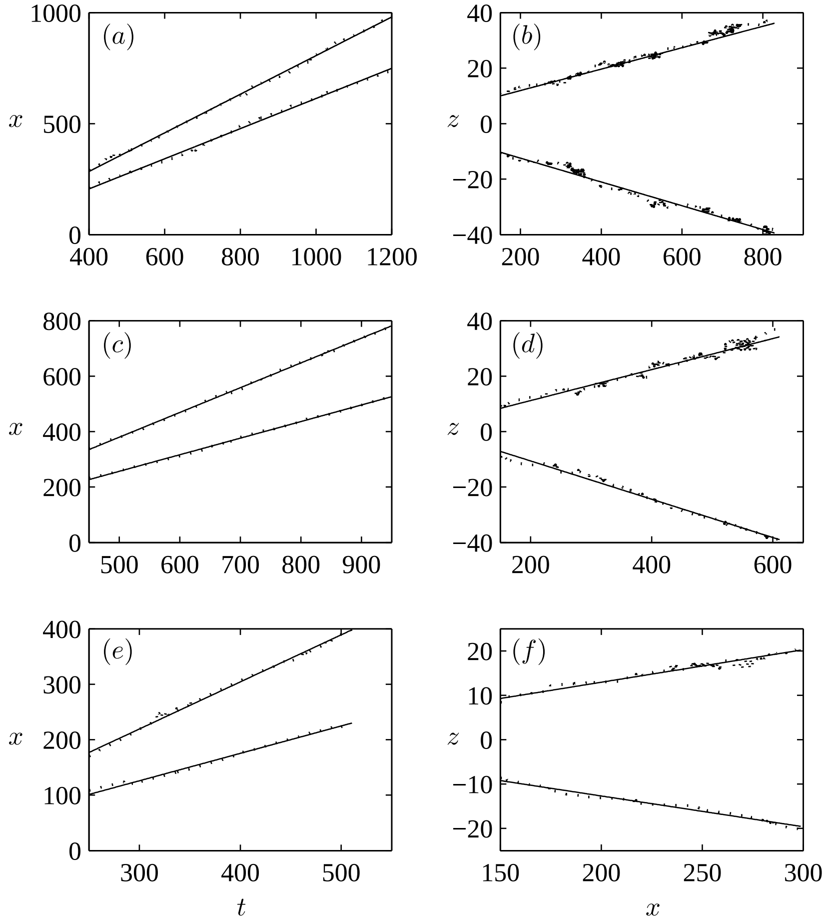

FIGURE 9. Horizontal spreading of turbulent spots for $Re =$ 500 (a, b), 800 (c, d) and 1200 (e, f). Linear fits (—) to the DNS data $(\cdots)$ for the intervals showed in the figures. (a, c, e) Streamwise spreading versus time. (b, d, f) Lateral spreading versus streamwise coordinate.

In order to evaluate the spreading rate of the turbulent spot in the wall-parallel plane at $y = 1$, the streamwise derivative of the streamwise velocity provides a well-define measure. The region of turbulence is decided to be represented by the criteria $\partial u/\partial x \geq 0.05$, which concurs well with other similar conditions as well as visual examinations of the flow (figures 7*a*–8*a*). This condition is chosen because it is easy to measure in an experiment and it filters away the laminar streaks. Figure 9 shows the horizontal spreading of the simulated turbulent spots with the propagation of the leading and trailing edges displayed in figures 9(a, c, e) and the lateral spreading displayed in

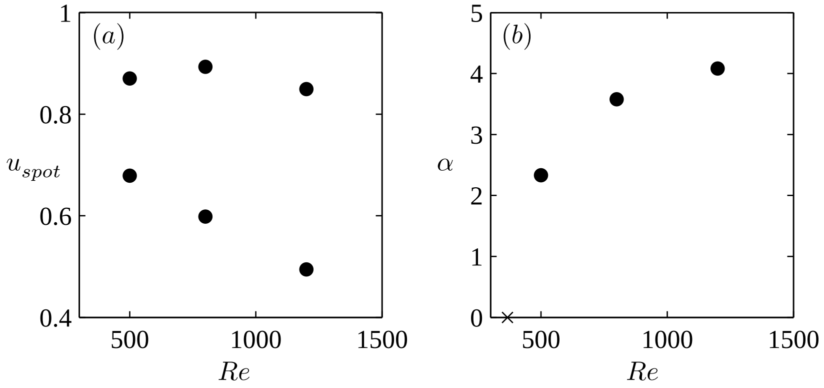

FIGURE 10. Spreading of turbulent spots versus Reynolds number. (*a*) Propagation velocities, u_{spot}, of the leading and trailing edges. (*b*) Mean half-width angle α. The cross indicates the critical Reynolds number.

figures 9(b, d, f). The dotted lines correspond to data extracted from the simulations and the solid lines are linear fits to the data for the intervals showed in the figures. Hence, for the evaluation of the spreading rates, the initial evolution of the spots is disregarded. In agreement with spots in other flows, the length and the width of the turbulent spots assume a linear growth. A closer look at the propagation of the leading and trailing edges for $Re = 500$ reveals that the slopes of the dotted lines are locally more flat with jumps in between. This is because the individual structures, in the considered plane, propagate in a slower rate than the leading and trailing edges themselves. New turbulent structures are born in the laminar streaks preceding the turbulent region and at the trailing edge structures move out of the spot and undergo relaminarization. This corresponds to the jumps in the dotted lines. The data from the lateral spreading is more scattered since the widest part of the spots move back and forth somewhat as new structures are born. It can also be noted that the spreading differs between the both sides owing to the randomness introduced by the initial noise.

The main characteristics of the spreading of the three simulated spots are summarized in figure 10. As can be seen in figure 10(a), the velocity of the leading edge is about 0.85 to 0.9 for all simulated Reynolds numbers and this is in agreement with the turbulent spot in the flat-plate boundary layer. The trailing edge velocity, on the other hand, decreases with increasing Reynolds number. The half-width angle, which is taken as the mean value from both sides, also indicates a Reynolds number dependence at low Reynolds numbers. As can be seen in figure 10(b), the half-width angle increases with increasing Reynolds number. However, it seems to level off to a constant value at high

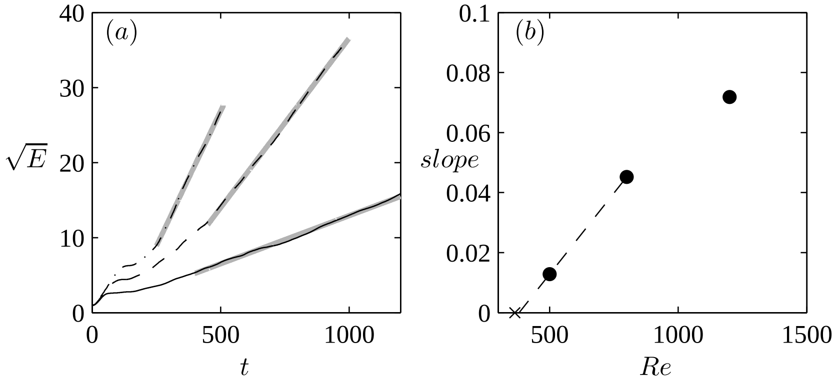

FIGURE 11. Evolution of the disturbance energy within turbulent spots. (*a*) Square root of the energy versus time for $Re = 500$ (—), 800 (– – –) and 1200 (– · –). Grey lines are linear fits to the data within the plotted intervals. (*b*) Slopes of the fitted lines versus Reynolds number. The cross indicates the critical Reynolds number.

Reynolds numbers. In this figure, the cross indicates the reasonable assumption of a zero spreading angle at the critical Reynolds number.

As the spot grows linearly in length and width and the wall-normal growth is negligible in comparison, it is reasonable to expect a quadratic growth of the disturbance energy in the fully developed turbulent spot. To assess whether this is true or not, the square root of the disturbance energy is plotted versus time in figure 11(*a*). Linear fits to the data are represented by the grey lines and confirm the assumption of a quadratic growth of the disturbance energy. The agreement becomes better for higher Reynolds numbers. An explanation for this is that the turbulent structures within the spot is larger for lower Reynolds numbers, and hence, the evolution of the energy is more affected by the growth or decay of individual structures. In figure 11(*b*), the slopes of the fitted lines are plotted versus Reynolds number. An interesting observation is that if we assume a linear increase of the slope with increasing Reynolds number for $Re \leq 800$ (dashed line), the Reynolds number for a zero growth of the disturbance energy falls very close to the critical Reynolds number found in § 3.1. This might provide an additional approach of finding the critical Reynolds number for the onset of a turbulent spot.

4. Summary and conclusion

The first study of the development of localized disturbances and turbulent spots in the asymptotic suction boundary layer are carried out using direct numerical simulations. The localized disturbance is superposed to the initial velocity field in the form of two counter-rotating vortex pairs. This type of initial disturbance can be experimentally reproduced with the down-up motion of a membrane located at the wall (Breuer & Haritonidis 1990). A parametric study of the horizontal scales of the initial disturbance is performed. It is found that keeping the initial disturbance energy constant rather than the initial disturbance amplitude is appropriate when comparing the growth of disturbances with different scales. The disturbance scales that lead to the highest growth under the conditions investigated are used in the simulations.

The threshold amplitude for breakdown of the localized disturbance into a turbulent spot is investigated for the Reynolds numbers $Re = 500$, 800 and 1200, based on the free-stream velocity and the displacement thickness. It is found that the threshold amplitude, defined as the maximum wall-normal disturbance velocity, scales like $Re^{-1.5}$ for the numerical set-up and the considered Reynolds numbers. For $Re \leq 367$, the localized disturbance decays after the initial transient growth.

The vortical structures within the early breakdown mechanism of the localized disturbance is studied for $Re = 500$. The initial disturbance develops into a hairpin vortex aligned with the streamwise direction. Its legs are close to the wall at the trailing edge of the disturbance while the head is located higher up and further downstream. This head is detached as a result of vortex stretching and a new head is formed in its place. This process continues resulting in a row of hairpin vortex heads. In a previous numerical study of Singer & Joslin (1994), the same behaviour was found in the flat-plate boundary layer. The young turbulent spot consists of many hairpin and spiral vortices that increase the size of the spot through the addition of new structures.

The shape and spreading rate of the turbulent spot are determined for $Re = 500$, 800 and 1200. Flow visualizations reveal that the turbulent spot takes a bullet-shaped form with a rounded leading edge and a straight trailing edge. This shape becomes more distinct for higher Reynolds numbers as the scales within the spot get smaller. The leading edge develops an overhang over the laminar flow. Beneath this overhang, long streaks extend from the turbulent region close to the wall and the breakdown of these streaks is responsible for the streamwise growth of the spot. Behind the trailing edge of the spot, shorter streaks persist and evolve from turbulent structures that move in a slower rate than the trailing edge itself. The spot is followed by a calm wake with accelerated flow.

The fully developed turbulent spot is found to grow linearly both in length and width while the wall-normal spreading is very small. As a result, the disturbance energy within the spot assumes a quadratic growth, which becomes more legible for higher Reynolds numbers. The leading edge is found to propagate at about 85-90 % of the free-stream velocity while the trailing edge velocity decreases with increasing Reynolds number. The half-width angle is found to increase with increasing Reynolds number. However, it seems to level off to a constant value at high Reynolds numbers.

To summarize, the turbulent spot in the asymptotic suction boundary layer bears many similarities to spots in other flows. Its shape and spreading rates are reminiscent of the turbulent spot in boundary layers subjected to a favourable pressure gradient. In common with spots in plane Couette flow and plane Poiseuille flow, the spreading rates are dependent of the Reynolds number.

This work was funded by the Swedish Energy Agency (Energimyndigheten). The direct numerical simulations was performed at the Center for Parallel Computers at KTH.

References

Alavyoon, F., Henningson, D. S. & Alfredsson, P. H. 1986 Turbulent spots in plane Poiseuille flow–flow visualization. *Phys. Fluids* **29**, 1328–1331.

Andersson, P., Berggren, M. & Henningson, D. S. 1999 Optimal disturbances and bypass transition in boundary layers. *Phys. Fluids* **11**, 134–150.

Baggett, J. S. & Trefethen, L. N. 1997 Low-dimensional models of subcritical transition to turbulence. *Phys. Fluids* **9**, 1043–1053.

Balakumar, P. & Hall, P. 1999 Optimum suction distribution for transition control. *Theoret. Comput. Fluid Dyn.* **13**, 1–19.

Bech, K. H., Henningson, D. S. & Henkes, R. A. W. M. 1998 Linear and nonlinear development of localized disturbances in zero and adverse pressure gradient boundary-layers. *Phys. Fluids* **10**, 1405–1418.

Breuer, K. S. & Haritonidis, J. H. 1990 The evolution of a localized disturbance in a laminar boundary layer. Part 1. Weak disturbances. *J. Fluid Mech.* **220**, 569–594.

Breuer, K. S. & Landahl, M. T. 1990 The evolution of a localized disturbance in a laminar boundary layer. Part 2. Strong disturbances. *J. Fluid Mech.* **220**, 595–621.

Cantwell, B., Coles, D. & Dimotakis, P. 1978 Structure and entrainment in the plane of symmetry of a turbulent spot. *J. Fluid Mech.* **87**, 641–672.

Carlson, D. R., Widnall, S. E. & Peeters, M. F. 1982 A flow-visualization of transition in plane Poiseuille flow. *J. Fluid Mech.* **121**, 487–505.

Chapman, S. J. 2002 Subcritical transition in channel flows. *J. Fluid Mech.* **451**, 35–97.

Dauchot, O. & Daviaud, F. 1995 Finite amplitude perturbation and spots growth mechanism in plane Couette flow. *Phys. Fluids* **7**, 335–343.

Elder, J. W. 1960 An experimental investigation of turbulent spots and breakdown to turbulence. *J. Fluid Mech.* **9**, 235–246.

Emmons, H. W. 1951 The laminar-turbulent transition in a boundary layer. Part I. *J. Aero. Sci.* **18**, 490–498.

Fransson, J. H. M. & Alfredsson, P. H. 2003 On the disturbance growth in an asymptotic suction boundary layer. *J. Fluid Mech.* **482**, 51–90.

Fransson, J. H. M. & Corbett, P. 2003 Optimal linear growth in the asymptotic suction boundary layer. *Eur. J. Mech. B/Fluids* **22**, 259–270.

Fransson, J. H. M., Matsubara, M. & Alfredsson, P. H. 2005 Transition induced by free-stream turbulence. *J. Fluid Mech.* **527**, 1–25.

Griffith, A. A. & Meredith, F. W. 1936 The possible improvement in aircraft performance due to boundary layer suction. *Tech. Rep.* 2315. Rep. Aero. Res. Coun.

Henningson, D. S. & Alfredsson, P. H. 1987 The wave structure of turbulent spots in plane Poiseuille flow. *J. Fluid Mech.* **178**, 405–421.

Henningson, D. S. & Kim, J. 1991 On turbulent spots in plane Poiseuille flow. *J. Fluid Mech.* **228**, 183–205.

Henningson, D. S., Lundbladh, A. & Johansson, A. V. 1993 A mechanism for bypass transition from localized disturbances in wall-bounded shear flows. *J. Fluid Mech.* **250**, 169–238.

Henningson, D. S., Spalart, P. & Kim, J. 1987 Numerical simulations of turbulent spots in plane Poiseuille and boundary-layer flow. *Phys. Fluids* **30**, 2914–2917.

Hocking, L. M. 1975 Non-linear instability of the asymptotic suction velocity profile. *Quart. J. Mech. Appl. Math.* **28**, 341–353.

Jeong, J., Hussain, F., Schoppa, W. & Kim, J. 1997 Coherent structures near the wall in a turbulent channel flow. *J. Fluid Mech.* **332**, 185–214.

Joslin, R. D. 1998 Aircraft laminar flow control. *Annu. Rev. Fluid Mech.* **30**, 1–29.

Katz, Y., Seifert, A. & Wygnanski, I. 1990 On the evolution of the turbulent spot in a laminar boundary layer with a favourable pressure gradient. *J. Fluid Mech.* **221**, 1–22.

Kreiss, G., Lundbladh, A. & Henningson, D. S. 1994 Bounds for threshold amplitudes in subcritical shear flows. *J. Fluid Mech.* **270**, 175–198.

Levin, O., Davidsson, E. N. & Henningson, D. S. 2005 Transition thresholds in the asymptotic suction boundary layer. *Phys. Fluids* To appear.

Lundbladh, A., Berlin, S., Skote, M., Hildings, C., Choi, J., Kim, J. & Henningson, D. S. 1999 An efficient spectral method for simulation of incompressible flow over a flat plate. *Tech. Rep.* KTH, Department of Mechanics, Stockholm.

Lundbladh, A., Henningson, D. S. & Reddy, S. C. 1994 Threshold amplitudes for transition in channel flows. In *Transition, Turbulence, and Combustion* (eds. M. Y. Hussaini, T. B. Gatski & T. L. Jackson), vol. 1, pp. 309–318. Kluwer Academic Publishers.

Lundbladh, A. & Johansson, A. V. 1991 Direct simulation of turbulent spots in plane Couette flow. *J. Fluid Mech.* **229**, 499–516.

Mathew, J. & Das, A. 2000 Direct numerical simulations of spots. *Current Science* **79**, 816–820.

Nordström, J., Nordin, N. & Henningson, D. S. 1999 The fringe region technique and the Fourier method used in the direct numerical simulation of spatially evolving viscous flows. *SIAM J. Sci. Comput.* **20**, 1365–1393.

Perry, A. E., Lim, T. T. & Teh, E. W. 1981 A visual study of turbulent spots. *J. Fluid Mech.* **104**, 387–405.

Pralits, J. O., Hanifi, A. & Henningson, D. S. 2002 Adjoint-based optimization of steady suction for disturbance control in incompressible flows. *J. Fluid Mech.* **467**, 129–161.

Reddy, S. C., Schmid, P. J., Baggett, J. S. & Henningson, D. S. 1998 On stability of streamwise streaks and transition thresholds in plane channel flows. *J. Fluid Mech.* **365**, 269–303.

RILEY, J. J. & GAD-EL-HAK, M. 1985 The dynamics of turbulent spots. In *Fronties in Fluid Mechanics* (eds. S. H. Davis & J. L. Lumley), pp. 123–155. Springer.

SANKARAN, R., SOKOLOV, M. & ANTONIA, R. A. 1988 Substructures in a turbulent spot. *J. Fluid Mech.* **197**, 389–414.

SCHRÖDER, A. & KOMPENHANS, J. 2004 Investigation of a turbulent spot using multi-plane stereo particle image velocimetry. *Exps. Fluids* **36**, 82–90.

SEIFERT, A. & WYGNANSKI, I. J. 1995 On turbulent spots in a laminar boundary layer subjected to a self-similar adverse pressure gradient. *J. Fluid Mech.* **296**, 185–209.

SINGER, B. A. 1996 Characteristics of a young turbulent spot. *Phys. Fluids* **8**, 509–521.

SINGER, B. A. & JOSLIN, R. D. 1994 Metamorphosis of a hairpin vortex into a young turbulent spot. *Phys. Fluids* **6**, 3724–3736.

TILLMARK, N. & ALFREDSSON, P. H. 1992 Experiments on transtion in plane Couette flow. *J. Fluid Mech.* **235**, 89–102.

TREFETHEN, L. N., TREFETHEN, A. E., REDDY, S. C. & DRISCOLL, T. A. 1993 Hydrodynamic stability without eigenvalues. *Science* **261**, 578–584.

WYGNANSKI, I., HARITONIDIS, J. H. & KAPLAN, R. E. 1979 On a Tollmien–Schlichting wave packet produced by a turbulent spot. *J. Fluid Mech.* **92**, 505–528.

WYGNANSKI, I., SOKOLOV, M. & FRIEDMAN, D. 1976 On a turbulent 'spot' in a laminar boundary layer. *J. Fluid Mech.* **78**, 785–819.

YOSHIOKA, S., FRANSSON, J. H. M. & ALFREDSSON, P. H. 2004 Free stream turbulence induced disturbances in boundary layers with wall suction. *Phys. Fluids* **16**, 3530–3539.

ZUCCHER, S., LUCHINI, P. & BOTTARO, A. 2004 Algebraic growth in a Blasius boundary layer: optimal and robust control by mean suction in the nonlinear regime. *J. Fluid Mech.* **513**, 135–160.

Paper 6

Early turbulent evolution of the Blasius wall jet

By Ori Levin, Astrid H. Herbst and Dan S. Henningson

KTH Mechanics, SE-100 44 Stockholm, Sweden

The first direct numerical simulation that is sufficiently large to study the self-similar behaviour of a turbulent wall jet is performed. The investigation is an extension of the simulation performed by Levin *et al.* (2005). The same numerical method is used, but a significantly larger computational domain enables to follow the development of the flow throughout the transition into its early turbulent evolution. Two-dimensional waves and streamwise elongated streaks, matched to measured disturbances, are introduced in the flow to trigger a natural transition mechanism. The Reynolds number is 3090 based on the inlet velocity and the nozzle height. The simulation provides detailed visualizations of the flow structures and statistics of mean flow and turbulent stresses. A weak subharmonic behaviour in the transition region is revealed by animations of the flow. The averaged data is presented in both inner and outer scaling in order to identify self-similar behaviour. Despite the low Reynolds number and the short computational domain, the turbulent flow exhibits a reasonable self-similar behaviour, which is most pronounced with inner scaling in the near-wall region.

1. Introduction

A plane wall jet may be considered as a flow which is created by the injection of high-velocity fluid in a thin layer close to a wall. The wall jet consists of an inner region, which is similar to a boundary layer, and an outer region wherein the flow resembles a free shear layer. These layers interact strongly and form a complex flow pattern. Besides the interesting physics, wall jets are of great interest from an engineering point of view, for instance in film cooling of gas turbine blades, in combustion chambers in defrosters and for separation control on airfoils.

The first study on a turbulent wall jet was carried out experimentally by Förthmann (1934), who found that the mean velocity field is self-similar, the half-width, which is the distance from the wall where the velocity in the outer region reaches half the local maximum velocity, grows linearly and that the maximum velocity is inversely proportional to the square-root of the streamwise distance. The experimental work on turbulent wall jets up to 1980 has been reviewed by Launder & Rodi (1981). For the turbulent plane wall jet in a quiescent surrounding, one main feature is the displacement of the position of zero shear stress from the position of maximum velocity. Up to that time, a semi-logarithmic variation of the velocity near the wall was assumed, but considerable differences occur in the constants. For the Reynolds stresses, the early experimental data shows a considerable scatter and most of the experimental set-ups did not assure two-dimensionality.

Preserving this feature, Abrahamsson *et al.* (1994) presented measurements of Reynolds stresses and wall shear stresses for a wall jet at Reynolds numbers $Re = 10000$, 15000 and 20000, based on the nozzle height and the inlet velocity. The streamwise development of the half-width and the maximum velocity were found to be independent of the Reynolds number using momentum scaling as proposed by Narasimha *et al.* (1973). Abrahamsson *et al.* (1994) questioned the existence of a constant shear-stress layer. Their measurements support Launder & Rodi (1981) claiming a transport of positive outer shear stress into the wall region.

Using Laser Doppler measurement technique, Schneider & Goldstein (1994) found for their measurements at $Re = 14000$ that the measured turbulent normal stresses are higher compared to the existing hot-wire data. The hot wires are shown to indicate low values of the Reynolds stresses in the turbulent outer regions where they are effected by strong flow reversals. Laser Doppler measurements by Eriksson *et al.* (1998) resolved for the first time the inner peak in the streamwise turbulence intensity as well as the inner (negative) peak in the shear stress of a turbulent wall jet at $Re = 9600$.

The applicability of various scaling laws to the turbulent wall jet was studied by Wygnanski *et al.* (1992) based on experimental data for Reynolds numbers in the range 3000 to 30000. They discarded the traditional wall-jet scaling as earlier suggested by Narasimha *et al.* (1973) and proposed a self-similarity scaling based on the momentum flux at the nozzle and on the viscosity of the fluid. They showed that a logarithmic velocity distribution cannot be derived based on the assumption on the constancy of the Reynolds stress or on the thinness of the logarithmic region relative to the thickness of the inner layer. In an investigation based mostly on experimental data by Eriksson *et al.* (1998) and Abrahamsson *et al.* (1994), George (2000) reasoned that neither the inner nor the outer scaling can perfectly collapse the data at finite Reynolds numbers due to the fact that the interaction region remains Reynolds number dependent.

Turbulent wall jets are challenging flow cases for computations. Recently Dejoan & Leschziner (2005) performed a large eddy simulation (LES) of a turbulent wall jet at $Re = 9600$ matching the experiments of Eriksson *et al.* (1998). The profiles of velocity and turbulent stresses in the self-similar region are compared to the experimental data and agree well. However, with an LES, the transition process in the outer shear layer and especially in the boundary layer is extremely difficult to reproduce with high accuracy, as also pointed out by Dejoan & Leschziner (2005). Therefore some discrepancies with the experimental data occur. Examining the budgets for the turbulent energy and the Reynolds stresses, the turbulent transport is seen to be very important where the outer shear layer overlaps with the boundary layer.

Direct numerical simulations (DNS) have to the authors current knowledge so far only been performed for transitional wall-jets. Wernz & Fasel (1996, 1997) studied the importance of three-dimensional effects in the transitional process and Visbal *et al.* (1998) investigated the breakdown process in a finite-aspect-ratio wall jet by the means of DNS. Levin *et al.* (2005) studied the breakdown initiated by the interaction between waves and streaks.

The present work is an extension of the work by Levin *et al.* (2005), who studied a wall jet both experimentally and numerically by means of highly resolved three-dimensional DNS. The experimental flow was matched in the vicinity of the nozzle outlet by a solution to the boundary-layer equations. In the experiment, the Kelvin–Helmholtz instability and naturally appearing streaks were observed to lead to breakdown. Two-dimensional waves and optimal streaks corresponding to the most unstable scales were calculated with the parabolized stability equations and introduced in the DNS. They found that in the presence of streaks, pairing is suppressed and breakdown to turbulence is enhanced.

In the present paper, the early turbulent evolution of the Blasius wall jet at $Re = 3090$ is studied with DNS using the same disturbance forcing but with a four times larger box than used by Levin *et al.* (2005). A Reynolds number matching the experimental investigations (Abrahamsson *et al.* 1994; Schneider & Goldstein 1994; Eriksson *et al.* 1998) is not feasible at the present stage, however in advantage to an LES, all scales are resolved and the transitional behaviour is reproduced correctly. In section 2, the numerical methods are briefly outlined. The animations and flow structures are discussed in section 3.1. In section 3.2, the averaged flow characteristics are presented in outer and inner scalings. Finally, conclusions are drawn in section 4.

2. Numerical methods

2.1. *Base flow*

Consider a wall jet where fluid is blown out through a nozzle and tangentially along a wall, where x, y and z denote the streamwise, wall-normal and spanwise coordinates, respectively. The corresponding velocity components are $\boldsymbol{u} = (u, v, w)$. The base flow consists of the Blasius wall jet, which is a solution to the boundary-layer equations with a coupling of the Blasius boundary layer and the Blasius shear layer as an initial condition. The flow is matched to an experimental set-up (Levin *et al.* 2005), where the nozzle height is $b = 3\,\mathrm{mm}$ and the inlet velocity is $U_0 = 15.4\,\mathrm{m\,s^{-1}}$, corresponding to the Reynolds number $Re = U_0 b/\nu = 3090$, where ν is the kinematic viscosity of the fluid. Figure 1(a) shows the computed base flow compared to data measured 16 mm downstream of the nozzle outlet.

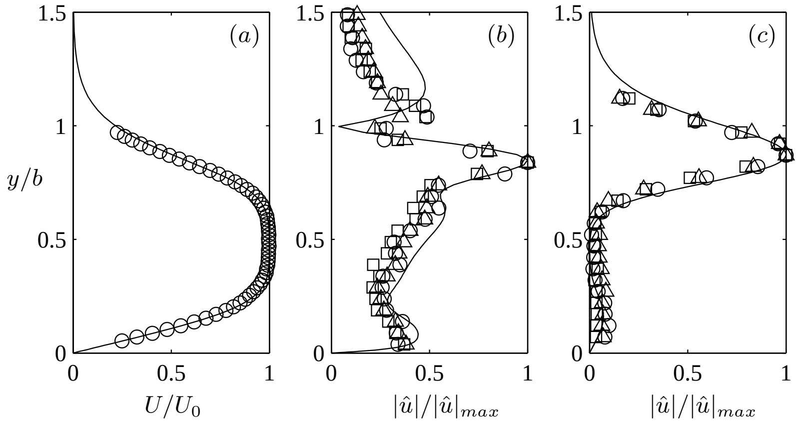

FIGURE 1. Comparison between calculations (solid lines) and experiments (symbols) from Levin *et al.* (2005) at $x/b = 5.3$ for $Re = 3090$. (*a*) Blasius wall jet. (*b*) Streamwise wave amplitude for $\omega b/U_0 = 1.49$. Experimental amplitudes are 0.3 % (○), 1.1 % (□) and 1.7 % (△). (*c*) Streamwise streak amplitudes. The wavenumber for the PSE is $\beta b = 3.77$ and for the experiments $\beta b = 3.15$ (○), 3.90 (□) and 4.72 (△).

2.2. *DNS technics*

The numerical code (see Lundbladh *et al.* 1999) uses spectral methods to solve the three-dimensional time-dependent incompressible Navier–Stokes equations. The discretization in the streamwise and spanwise directions makes use of Fourier series expansions, which enforce periodic solutions. The discretization in the normal direction is represented with Chebyshev polynomial series. A pseudospectral treatment of the nonlinear terms is used. The time advancement is a second-order Crank–Nicolson method for the linear terms and a four-step low-storage third-order Runge–Kutta method for the nonlinear terms. Aliasing errors arising from the evaluation of the convective terms are removed by dealiasing by padding and truncation using the 3/2-rule when the FFTs are calculated in the horizontal planes. In the wall-normal direction, it has been found that increasing the resolution is more efficient than the use of dealiasing.

At the wall, a no-slip boundary condition is set and at the upper edge of the computational box, a generalized boundary condition is applied in Fourier space with different coefficients for each wavenumber. The condition represents a potential-flow solution decaying away from the upper edge of the computational box. In the horizontal directions, periodic boundary conditions are used.

Flows such as boundary layers and wall jets are spatially growing and to fulfil the necessary periodic boundary condition in the streamwise direction, required by the spectral discretization, a fringe region (see Nordström *et al.* 1999) is added in the downstream end of the physical domain, in which the outgoing flow is forced to its initial state. In this region, the function $\lambda(x)$ is smoothly raised from zero and the flow is forced to a desired solution $\boldsymbol{v}$ through the forcing term $\lambda(x)(\boldsymbol{v}-\boldsymbol{u})$ added to the momentum equations, where $\boldsymbol{u}$ is the solution vector. The forcing vector $\boldsymbol{v}$, which may depend on the three spatial coordinates and time, is smoothly changed (blended) from the undisturbed wall-jet solution of the boundary-layer equations at the beginning of the fringe region to the prescribed inflow velocity vector. In the case of forcing a disturbance in the flow, it is also added to the forcing vector in the end of the fringe region.

2.3. *Disturbance forcing and numerical parameters*

In the experiment presented in Levin *et al.* (2005), naturally appearing waves and streaks were observed to lead to breakdown. In order to simulate a natural transition mechanism of the wall jet from its laminar state to a fully developed turbulent wall jet, two-dimensional waves $\boldsymbol{v}_w$ and stationary longitudinal streaks $\boldsymbol{v}_s$ that are matched to the measured disturbances are introduced. These disturbances are calculated with linear disturbance equations as described in Levin *et al.* (2005) and are added to the blended Blasius wall-jet solution $\boldsymbol{v}_0$ to give a forcing vector of the form $\boldsymbol{v} = \boldsymbol{v}_0 + \boldsymbol{v}_w + \boldsymbol{v}_s$. The waves and the streaks can then be forced in the fringe region. The forcing is turned on smoothly in both space and time. No noise is forced in the simulation, but a small level of noise evolving from the turbulent flow passes through the fringe region. However, the fringe region damps the energy of the incoming disturbances about seven decades.

Figures 1(*b*) and 1(*c*) show the computed amplitude functions of the wave and the streak, respectively, compared to measured data from Levin *et al.* (2005). The waves in the experiment were triggered by a loudspeaker at 1221 Hz, corresponding to an angular frequency of $\omega b/U_0 = 1.49$. This is close to the most amplified frequency predicted by linear stability calculations. The spanwise wavenumber of the streaks is $\beta b = 3.77$, which is close to that of the naturally appearing streaks in the experiment. However, the stationary streaks in the experiment were introduced in the flow by periodically distributed roughness elements, positioned on the top lip of the nozzle. The peak in the shear-layer region is in antiphase to the peak near the wall in the boundary-layer region both for the waves and the streaks. The streamwise amplitudes of the waves and the streaks are prescribed at the beginning of the computational box to $0.001U_0$ and $0.03U_0$, respectively.

The computational box is shown in figure 2. It extends from the nozzle outlet to 49.7 nozzle heights in the streamwise direction including the fringe region, which begins at $x/b = 44$. The height of the box is $14.4b$ and the width is $3.33b$, which is two spanwise wavelengths of the forced streaks. After considering two-point correlations of the fluctuating streamwise velocity in the spanwise direction, the box proved to be sufficiently wide upstream of about $x/b = 25$ to 30. At about the same location, an other problem arises, namely a

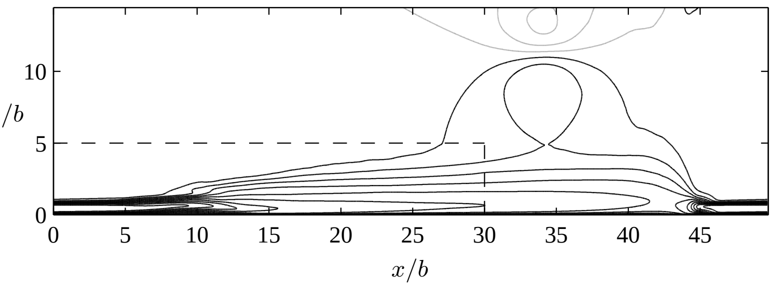

FIGURE 2. Streamwise mean velocity, averaged over a period of $213b/U_0$ and in the spanwise direction. Contour spacing is $0.1U_0$ and grey lines show negative values.

large external vortex that can be seen in the contours of the streamwise mean flow shown in figure 2. This vortex evolves from a start-up vortex that slowly convects downstream and then remains in the ambient flow in front of the fringe region. Such an external flow exists for wall jets in experimental set-ups as well, but as the computational box is not as large as the surrounding space in an experiment, the problem is more prominent. It is possible to avoid the vortex by specifying the entrainment velocity at the upper boundary. Dejoan & Leschziner (2005) used such a boundary condition based on the laminar free plane jet. However, we choose not to constrain the wall jet by prescribing the entrainment velocity. With the issues of the box width and the external flow in consideration, the flow quantities downstream of $x/b = 30$ should not be considered well represented by the DNS. The relevant part of the computational box is marked with the dashed line in figure 2.

A grid of about 62.3 million modes with 900 streamwise modes, 541 wall-normal modes and 128 spanwise modes is used, corresponding to the same resolution in the horizontal plane as for the smaller box used by Levin *et al.* (2005), while the wall-normal resolution is 20 % coarser. Dealiasing in the streamwise and spanwise directions increases the computational resolution in the simulation with a factor of 2.25 (1.5 in each direction). In figure 3(a), the energy contained in the streamwise, wall-normal and spanwise spectral modes demonstrate a decay of at least five decades. The time step is set adaptively to keep the CFL number close to a fixed number. Figure 3(b) shows the frequency spectra of the streamwise velocity fluctuation evaluated for a period of $21.7b/U_0$ and averaged over the spanwise direction at $x/b = 25$, $y/b = 0.96$. At this location, no peak of the forced frequency remains. The familiar decay law $\omega^{-5/3}$ in the inertial subrange is evident in the frequency range $0.6 < \omega b/U_0 < 6$. Beyond this range, dissipation is the dominant process giving a faster decay.

A shared memory parallelization is implemented in the numerical code. The current study uses 16 computer nodes, each with two processors. With a wall clock time of 60 h, a typical simulation calculates a period of about

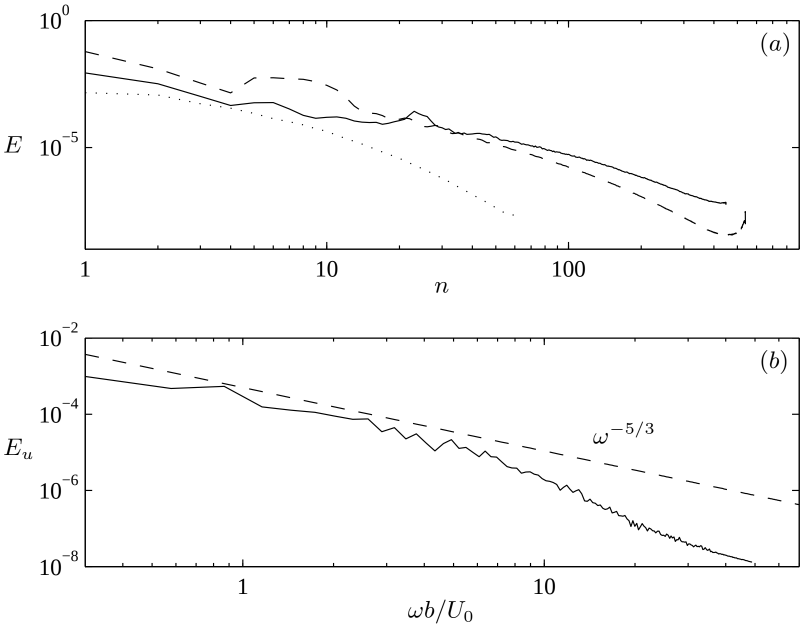

FIGURE 3. (*a*) Energy contained in streamwise (solid line), wall-normal (dashed line) and spanwise (dotted line) modes n. (*b*) Frequency spectra of streamwise velocity fluctuation averaged in the spanwise direction at $x/b = 25$, $y/b = 0.96$.

$3.5b/U_0$. The sampling of statistics is turned on at $tU_0/b = 329$ and finished at $tU_0/b = 542$, corresponding to five months of non-stop simulations.

3. Results

3.1. *Flow structures*

In order to visualize the whole wall jet from its laminar part in the vicinity of the nozzle outlet where the waves and the streaks grow, the transition region and its downstream turbulent part, three animations are made available. The animations show a time period of four fundamental periods of the forced waves and the streamwise extend is from the nozzle outlet to $x/b = 38.5$. The dark areas display regions of high streamwise velocity and the white areas display regions of backflow.

Animation I shows the (x, y)-plane in the middle of the computational domain, where the low-velocity streak is present in the outer shear layer. The height of the plane is $y/b = 4.8$. Figure 4(*a*) shows a snapshot corresponding to the first frame of the animation. In the shear-layer region, anticlockwise rotating rollers are created by the Kelvin–Helmholtz instability and follow the flow downstream. In the boundary-layer region, clockwise rotating rollers are

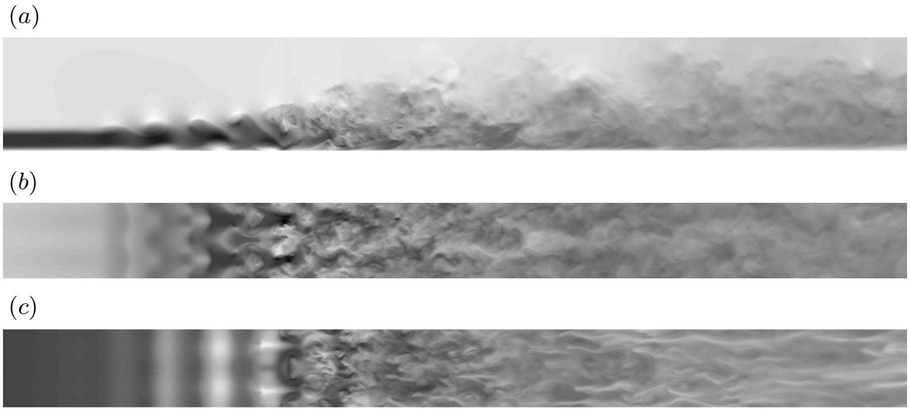

FIGURE 4. Visualization of streamwise velocity with dark areas displaying high velocity and white areas dislaying regions of backflow. The flow is from left to right and the streamwise extend of the planes are from the nozzle outlet to $38.5b$. (*a*) (x, y)-plane at the middle of the box, the height of the plane is $4.8b$. (*b*) Horizontal plane at $y/b = 0.96$. (*c*) Horizontal plane at $y/b = 0.19$.

formed and are associated with small separation bubbles. In this plane, the boundary-layer rollers move faster than the rollers in the shear-layer region. This is due to the spanwise modification of the flow by the streaks with a low-velocity streak in the shear-layer region and a weak high-velocity streak in the boundary-layer region. The shear-layer and boundary-layer rollers move at the same rate in the plane located half a spanwise wavelength to the side where a high-velocity streak is present in the outer shear layer. A weak tendency of a subharmonic instability can be seen by looking at the roll-ups in the outer shear layer; every other roll-up is moving slightly more upwards than the roll-ups in between. The breakdown to turbulence appears first in the shear-layer region and then spreads down to the boundary-layer region. The turbulent part of the wall jet behaves as expected, the velocity is faster in the inner region and slower in the outer region. Downstream, the velocity in the whole wall jet slows down while the wall jet spreads and the largest scales increases.

Animation II and III show the horizontal planes at $y/b = 0.96$ and 0.19, respectively, which are in the middle of the outer shear layer and the inner boundary layer of the laminar part of the wall jet. The width of the planes shows the entire spanwise extend of the computational box. Figures 4(*b*) and 4(*c*) show snapshots corresponding to the first frame of animation II and III, respectively.

In animation II, two spanwise periods of the streaks are visible in the upstream part of the plane. At about four nozzle heights downstream of the

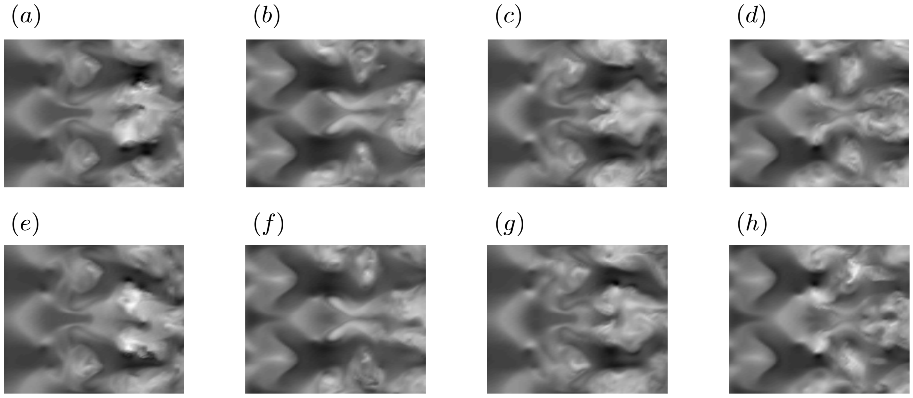

FIGURE 5. Grayscale as in figure 4. Time sequence of the flow in a horizontal plane at $y/b = 0.96$ with length $x/b = 9$ to 13. The time period between the planes is half a fundamental period $T/2 = 2.11b/U_0$: (*a*) $t = 0$, (*b*) $t = T/2$, (*c*) $t = T$, (*d*) $t = 3T/2$, (*e*) $t = 2T$, (*f*) $t = 5T/2$, (*g*) $t = 3T$, (*h*) $t = 7T/2$.

nozzle outlet, the waves start to appear. Further downstream, the interaction between the waves and the streaks forms a staggered pattern. The streaks play an important role in the breakdown process, where their growth is transformed from algebraic to exponential as they become part of the secondary instability of the waves, see Levin *et al.* (2005). In the turbulent flow downstream of the rapid breakdown, the influence of the streaks can be seen to remain for some distance. Figure 5 shows a series of snapshots taken from the animation. The streamwise extend of the snapshots is $x/b = 9$ to 13, which is the region of transition, and the time period between them is half a fundamental period $T/2 = 2.11b/U_0$ of the forced waves. Figure 5(*a*) corresponds to the first frame of the animation. The presence of the subharmonic waves can be distinguished by comparing the difference of the flow structures one fundamental period apart e.g. between figure 5(*b*) and 5(*d*). The flow structures two fundamental periods apart, as shown in e.g. figure 5(*b*) and 5(*f*) look much more alike.

In animation III, the waves are more pronounced than the streaks in the beginning of plane. However, the spanwise modification of the flow becomes strong well before the breakdown, which appears about two nozzle heights downstream of the breakdown position in the upper shear layer. The influence of the forced streaks does not remain in the turbulent flow as in the shear-layer region of the wall jet. Instead, new streaky structures with smaller scales typical for turbulent boundary layers are born and prevail throughout the length of the plane. In this plane, the presence of the subharmonic waves is easier to detect. Figure 6 shows a series of snapshots taken from the animation and the time instants are the same as for figure 5. The streamwise extend of the snapshots

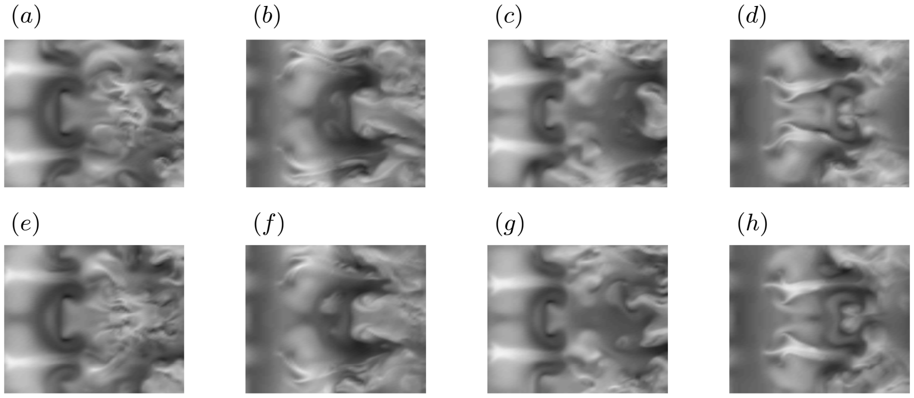

Figure 6. Visualization as figure 5 for a horizontal plane at $y/b = 0.19$ with length $x/b = 11$ to 15.

is $x/b = 11$ to 15, corresponding to the more downstream transition location. By comparing the same time instants as before, i.e. figure 6(*b*) with 6(*d*) and figure 6(*b*) with 6(*f*), the subharmonic appearance becomes clear.

Vortical structures can be identified in the flow by plotting regions where the second largest eigenvalue λ_2 of the Hessian of the pressure assumes negative values (Jeong *et al.* 1997). Levin *et al.* (2005) studied these structures and observed the following five stages in the transition mechanism: (i) Spanwise rollers are formed in the wave troughs in the outer shear layer and move downstream. In the boundary layer close to the wall beneath the wave crests, counter-rotating rollers are formed. (ii) In the presence of streaks, the shear-layer rollers are sinuously modified in the spanwise direction with the boundary-layer rollers deforming in the opposite direction. (iii) Vortex ribs are formed in the braids of the waves, extending from the top of the shear-layer roller to the bottom of the previous one. (iv) The vortex ribs follow the upward flow between two neighbouring shear-layer rollers and are associated with mushroom-shaped structures ejected from the wall jet into the ambient flow. (v) The tail legs of the vortex ribs, generated one fundamental period earlier, separate and form a vortex ring around the upcoming vortex ribs and additional counter-rotating vortex rings are created preceding breakdown to turbulence. Animation IV shows the development of the vortical structures during two fundamental periods. It shows a constant negative value of λ_2 in a box of streamwise extend from 6 to 13.6 nozzle heights, $4b$ high and one wavelength of the forced streaks wide.

To illustrate the flow structures further downstream in the turbulent wall jet, figure 7 shows the vortical structures in an instantaneous flow field. In figure 7(*a*), the transition and the early turbulent region where the turbulence has not yet reached the self-similar state is shown. The level of the isosurfaces

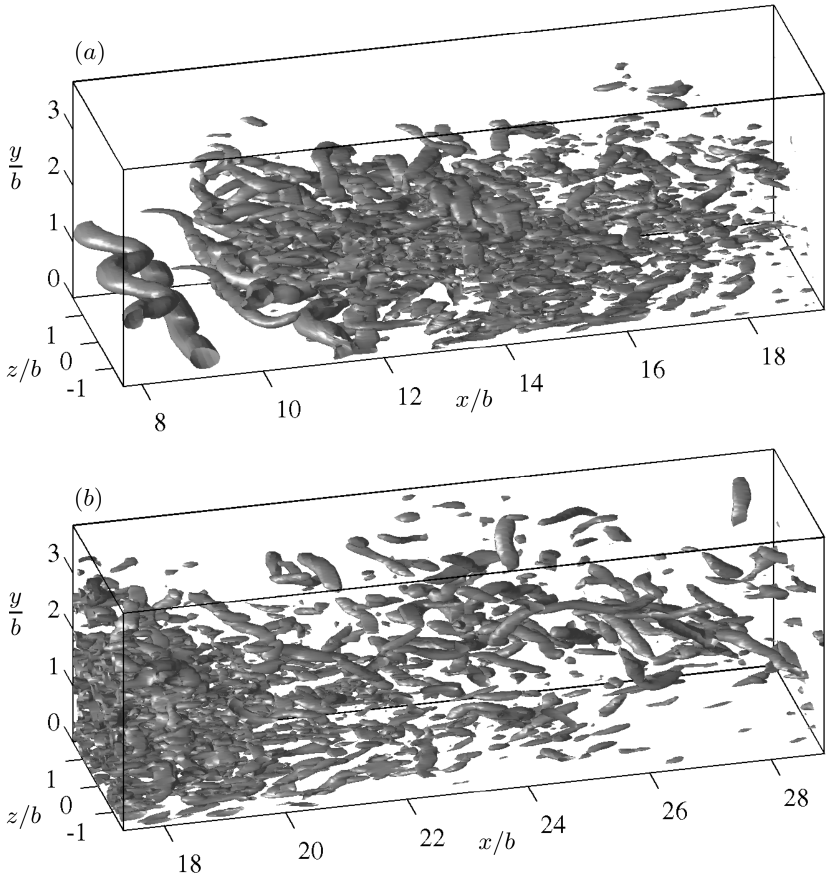

FIGURE 7. Vortex visualization of instantaneous data. The isosurfaces show a constant level of (*a*) $\lambda_2 = -\lambda_c$ and (*b*) $\lambda_2 = -\lambda_c/3$.

is the same as in animation IV. Figure 7(*b*) shows the turbulent structures further downstream where the turbulence begins to reach a self-similar state. The level of the isosurfaces is one third of the level in figure 7(*a*). Close to the wall and at about two nozzle heights above the wall, streamwise elongated structures can be seen and correspond to the vortex stretching in the layers of maximum mean shear. The structures in the outer layer, however, are stronger consistent with the larger outer peak of turbulence kinetic energy shown in figure 13(*d*).

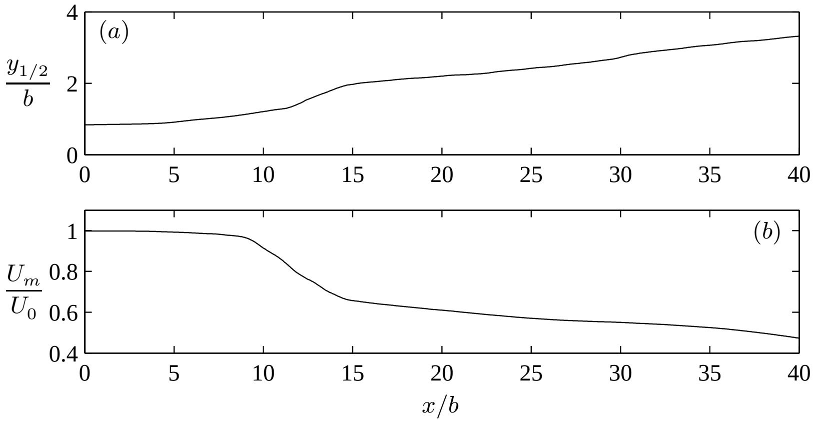

FIGURE 8. (*a*) Growth rate of the wall jet. (*b*) Decay of the wall jet velocity.

3.2. *Averaged flow characteristics*

While the preceding section concerned the dynamics of the flow, the following sections are designated to present the flow characteristics averaged in both time and spanwise direction. The data is presented in inner and outer scaling in order to identify self-similar behaviour. However, due to the low Reynolds number and the short computational domain, the data is not sufficient to contribute to a discussion of different approaches to scaling as presented recently by Wygnanski *et al.* (1992) and George (2000).

3.2.1. *Outer scaling*

Scaling with outer variables is used to identify self-similar behaviour in the outer shear layer. Here we apply the traditional scaling with the maximum velocity of the wall jet U_m and the half-width $y_{1/2}$. In comparison with data at higher Reynolds numbers, it has to be taken into account that the shear stress in the outer layer and therefore also the other properties are dependent on the Reynolds number.

The streamwise development of the variables $y_{1/2}$ and U_m governing the outer scaling is shown in figure 8. In the downstream direction, the thickness of the wall jet increases and its velocity decays as the wall jet spreads out in the quiescent surrounding. The laminar region in the vicinity of the inlet is followed by the clearly visible transitional region at about $x/b = 10$ to 15. In this region, the half-width undergoes a substantial rise whereas the maximum velocity of the wall jet decays rapidly. In the downstream region, at $x/b = 30$ to 40, the influence of the large outer vortex in the ambient flow affects the behaviour somewhat.

Figures 9(*a*) and 9(*b*) show the streamwise and wall-normal mean velocities, respectively, scaled in outer scaling. The streamwise velocity profiles between

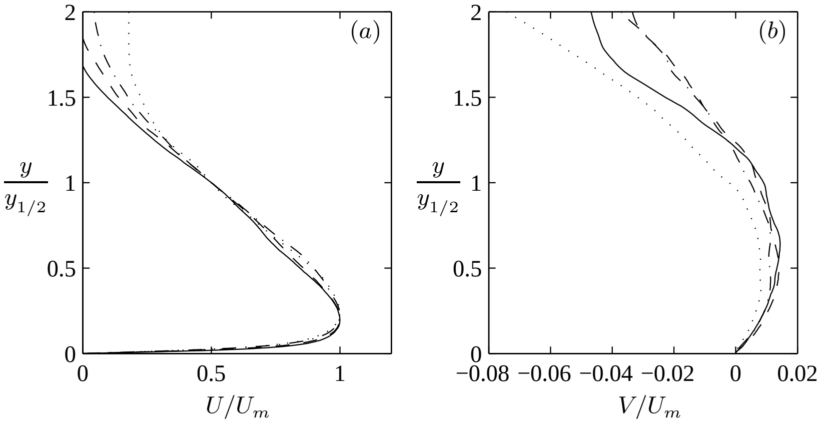

FIGURE 9. Mean velocity at $x/b = 17$ (solid line), 20 (dashed line), 25 (dashed-dotted line) and 30 (dotted line). (*a*) Streamwise component. (*b*) Wall-normal component.

$x/b = 20$ and 30 collapse reasonably well up to $y/y_{1/2} = 1$. Further away from the wall, the profiles deviate from each other owing to a secondary flow induced by the large external vortex. For the wall-normal velocity profiles, the self-similar behaviour is only obtained between $x/b = 20$ and 25. Further upstream, the deviation originates from the transition to turbulence. The outer vortex in the ambient flow compresses the downstream part of the wall jet slightly, causing the profile at $x/b = 30$ to deviate towards lower values. This deviation is larger than for the streamwise component indicating that the wall-normal velocity is effected in a higher degree than the streamwise velocity.

The streamwise, wall-normal and shear stresses and the turbulent kinetic energy in outer scaling are shown in figure 10 for the same streamwise positions as in figure 9. The profiles at $x/b = 25$ and 30 collapse reasonably well up to about $y/y_{1/2} = 1$. The levels of the stresses are substantially larger at the position $x/b = 17$ and decay thereafter in the downstream direction. In general, the turbulent quantities scaled with outer variables, are higher in the transitional region than in the self-similar region. Dejoan & Leschziner (2005) found the same tendency in their LES study, but Eriksson *et al.* (1998) measured the opposite trend for the streamwise Reynolds stress in outer scaling.

3.2.2. *Inner scaling*

The streamwise development of the wall thickness $\eta = \nu/u_\tau$ and the friction velocity u_τ, which are relevant for the inner scaling, can be interfered from figures 11(*a*) and 11(*b*). Consistent with the behaviour of a wall jet, the wall thickness increases downstream while the friction velocity decays. The streamwise evolution of the ratio between the half-width, used for the outer scaling, and the wall thickness, governing the inner scaling, is shown in figure 11(*c*).

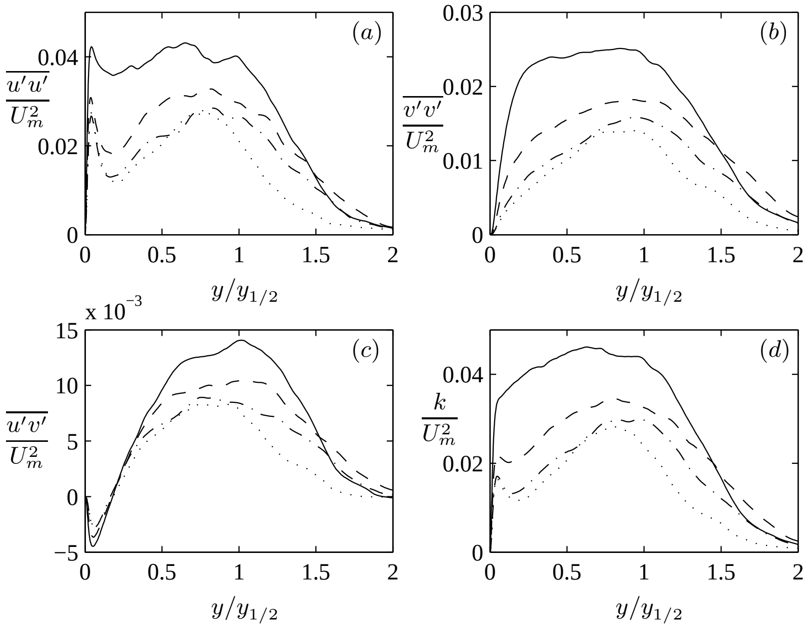

FIGURE 10. Profiles of (*a*) $\overline{u'u'}$, (*b*) $\overline{v'v'}$, (*c*) Reynolds shear stress and (*d*) turbulence kinetic energy scaled with outer variables. Lines as in figure 9.

Quantities scaled with the inner scaling are conventionally denoted with a plus (e.g. $y^+ = y/\eta$ and $u^+ = \sqrt{\overline{u'u'}}/u_\tau$). Using this notation we can see that the half-width corresponds to about 300 units in inner scaling, a value that increases with Reynolds number.

Figure 12(*a*) shows the near-wall region of the streamwise mean velocity scaled with inner scaling. Within the viscous sublayer, the profiles follow a linear law $U^+ = y^+$, shown as the grey line, up to about $y^+ = 4$. Further away from the wall, the profiles start to deviate from the linear behaviour, earlier than for a turbulent boundary layer that typically starts to deviate for values $y^+ \geq 8$. This observation agrees well with the behaviour interfered from the data measured by Eriksson *et al.* (1998) at $Re = 9000$.

In figure 12(*b*), the ratio between the rms of the fluctuating streamwise velocity and the mean streamwise velocity is shown. This value has previously been shown to be constant in the viscous sublayer, up to about $y^+ = 5$, and Alfredsson *et al.* (1988) found the value to be 0.4 in turbulent boundary-layer and channel flows. This value seems to approximately hold even for the turbulent wall jet as can be seen in the figure. A comparison has been done to numerical data computed by Kim *et al.* (1987) in turbulent channel flow. Their data which also was computed at a low Reynolds number shows a good agreement with the present simulation.

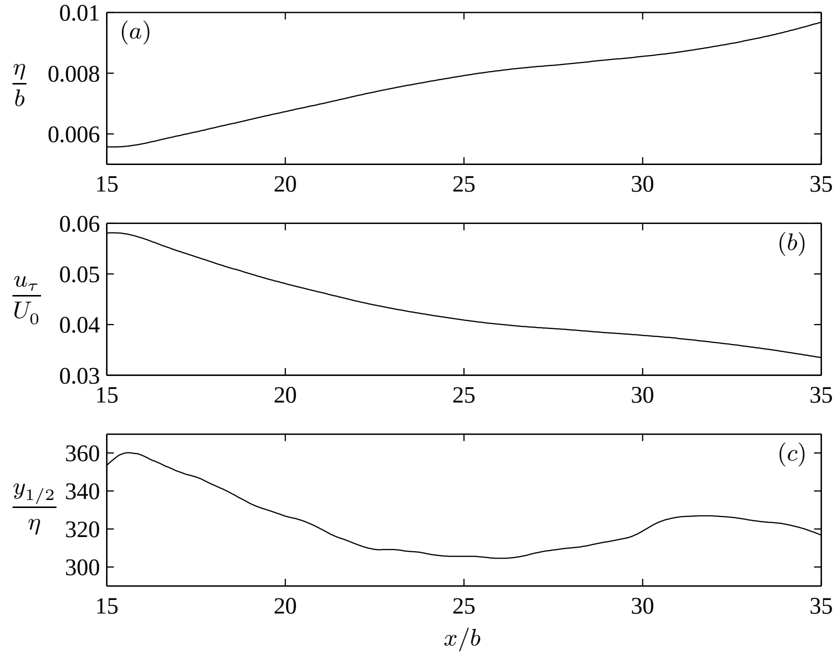

FIGURE 11. Streamwise evolution of (*a*) wall thickness, (*b*) friction velocity and (*c*) $y_{1/2}/\eta$.

The turbulent stresses shown in figure 10 are rescaled with inner scaling and displayed in figure 13. The profiles collapse reasonably well for the streamwise positions $x/b = 20$ to 30 indicating that the flow has started to exhibit a self-similar behaviour. It can be noted that the collapse provided with inner scaling is much better than with outer scaling. The profile at the position $x/b = 17$ is, however, still close to the transitional region and deviates from the other profiles. Downstream of the position $x/b = 30$, the vortex present in the end of the computational domain causes the flow to depart from the self-similar behaviour and profiles from this region are therefore not taken into account.

Unfortunately, recent measurements of turbulent stresses are not available for the Reynolds number at which our simulation is performed. As pointed out in the introduction, the recent measurements of the turbulent quantities with Laser-Doppler technique show significant differences from the earlier hot-wire measurements. The difference can be explained with the occurrence of reverse flow resulting in too low values for these components in the hot-wire measurements (Schneider & Goldstein 1994; Eriksson *et al.* 1998). However, in comparison with the data presented by Eriksson *et al.* (1998) at $Re = 9000$, the positions of the inner maxima of u^+ and k^+ agree well, whereas the levels of the turbulent fluctuations are lower due to the lower Reynolds number. The

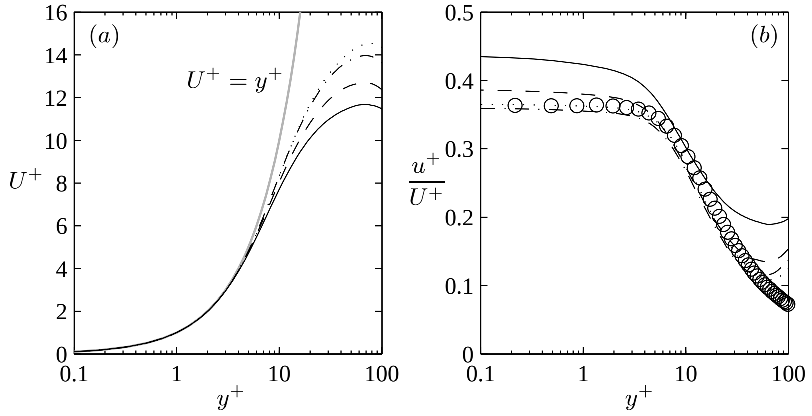

FIGURE 12. Near-wall behaviour of (*a*) streamwise mean velocity and (*b*) u^+/U^+. Data from Kim *et al.* (1987) (○). Lines as in figure 9.

profiles of the Reynolds shear stress collapse very well in inner scaling but the inner negative peak occurs closer to the wall than in the measurements by Eriksson *et al.* (1998).

As can be seen in the animations, the transition starts in the shear-layer region. This process is further studied by looking at the initial development of the fluctuation v^+ as shown in figure 14. A peak in the outer layer is clearly visible close to the transitional region at $x/b = 6$, were the flow still is laminar. In the inner layer, the formation of a plateau can be seen. A new peak starts to develop out of this plateau as the flow proceeds downstream and undergoes transition. The two peaks in the inner and outer layer evolve into a new plateau for the normal stress as the turbulent mixing increases indicating that the process of merging of the inner and the outer layer is progressing (see figure 13). It is, however, less pronounced in the DNS data than in the measurements by Eriksson *et al.* (1998) performed at the higher Reynolds number. The plateau diminishes as the flow propagates downstream. Eriksson *et al.* (1998) also observed that the plateau decays in the far field.

4. Conclusions

The first direct numerical simulation that is sufficiently large to study the self-similar behaviour of a turbulent wall jet is carried out. The Blasius wall jet and its early turbulent evolution are studied at $Re = 3090$. Two-dimensional waves and streamwise elongated streaks are introduced in the flow to trigger a natural transition mechanism. The disturbance forcing, which is matched to experimental conditions, is the same as in the previous study by Levin *et al.* (2005), but a four times larger computational box enables to study not only the transitional region but the early turbulent evolution. The simulation provides

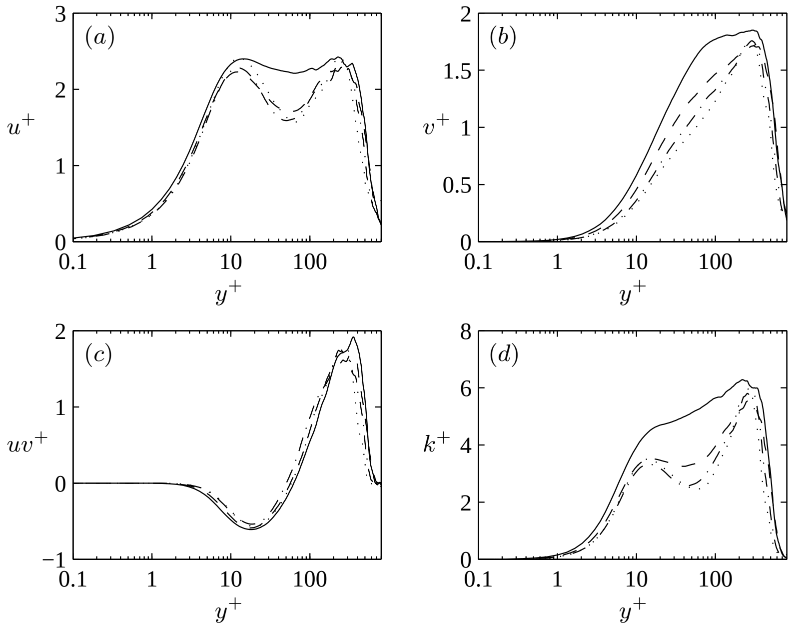

FIGURE 13. Profiles of (*a*) rms of u', (*b*) rms of v', (*c*) Reynolds shear stress and (*d*) turbulence kinetic energy. Lines as in figure 9.

detailed visualizations of the flow structures and statistics of mean flow and turbulent stresses.

In order to visualize the whole wall jet from its laminar part where the waves and streaks grow, the transition region and its downstream turbulent part, three animations are made available. They show the propagation of spanwise modified roll-ups in the outer shear layer and in the inner shear layer. Small regions of separated flow are associated with the boundary-layer rollers. A weak subharmonic wave is present in the transition region. The breakdown to turbulence appears first in the shear-layer region where the low-velocity streak exists. In the turbulent flow downstream of the rapid breakdown, the influence of the streaks can be seen to remain for some distance. About two nozzle heights downstream of the breakdown position in the outer shear layer, the inner shear layer undergoes transition. Streaky structures typical for turbulent boundary layers are born in the near-wall region of the turbulent wall jet. A forth animations shows the development of vortical structures in the region of transition. It shows that transition appears in the mushroom-shaped structures that are associated with vortex ribs that are ejected from the wall jet into the ambient flow.

The averaged data is presented in both inner and outer scaling in order to identify self-similar behaviour. Applying the traditional outer scaling with

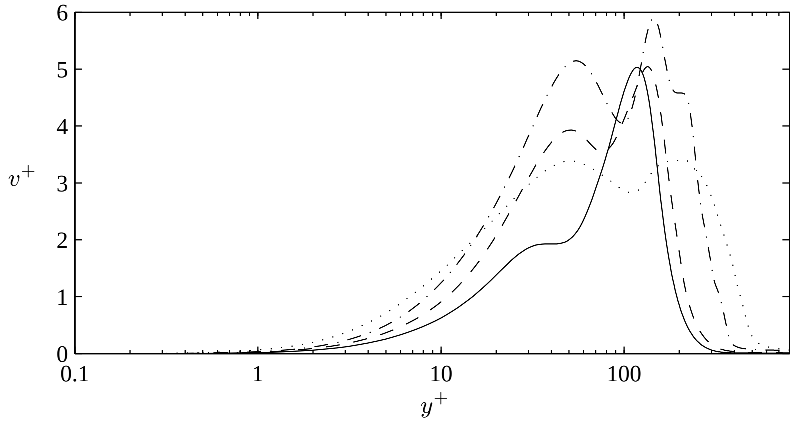

FIGURE 14. Profiles of rms of v' close to transition at $x/b = 6$ (solid line), 8 (dashed line), 10 (dashed-dotted line) and 13 (dotted line).

the maximum velocity of the wall jet and the jet half-width, the profiles of the mean streamwise velocity collapse reasonably well between $x/b = 20$ and 30 up to the half-width of the jet. Components of the Reynolds stress agree reasonably well between $x/b = 25$ and 30 up to the same wall-normal position. Downstream of $x/b = 30$, a large vortex in the ambient flow exists due to the limited numerical region. Such an external flow arises for all wall jets, even in experimental set-ups. However, the strength of the vortex decreases as the region it is allowed to occupy increases. The wall-normal velocity is effected by this vortex in a higher degree than the streamwise velocity, the self-similar behaviour is only obtained between $x/b = 20$ and 25. The turbulent quantities scaled with outer variables are higher in the transitional region than in the self-similar region. Dejoan & Leschziner (2005) found the same tendency in their LES study, but Eriksson *et al.* (1998) measured the opposite trend for the streamwise Reynolds stress in outer scaling.

Within the viscous sublayer, the profiles follow a linear law $U^+ = y^+$ up to about $y^+ = 4$. The profiles start to deviate from the linear behaviour, earlier than for a turbulent boundary layer that typically starts to deviate for values $y^+ \geq 8$ agreeing well with the behaviour found by Eriksson *et al.* (1998) at $Re = 9000$. The ratio between the rms of the fluctuating streamwise velocity and the mean streamwise velocity is found to be constant in the viscous sublayer up to about $y^+ = 3$ and the value for turbulent boundary-layer and channel flows found by Alfredsson *et al.* (1988) seems to approximately hold even for the turbulent wall jet. The profiles of the turbulent stresses collapse well for the streamwise positions $x/b = 20$ to 30 indicating that the flow has started to exhibit a self-similar behaviour in the near wall region.

It can be noted that the collapse provided with inner scaling is much better than with outer scaling. Despite the low Reynolds number and the short computational domain, in comparison to available experiments, the turbulent flow exhibits a reasonable self-similar behaviour, which is most pronounced with inner scaling in the near-wall region.

This work was funded by the Swedish Energy Agency (Energimyndigheten). The direct numerical simulation was performed at the Center for Parallel Computers at KTH. Many thanks to Stefan Wallin for valuable discussions about the turbulent statistics.

References

Abrahamsson, H., Johansson, B. & Löfdahl, L. 1994 A turbulent plane two-dimensional wall-jet in a quiescent surrounding. *Eur. J. Mech. B/Fluids* **13**, 533–556.

Alfredsson, P. H., Johansson, A. V., Haritonidis, J. H. & Eckelmann, H. 1988 The fluctuating wall-shear stress and the velocity field in the viscous sublayer. *Phys. Fluids* **31**, 1026–1033.

Dejoan, A. & Leschziner, M. A. 2005 Large eddy simulation of a plane turbulent wall jet. *Phys. Fluids* **17**, 025102.

Eriksson, J. G., Karlsson, R. I. & Persson, J. 1998 An experimental study of a two-dimensional plane turbulent wall-jet. *Exps. Fluids* **25**, 50–60.

Förthmann, E. 1934 über turbulente strahlausbreitung. *Ing. Arch.* **5**, 42–54.

George, W. K. 2000 A similarity theory for the turbulent plane wall jet without external stream. *J. Fluid Mech.* **425**, 367–411.

Jeong, J., Hussain, F., Schoppa, W. & Kim, J. 1997 Coherent structures near the wall in a turbulent channel flow. *J. Fluid Mech.* **332**, 185–214.

Kim, J., Moin, P. & Moser, R. 1987 Turbulence statistics in fully developed channel flow at low Reynolds number. *J. Fluid Mech.* **177**, 133–166.

Launder, B. E. & Rodi, W. 1981 The turbulent wall jet. *Prog. Aerospace Sci.* **19**, 81–128.

Levin, O., Chernoray, V. G., Löfdahl, L. & Henningson, D. S. 2005 A study of the Blasius wall jet. *J. Fluid Mech.* **539**, 313–347.

Lundbladh, A., Berlin, S., Skote, M., Hildings, C., Choi, J., Kim, J. & Henningson, D. S. 1999 An efficient spectral method for simulation of incompressible flow over a flat plate. *Tech. Rep.* KTH, Department of Mechanics, Stockholm.

Narasimha, R., Narayan, K. Y. & Parthasarathy, S. P. 1973 Parametric analysis of turbulent wall jets in still air. *Aeronaut. J.* **77**, 335–339.

Nordström, J., Nordin, N. & Henningson, D. S. 1999 The fringe region technique and the Fourier method used in the direct numerical simulation of spatially evolving viscous flows. *SIAM J. Sci. Comput.* **20**, 1365–1393.

Schneider, M. & Goldstein, R. 1994 Laser Doppler measurement of tubulence parameters in a two-dimensional plane wall jet. *Phys. Fluids* **6**, 3116–3129.

Visbal, M. R., Gaitonde, D. V. & Gogineni, S. P. 1998 Direct numerical simulation of a forced transitional plane wall jet. *AIAA Paper* 98-2643.

Wernz, S. & Fasel, H. F. 1996 Numerical investigation of unsteady phenomena in wall jets. *AIAA Paper* 96-0079.

Wernz, S. & Fasel, H. F. 1997 Numerical investigation of forced transitional wall jets. *AIAA Paper* 97-2022.

Wygnanski, I., Katz, Y. & Horev, E. 1992 On the applicability of various scaling laws to the turbulent wall-jet. *J. Fluid Mech.* **234**, 669–690.